REPRESENTING TROPOSPHERIC AEROSOLS AND THEIR CLIMATIC EFFECTS IN GLOBAL MODELS

Thesis by

Peter Jonathan Adams

In Partial Fulfillment of the Requirements

For the Degree of

Doctor of Philosophy

California Institute of Technology

Pasadena, California

2002

(Defended July 16, 2001)

Acknowledgments

During the past five years, I have benefited both professionally and personally from too many people to name, but I will try to start a list here. First, I would like to thank John Seinfeld for being the best kind of thesis advisor: supportive, yet not overbearing. John stayed away when I needed to figure things out for myself, kept his door open when I wanted advice, always listened attentively to my opinion, provided professional support and counsel, was understanding in time of personal emergency, and started me in an exciting area of research. It would be difficult to say enough good things about his mentoring, and I thank him for helping to ensure that these years were productive and happy ones.

A great advisor attracts a great research group, of course. It has been a pleasure and a big help to be part of the Seinfeld group and I thank past and current group members for friendship and helpful discussions. In particular, I would like to thank Rob Griffin, Athanasios Nenes, Tim VanReken, Serena Chung, and Miao-Ling Lu, for making Spalding 107 a fun home for the "Gobal Modeling Group." The uninitiated should know that the misspelling is intentional. Special thanks to Serena for teaching me to always back up my data, and to Tim for reminding me to not call it "data" anymore. Gracias a Thanos por haber soportado las provocaciones de un defendor de los turcos. To Miao-Ling, I would bequeath my cats if I could. Thanks to Rob for being "El Crucero." I hope all of our paths cross many times again.

I have benefited greatly from collaborating with some first-rate individuals over the course of this project. I would like to thank Dorothy Koch for giving me my start in

global aerosol modeling and Daniel Jacob for helpful feedback and advice. I would also like to thank both of them, Daniel's group at Harvard, and all the people at the Goddard Institute of Space Studies for help and hospitality during my visits.

Moving on to more personal acknowledgments, a number of friends have made this time in Pasadena worthwhile. In addition to members of the Seinfeld group already mentioned, Jeff Eldredge and Asimina Sierou were company on some memorable backpacking trips and were always available. Dan Giammar tried to get me in shape with his regimen of mountain biking and soccer. I feel lucky that there are many other people I would like to name here, but this thesis is long enough as it is.

Being welcomed into Jeannette and Tom's family was one of the best parts of the last five years. My appreciation goes to them, my brothers, sisters, their spouses and children for their support. Time with them was always a reminder to stay focused on the important things. I wish to thank my parents for almost twenty-nine years of their support, inspiration, example, unconditional love and acceptance. Finally, this thesis is dedicated to Amy who has seen me through all of it and will see me through much more, I'm sure. Amy, next time I dedicate something to you, I promise to make it more interesting.

Abstract

In order to better understand and quantify the direct and indirect effect of aerosols on climate, an earlier general circulation model (GCM) simulation of tropospheric sulfate has been extended by incorporating aerosol thermodynamics and microphysics. The thermodynamic simulation allows the prediction of nitrate, ammonium, and aerosol water concentrations. It is estimated that nitrate contributes as much to total aerosol mass as sulfate on regional scales in parts of Europe and North America. The direct radiative forcing associated with the sulfate-nitrate-ammonium-water mixture is estimated to be -1.14 W m^{-2} for the present day. Based on a future emissions scenario, this could increase to as much as -2.13 W m^{-2} by the year 2100, an increase that results from increased nitrate concentrations. Although currently a minor contributor to aerosol direct radiative forcing, nitrate is predicted to exceed sulfate in its contribution by the end of the century for this emissions scenario. It is also found that direct radiative forcing estimates are highly sensitive to aerosol behavior at relative humidity above 90%, highlighting the shortcomings of global models in their treatment of aerosol water uptake under partly cloudy conditions. The microphysical simulation allows the prediction of tropospheric aerosol number concentrations and size distributions, key parameters in determining the indirect effect of aerosols on clouds. A two-moment sectional algorithm is used to simulate the microphysical processes of condensation/evaporation and coagulation. It has been tested by performing a simulation of sulfate microphysics. Predicted aerosol number concentrations generally agree with observations to within 25%. The microphysical simulation also reproduces key features of the tropospheric aerosol such as increasing number concentrations with altitude and land-sea contrasts in cloud condensation nuclei concentrations. It is found that there are important uncertainties in the source rates of new particles to the atmosphere, whether from in situ nucleation or emissions of particulates, that can significantly impact predicted aerosol number and cloud condensation nuclei concentrations.

Table of Contents

List of Figures

ratios. Note that 1 μg m^{-3} NO_3^- = 400 pptv NO_3^- at 298 K and 1 bar. Above each plot, the pressure level of the corresponding model layer is indicated, as is the average mixing ratio in that layer. Contour lines are 1, 3, 10, 30, 100, 300, 1000, 3000, 10,000, and 30,000 pptv.

Figure 2.3. Scatter plot of simulated ammonium mixing ratios versus observations taken from (a) the EMEFS database, (b) the EMEP database, (c) polluted continental areas, (d) remote continental areas, and (e) marine areas.

Figure 2.4. Scatter plot of simulated ammonia mixing ratios versus observations taken from (a) the EMEFS database, (b) polluted continental areas, and (c) remote continental areas. Dashed lines indicate 2:1 and 1:2 ratios.

Figure 2.5. Global and annual average ammonia budget. Arrows indicate net fluxes. Burdens and lifetimes of ammonia and ammonium are shown in their respective boxes. Values inside parentheses are taken from a sensitivity study in which nitric acid is neglected.

Figure 2.6. Scatter plot of simulated nitrate mixing ratios versus observations taken from (a) the EMEFS database, (b) the EMEP database, (c) polluted continental areas, (d) remote continental areas, and (e) marine areas. Dashed lines indicate 2:1 and 1:2 ratios.

Plate 2.4. (a) Percent of total HNO_3 occurring in the aerosol phase. (b) Percent of acidic anions (sulfate and nitrate) neutralized by aerosol ammonium (see definition of DON in text). (c) Nitrate to sulfate molar ratios. Above each plot, the pressure level of the corresponding model layer is indicated, as is the average value for that layer.

Plate 2.5. (a) The gas ratio (defined in text). (b) Annual average aerosol water mixing ratios. (c) Aerosol water to sulfate molar ratios. Above each plot, the pressure level of the corresponding model layer is indicated as well as average values for Plates 2.5b and 2.5c.

Plate 2.6. (a) Annual average aerosol mass mixing ratios. (b) Nitrate enhancement of total aerosol mass (ratio of annual average aerosol mass to that assuming no HNO_3). Above each plot, the pressure level of the corresponding model layer is indicated, as is the average value for that layer.

Figure 2.7. Comparison of simulated and observed seasonal cycles in the mixing ratios of model species at four EMEFS sites. Mixing ratios are monthly mean (ppbv). Solid lines indicate model values and squares indicate observed values.

Figure 3.1. Estimates of anthropogenic sulfate direct forcing (W m^{-2}) versus anthropogenic sulfate burden (Tg S). Circles represent estimates from this work: SO_4^{2-}, sulfate forcing computed using composition-dependent optical properties; SO_4^{2-}/NO_3^-, sulfate and nitrate forcing using same method; SO_4^{2-} - *f*(RH), sulfate forcing computed

using α x f(RH) parameterization of aerosol optical properties. Diamonds represent other published estimates: BA95, *Boucher and Anderson* [1995]; C91, *Charlson et al.* [1991]; F97, *Feichter et al.* [1997]; KB93, *Kiehl and Briegleb* [1993]; K99, *Koch et al.* [1999]; K00, *Kiehl et al.* [2000]; P98, *Penner et al.* [1998]. Dashed lines represent the range of sulfate forcing efficiencies implicit in these estimates.

Figure 3.2. Sulfate aerosol scattering cross sections (m^2 g^{-1} SO_4^{2-}) as a function of relative humidity (%). Solid lines illustrate optical properties for sulfuric acid and ammonium sulfate computed with the composition-dependent Mie scattering calculations described in this work. For comparison, the dashed line represents those computed with the α x f(RH) parameterization.

Figure 3.3. Geographic distribution of annual average anthropogenic total (sulfate and nitrate) direct aerosol forcing (W m^{-2}) for a) modern day (2000) and b) future (2100) emissions scenarios. Values in the upper right corner of each map show the corresponding global average forcing.

Figure 3.4. A comparison of anthropogenic forcing estimated based on composition-dependent optical properties with that based on the α x f(RH) parameterization. This map shows the geographic distribution of the difference in the calculated annual average forcings for the modern day scenario. Negative values, shown in blue, indicate areas where the composition-dependent approach results in more aerosol forcing.

Figure 4.6. Model predictions of aerosol size distributions compared with observed size distributions for a) the North Atlantic, b) the free troposphere, and c) tropopause. For part a), model predictions from three modern-day scenarios are shown. In parts b) and c), only predictions from the primary emissions scenario, judged to be the most realistic overall, are shown.

Plate 4.1. Zonal average CN and CCN (0.2%) concentrations (cm^{-3}) for four model scenarios. Contours of CN concentrations are 0, 10, 20, 50, 100, 200, 500, 1000, 2000, 5000, and 10,000. Contours of CCN (0.2%) concentrations are 0, 1, 2, 5, 10, 20, 50, 100, 200, 500, and 1000.

Plate 4.2. Latitude-longitude map of annual-average a) CN and b) CCN (0.2%) concentrations (cm^{-3}) in the model surface layer for four model scenarios. Values in the upper right corners represent layer averages.

Plate 4.3. Latitude-longitude map of annual-average a) CN and b) CCN (0.2%) concentrations (cm^{-3}) in the free troposphere (634 mb) for four model scenarios. Values in the upper right corners represent layer averages.

Plate 4.4. Latitude-longitude map of annual-average a) CN and b) CCN (0.2%) concentrations (cm^{-3}) in the tropopause region (201 mb) for four model scenarios. Values in the upper right corners represent layer averages.

List of Tables

Chapter One: Introduction

In the past decade, it has been shown that airborne particulate matter, or aerosols, is an important component of the earth's climate system. It has also been realized that anthropogenic changes to tropospheric aerosols can impact climate in at least two ways. Their first impact is to scatter and absorb incoming solar radiation, thereby influencing the earth's energy budget, a process known as the direct effect. The second impact, also known as the indirect effect, is to alter the properties of clouds. This occurs because cloud droplets form when preexisting aerosol particles enter a region of the atmosphere that is supersaturated with water vapor such that they grow in size dramatically, a process known as activation. Therefore, a change in the number of aerosol particles that can act as cloud condensation nuclei (CCN) results in changes in the brightness and lifetime of the cloud.

The magnitudes of the corresponding changes in the earth's energy budget imposed by anthropogenic activities are termed the direct and indirect aerosol radiative forcings. By convention, a negative sign is given to processes that tend to cool the climate and a positive to those that tend to warm the earth, such as the greenhouse effect. The radiative forcing of greenhouse gases is relatively well quantified at +2.5 W m^{-2} with an uncertainty of +/- 10%. While the direct effects of mineral dust and black carbon aerosols also tend to warm the earth, the direct effects of other aerosol constituents and the indirect effect have a cooling effect. In contrast to the greenhouse radiative forcing, they are poorly quantified. The direct radiative forcing of sulfate is estimated at –0.4 W m^{-2}, but with an uncertainty of a factor of two. The indirect effect of aerosols via cloud

brightness may be negligibly small or as large as -2.0 W m^{-2}. The uncertainty in estimates of the indirect effect of aerosols via cloud lifetime has not been adequately constrained. The uncertainties inherent in the climatic effects of aerosols have complicated our understanding of climate change and make it difficult to forecast future changes. One reason that estimates of aerosol radiative forcings remain uncertain is that aerosols have not been adequately represented in global climate and chemistry models used to generate these estimates. The unifying theme of the thesis work presented here is to better quantify aerosol radiative forcing and increase our understanding of the relevant processes by improving the representation of aerosols in global models.

Chapters 2 and 3 of this thesis are motivated primarily by a desire to better represent the direct effect of aerosols. A key factor in determining the magnitude of the direct effect is water uptake by the aerosol as this can significantly enhance the total amount of mass associated with the aerosol and influence its size distribution as well. Water uptake, in turn, depends on the composition of the aerosol. For example, sulfuric acid aerosol is more hygroscopic than ammonium sulfate. In addition, nitrate aerosol can form when sufficient ammonia is present. Chapter 2, therefore, describes the simulation of the tropospheric sulfate-nitrate-ammonium-water aerosol system. This is accomplished by incorporating an aerosol thermodynamic equilibrium module in a general circulation model (GCM). Chapter 3 is the logical extension of that work, in which the direct radiative forcing of the sulfate-nitrate-ammonium-water system is estimated for the present day and for a future emissions scenario.

The last segment of this thesis work is concerned with global simulations of aerosol microphysics. This work is motivated by the large outstanding uncertainty in the

indirect effect of aerosols. Previous estimates of the magnitude of the indirect effect have been based on global aerosol models that were limited in that they predicted only the total aerosol mass of a given component. Since the indirect effect is sensitive to the number of particles and their size distribution, one would ideally like a global model that predicts this type of information. To do so, one needs a global aerosol model that explicitly represents the microphysical processes of condensation/evaporation, coagulation, and nucleation. The development and initial testing of such a model is described in Chapter 4. Results and conclusions of the thesis as a whole are presented in Chapter 5.

Chapter Two: Global Concentrations of Tropospheric Sulfate, Nitrate, and Ammonium Aerosol Simulated in a General Circulation Model

Reference: Adams, P. J., J. H. Seinfeld, and D. M. Koch, Global concentrations of tropospheric sulfate, nitrate, and ammonium simulated in a general circulation model, *J. Geophys. Res., 104,* 13,791-13,823, 1999.

Abstract. Global sulfate aerosol composition is simulated online in the Goddard Institute for Space Studies general circulation model II′ (GISS GCM II-prime). Four sulfur species, hydrogen peroxide, gas-phase ammonia, and particulate ammonium are the prognostic tracer species, the emissions, transport, and deposition of which are explicitly simulated. Nitric acid fields are prescribed based on a global chemical transport model. An online thermodynamic equilibrium calculation determines the partitioning of ammonia and nitrate between gas and aerosol phases, and the quantity of aerosol water based on the temperature, relative humidity, and sulfate concentration in each GCM grid cell. The total global burden of sulfate, nitrate, ammonium, and aerosol water is 7.5 Tg and is most sensitive to changes in sulfur emissions. Tropospheric lifetimes for ammonium and ammonia are 4.2 and 0.9 days, respectively; the tropospheric ammonium burden is 0.30 Tg N, compared with 0.14 Tg N for ammonia. Simulated ammonium concentrations are generally within a factor of 2 of observations. Subgrid variability in measured concentrations hinders comparison of observations to predictions. Ammonium nitrate aerosol plays an important role in determining total aerosol mass in polluted continental areas. In the upper troposphere and near the poles, cold temperatures allow unneutralized nitric acid to condense into the aerosol phase. Acidic aerosol species tend to be neutralized by ammonia to a greater degree over continents than over oceans. The aerosol is most basic and gas-phase ammonia concentrations are highest over India. Water uptake per mole of sulfate aerosol varies by two orders of magnitude because of changes in relative humidity and aerosol composition. Spatial variations in aerosol

composition and water uptake have implications for direct and indirect aerosol radiative forcing.

2.1. Introduction

In recent years, substantial progress has been made towards understanding how airborne aerosols, especially sulfate, influence the earth's climate and atmospheric chemistry [*Intergovernmental Panel on Climate Change (IPCC),* 1996; *National Research Council,* 1996]. Sulfate aerosols directly perturb the atmospheric radiation balance by scattering sunlight back into space. Sulfate particles are also an important source of cloud condensation nuclei (CCN), and the number and composition of sulfate particles help to determine resulting cloud properties. In such a way, changes in aerosol sulfate may indirectly perturb the atmospheric radiation balance by influencing the optical properties of clouds. Determining the magnitude and geographical distribution of climate forcing from sulfate aerosols is one of the key outstanding issues in assessing anthropogenic influence on climate. The aerosol sulfate anion is just one of many forms of atmospheric sulfur, including sulfur dioxide (SO_2), dimethyl sulfide (DMS), methanesulfonic acid (MSA), hydrogen sulfide (H_2S), carbon disulfide (CS_2), carbonyl sulfide (COS), dimethylsulfoxide (DMSO), and dimethyl sulfone ($DMSO_2$). Most anthropogenic sulfur is emitted into the atmosphere in the form of sulfur dioxide by activities such as fossil fuel combustion and biomass burning, although a small amount is emitted as sulfate as well. Volcanic activity is a small, but important, natural source of

sulfur dioxide. The largest natural source of sulfur, however, is the flux of DMS from the oceans. The biosphere is also a source of a variety of reduced sulfur compounds. DMS is oxidized in the atmosphere by OH and NO_3 radicals to form sulfur dioxide as well as MSA and DMSO. Sulfur dioxide oxidation to form sulfate occurs either in the gas-phase by the OH radical or in cloud droplets by hydrogen peroxide (H_2O_2) and, to a lesser extent, ozone. Predominant sinks of atmospheric sulfur include wet and dry deposition of sulfur dioxide and sulfate, leading to lifetimes of about a day, in the case of SO_2, and 4-6 days for sulfate. A significant amount of tropospheric sulfate occurs as part of the sea salt aerosol. These particles tend to be sufficiently large, however, that they have a much shorter lifetime. As a result, sea salt sulfate is typically excluded from consideration as a part of the tropospheric sulfur cycle.

Sulfate aerosols typically contain substantial amounts of condensable gases such as ammonia and nitric acid that exist in particle form as the ammonium, NH_4^+, and nitrate, NO_3^-, ions, respectively. Besides contributing to the total aerosol mass, the quantities of ammonium and nitrate in the sulfate aerosol affect the amount of water uptake at a given relative humidity, and also influence the optical properties of the aerosol via the refractive index. The composition of the aerosol therefore plays an important role in both the direct and indirect effects on climate.

At thermodynamic equilibrium, the amount of water contained in an aerosol particle depends on temperature, relative humidity, and composition [*Seinfeld and Pandis,* 1998]. For example, at 298 K and 80% relative humidity the volume of an aqueous solution of sulfuric acid is about 5.5 times greater than its volume at 0% relative humidity, whereas

the volume of an ammonium bisulfate particle is only 3.5 times greater. If metastable equilibria are considered, water uptake also depends on the history of the particle. The reason the particle's history plays a role in water uptake is because of the hysteresis effect in which the relative humidity required for a single-component dry solid particle to deliquesce is higher than the relative humidity at which an aqueous droplet crystallizes. The deliquescence and crystallization relative humidities depend, in turn, on particle composition. An ammonium sulfate particle crystallizes at 40% relative humidity, while ammonium bisulfate retains water to much lower relative humidities. For multicomponent mixtures the deliquescence and crystallization behavior is even more complex. Whereas the size a particle attains via uptake of water is influenced, as described above, by its composition, its refractive index is also determined by composition. Sulfuric acid is more hygroscopic than ammonium bisulfate or ammonium sulfate, but ammonium sulfate has the highest refractive index of the three. The overall climate forcing efficiency of sulfate aerosol increases with both water uptake and refractive index, so that the higher hygroscopicity of sulfuric acid is partly compensated by its lower refractive index and vice versa. For example, *Boucher and Anderson* [1995] found that at 80% relative humidity, the climate forcing efficiency of the sulfate ion is –132 W g^{-1} SO_4^{2-} for sulfuric acid, -104 W g^{-1} SO_4^{2-} for ammonium bisulfate, and –125 W g^{-1} SO_4^{2-} for ammonium sulfate. The degree to which sulfate is neutralized by ammonium therefore can influence its climate forcing efficiency by more than 25%.

Beyond modifying the hygroscopic and radiative properties of sulfate aerosol, ammonia and nitrate merit study for their own reasons. Ammonia is the only base present

in sufficient quantities to neutralize a significant fraction of the sulfuric and nitric acids found in the troposphere. As such, it plays a key role in determining the pH of cloud condensation nuclei and precipitation. The pH of the atmospheric aqueous phase affects, in turn, the rates of several important chemical reactions. Since it has been estimated that the anthropogenic contribution to the ammonia budget is nearly four times the natural contribution [*Bouwman et al.,* 1997], this has created interest in two effects of ammonia and ammonium deposition on the biosphere. Such deposition increases the supply of fixed nitrogen available for plant growth and also, somewhat paradoxically, has been implicated in soil acidification [*Galloway,* 1995]. Finally, since the rate of nucleation of the ternary H_2SO_4-NH_3-H_2O system is estimated to be several orders of magnitude higher than that of the binary H_2SO_4-H_2O system [*Coffman and Hegg,* 1995], the rate of new particle formation in the presence of ammonia might be influential in the marine boundary layer.

Important anthropogenic sources of ammonia include emissions from domestic animals, fertilizer application, crops, and biomass burning [*Bouwman et al.,* 1997]. Emissions from the oceans, undisturbed soils, and natural vegetation are the primary natural emissions of ammonia. Once in the atmosphere, gaseous ammonia may absorb into the aerosol phase, especially in the presence of sulfate, to form the ammonium (NH_4^+) ion. Both ammonia and ammonium are removed from the atmosphere via wet and dry deposition. Like sulfur dioxide and sulfate, they have short lifetimes of about a day and between four and six days, respectively.

Aerosol nitrate is formed from nitric acid, which can dissolve directly in an aqueous aerosol solution or react with ammonia to form ammonium nitrate aerosol. Atmospheric nitric acid is the oxidation product of NO_x and is therefore found in areas with high emissions of NO_x. Fossil fuel combustion, release from soils, biomass burning, and lightning are the primary producers of NO_x. By serving as a reactive odd nitrogen (NO_y) reservoir, nitric acid couples aerosol dynamics to gas-phase photochemistry. Modeling nitrate aerosol will allow this coupling to be examined in the future. Moreover, nitrate aerosol contributes to total aerosol radiative forcing on a regional basis. For example, radiative forcing attributable to nitrate alone has been estimated to be as large as –0.8 W m^{-2} in western Europe [*van Dorland et al.*, 1997].

The tropospheric sulfur cycle has been modeled extensively in global chemical transport models (CTMs) [*Erickson et al.*, 1991; *Langner and Rodhe,* 1991; *Pham et al.*, 1995; *Chin et al.,* 1996; *Kasibhatla et al.,* 1997], and also in general circulation models (GCMs) [*Penner et al.*, 1994; *Feichter et al.,* 1996; *Lelieveld et al.,* 1997; *Kjellstrom,* 1998; *Roelofs et al.,* 1998; *Koch et al.,* 1999]. All of these studies focus on total mass concentration of sulfate particles, ignoring the ammonium, nitrate, and water that also comprise the aerosol.

Several studies have been made of both the direct and indirect radiative effects of sulfate aerosols. Studies of the direct effect may be roughly divided into two categories. In the first category [*Charlson et al.,* 1991; *Mitchell et al.*, 1995a, b; *Mitchell and Johns,* 1997], the direct effect of sulfate aerosol on the atmospheric radiation budget is parameterized as a change in the planetary reflectivity proportional to the sulfate burden

[*Charlson et al.,* 1991]. In this category of studies, a uniform empirical value of the sulfate mass scattering coefficient is used. Assumptions about the size, composition, and water content of the sulfate aerosol are implicit in the choice of the value for the mass scattering coefficient, and therefore, using a uniform value ignores variation in these properties. In a second category of studies of the direct effect [*Kiehl and Briegleb,* 1993; *Haywood and Shine,* 1995; *Chuang et al.,* 1997; *Feichter et al.,* 1997; *Haywood et al.,* 1997; *van Dorland et al.*, 1997; *Haywood and Ramaswamy,* 1998], Mie theory is used to calculate the optical properties of the aerosol, which may then be used in a simple radiation scheme such as that of *Charlson et al.* [1991] or, more often, serve as input to a GCM radiation calculation. Aerosol optical properties depend on aerosol composition, size distribution, and water uptake. Table 2.1 summarizes various assumptions made in Mie theory calculations with regards to these aerosol properties. Typically, the aerosol has been assumed to follow a log normal size distribution. The degree to which sulfate is neutralized by ammonium has been assumed to be uniform throughout the troposphere, usually in the form of ammonium sulfate. Except for *van Dorland et al.* [1997], who assumed that 50% of boundary layer HNO_3 and 25% of free tropospheric HNO_3 occurs as nitrate aerosol with the same optical properties as sulfate, nitrate has been ignored in calculations of the global radiative effect of sulfate aerosols. Many of the studies treat water uptake by the aerosol as unvarying throughout the atmosphere, either by assuming a fixed relative humidity or by applying a uniform relative humidity growth factor. Therefore Mie theory calculations have also made assumptions about the composition and water content of the sulfate aerosol, and ignore spatial variations in these properties.

Previous work indicates that an online GCM model of sulfate composition, including explicit treatment of ammonium, nitrate, and water, will lead to more realistic estimates of the magnitude and distribution of direct radiative forcing than those that result from imposing assumptions of uniform composition and water uptake on sulfur-only concentration fields. For example, *van Dorland et al.* [1997] estimated that the global and annual average direct radiative forcing from sulfate aerosols is –0.36 W m^{-2} assuming a uniform relative humidity of 80%, but only –0.32 W m^{-2} taking into account local variations in relative humidity. Although this is a small effect when globally averaged, locally the effect of relative humidity was larger. Whereas the effect of relative humidity variations may be small when globally averaged, this averaging disguises large differences in the spatial distribution of forcing that cannot be determined by radiative calculations that assume a fixed relative humidity. As mentioned above, sensitivity tests on the ammonium content have shown that it has more than a 25% effect on sulfate forcing efficiency. Given the local variations in global ammonia emissions, this too could alter the spatial distribution of the forcing. Simulating aerosol composition and water uptake online in a GCM therefore can reduce uncertainties in calculating direct radiative forcing and generate a spatial distribution of forcing that realistically accounts for variations in aerosol properties.

Aerosol composition also plays a role in determining the magnitude of the indirect effect, although there are still too many unanswered questions for GCM estimates of the indirect effect to take account of this in a detailed way. One GCM study of climate response to indirect sulfate forcing arbitrarily chose a climate forcing of -4 W m^{-2} with a

spatial distribution in proportion to local sulfate concentrations [*Erickson et al.*, 1995], while another study used satellite measurements of cloud droplet effective radii as input to a GCM [*Boucher,* 1995]. Most commonly, observational data are used to derive empirical relationships between cloud droplet number concentration and sulfate mass [*Jones et al.,* 1994; *Boucher and Lohmann,* 1995; *Feichter et al.,* 1997; *Lohmann and Feichter*, 1997]. Another method, in which the aerosol size distribution is determined by the fraction of anthropogenic sulfate formed via aqueous oxidation with the number of CCN depending on this size distribution, total number of aerosol particles, and the mean vertical velocity of the GCM, is described by *Chuang et al.* [1997]. No GCM study of the indirect effect therefore has considered aerosol composition as a variable, although water uptake by aerosol particles, and hence cloud droplet activation, depends on aerosol composition. Recent work [*Kulmala et al.,* 1993] also suggests that the presence of nitric acid can enhance cloud droplet activation by contributing soluble material to aerosol particles. A GCM simulation of aerosol composition therefore lays the groundwork for a more thorough parameterization of the indirect effect in GCMs, although substantial work must still be done before this is feasible.

While several models of atmospheric ammonia on the regional scale exist [*Iversen et al.*, 1991; *Asman and van Jaarsveld,* 1992; *Fekete and Gyenes,* 1993; *Hov et al.,* 1994; *Galperin and Sofiev*, 1998; *Metcalfe et al.,* 1998; *Singles et al.,* 1998; *Syri et al.,* 1998], only one global modeling effort has been reported [*Dentener and Crutzen,* 1994] (hereinafter referred to as DC94). This study was the first to derive a 10° x 10° emissions inventory for ammonia and calculate global distributions of ammonia and ammonium

using a three-dimensional model. It was limited, however, by coarse horizontal resolution and a thick boundary layer, as well as simple boundary layer and cloud parameterizations. It also treated condensation of ammonia on sulfate as a pseudo-first-order kinetic process and artificially imposed a maximum limit on neutralization of 1.5 mol of ammonium per mole of sulfate.

Radiative forcing attributable to nitrate aerosol was estimated by *van Dorland et al.* [1997], but they obtained their aerosol nitrate concentrations by assuming that 50% of all boundary layer and 25% of free tropospheric HNO_3 was present as accumulation mode nitrate aerosol. They found that the average radiative forcing in the Northern Hemisphere due to nitrate was about 10% of that due to sulfate, but more significant in localized regions such as western Europe. To the best of our knowledge, no one has calculated the amount of particulate nitrate in a three-dimensional global model.

In this study, we simultaneously model the transport of sulfur species, ammonium, and ammonia in a general circulation model and compute the ammonium, nitrate, and water content of sulfate aerosols according to thermodynamic equilibrium. Assuming thermodynamic equilibrium in each cell of the GCM allows us to understand how aerosol composition varies from region to region of the globe and also alleviates the necessity of arbitrarily specifying the ammonium to sulfate molar ratio.

The following section describes the GCM used in this study, the model of sulfur transport used as a starting point for this work, and the enhancements made to model aerosol composition. We then present and discuss simulated concentration fields of ammonia, ammonium, nitrate, and aerosol water content and compare them to available

observations. Sensitivity studies are also analyzed to demonstrate how total aerosol mass is affected by the availability of various precursors. The final section summarizes important conclusions drawn from this work.

2.2. Model Description

2.2.1. GISS GCM II-Prime

Tracer transport is handled online in the Goddard Institute for Space Studies General Circulation Model II-prime (GISS GCM II-prime). A description of the older GISS GCM II is given by *Hansen et al.* [1983]; *Rind and Lerner* [1996] provide a discussion of recent improvements relevant to tracer studies. The resolution of the GISS GCM II-prime is 4° latitude by 5° longitude in the horizontal directions, with nine sigma layers in the vertical, from the surface to 10 mbar. The model surface layer is 50 mbar thick. The top one or two layers, centered around 27 and 103 mbar, are situated in the lower stratosphere. The model time step for tracer processes is 1 hour. The version of the GCM used in this study uses a quadratic upstream module for advection of heat and moisture, and a fourth-order scheme for tracer advection. The GCM carries liquid water as a prognostic variable in the large-scale cloud scheme [*Del Genio et al.,* 1996]. Moist convection is implemented by a variable mass flux scheme that includes two plumes, one entraining and one nonentraining, as well as a downdraft [*Del Genio and Yao,* 1993]. The boundary layer parameterization uses a new scheme that incorporates a finite modified Ekman layer [*Hartke and Rind,* 1997]. The improved parameterizations of these processes make this model especially suitable for studying aerosol sulfate, which resides mostly in the boundary layer and of which a substantial amount is formed via in-cloud oxidation.

2.2.2. Sulfur Cycle

An online sulfur model [*Koch et al.,* 1999] that predicts the concentrations of SO_2, SO_4^{2-}, DMS, MSA, and H_2O_2 was used as the starting point for this work. Hydrogen peroxide is included as a prognostic species because it is depleted by reaction with SO_2 in heavily polluted areas during winter [*Chin et al.,* 1996]. This model includes Global Emissions Inventory Activity (GEIA) emissions of SO_2 and SO_4^{2-} from fossil fuel combustion and industrial activities, SO_2 emissions from biomass burning, aircraft, and noneruptive volcanoes, as well as an oceanic DMS source. SO_2 is oxidized in cloud by H_2O_2 and in the gas phase by the OH radical. Including H_2O_2 as a prognostic species has the effect of limiting the amount of SO_2 that oxidizes to SO_4^{2-} in polluted areas in the winter. As a result, less ammonia will condense into the aerosol phase so more gas-phase ammonia will be available for the formation of ammonium nitrate. Both OH and NO_3 radicals oxidize DMS. Dry deposition of all species in the sulfur model, except DMS, uses a resistance-in-series parameterization [*Wesely and Hicks,* 1977] and is implemented as described by *Chin et al.* [1996], except that GCM surface momentum and heat fluxes are used to calculate the aerodynamic resistances. No subgrid deposition parameterization is used.

Wet deposition of dissolved tracers generally follows the GCM treatment of liquid water [*Del Genio and Yao,* 1993; *Del Genio et al.*, 1996]. The GCM distinguishes between large-scale and convective clouds. After reacting with each other, the remaining SO_2 and H_2O_2 dissolve into cloud water according to effective Henry's law coefficients assuming a pH of 4.5. Sulfate and MSA aerosols are assumed to be infinitely soluble.

The GCM convective scheme considers both entraining and nonentraining plumes as well as compensating subsidence and downdrafts. All liquid water associated with convective clouds either precipitates, evaporates, or detrains into the large-scale cloud cover within the one-hour time step of the model, and dissolved tracer species are either deposited or returned to the atmosphere in corresponding proportions. The large-scale cloud scheme of the GCM carries liquid cloud water content as a prognostic variable. Large-scale clouds therefore may persist for several model time steps. Tracer budgets, on the other hand, do not distinguish between dissolved and undissolved tracer. Instead, tracers are scavenged in large-scale clouds according to a first-order rate loss parameterization that depends on the rate of conversion of cloud water into rainwater. Below both types of clouds, aerosols and soluble gases are scavenged according to a first-order parameterization that depends on the amount of precipitation. Dissolved tracer is also returned to the atmosphere if precipitation from either type of cloud evaporates.

The model year used for this study has an average sulfate burden of 0.73 Tg S. This value is intermediate in comparison with other sulfur models that exhibit burdens from 0.53 Tg S [*Chin et al.,* 1996] to 1.05 Tg S [*Lelieveld et al.*, 1997].

The model of sulfate composition has been developed by adding species to the sulfur model described above. Sulfur, ammonia, ammonium, and nitrate are all considered in the standard model run, while nitrate is omitted in a subsequent sensitivity run.

2.2.3. Ammonia Cycle

The ammonia cycle was simulated by adding two tracers: gas-phase ammonia (NH_3) and aerosol ammonium (NH_4^+). Ammonia emissions were specified according to a recent GEIA inventory [*Bouwman et al.*, 1997]. The total ammonia source in this inventory was estimated to be 53.6 Tg N yr^{-1}, and Table 2.2 shows this total according to source type. Domestic animals contribute most to total emissions, followed by fertilizers, oceans, soils under natural vegetation, crops, and others. The fact that agricultural activities contribute most to ammonia emissions implies that densely populated regions tend to have the highest ammonia emissions. The geographic distribution of NH_3 emissions is shown in Plate 2.1. The strongest source regions occur in eastern China, India, Europe, the American Midwest, and southern Brazil. The total emissions estimate of the GEIA inventory used here is higher than the 45 Tg N yr^{-1} used by DC94 in their model of the ammonia cycle, lower than the 75 Tg N yr^{-1} estimate of *Schlesinger and Hartley* [1992], and practically the same as the 54 Tg N yr^{-1} estimate of *Warneck* [1988]. The GEIA inventory specifies the seasonality of the oceanic source only, leaving all other emissions estimates as annual averages. It is obvious, however, that ammonia emissions from crops and fertilizer application will occur overwhelmingly during the growing season. Ammonia volatilization from animal excreta increases with temperature [*Bouwman et al.*, 1997] and seasonal differences in waste management, animal housing, and urease activity could also lead to seasonality in emissions from domestic animals. Therefore, following DC94, a seasonal cycle was imposed on the domestic animals, fertilizers, and crops

sources by weighting emissions by the number of daylight hours. While the choice of this scheme is completely arbitrary, in the absence of any more detailed information, this is the simplest way to achieve a plausible temporal distribution of ammonia emissions. The GEIA inventory specifies the oceanic flux as a function of location and month. This flux has been calculated assuming an atmospheric ammonia concentration of zero such that the 8.2 Tg N yr^{-1} represents the potential, rather than the net, oceanic emission of ammonia to the atmosphere. This is appropriate since the GCM calculates dry deposition of gas-phase ammonia to the ocean surface. The uncertainty in the global annual emission of ammonia was estimated to be ± 25% [*Bouwman et al.,* 1997], and uncertainties on shorter spatial and temporal scales are expected to be larger. This should be kept in mind when evaluating model results.

Atmospheric ammonia undergoes reaction with the OH radical according to [*DeMore et al.,* 1997]

$$NH_3 + OH \rightarrow NH_2 + H_2O$$

At 298 K, at an OH concentration of 5 x 10^5 molecules cm^{-3}, the lifetime of ammonia with respect to this reaction is about 150 days. As this lifetime is much longer than the actual lifetime of ammonia, this reaction plays only a very small role in the global ammonia budget. Nevertheless, this reaction is accounted for in the GCM using three-dimensional fields of five-day average OH radical concentrations (C. Spivakovsky, personal communication, 1998). To account for the diel variation in OH radical

concentrations, an instantaneous value is obtained by scaling the five-day average value to the cosine of the solar zenith angle.

Both wet and dry deposition of ammonia and ammonium follow the sulfur model. For purposes of wet deposition, the effective Henry's law coefficient for ammonia in precipitation at an assumed pH of 4.5 is 3.3×10^6 M atm^{-1}. The necessary data to estimate the surface resistance for dry deposition of ammonia are given by *Wesely* [1989]. The deposition velocity of ammonium is assumed to be the same as that of sulfate. Ammonium, like sulfate, is assumed to be infinitely soluble in rainwater.

2.2.4. Timescales for Gas-Aerosol Equilibration

We assume that the volatile species ammonia and nitric acid achieve an equilibrium partitioning between gas and aerosol phases during the one-hour model time step. Therefore mass transport between gas and aerosol phases is not considered in the simulations presented here. Detailed box model calculations [*Meng and Seinfeld,* 1996] have shown that the time required for a particle to achieve equilibrium with the gas phase depends primarily on its size. In general, ammonia reached gas-aerosol equilibrium with the accumulation mode sulfate particles that are the focus of this study in less than an hour. The time to reach equilibrium was somewhat longer than an hour for the lower aerosol concentrations encountered in remote marine regions. The same was true for nitric acid except at lower relative humidities, where the time to reach equilibrium was 1.59 and 1.24 hours for 60% and 50% relative humidity, respectively. This is only slightly longer than the model time step, so the assumption that gas-aerosol equilibrium is

attained should not significantly compromise our results. Moreover, we can expect that the characteristic time for significant changes in GCM temperature, relative humidity, sulfate, or ammonia concentrations that perturb nitric acid gas-aerosol equilibrium to occur will generally be longer than a single one-hour time step. For example, assuming an east-west wind speed of 4 m s^{-1}, the time required for an air parcel to traverse a midlatitude GCM grid cell (about 400 km) is about 28 hours. In other words, the temporal and spatial scales in the GCM effectively filter out most high-frequency variability that exists in the real atmosphere. The aerosol populations simulated here experience mostly lower-frequency variability, such as diurnal temperature cycles, large-scale weather patterns, and seasonal changes in temperature, emissions, and sulfur chemistry. Since the characteristic time for gas-aerosol mass transfer is much shorter than these timescales, it is reasonable to assume that thermodynamic equilibrium is attained. The only exception to this is convective mixing, which has the potential to change temperature and humidity profiles on a timescale comparable to some of the longer gas-aerosol equilibrium timescales.

2.2.5. Aerosol Thermodynamics

Volatile atmospheric species tend to partition themselves between gas and aerosol phases in accordance with thermodynamic equilibrium [*Seinfeld and Pandis,* 1998]. Several thermodynamic models describing gas-aerosol equilibrium for inorganic species, such as nitrate and ammonium, have been developed over the last decade or more [*Bassett and Seinfeld,* 1983, 1984; *Saxena et al.,* 1986; *Pilinis and Seinfeld,* 1987; *Wexler*

and Seinfeld, 1990, 1991; *Kim et al.,* 1993a, b; *Kim and Seinfeld,* 1995; *Meng et al.,* 1995; *Jacobson et al.,* 1996; *Clegg et al.,* 1992, 1998a, b; *Nenes et al.,* 1998]. We compute equilibrium using the thermodynamic equilibrium code ISORROPIA [*Nenes et al.,* 1998], which partitions the total amount of ammonia and nitric acid between the gas and aerosol phases. ISORROPIA provides the capability of computing the equilibrium composition of an internally mixed aerosol particle consisting of sulfate, nitrate, chloride, ammonium, sodium, and water. Sodium and chloride were not considered during any of the simulations presented here. Inclusion of ISORROPIA as an online component of the simulation imposes a significant, but manageable, computational burden. A 12-month simulation requires slightly less than four days for completion on one node of a 135-MHz IBM SP2 system. Although the complete thermodynamic equilibrium calculations account for roughly three quarters of processor time, they alleviate the need for a thermodynamic parameterization or simplifying assumptions about the ammonium to sulfate ratio. Furthermore, it has been shown that ISORROPIA gives results similar to those of other equilibrium codes (e.g., SCAPE, SEQUILIB) but is 10 times or more faster [*Nenes et al.*, 1998].

During its lifetime a typical sulfate particle passes into a cloudy area, rapidly takes up water, and grows to a size typical of cloud droplets (between 3 and 100 μm). More often than not, the same particle leaves the supersaturated cloudy region and loses water by evaporation, shrinking into the accumulation mode aerosol size range (between 0.1 and 1 μm). Overall sulfate residence time considerations suggest that a typical sulfate particle repeats this cycle many times before being removed from the atmosphere. Because of

the deliquescence-crystallization hysteresis effect mentioned above, once activated, these particles will never fully dry unless they experience an unusually low relative humidity (less than 40% for fully neutralized ammonium sulfate and lower for ammonium bisulfate). Consequently, we assume that most sulfate particles have activated during their history and therefore lie thermodynamically on the metastable branch of the aerosol activation hysteresis loop. As a result of this assumption, solid phases are not considered to be present during the equilibrium calculation. Even though this assumption has the side effect of forcing the aerosol phase to contain water even below the crystallization relative humidity, this situation occurs rarely because most sulfate mass resides in the humid midlatitudes, and the aerosol in the dry upper troposphere tends to contain ammonium bisulfate and unneutralized sulfuric acid, which remain in aqueous solution at very low relative humidities. Moreover, the mass of water forced into the aerosol phase below the crystallization relative humidity is small compared with the aerosol mass itself (about 7% of total aerosol mass for ammonium sulfate). With any solid phase species eliminated from consideration, as well as species containing sodium or chloride, the species considered in the equilibrium calculation are

Gas phase:

NH_3, HNO_3, H_2O

Liquid phase:

NH_4^+, H^+, NO_3^-, SO_4^{2-}, HSO_4^-, OH^-,H_2O

The equilibrium relations involving these species, applicable equilibrium constants at 298 K, and other relevant thermodynamic quantities are given in Table 2.3.

Tropospheric temperatures can range from 210 K to 320 K, and the temperature dependence of gas-aerosol equilibrium is important. ISORROPIA calculates the temperature dependence of equilibrium constants with the van't Hoff equation,

$$\frac{d \ln K(T)}{dT} = \frac{\Delta H^{\circ}(T)}{RT^{2}} \tag{1}$$

where K is the equilibrium constant, T is the temperature (in Kelvins), R is the gas constant, and ΔH° is the standard enthalpy change of the reaction. The enthalpies of all species are assumed to vary linearly with temperature, on the basis of constant heat capacities. With this assumption the equilibrium constant is

$$K(T) = K_0 \exp\left[-\frac{\Delta H^{0}(T_0)}{RT}\left(\frac{T_0}{T} - 1\right) - \frac{\Delta c_p^{0}}{R}\left(1 + \ln\left(\frac{T_0}{T}\right) - \frac{T_0}{T}\right)\right] \tag{2}$$

where K_0 is the equilibrium constant at the reference temperature, T_0, and Δc_p^{0} is the difference in heat capacities between products and reactants at the reference temperature. The equilibrium constant at the reference temperature is

$$K_0 = \exp\left[-\frac{\sum_i \nu_i \mu_i^{\circ}(T_0)}{RT_0}\right] \tag{3}$$

In this expression, ν_i is the stoichiometric coefficient of the ith species in the equilibrium relation, and μ_i^o is its chemical potential at the reference temperature. The Gibbs free energy of formation, enthalpy of formation, and heat capacity of each species are given in Table 2.4.

An example of characteristic behavior of the sulfate-nitrate-ammonium aerosol system is shown in Figure 2.1. The predictions show how equilibrium aerosol composition varies as a function of total sulfate mass at 285 K and 80% relative humidity. The calculation was carried out assuming a fixed total mass of 4.5 $\mu g\ m^{-3}$ of ammonia and 6.0 $\mu g\ m^{-3}$ of nitric acid. Sulfate has a sufficiently low vapor pressure that it can be assumed to reside completely in the aerosol phase. Ammonia and nitric acid, on the other hand, partition themselves between both gas and aerosol phases. At these conditions, nitric acid can exist in the aerosol phase in the form of the nitrate ion, but only when neutralized by ammonium. At low sulfate concentrations the ammonium nitrate aerosol represents about a third of the total ammonia in the system and nearly all of the nitric acid. Ammonium concentrations increase with increasing sulfate concentrations until essentially all the ammonia is drawn into the aerosol phase. At this point, because of the lack of free ammonia, additional sulfate tends to force nitrate out of the aerosol phase. As a result of the thermodynamic competition between sulfate and nitrate, the total aerosol mass, dry or wet, is a nonlinear function of the amount of sulfate in the system.

2.2.6. Aerosol Nitrate

Aerosol nitrate was generated by providing the thermodynamic equilibrium module with total (gas plus aerosol) concentrations of nitric acid. The resulting concentrations of aerosol nitrate were stored as model output but were not allowed to undergo advection or deposition. In a sensitivity run, nitric acid concentrations were taken to be zero. A limitation of the nitrate simulation presented here is that neither sea salt nor mineral dust is included. Since both these types of aerosols are known to take up nitrate from the gas phase [*Tabazadeh et al.*, 1998], we expect to underestimate particulate nitrate concentrations wherever these processes are important. The aerosol nitrate concentrations calculated here represent therefore the sum of ammonium nitrate and dissolved nitric acid and neglect species such as $NaNO_3$ and $Ca(NO_3)_2$.

We use three-dimensional monthly average nitric acid concentration fields taken from the Harvard CTM photochemical model, which uses an archived meteorology based on the GISS GCM II [*Horowitz et al.*, 1998; *Horowitz and Jacob,* 1999]. Plate 2.2a shows the annual average of these monthly fields for selected model layers. Although the Harvard CTM accounts for both heterogeneous and gas-phase production of nitric acid, all nitric acid is assumed to reside in the gas phase for purposes of deposition. Since gas-phase nitric acid tends to undergo dry deposition more rapidly than particulate nitrate, the CTM may overestimate somewhat the dry deposition of total nitric acid.

Horowitz et al. [1998] reported that simulated HNO_3 concentrations were about 25% larger than observed concentrations at the three North American sites that were used for

comparison. Two reasons for this discrepancy were suggested. First, HNO_3 undergoes rapid dry deposition, resulting in a strong vertical gradient near the surface. One therefore expects that model predictions, which reflect conditions throughout the lowest 500 m of the atmosphere, should exceed observed concentrations at the surface. Second, CTM HNO_3 is the sum of gas-phase nitric acid and aerosol nitrate, whereas the observations are of gas-phase nitric acid only. This suggests that the Harvard CTM nitric acid fields used in this study are within 25% of actual values for North America, although this conclusion is based on observations at only three sites. Predictions in the remote troposphere are frequently several times larger than observations. Moreover, no comparison with European observations of HNO_3 has been made. In light of the above, it must be concluded that the HNO_3 concentration fields used as input, although the best currently available, represent a potentially considerable source of uncertainty. It is likely that HNO_3 predictions are too high, especially in remote areas, and could result in an overprediction of nitrate aerosol concentrations. Fortunately, this problem is mitigated by the fact that ammonium nitrate formation in remote areas is limited by the availability of ammonia.

The equilibrium water content of the aerosol was also tracked by the model. As with particulate nitrate, aerosol water was not allowed to undergo tracer transport.

All simulations were integrated over 13 months starting from zero concentrations. Data from the first month were ignored to allow the model to spin-up. Unless otherwise specified, all results shown here are annual averages over the remaining 12 months.

2.3. Global Aerosol Concentration Fields

This section presents predicted aerosol concentration fields, as well as several derived fields that highlight interactions among various species, such as the degree of aerosol neutralization. Aerosol concentrations and compositions have been compared with several observational databases. These databases will first be described.

2.3.1. Observational Data Sets

From June 1988 to May 1990, participants in the Eulerian Model Evaluation Field Study (EMEFS), took daily aerosol measurements at approximately 130 sites spread throughout eastern North America [*McNaughton and Vet,* 1996]. We have computed annual average sulfate, ammonium, and nitrate concentrations for 75 of these locations, and gas-phase ammonia concentrations have been computed for 59 sites. Table 2.5 lists the EMEFS sites as well as observed and simulated annual mean mixing ratios. The long-term nature of the observations, inclusion of all the major aerosol ions and ammonia, and the large number of sampling locations (including several instances of more than one sampling location in a GCM grid cell) make this database an excellent test of model performance in eastern North America.

Aerosol composition data for Europe have been made available under the auspices of the Co-operative Programme for Monitoring and Evaluation of the Long-Range Transmission of Air Pollutants in Europe (European Monitoring and Evaluation

Programme, EMEP) from 1986 to 1995 [*Hjellbrekke and Hanssen,* 1998]. Realizing that it is not feasible for our simulation, which is based on fixed emissions inventories, to accurately represent a 10-year period during which emissions changed, we compare our model predictions only with data taken during 1990. This year was chosen because it is the year in which simulated sulfate concentrations most closely match reported values. This facilitates comparison of other simulated aerosol components with observations, since errors in the sulfate simulation only compound errors and uncertainties in the treatment of other components. Fourteen EMEP sites reported annual average aerosol composition data for 1990, though not all sites reported data for all species. Table 2.6 shows these locations along with observed and simulated mixing ratios. Although the subset of the EMEP database used here is not as extensive as that of EMEFS, it still includes a reasonable number of long-term observations for sulfate and ammonium. The small number of ammonia and nitrate observations, however, makes assessment of model performance in Europe with respect to these species preliminary.

Since the sites that contributed to the two databases just described are all in or near industrialized regions, an effort was made to supplement these data with observations in other regions of the globe. DC94 compared their simulated sulfate and ammonium concentrations with a set of observed concentrations taken from the literature. We have extended this set to include a larger number of sites, as well as to include aerosol nitrate and gas-phase ammonia. Many of these observations were taken in marine and remote continental areas, and the inclusion of aircraft observations helps to evaluate model behavior in the boundary layer and free troposphere. A major drawback of these data is

that the vast majority of them were gathered over only relatively short time periods, usually a few days or weeks, and strongly reflect the prevailing meteorological conditions. One must bear this in mind when comparing these data with GCM-simulated concentrations, which are not based on the same meteorology. Because these observations were taken at a wide variety of sites, they have been divided into three categories: polluted continental, remote continental, and marine. The observations, with corresponding simulated values, are given in Table 2.7.

2.3.2. Sulfate

Results of the sulfur model used in this work have already been presented and compared with observations [*Koch et al.,* 1999]. Therefore we will present here only the sulfate results that are necessary for understanding the behavior of the other aerosol components that are the focus of this study. Annual average sulfate mixing ratios for selected GCM layers are shown in Plate 2.2b. The highest sulfate mixing ratios occur in the industrialized areas of Europe, North America, and eastern Asia, where they exceed 1 ppbv (1 $\mu g\ m^{-3}\ SO_4^{2-}$ = 258 pptv SO_4^{2-} at 298 K and 1 bar). Sulfate mixing ratios also exceed 1 ppbv in central Asia as a result of transport of sulfur species from Europe as well as local anthropogenic sources. Sulfate mixing ratios in remote continental areas range from 30 pptv to 300 pptv. Marine mixing ratios generally exceed 100 pptv in the Northern Hemisphere and are lower in the Southern Hemisphere. The lowest sulfate mixing ratios, less than 30 pptv, occur in the remote Pacific and Indian Oceans, mostly in the southern tropics. Sulfate mixing ratios are fairly uniform with altitude throughout the

boundary layer, but decrease in the free troposphere, with the average mixing ratio at the tropopause being about 25% of the surface layer value.

Figure 2.2 shows scatter plots of simulated sulfate mixing ratios versus observed values for each of the databases described above. In order to evaluate whether or not the model has a tendency to overpredict or underpredict aerosol concentrations, we took the geometric mean of the ratios of simulated values to observed values at each data point. The geometric mean ratio for each data set is shown in the corresponding scatter plot, and Table 2.8 shows the computed geometric mean for each data set and species. The model is able to predict annual average sulfate mixing ratios to within a factor of 2 at all the EMEFS and EMEP sites, although it tends to be about 15% high on average in North America. Comparison of simulated sulfate mixing ratios with the other data sets shows several locations where there is more than a factor of 2 discrepancy, but greater variation is expected from these observed concentrations, as they were collected over short time periods.

2.3.3. Ammonia

Annual average mixing ratios of gas-phase ammonia at selected model layers are shown in Plate 2.3a. The highest surface mixing ratios, in excess of 3 ppbv (1 $\mu g\ m^{-3}$ NH_3 = 1457 pptv NH_3 at 298 K and 1 bar), are found in India, China, eastern Europe, and Brazil. Continental mixing ratios exceed 100 pptv everywhere except the Arctic, western Sahara, and southwestern Australia. Marine concentrations are highest near the equator as a result of high ammonia emissions in that part of the ocean; otherwise, they are less than

100 pptv. Ammonia mixing ratios are negligibly small (less than 1 pptv) over most of Antarctica and only 3 to 10 pptv in the middle of the oceanic gyres. Emissions of ammonia and uptake by sulfate are the two factors that most strongly determine surface concentrations. Ammonia concentrations decline much more rapidly with altitude than do sulfate concentrations; the average mixing ratio at the tropopause is only 1% of the surface layer value, but concentrations are most persistent above India.

Annual average mixing ratios of particulate ammonium are shown in Plate 2.3b. Industrialized areas with high sulfate concentrations, such as the eastern United States, Europe, and China, tend to exhibit the largest ammonium mixing ratios, over 3 ppbv (1 $\mu g\ m^{-3}\ NH_4^+$ = 1377 pptv NH_4^+ at 298 K and 1 bar). Whereas mixing ratios in the Southern Oceans tend to fall in the 30-100 pptv range, they are 100-300 pptv in the northern oceans. Continental mixing ratios generally exceed 300 pptv. The lowest mixing ratios are found in Antarctica and the remote Pacific, where they range from 10 to 30 pptv. Ammonium mixing ratios at the tropopause are, on average, 16% of those at the surface. The decline in ammonium concentrations with altitude therefore is stronger than that of sulfate, but not as steep as that of ammonia.

The explanation for the stronger decline with altitude in ammonia and ammonium concentrations than for sulfate is that ammonia sources are located exclusively at the surface, while sulfate is produced chemically throughout the troposphere, although it has its own vertical gradient due to the distribution of its precursor, SO_2 [*Dentener and Crutzen,* 1994]. Gas-phase ammonia has a steeper vertical gradient than ammonium because ammonia partitions preferentially into the particle phase. High concentrations of

gas-phase NH_3 exist only in polluted areas near the surface, where ammonia emissions exceed the capacity of the sulfate aerosol to absorb them. As the stoichiometric balance between ammonia and sulfate shifts toward sulfate higher in the atmosphere, a larger fraction of the total ammonia partitions into the aerosol phase.

Ammonium concentrations calculated here are similar to those of DC94, including locations and magnitudes of the peak ammonium levels in China, Europe, North America, and South Africa and the pattern of oceanic ammonium concentrations. More discrepancies can be found when comparing ammonia concentrations. While similar peaks in ammonia concentrations are found over India, we predict maxima over China, Europe, North America, and Brazil, not found in DC94. This difference can be explained by a combination of higher ammonia emissions and a slightly lower sulfate burden. The sulfate burden in this model, 0.73 Tg S, is just slightly lower than that reported by *Langner and Rodhe* [1991], 0.77 Tg S, upon which the sulfate component of DC94 is based. The updated ammonia emissions inventory used here, however, is about 20% higher than that used by DC94. The combination of higher ammonia emissions and lower sulfate burden results in significantly higher gas-phase ammonia concentrations in areas, such as those mentioned above, where the sulfate aerosol is nearly fully neutralized. Also, the coarse horizontal resolution of the model used by DC94 may have limited their ability to resolve some of these maxima. Oceanic ammonia concentrations, on the other hand, tend to be lower than those found in DC94.

Figure 2.3 shows scatter plots of simulated versus observed ammonium mixing ratios for the databases described above. It can be seen that predictions are within a factor of 2

of most observed ammonium mixing ratios. Comparison of simulated mixing ratios with the EMEFS database is especially close. This agreement is significant because the EMEFS database offers the highest quality observations, from the standpoint of both number of sites and length of sampling period. This suggests that some of the scatter in comparisons with other data sets may be a result of subgrid variability, interannual variability, short sampling times, or other sources of variability that one would not expect the GCM to resolve. Table 2.8 shows that the geometric mean ratios for ammonium are within about 25% of unity for all but the EMEP data set. Considering that the uncertainty in the ammonia emissions inventory is estimated to be 25% on a global scale and larger on a regional scale, one cannot expect better predictions without also evaluating the emissions inventory itself. Furthermore, Table 2.8 shows that some of the ammonium overprediction in North America and underprediction of ammonium in the polluted continental and marine data sets must be ascribed to corresponding deviations in the sulfate fields. Predicted ammonium mixing ratios for Europe, on the other hand, seem distinctly high, although some allowance has to be made for the fact that the EMEP 1990 database represents fewer sites than the others. It is also worth noting that relative to sulfate, ammonium is overpredicted in all the data sets except the remote continental.

Excessive ammonium nitrate formation is one potential explanation for the high predicted ammonium levels in Europe. Ammonium overprediction is strongest in Europe, the area with the highest ammonium nitrate concentrations. As we will see later, simulated nitrate concentrations for Europe are also high compared with observations, further suggesting that ammonium nitrate in Europe is overestimated in the model.

Comparing predicted gas-phase ammonia concentrations to observations is more problematic than doing so for ammonium. Fewer data are available, and risk of contamination [*Quinn et al.*, 1987] makes sampling gas-phase ammonia much more difficult. Since ammonia partitions preferentially into the particle phase, errors in modeling sulfate and ammonium tend to compound ammonia modeling errors. If total ammonium and sulfate concentrations are roughly in balance, a small overprediction of sulfate or a low estimate of ammonia emissions will dramatically lower the predicted concentration of gas-phase ammonia, and vice versa. Finally, the lifetime of gas-phase ammonia is significantly shorter than those of sulfate and ammonium, so even stronger concentration gradients exist. Figure 2.4 shows scatter plots of how simulated ammonia mixing ratios compare with observations taken from EMEFS and the literature. No scatter plots are shown for the EMEP and marine databases, since they represent only four sites between them.

Roughly 40% of the simulated ammonia mixing ratios are within a factor of 2 of the literature observations, and the geometric mean ratio of 1.95 for the comparison indicates a significant high bias in the simulated values. While many of the simulated ammonia mixing ratios compare well with the EMEFS database, the GCM simulation does not seem to exhibit as much variability as the observational data. In particular, predicted ammonia mixing ratios uniformly exceed observations at a number of sites. A close examination of the EMEFS database, however, demonstrates that much of the variability in observed ammonia concentrations occurs on spatial scales that the GCM cannot resolve. The three GCM grid cells with the most sites had 16, 8, and 6 EMEFS

observational sites. Observed ammonia mixing ratios in these grid cells ranged from 47 to 1782 pptv, 61 to 574 pptv, and 164 to 1044 pptv, respectively; thus, observed ammonia mixing ratios varied by an order of magnitude or more on the subgrid scale. Predicted ammonia mixing ratios for these three cells were 612, 442, and 854 pptv, which are within the respective ranges of observed values.

Figure 2.5 shows the annual average ammonia budget for the global troposphere. Nearly half of the 53.6 Tg N of ammonia emitted each year is taken up by the aerosol phase. As a result, the deposition flux of gas-phase ammonia is almost exactly the same as that of particulate ammonium. However, 72% of NH_3 total deposition is dry, while 75% of NH_4^+ deposition is wet. Only 1.1 Tg N yr^{-1} of ammonia, about 2% of emissions, undergoes reaction with the OH radical. This is lower than the value of DC94, 1.8 Tg N yr^{-1} because of the current lower ammonia burden. As expected, the lifetime of particulate ammonium, 4.2 days, is longer than that of gas-phase ammonia, 1 day. The lifetime of NH_x ($NH_3 + NH_4^+$) is 3 days. The NH_4^+ lifetime is similar to that calculated by DC94, 4.5 days. On the other hand, the DC94 ammonia lifetime, 2.1 days, is significantly longer than that predicted here. Our lifetimes with respect to ammonium formation and wet deposition are both about half of those implied by the budget figures of DC94, while the lifetime of NH_3 with respect to dry deposition is one third of the corresponding value in DC94. Dry deposition, wet deposition, and gas-to-particle conversion therefore all contribute to the lower NH_3 lifetime in our model, with the contribution of dry deposition being somewhat more important. DC94 used a canopy compensation point concept to model emission from and dry deposition to the soil-vegetation complex, and this

difference in accounting means our budget figures are not directly comparable. Other differences in dry deposition between the two models could result from different surface layer thicknesses as well as differing ways in which the respective models estimate the aerodynamic resistance to dry deposition. DC94 used a parameterized treatment of wet deposition based on a climatology of precipitation rates, which can be expected to lead to very different results from the GCM treatment of precipitation and wet deposition used here. Finally, DC94 limited ammonia uptake by sulfate aerosols to a point where the molar ratio of ammonium to sulfate was 1.5. We allow neutralization of sulfate (and nitrate) to occur according to thermodynamic equilibrium. Later, we show that the aerosol is almost completely neutralized in many regions with high ammonia emissions. This additional uptake of ammonia, beyond that allowed by DC94, also contributes substantially to the shorter lifetime of ammonia in our model.

As a result of the longer lifetime of NH_4^+ than NH_3, on an annual average basis, there is about twice as much particulate NH_4^+ as gas-phase NH_3. The calculated burden of NH_4^+ is 0.30 Tg N, while that of NH_3 is 0.14 Tg N. DC94 report a similar NH_4^+ burden, 0.33 Tg N, but their NH_3 burden is nearly twice as large, 0.26 Tg N. The reasons for the discrepancy in NH_3 burden are the same as those discussed in regard to the difference in NH_3 lifetimes. As a final note, comparing the values for the standard model run with those from the sensitivity run with zero nitric acid, shown in parentheses in Figure 2.5, demonstrates that the formation of NH_4NO_3 aerosol has a modest effect on the overall ammonia budget by converting an additional 3.7 Tg N yr^{-1} of ammonia to ammonium.

2.3.4. Nitrate

Annual average mixing ratios of nitrate aerosol are shown in Plate 2.3c. We predict a large area of significant nitrate aerosol formation in Europe, with smaller areas in China and the eastern United States. Nitrate mixing ratios exceed 1 ppbv (1 $\mu g\ m^{-3}\ NO_3^-$ = 400 pptv NO_3^- at 298 K and 1 bar) in these regions. Most continental areas in the Northern Hemisphere have nitrate mixing ratios exceeding 100 pptv. In the Southern Hemisphere, this is only true in highly localized areas, such as parts of South America and South Africa. Marine mixing ratios of nitrate aerosol are negligible (less than 1 pptv) nearly everywhere. Nitrate concentrations decrease rapidly up to the middle troposphere but show a modest increase in the upper troposphere and lower stratosphere. This increase results from higher HNO_3 concentrations near the tropopause, as well as an increased solubility of HNO_3 in the aerosol phase at lower temperatures.

Two different types of aerosol nitrate formation occur. At midlatitudes and near the surface, where temperatures are warmer, thermodynamic considerations require that aerosol nitrate occur only as neutralized ammonium nitrate. Nitrate formation in developed areas therefore is enhanced by available ammonia and reduced by the presence of sulfate, which reacts preferentially with ammonia. In colder areas near the poles and in the upper troposphere, the solubility of nitric acid in water is high, and aerosol nitrate occurs here despite the lack of available ammonia to neutralize it. Sulfate enhances the formation of aerosol nitrate in cold areas by providing the aerosol water that solvates the nitric acid.

For several reasons, comparing simulated nitrate concentrations to observed values is also problematic. First, there are fewer observations of nitrate than of sulfate and ammonium. Second, as described above, there is uncertainty in the HNO_3 fields taken as input for this model, especially in remote areas. Another potential problem is that particulate nitrate may evaporate from filter packs, and the resulting measurements may be biased by as much as 24% [*Pakkanen et al.,* 1999]. Finally, formation of nitrate aerosol in the boundary layer depends on the availability of excess ammonia beyond that required to neutralize sulfate. As a result, nitrate concentrations in the model can be sensitive to small errors in predicted ammonia concentrations. Comparisons of predicted and observed annual average nitrate mixing ratios are shown in Figure 2.6. Most of the model predictions are within a factor of 2 of the EMEP observations. We seem to overpredict nitrate aerosol in Europe, although this is difficult to assess based on the few observations available. In North America, predictions match observations at many locations but tend to overestimate at sites with low levels of observed nitrate. The most serious discrepancy between simulated nitrate mixing ratios and observations occurs at marine locations. Here the model predicts nitrate mixing ratios of about 1 pptv or less, while mixing ratios of 50-500 pptv are typically observed. This is attributed to the absence in the model of sea salt upon which nitric acid is known to condense. Predictions seem too low when compared with observations of nitrate in polluted and remote continental areas, but it is difficult to draw any meaningful conclusions from a comparison between GCM output and short-term observations.

Besides the absolute concentration of nitrate aerosol, it is also interesting to examine the partitioning of total nitrate, gas and aerosol, between the two phases. Plate 2.4a shows the percent of total nitrate occurring in the aerosol phase. We note that throughout most areas of the atmosphere, less than 10% of total nitrate is in the aerosol phase. However, the availability of excess ammonia, beyond that which is necessary to neutralize sulfate, drastically changes this situation in key areas. More than half of total nitrate is found in the aerosol phase in eastern Asia, across a broad area of Europe and into western Russia, as well as in the North American Midwest. In contrast, nitrate does not partition as strongly into the particle phase in other areas with similarly high gas-phase ammonia concentrations, such as Brazil, India, and equatorial Africa, where warmer temperatures make gaseous nitric acid thermodynamically more favorable. At least 10% of total nitrate is found in the aerosol phase throughout most continental areas in the northern midlatitudes. The only marine areas where more than 10% of nitrate is found in the aerosol phase are polar regions, where HNO_3 is soluble in aerosol water because of the cold temperatures. Partitioning of HNO_3 into the aerosol phase decreases with altitude up through the lower to middle troposphere because of a lack of free ammonia, but increases again in the upper troposphere because of the enhanced solubility of nitric acid in aerosol water at colder temperatures. The only exception to this behavior is India, where less than 10% of nitric acid occurs as aerosol in the model surface layer but over 50% occurs as aerosol at around 400 mbar. This can also be explained in terms of free NH_3 and temperature. High concentrations of free NH_3 exist near the surface in India, but warm temperatures prevent the formation of nitrate aerosol. In the colder

middle troposphere, the area above India is the only region with sufficiently high concentrations of free NH_3 for nitrate formation.

2.3.5. Interactions Among Species

Having calculated global concentration fields for sulfate, nitrate, and ammonium, we would like to explore to what degree the acidic aerosol species, sulfate and nitrate, are neutralized by particulate ammonium. We define degree of neutralization (DON) as the equivalents of basic species divided by the equivalents of acidic species,

$$DON = \frac{[NH_4^+]}{2[SO_4^{2-}] + [NO_3^-]} \tag{4}$$

The degree of neutralization is analogous to the ammonium-sulfate molar ratio for a system without nitrate. A neutralization of 100% indicates that all sulfate and nitrate exist as ammonium sulfate and ammonium nitrate, respectively. A lower neutralization indicates a more acidic aerosol. Note that ammonium, sulfate, and nitrate are not the only particulate species that contribute to the pH of the aerosol phase. For example, formic and acetic acids are sometimes the dominant sources of acidity in precipitation in remote areas [*Talbot et al.,* 1992; *Seinfeld and Pandis,* 1998], so the degree of neutralization does not exactly correspond to pH. The degree of neutralization of the global aerosol is shown in Plate 2.4b. Near the surface, the results show a high degree of spatial variability with a pattern that does not neatly correspond to a typical division among industrialized, remote continental, and marine areas. Values of the degree of neutralization range from a

low around 10% for Antarctica to completely neutralized for large regions of the globe centered around the equator. This pattern of aerosol neutralization could not be captured except in a three-dimensional transport model with an aerosol thermodynamic calculation.

Aerosols in the continental areas with the highest ammonia emissions, China, India, eastern Europe, and central North America, are all nearly completely neutralized. For the most part, areas with high ammonia emissions, usually a product of intense agricultural activity, generally correspond to industrialized areas that have high sulfate concentrations. The aerosol in industrialized areas of Europe and China therefore tends to be neutralized. This is not the case in the eastern United States where ammonia emissions are not sufficient in magnitude, and occur somewhat too far westward, to completely neutralize the aerosol here. In some remote continental areas, such as South America and equatorial Africa, the aerosol is completely neutralized, while in other areas, such as Siberia, the aerosol is less than half neutralized. The large amount of excess NH_3 over India produces an interesting result. Here, there is a small area with a "neutralization" that exceeds 100%, indicating that NH_3 concentrations are sufficiently high not only to neutralize the sulfate and nitrate, but also to force an extra amount of ammonia into the aerosol phase via Henry's law solubility.

The degree of neutralization over the oceans reflects the balance between DMS and ammonia emissions. The pattern of the oceanic gyres can be seen in Plate 2.4b, with the aerosol in the more biologically active gyres tending to be neutralized to a greater degree than that found in the central oceans. While this result is highly uncertain because of the

large uncertainties associated with oceanic emissions, it seems to be consistent with the observations found in Table 2.7.

Despite considerable variability of the degree of aerosol neutralization within both continental and marine areas, it is worth pointing out that, on average, continental aerosol is more neutralized than marine. The model predicts this result, which is consistent with observations, because of its realistic thermodynamic treatment of gas-aerosol partitioning.

A final observation is that the degree of neutralization of the aerosol decreases with altitude. This is expected because sulfate and nitrate are both produced via gas-phase and heterogeneous chemistry at all levels of the atmosphere, whereas ammonia is emitted at the surface and has no sources above the surface. As a result, upper tropospheric aerosol tends to be more acidic than that at the surface. The decrease in the degree of neutralization, however, is not drastic, from an average of 63% near the surface to 40% at the tropopause.

In order to make a general assessment of the relative importance of nitrate as an aerosol constituent, Plate 2.4c shows the global molar ratio of aerosol nitrate to sulfate. Over most of the globe, molar concentrations of nitrate aerosol are small compared with those of sulfate (the average value is less than 10%), but nitrate is regionally important in eastern Asia, Eurasia, and the North American Midwest. In these areas, there is as much nitrate as sulfate on a molar basis. These nitrate "hotspots" disappear rapidly with altitude; even in the second model layer near 900 mbar, these are only faint echoes of their surface values. In the upper troposphere and lower stratosphere, nitrate becomes

significant once again. Here, however, instead of localized areas of extreme importance, nitrate has a more modest importance across a much larger area.

With respect to gas-aerosol sulfate-nitrate-ammonia equilibrium, *Ansari and Pandis* [1998] have defined the gas ratio (GR) as

$$GR = \frac{\left[NH_3^F\right]}{\left[HNO_3^T\right]} = \frac{\left[NH_3^T\right] - 2\left[SO_4^{2-}\right]}{\left[HNO_3^T\right]} \tag{5}$$

where $[HNO_3^T]$ is the total (gas plus aerosol) nitric acid concentration, $[NH_3^T]$ is the total (gas plus aerosol) ammonia concentration, and $[SO_4^{2-}]$ is the sulfate concentration. Free ammonia, $[NH_3^F]$, is the amount of ammonia available, after neutralizing sulfate, for ammonium nitrate formation. The significance of the gas ratio is that it indicates which reactant, ammonia or nitric acid, limits the formation of ammonium nitrate. A gas ratio that is greater than 1 indicates that nitric acid is limiting, while a ratio between 0 and 1 indicates that while some ammonia is available for reaction with nitric acid, ammonia is limiting. A gas ratio that is less than 0 indicates that ammonia is severely limiting. In this case, formation of ammonium nitrate is impossible because all ammonia will first react with sulfate.

Plate 2.5a shows the global gas ratio computed from annual average concentrations. On an annual average basis, throughout most of the atmosphere, there is no free ammonia, so ammonium nitrate formation generally does not occur. Note that even in locations where the gas ratio, based on annual average concentrations, is less than zero,

free ammonia may exist during certain parts of the year, and ammonium nitrate formation can occur during those times.

However, free NH_3 exists on a regular basis in many of the most populated areas of the globe. Ammonium nitrate formation in the areas with the highest nitrate concentrations, Europe, China, and the American Midwest, is generally limited by HNO_3 concentrations. It is not surprising to see that other areas with high ammonia NH_3, such as Brazil and India, have high gas ratios. The concentrations of ammonium nitrate in these areas could increase dramatically given an increase in HNO_3 concentrations. On the other hand, ammonia tends to be limiting in remote continental and marine areas. The gas ratio decreases with altitude because, for reasons discussed above, the concentrations of total ammonia decrease more rapidly than those of sulfate.

2.3.6. Aerosol Water

Annual average mixing ratios of aerosol water are shown in Plate 2.5b. Broadly speaking, there are no major surprises in this picture. Aerosol water mixing ratios are usually highest in industrialized areas with high sulfate concentrations, reaching values greater than 100 ppbv in Europe. Aerosol water mixing ratios in continental areas are greater than 1 ppbv almost everywhere. Low mixing ratios of aerosol water, 100 to 300 pptv, are found in the areas of lowest sulfate concentrations, the remote Pacific and Indian Oceans. Marine mixing ratios may be as high as 10 ppbv, however, in cold areas with high sulfate concentrations. It is clear from this figure that aerosol water content decreases rapidly with altitude, even more rapidly than sulfate concentrations. The

average aerosol water mixing ratio at 200 mbar is 2% of the surface value. Obviously, relative humidity plays an important role here. A close comparison of aerosol water and sulfate concentrations shows that even in the lowest model layer, sulfate concentration is not the only parameter with a significant effect on aerosol water. Both relative humidity and presence of nitrate are also important.

The effects of relative humidity and nitrate level can be more clearly seen in Plate 2.5c. Plate 2.5c shows the molar ratio of water to sulfate, which varies by roughly 2 orders of magnitude as a result of water uptake by nitrate as well as the effects of relative humidity and degree of neutralization. For example, a region of very dry aerosol over the desert area extends from northwestern India, past Saudi Arabia, and through northern Africa. Aerosol transported from Europe to this dry area will be less effective at radiative forcing than aerosol that remains in more humid areas. The molar ratio of water to sulfate is apparently very high in Europe (greater than 100 mol of water per mole of sulfate), but this is mostly due to water uptake by aerosol nitrate. Finally, there is a small band of enhanced sulfate concentrations in the Southern Ocean between South America and Antarctica, which is mostly unneutralized. Plate 2.5c shows how this unneutralized sulfate is more efficient in taking up water than is neutralized sulfate. These results are important because most studies of radiative forcing due to sulfate aerosol have assumed a uniform water uptake per mole of sulfate. Although local variations in water uptake due to composition and relative humidity may not significantly alter global and annual average forcing, they can distinctly change its spatial distribution.

2.3.7. Aerosol Mass

Aerosol mass mixing ratio, the sum of all aerosol components considered here (sulfate, nitrate, ammonium, and aerosol water), is shown in Plate 2.6a. Highest aerosol mass mixing ratios predicted by the model occur in central Europe, where they exceed 100 ppbm, but mixing ratios exceed 30 ppbm over a much larger area as well as in China and around the Great Lakes in North America. Aerosol mass mixing ratios exceed 1 ppbm nearly everywhere in the Northern Hemisphere, whereas marine areas in the Southern Hemisphere generally exhibit mixing ratios less than 1 ppbm. It is interesting to note the band in the Southern Ocean around Antarctica where aerosol mixing ratios exceed 3 ppbm. Sulfate aerosol produced by oxidation of DMS in this region is highly acidic, being a mixture of sulfuric acid and ammonium bisulfate, which is especially hygroscopic at the colder temperatures found around Antarctica. The remote Pacific and Indian Oceans show the lowest aerosol mass mixing ratios, 100 to 300 pptm. As expected, aerosol concentrations quickly decrease with altitude and are about an order of magnitude lower at the tropopause than at the surface.

2.3.8. Seasonal Cycles

Seasonal cycles in sulfate concentrations, total nitric acid concentrations, ammonia emissions, temperature, and precipitation can all give rise to seasonal cycles in ammonia, ammonium, and nitrate concentrations. Here we examine the temporal behavior of the GCM predictions.

Figure 2.7 shows the seasonal cycles in simulated sulfate, nitrate, ammonium, and ammonia mixing ratios compared with observations at four EMEFS sites. In order to focus on the seasonal behavior of nitrate, ammonium, and ammonia, these sites were chosen because their simulated sulfate cycles closely resemble observations. In North America, sulfate concentrations typically peak during summer or early fall because higher OH and H_2O_2 concentrations in those months rapidly oxidize sulfur dioxide to sulfate. Since most ammonium is formed via uptake by sulfate aerosol, the observations show that ammonium concentrations tend to follow the same pattern of high summer concentrations. Formation of ammonium nitrate, on the other hand, is thermodynamically favored at lower temperatures, such that nitrate mixing ratios are 4-8 times higher during the winter at the sites shown here. Ammonia concentrations are low during the winter because emissions, which are primarily from agricultural activities, are also lowest then.

The most striking thing about the comparison of model behavior with observations is the nitrate concentrations, which are too high at the New York sites throughout the year and too high at the other sites during winter. The excessive amount of nitrate formation produces corresponding discrepancies in the ammonium concentrations. One explanation for the overestimation of NH_4NO_3 is that there is too much total ammonia, aerosol, and gas phase. The observations show that formation of NH_4NO_3 is suppressed during winter by the lack of free ammonia, as evidenced by the low gas-phase NH_3 concentrations. In the model, on the other hand, gas-phase NH_3 is too high throughout the year at Ithaca and Piseco, resulting in high nitrate concentrations. In fact, predicted concentrations of NH_3 tend to be highest during some of the winter months, allowing formation of ammonium

nitrate. The model is therefore sensitive to the balance between ammonia and sulfate, and excess ammonia can dramatically increase nitrate concentrations.

2.4. Sensitivity Studies

To determine the effect of nitrate on total aerosol mass, a sensitivity study was performed in which the nitric acid concentration fields were set to zero. After generating annual average concentrations in the absence of nitrate, the total aerosol mass concentrations of this sensitivity study were compared with those of the base run. By comparing total aerosol mass, we see not only the additional mass of the nitrate ion itself, but also the mass of any accompanying ammonium and water. Plate 2.6b shows the ratio of total aerosol mass in the presence of nitric acid to that calculated in its absence. Because different runs do not identically reproduce all processes affecting tracer concentrations, a certain amount of noise is introduced into the comparison in the form of physically insignificant variability between runs. Although this noise is visible in the results, it is small in comparison with the effects we are examining.

Plate 2.6b shows that nitric acid has the most substantial effect on aerosol mass in and around the developed regions of the Northern Hemisphere. Accumulation mode nitrate formation does not substantially affect total aerosol mass in marine areas. In a large part of Europe and extending into Russia, aerosol mass concentrations in the model are more than double what they are in the absence of nitrate formation. The effect of nitric acid in eastern Asia is more modest, but still significant. Here, nitrate formation increases total aerosol mass between 50% and 100% in the most heavily influenced areas, and by at least

20% throughout the rest of the region. In the eastern United States the effect may be 20% to 50% or more, but HNO_3 affects central North America more strongly. In this area, with its high NH_3 emissions and relatively lower sulfate concentrations, ammonium nitrate formation is favored, and total aerosol mass more than doubles because of the presence of nitric acid. Since the particulate nitrate concentrations presented here seem to be higher than those observed, these estimates should be considered upper limits.

Another result to note is the influence of nitrate above India, where it is fairly unimportant near the surface, but has a more significant effect in the middle troposphere. In most other areas of the world, gas-phase NH_3 mixing ratios exceed 1 ppbv only near the surface and in the boundary layer. Above India, however, the high ammonia emissions and relatively low sulfate concentrations result in significant amounts of gas-phase NH_3 penetrating into the middle troposphere, allowing the formation of NH_4NO_3 aerosol at a higher altitude than anywhere else.

For reasons already mentioned above, nitrate formation is most important near the surface, where it increases total aerosol mass by 12% on average, and declines in importance to an average increase of 3% around 700 mbar. Nitrate importance increases again as one approaches the tropopause where it increases aerosol mass by 19%.

Total aerosol mass may be a nonlinear function of the availability of the various precursors: sulfur, nitric acid, and ammonia [*West et al.,* 1998]. For example, as sulfate concentrations decline, perhaps because of lower sulfur emissions, total aerosol mass may not decrease linearly if this decrease frees ammonia that is able to react to form

ammonium nitrate. The GCM simulation allows us to examine the sensitivity of total aerosol mass to the availability of precursor species.

In a set of six sensitivity runs, we integrate the model through 1 year during which the availability of one of the three precursors, sulfur, ammonia, and nitric acid, is either increased or decreased by 25%. In the cases of sulfur or ammonia, this was accomplished by uniformly scaling global emissions. For nitric acid, the input concentration fields were changed by 25%. Table 2.9 shows the annual average global burden of the various aerosol species for the base run, the six sensitivity runs just described, as well as the sensitivity run without HNO_3.

In the standard scenario, the global burden of inorganic aerosol ions is 2.6 Tg. With 4.9 Tg of accompanying aerosol water, the total global aerosol burden is 7.5 Tg. Globally averaged, water makes up about two thirds of aerosol mass. The scenario without nitrate indicates that the total aerosol burden would be about 11% lower in the absence of nitric acid.

The six precursor sensitivity runs show that while total aerosol mass in certain regions of the globe may exhibit a nonlinear dependence on sulfate concentrations, most regions of the globe display a linear dependence on sulfate concentration. Nonlinear behavior is observed only in regions with substantial amounts of ammonium nitrate. As a result, the global aerosol burden responds nearly linearly with changes in sulfur emissions and is insensitive to changes in ammonia emissions or nitric acid concentrations.

Changes in sulfate concentrations are virtually linear with changes in sulfur emissions. Although changes in nitrate concentrations do partly compensate for changes

in sulfate concentrations, this has a small effect on the global burden. As for ammonium concentrations and water content, these are more affected by sulfate than nitrate, so they decrease when sulfate decreases, and vice versa. The net result is that the total aerosol burden changes by about 20% for a 25% change in sulfur emissions. However, in areas where nitrate formation is important, such as Europe as well as parts of North America and China, the change in aerosol mass due to a 25% change in sulfur emissions is only 5-10%. This implies that in the polluted regions that are most interesting when discussing anthropogenic perturbations to the atmospheric aerosol system, nitrate aerosol needs to be accounted for when assessing the results of declining sulfur emissions.

Aerosol nitrate concentrations change nearly linearly with changes in nitric acid concentrations, but the concentrations of other aerosol components are practically unchanged. Changes in ammonia emissions affect ammonium concentrations by 15% in the case of an increase and by 20% in the case of a decrease. Nitrate concentrations are affected by changes in ammonia emissions even more strongly than ammonium concentrations are, but sulfate concentrations and aerosol water content are nearly unchanged. Since sulfate and water constitute over 90% of aerosol mass, even 25% changes in nitric acid concentrations or ammonia emissions have little effect on total aerosol mass, since they have little effect on these two important components.

2.5. Conclusions

The global tropospheric sulfur and ammonia cycles, including emissions, chemistry, and wet and dry deposition, have been simulated together online in the GISS GCM II-

prime. The local ammonium, nitrate, and water present in the aerosol at equilibrium for the conditions of temperature and relative humidity in each GCM grid cell have been calculated over a typical year. The output of a photochemical CTM has been used to specify the total amount of nitric acid available as a function of location and month. Concentrations of ammonia, ammonium, and nitrate simulated by the GCM have been compared with long-term surface observations made in North America and Europe, as well as to short-term observations in other regions and at higher altitudes.

The two factors that most strongly influence simulated ammonium concentrations are ammonia emissions and sulfate concentrations. Ammonium concentrations were high in most areas with high sulfate concentrations because these areas typically also have high ammonia emissions. Simulated ammonium concentrations were generally within a factor of 2 of annual average observed values. Ammonium concentrations were sometimes overestimated when associated with formation of nitrate aerosol. This seems to be the case in Europe, where the greatest tendency to overestimate ammonium concentrations occurred, as well as at some locations in North America.

Gas-phase NH_3 concentrations are high in areas with high ammonia emissions, particularly if little sulfate is present. Ammonia concentrations are found to be highest globally in India. High ammonia concentrations are found almost exclusively within the boundary layer and decrease rapidly with altitude. Although our lowest model layer is only half as thick as that of DC94, our boundary layer resolution is still relatively coarse. This complicates comparison between model-generated surface layer concentrations and ground observations. It also introduces uncertainty into the calculated vertical transport of

species in the boundary layer where the concentrations are largest, especially gas-phase ammonia, which has the strongest vertical gradient. Simulated NH_3 concentrations did not compare as well with observations as did NH_4^+ concentrations. The ammonia concentration predicted by the model was within a factor of 2 of the observed value at just under half of the sites considered here. Much of the difficulty in comparing predicted ammonia concentrations with observations stems from its short lifetime, which implies that strong concentration gradients exist on spatial scales that the GCM cannot resolve.

It is estimated that about half of the 53.6 Tg N yr^{-1} of ammonia emissions is taken up by the aerosol phase to form ammonium. Ammonium has a longer lifetime, about 4 days, than ammonia, which has a lifetime of just 1 day. Three quarters of ammonia deposition occurs via dry processes, while wet deposition removes a similar fraction of ammonium from the atmosphere. Although the concentrations of ammonia and ammonium are similar in the model surface layer, the total tropospheric burden of ammonium, 0.30 Tg N, is about twice that of ammonia, 0.14 Tg N.

Substantial amounts of nitrate formation occur in polluted continental areas, especially during winter. In these areas, nitrate formation depends on the availability of ammonia in excess of that needed to neutralize sulfate. Nitrate and associated ammonium and water account for as much of the total aerosol mass as sulfate in midwestern North America as well as in a broad region of Europe and western Asia. Comparison with observations shows, however, that these predicted nitrate concentrations are high. On a global basis, the contribution of nitrate, with associated ammonium and water, to total aerosol mass is much smaller, only 11%. In marine areas,

simulated nitrate concentrations are low in comparison to observations because uptake of nitric acid by sea salt is neglected in this work. In cold areas, such as in polar regions and the upper troposphere, nitrate aerosol can form in the absence of free ammonia because of its high solubility in water at lower temperatures.

Aerosol water content was generally highest in areas with high sulfate concentrations, although the effects of relative humidity and nitrate can also be seen. Because of these two factors, the amount of aerosol water uptake per mole of sulfate varied by 2 orders of magnitude. An accurate assessment of aerosol composition and water content is essential for a rigorous determination of the spatial distribution of aerosol radiative forcing.

The total global aerosol burden, including sulfate, nitrate, ammonium, and water, was estimated to be 7.5 Tg. Water constitutes, by itself, two thirds of the total aerosol mass, while the sulfate ion accounts for about 28%. The contributions of ammonium and nitrate to the overall burden were much lower, 5% and 1.7%, respectively. Several sensitivity runs were performed in which ammonia emissions, sulfur emissions, and nitric acid concentrations were each increased or decreased by 25% to evaluate how aerosol formation responds to changes in its precursors. Changes in sulfur emissions have by far the largest impact on the global aerosol burden, with a 21% increase and 22% decrease, corresponding to a 25% increase and decrease in emissions, respectively. The effect of changing sulfur emissions on the global aerosol burden is very close to, but not quite, linear, because in polluted midlatitude regions, opposing changes in nitrate concentrations partly compensate for changes in sulfate levels. Nitrate therefore needs to be taken into account when calculating the total aerosol mass in anthropogenically influenced areas, or

when predicting how aerosol mass will respond to changes in sulfate concentrations in these areas. Changes in HNO_3 concentrations have an effect on the nitrate burden, and changes in NH_3 emissions influence both the nitrate and ammonium burdens, but have little effect on total aerosol mass, which is dominated by water and sulfate.

The results of this study suggest several avenues for improvement and future research. First, the ammonia emissions inventory and nitric acid concentration fields need improvement to bring the amount of ammonium nitrate formation in the model into better agreement with the limited available observations. For example, both ammonia and ammonium tend to be too high in the simulation compared with EMEFS observations, indicating that the GEIA ammonia emissions inventory may simply be too high. Since formation of nitrate aerosol is sensitive to the availability of free ammonia and to the amount of total nitric acid present, observations of nitrate concentrations could provide a useful constraint on ammonia emissions and photochemical models. In particular, the correlation between high winter nitrate concentrations and high ammonia concentrations suggests that ammonia emissions may be too high during that time of year. Second, more long-term observations, especially outside North America and Europe and of ammonia and nitrate, are required to better evaluate global simulations. A greater density of observational sites can help eliminate the problem of subgrid variability that arises when comparing output from such a large-scale model with observations because of the short lifetimes of aerosol ions and ammonia. Another improvement that could be made would be to simulate nitric acid in a way that is more consistent with the rest of the aerosol simulation. Ideally, the simulation of the sulfur and ammonia cycles presented here

would be fully coupled to a photochemical model. Another possibility would be to use production rates of nitric acid taken from a photochemical CTM as input to this model. In that case, gas-phase nitric acid and particulate nitrate would be included in the GCM as tracers, and their transport, deposition, and chemical destruction (i.e., photolysis of gas-phase nitric acid) would be explicitly included in the GCM simulation. This would allow the wet and dry deposition schemes to take into account the gas-aerosol partitioning of total nitrate and the GCM to calculate a total nitrate budget rather than just the burden of particulate nitrate. Finally, a natural extension of the present work is to evaluate the effect of variable aerosol composition and water uptake on global and regional radiative forcing.

Acknowledgments. This work has been supported by a graduate fellowship from the Fannie and John Hertz Foundation as well as by the National Aeronautics and Space Administration Earth Observing System Interdisciplinary Science program (NASA EOS-IDS). We would also like to acknowledge the Center for Advanced Computing Research at Caltech for computational resources, Loretta Mickley and fellow researchers at Harvard University for nitric acid concentration fields from the Harvard CTM, and Lex Bouwman at the National Institute of Public Health and the Environment in Bilthoven, Netherlands, for providing us with the GEIA ammonia emissions inventory in advance of publication. The EMEFS data utilized in this study were collected and prepared under the sponsorship of the Electric Power Research Institute. EMEP data were obtained from the Norwegian Institute for Air Research. We also thank two anonymous reviewers for helpful comments and constructive criticism.

References

Andreae, M. O., H. Berresheim, T. W. Andreae, M. A. Kritz, T. S. Bates, and J. T. Merrill, Vertical distribution of dimethyl sulfide, sulfur dioxide, aerosol ions, and radon over the northeast Pacific Ocean, *J. Atmos. Chem., 6*, 149-173, 1988.

Ansari, A. S., and S. N. Pandis, Response of inorganic PM to precursor concentrations, *Environ. Sci. Technol., 32*, 2706-2714, 1998.

Asman, W. A. H., and H. A. van Jaarsveld, A variable-resolution transport model applied for NH_x in Europe, *Atmos. Environ., Part A, 26,* 445-464, 1992.

Bassett, M. E., and J. H. Seinfeld, Atmospheric equilibrium model of sulfate and nitrate aerosol, *Atmos. Environ., 17*, 2237-2252, 1983.

Bassett, M. E., and J. H. Seinfeld, Atmospheric equilibrium model of sulfate and nitrate aerosol, II, Particle size analysis, *Atmos. Environ., 18*, 1163-1170, 1984.

Berresheim, H., M. O. Andreae, G. P. Ayers, R. W. Gillett, J. T. Merrill, V. J. Davis, and W. L. Chameides, Airborne measurements of dimethyl sulfide, sulfur dioxide, and aerosol ions over the Southern Ocean south of Australia, *J. Atmos. Chem., 10*, 341-370, 1990.

Berresheim, H., M. O. Andreae, R. L. Iverson, and S. M. Li, Seasonal variations of dimethylsulfide emissions and atmospheric sulfur and nitrogen species over the western North Atlantic Ocean, *Tellus, Ser.B, 43,* 353-372, 1991.

Boucher, O., GCM estimate of the indirect aerosol forcing using satellite-retrieved cloud droplet effective radii, *J. Clim., 8*, 1403-1409, 1995.

Boucher, O., and T. L. Anderson, General circulation model assessment of the sensitivity of direct climate forcing by anthropogenic sulfate aerosols to aerosol size and chemistry, *J. Geophys. Res., 100,* 26,117-26,134, 1995.

Boucher, O., and U. Lohmann, The sulfate-CCN-cloud albedo effect, *Tellus, Ser. B, 47,* 281-300, 1995.

Bouwman, A. F., D. S. Lee, W. A. H. Asman, F. J. Dentener, K. W. Van Der Hoek, and J. G. J. Olivier, A global high-resolution emission inventory for ammonia, *Global Biogeochem. Cycles, 11,* 561-587, 1997.

Cadle, S. H., J. M. Dasch, and P. A. Mulawa, Atmospheric concentrations and the deposition velocity to snow of nitric acid, sulfur dioxide and various particulate species, *Atmos. Environ., 19,* 1819-1827, 1985.

Charlson, R. J., J. Langner, H. Rodhe, C. B. Leovy, and S. G. Warren, Perturbation of the northern hemisphere radiative balance by backscattering from anthropogenic sulfate aerosols, *Tellus, Ser. AB, 43,* 152-163, 1991.

Chin, M., D. J. Jacob, G. M. Gardner, M. S. Foreman-Fowler, and P. A. Spiro, A global three-dimensional model of tropospheric sulfate, *J. Geophys. Res., 101*, 18,667-18,690, 1996.

Chuang, C. C., J. E. Penner, K. E. Taylor, A. S. Grossman, and J. J. Walton, An assessment of the radiative effects of anthropogenic sulfate, *J. Geophys. Res., 102*, 3761-3778, 1997.

Church, T. M. , J. M. Tramontano, D. M. Whelpdale, M. O. Andreae, J. N. Galloway, W. C. Keene, A. H. Knap, and J. Tokos Jr., Atmospheric and precipitation chemistry over

the North Atlantic Ocean: Shipboard results, April-May 1984, *J. Geophys. Res., 96,* 18,705-18,725, 1991.

Clairac, B., R. Delmas, B. Cros, H. Cachier, P. Buat-Ménard, and J. Servant, Formation and chemical composition of atmospheric aerosols in an equatorial forest area, *J. Atmos. Chem., 6,* 301-322, 1988.

Clarke, A. D., and J. N. Porter, Pacific marine aerosol, 2, Equatorial gradients in chlorophyll, ammonium, and excess sulfate during SAGA 3, *J. Geophys. Res., 98,* 16,997-17,010, 1993.

Clegg, S. L., K. S. Pitzer, and P. Brimblecombe, Thermodynamics of multicomponent, miscible, ionic solutions. II. Mixture including unsymmetrical electrolytes, *J. Phys. Chem., 96,* 9470-9479, 1992. (Additions and corrections, *J. Phys. Chem., 98,* 1368, 1994; *J. Phys. Chem., 99,* 6755, 1995.)

Clegg, S. L., P. Brimblecombe, and A. S. Wexler, A thermodynamic model of the system H^+-NH_4^+-Na^+-SO_4^{2-}-NO_3^--Cl^--H_2O at 298.15 K, *J. Phys. Chem., 102,* 2155-2171, 1998a.

Clegg, S. L., P. Brimblecombe, and A. S. Wexler, A thermodynamic model of the system H^+-NH_4^+-Na^+-SO_4^{2-}-NO_3^--Cl^--H_2O at tropospheric temperatures, *J. Phys. Chem., 102,* 2137-2154, 1998b.

Coffman, D. J., and D. A. Hegg, A preliminary study of the effect of ammonia on particle nucleation in the marine boundary layer, *J. Geophys. Res., 100,* 7147-7160, 1995.

Covert, D. S., North Pacific marine background aerosol: Average ammonium to sulfate molar ratio equals 1, *J. Geophys. Res., 93,* 8455-8458, 1988.

Del Genio, A. D., and M.-S. Yao, Efficient cumulus parameterization for long-term climate studies: The GISS scheme, in *The Representation of Cumulus Convection in Numerical Models* Monogr. 46, edited by K. A. Emanuel and D. J. Raymond, pp. 181-184, Am. Meteorol. Soc., Boston, Mass., 1993.

Del Genio, A. D., M.-S. Yao, W. Kovari, and K. K.-W. Lo, A prognostic cloud water parameterization for global climate models, *J. Clim., 9,* 270-304, 1996.

DeMore, W. B., S. P. Sander, D. M. Golden, R. F. Hampson, M. J. Kurylo, C. J. Howard, A. R. Ravishankara, C. E. Kolb, and M. J. Molina, Chemical kinetics and photochemical data for use in stratospheric modeling: Evaluation number 12, JPL Publ., 97-4, 1997.

Dentener, F. J., and P. Crutzen, A three-dimensional model of the global ammonia cycle, *J. Atmos. Chem., 19,* 331-369, 1994.

Erickson, D. J., J. J. Walton, S. J. Ghan, and J. E. Penner, Three-dimensional modeling of the global atmospheric sulfur cycle: A first step, *Atmos. Environ., Part A, 25,* 2513-2520, 1991.

Erickson, D. J., R. J. Oglesby, and S. Marshall, Climate response to indirect anthropogenic sulfate forcing, *Geophys. Res. Lett., 22,* 2017-2020, 1995.

Feichter, J., E. Kjellstrom, H. Rodhe, F. Dentener, J. Lelieveld, and G.-J. Roelofs, Simulation of the tropospheric sulfur cycle in a global climate model, *Atmos. Environ., 30,* 1693-1707, 1996.

Feichter, J., U. Lohmann, and I. Schult, The atmospheric sulfur cycle in ECHAM-4 and its impact on the shortwave radiation, *Clim. Dyn., 13,* 235-246, 1997.

Fekete, K. E., and L. Gyenes, Regional-scale transport model for ammonia and ammonium, *Atmos. Environ. Part A, 27,* 1099-1104, 1993.

Galloway, J. N., Acid deposition: Perspectives in time and space, *Water, Air and Soil Pollution, 85,* 15-24, 1995.

Galperin, M. V., and M. A. Sofiev, The long-range transport of ammonia and ammonium in the Northern Hemisphere, *Atmos. Environ., 32,* 373-380, 1998.

Gras, J. L., Ammonia and ammonium concentrations in the Antarctic atmosphere, *Atmos. Environ., 17,* 815-818, 1983.

Gregory, G. L., et al., Air chemistry over the tropical forest of Guyana, *J. Geophys. Res., 91,* 8603-8612, 1986.

Hansen, J., G. Russell, D. Rind, P. Stone, A. Lacis, S. Lebedeff, R. Ruedy, and L. Travis, Efficient three-dimensional global models for climate studies: Models I and II, Mon. *Weather Rev., 111,* 609-662, 1983.

Hanssen, J. E., U. Pedersen, J. Schlaug, H. Dovland, J. M. Pacyna, A. Semb, and J. E. Skjelmoen, Summary report from the Chemical Co-ordinating Centre for the fourth phase of EMEP, *EMEP/CCC Rep. 2/90,* Norw. Inst. for Air Res., Lillestrom, 1990.

Harrison, R. M., and C. A. Pio, Size-differentiated composition of inorganic atmospheric aerosols of both marine and polluted continental origin, *Atmos. Environ., 17,* 1733-1738, 1983.

Hartke, G. J., and D. Rind, Improved surface and boundary layer models for the Goddard Institute for Space Studies general circulation model, *J. Geophys. Res., 102,* 16,407-16,422, 1997.

Haywood, J. M., and K. P. Shine, The effect of anthropogenic sulfate and soot aerosol on the clear sky planetary radiation budget, *Geophys. Res. Lett., 22,* 603-606, 1995.

Haywood, J. M., and V. Ramaswamy, Global sensitivity studies of the direct radiative forcing due to anthropogenic sulfate and black carbon aerosols, *J. Geophys. Res., 103,* 6043-6058, 1998.

Haywood, J. M., D. L. Roberts, A. Slingo, J. M. Edwards, and K. P. Shine, General circulation model calculations of the direct radiative forcing by anthropogenic sulfate and fossil-fuel soot aerosol, *J. Clim., 10,* 1562-1577, 1997.

Hjellbrekke, A.-G., and J. E. Hanssen, Data report 1996, 1, Annual summaries., *EMEP/CCC Rep. 1/98*, 85 pp., Norw. Inst. for Air Res., Lillestrom, 1998.

Horowitz, L. W., and D. J. Jacob, Global impact of fossil fuel combustion on atmospheric NO_x, *J. Geophys. Res., 104,* 23,823-23,840, 1999.

Horowitz, L. W., J. Liang, G. M. Gardner, and D. J. Jacob, Export of reactive nitrogen from North America during summertime: Sensitivity to hydrocarbon chemistry, *J. Geophys. Res., 103*, 13,451-13,476, 1998.

Hov, Ø., B. A. Hjøllo, and A. Eliassen, Transport distance of ammonia and ammonium in northern Europe, 1, Model description, J. *Geophys. Res., 99,* 18,735-18,748, 1994.

Huebert, B. J., Wang. Ming-Xing, and Lǚ Wei-Xiu, Atmospheric nitrate, sulfate, ammonium, and calcium concentrations in China, *Tellus, Ser. B, 40,* 260-269, 1988.

Huebert, B. J., L. Zhuang, S. Howell, K. Noone, and B. Noone, Sulfate, nitrate, methanesulfonate, chloride, ammonium, and sodium measurements from ship, island,

and aircraft during the Atlantic Stratocumulus Transition Experiment/Marine Aerosol Gas Exchange, *J. Geophys. Res., 101,* 4413-4423, 1996.

Intergovernmental Panel on Climate Change (IPCC), *Climate Change 1995*, edited by J. T. Houghton et al., Cambridge Univ. Press, New York, 1996.

Iversen T., N.E. Halvorsen, S. Mylona, and H. Sandnes, Calculated budgets for airborne acidifying components in Europe, 1985, 1987, 1988, 1989 and 1990, *EMEP/MSW-Rep. 1-91*, Norw. Inst. for Air Res., Lillestrom, 1991.

Jacob, D. J. , J. W. Munger, J. M. Waldman, and M. R. Hoffmann, The H_2SO_4-HNO_3-NH_3 sytem at high humidities and in fogs, 1, Spatial and temporal patterns in the San Joaquin Valley of California, *J. Geophys. Res., 91,* 1073-1088, 1986.

Jacob, D. J., et al., Simulation of summertime ozone over North America, *J. Geophys. Res., 98,* 14,797-14,816, 1993.

Jacobson, M. Z., A. Tabazadeh, and R. P. Turco, Simulating equilibrium within aerosols and nonequilibrium between gases and aerosols, *J. Geophys. Res., 101*, 9079-9091, 1996.

John, W., S. M. Wall, J. L. Ondo, and W. Winklmayr, Modes in the size distribution of atmospheric inorganic aerosol, *Atmos. Environ., Part A, 24,* 2349-2359, 1990.

Jones, A., D. L. Roberts, and A. Slingo, A climate model study of indirect radiative forcing by anthropogenic sulphate aerosols, *Nature, 370*, 450-453, 1994.

Kasibhatla, P., W. L. Chameides, and J. St. John, A three-dimensional global model investigation of seasonal variations in the atmospheric burden of anthropogenic aerosols, *J. Geophys. Res., 102,* 3737-3759, 1997.

Keeler, G. J., J. D. Spengler, and R. A. Castillo, Acid aerosol measurements at a suburban Connecticut site, *Atmos. Environ., Part A, 25,* 681-690, 1991.

Khemani, L. T., G. A. Momin, M. S. Naik, R. Vijayakumar, and B. V. Ramana Murty, Chemical composition and size distribution of atmospheric aerosols over the Deccan Plateau, India, *Tellus, 34,* 151-158, 1982.

Kiehl, J. T., and B. P. Briegleb, The relative roles of sulfate aerosols and greenhouse gases in climate forcing, *Science, 260,* 311-314, 1993.

Kim, Y. P., and J. H. Seinfeld, Atmospheric gas-aerosol equilibrium, III, Thermodynamics of crustal elements Ca^{2+}, K^{+}, and Mg^{2+}, *Aerosol Sci. Technol., 22,* 93-110, 1995.

Kim, Y. P., J. H. Seinfeld, and P. Saxena, Atmospheric gas-aerosol equilibrium, I, Thermodynamic model, *Aerosol Sci. Technol., 19,* 157-181, 1993a.

Kim, Y. P., J. H. Seinfeld, and P. Saxena, Atmospheric gas-aerosol equilibrium, II, Analysis of common approximations and activity coefficient calculation methods, *Aerosol Sci. Technol., 19,* 182-198, 1993b.

Kjellstrom, E., A three-dimensional global model study of carbonyl sulfide in the troposphere and the lower stratosphere, *J. Atmos. Chem., 29,* 151-177, 1998.

Koch, D., D. Jacob, I. Tegen, D. Rind, and M. Chin, Tropospheric sulfur simulation and sulfate direct radiative forcing in the Goddard Institute for Space Studies general circulation model, *J. Geophys. Res., 104,* 23,799-23,822, 1999.

Kulmala, M., A. Laaksonen, P. Korhonen, T. Vesala, and T. Ahonen, The effect of atmospheric nitric acid vapor on cloud condensation nucleus activation, *J. Geophys. Res., 98*, 22,949-22,958, 1993.

Kulshrestha, U. C., A. Saxena, N. Kumar, K. M. Kumari, and S. S. Srivastava, Chemical composition and association of size-differentiated aerosols at a suburban site in a semi-arid tract of India, *J. Atmos. Chem., 29,* 109-118, 1998.

Langford, A. O., F. C. Fehsenfeld, J. Zachariassen, and D. S. Schimel, Gaseous ammonia fluxes and background concentrations in terrestrial ecosystems of the United States, Global Biogeochem. *Cycles, 6*, 459-483, 1992.

Langner, J. and H. Rodhe, A global three-dimensional model of the tropospheric sulfur cycle, *J. Atmos. Chem., 13*, 225-263, 1991.

Lelieveld, J., G.-J. Roelofs, L. Ganzeveld, J. Feichter, and H. Rodhe, Terrestrial sources and distribution of atmospheric sulphur, *Philos. Trans. R. Soc. London, 352,* 149-158, 1997.

Lenhard, U., and G. Gravenhorst, Evaluation of ammonia fluxes into the free atmosphere over western Germany, *Tellus, 32*, 48-55, 1980.

Lindberg, S. E., M. Bredemeier, D. A. Schaefer, and L. Qi, Atmospheric concentrations and deposition of nitrogen and major ions in conifer forests in the United States and Federal Republic of Germany, *Atmos. Environ., Part A, 24,* 2207-2220, 1990.

Lohmann, U., and J. Feichter, Impact of sulfate aerosols on albedo and lifetime of clouds: A sensitivity study with the ECHAM4 GCM, *J. Geophys. Res., 102,* 13,685-13,700, 1997.

McNaughton, D. J., and R. J. Vet, Eulerian model evaluation field study (EMEFS): A summary of surface network measurements and data quality, *Atmos. Environ., 30,* 227-238, 1996.

Meng, Z., and J. H. Seinfeld, Time scales to achieve atmospheric gas-aerosol equilibrium for volatile species, *Atmos. Environ., 30,* 2889-2900, 1996.

Meng, Z., J. H. Seinfeld, P. Saxena, and Y. P. Kim, Atmospheric gas-aerosol equilibrium, IV, Thermodynamics of carbonates, *Aerosol Sci. Technol., 23,* 131-154, 1995.

Mészáros, E., and L. Horváth, Concentration and dry deposition of atmospheric sulfur and nitrogen compounds in Hungary, *Atmos. Environ., 18,* 1725-1730, 1984.

Mészáros, E., T. Barcza, A. Gelencsér, J. Hlavay, Gy. Kiss, Z. Krivácsy, A. Molnár, and K. Polyák, Size distributions of inorganic and organic species in the atmospheric aerosol in Hungary, *J. Aerosol Sci., 28,* 1163-1175, 1997.

Metcalfe, S. E., J. D. Whyatt, and R. G. Derwent, Multi-pollutant modelling and the critical loads approach for nitrogen, *Atmos. Environ., 32,* 401-408, 1998.

Mitchell, J. F. B., and T. C. Johns, On modification of global warming by sulfate aerosols, *J. Clim., 10,* 245-267, 1997.

Mitchell, J. F. B., T. C. Johns, J. M. Gregory, and S. F. B. Tett, Climate response to increasing levels of greenhouse gases and sulphate aerosols, *Nature, 376,* 501-504, 1995a.

Mitchell, J. F. B., R. A. Davis, W. J. Ingram, and C. A. Senior, On surface temperature, greenhouse gases, and aerosols: Models and observations, *J. Clim., 8,* 2364-2386, 1995b.

National Research Council, *A Plan for a Research Program on Aerosol Radiative Forcing and Climate Change*, edited by J. H. Seinfeld et al., Nat. Acad. Press, Washington, D.C., 1996.

Nenes, A., C. Pilinis, and S. N. Pandis, Isorropia: A new thermodynamic equilibrium model for multiphase multicomponent inorganic aerosols, *Aquat. Geochem., 4,* 123-152, 1998.

Ohta, S., and T. Okita, A chemical characterization of atmospheric aerosol in Sapporo, *Atmos. Environ., Part A, 24*, 815-822, 1990.

Ohta, S., N. Murao, and V. N. Makarov, *Geochemical study of atmospheric aerosols in Yakutsk*, paper presented at Permafrost Environment, Hokkaido Univ., Sapporo, Japan, 1992.

Oort, A. H., *Global atmospheric circulation statistics*, 1958-1973, NOAA Prof. Pap. 14, U.S. Gov. Print. Off., Washington, D. C., 1983.

Pakkanen, T. A., et al., Nordic intercomparison for measurement of major atmospheric nitrogen species, *J. Aerosol Sci., 30*, 247-263, 1999.

Parungo, F. P., C. T. Nagamoto, J. Rosinski, and P. L. Haagenson, A study of marine aerosols over the Pacific Ocean, *J. Atmos. Chem., 4,* 199-226, 1986.

Penner, J. E., C. S. Atherton, and T. E. Graedel, *Global emissions and models of photochemically active compounds, in Global Atmospheric-Biospheric Chemistry,* edited by R. G. Prinn, pp. 223-247, Plenum, New York, 1994.

Pham, M., J.-F. Muller, G. P. Brasseur, C. Granier, and G. Megie, A three-dimensional study of the tropospheric sulfur cycle, *J. Geophys. Res., 100*, 26,061-26,092, 1995.

Pierson, W. R., W. W. Brachaczek, R. A. Gorse Jr., S. M. Japar, and J. M. Norbeck, Atmospheric acidity measurements on Allegheny Mountain and the origins of ambient acidity in the northeastern United States, *Atmos. Environ., 23*, 431-459, 1989.

Pilinis, C., and J. H. Seinfeld, Continued development of a general equilibrium model for inorganic multicomponent atmospheric aerosols, *Atmos. Environ., 32,* 2453-2466, 1987.

Quinn, P. K., R. J. Charlson, and W. H. Zoller, Ammonia, the dominant base in the remote marine troposphere: a review, *Tellus, Ser. B, 39*, 413-425, 1987.

Quinn, P. K., T. S. Bates, J. E. Johnson, D. S. Covert, and R. J. Charlson, Interactions between the sulfur and reduced nitrogen cycles over the central Pacific Ocean, *J. Geophys. Res., 95*, 16,405-16,416, 1990.

Rind, D., and J. Lerner, The use of on-line tracers as a diagnostic tool in general circulation model development, 1, Horizontal and vertical transport in the troposphere, *J. Geophys. Res., 101*, 12,667-12,683, 1996.

Roelofs, G.-J., J., Lelieveld, and L. Ganzeveld, Simulation of global sulfate distribution and the influence on effective cloud drop radii with a coupled photochemistry-sulfur cycle model, *Tellus, Ser. B, 50*, 224-242, 1998.

Saxena, P., C. Seigneur, A. B. Hudischewskyj, and J. H. Seinfeld, A comparative study of equilibrium approaches to the chemical characterizations of secondary aerosols, *Atmos. Environ., 20,* 1471-1484, 1986.

Schlesinger, W. H., and A. E. Hartley, A global budget for atmospheric NH_3, Biogeochemistry, 15, 191-211, 1992.

Seinfeld, J. H., and S. N. Pandis, *Atmospheric Chemistry and Physics*, John Wiley, New York, 1998.

Singles, R., M. A. Sutton, and K. J. Weston, A multi-layer model to describe the atmospheric transport and deposition of ammonia in Great Britain, *Atmos. Environ., 32,* 393-399, 1998.

Suh, H. H., G. A. Allen, B. Aurian-Blajeni, P. Koutrakis, and R. M. Burton, Field method comparison for the characterization of acid aerosols and gases, *Atmos. Environ., 28,* 2981-2989, 1994.

Syri, S., M. Johansson, and L. Kangas, Application of nitrogen transfer matrices for integrated assessment, *Atmos. Environ., 32,* 409-413, 1998.

Tabazadeh, A., M. Z. Jacobson, H. B. Singh, O. B. Toon, J. S. Lin, R. B. Chatfield, A. N. Thakur, R. W. Talbot, and J. E. Dibb, Nitric acid scavenging by mineral and biomass burning aerosols, *Geophys. Res. Lett., 25,* 4185-4188, 1998.

Talbot, R. W., R. C. Harriss, E. V. Browell, G. L. Gregory, D. I. Sebacher, and S. M. Beck, Distribution and geochemistry of aerosols in the tropical North Atlantic troposphere: relationship to Saharan dust, *J. Geophys. Res., 91,* 5173-5182, 1986.

Talbot, R. W., M. O. Andreae, T. W. Andreae, and R. C. Harriss, Regional aerosol chemistry of the Amazon Basin during the dry season, *J. Geophys. Res., 93,* 1499-1508, 1988.

Talbot, R. W., M. O. Andreae, H. Berresheim, P. Artaxo, M. Garstang, R. C. Harriss, K. M. Beecher, and S. M. Li, Aerosol chemistry during the wet season in central

Amazonia: The influence of long-range transport, *J. Geophys. Res., 95,* 16,955-16,969, 1990.

Talbot, R. W., A. S. Vijgen, and R. C. Harriss, Soluble species in the Arctic summer troposphere: Acidic gases, aerosols, and precipitation, *J. Geophys. Res., 97,* 16,531-16,543, 1992.

van Dorland, R., F. J. Dentener, and J. Lelieveld, Radiative forcing due to tropospheric ozone and sulfate aerosols, *J. Geophys. Res., 102,* 28,079-28,100, 1997.

Wang, Y., D. J. Jacob, and J. A. Logan, Global simulation of tropospheric O_3-NO_x-hydrocarbon chemistry, 1, Model formulation, *J. Geophys. Res., 103,* 10,713-10,725, 1998a.

Wang, Y., D. J. Jacob, and J. A. Logan, Global simulation of tropospheric O_3-NO_x-hydrocarbon chemistry, 2, Model evaluation and global ozone budget, *J. Geophys. Res., 103,* 10,727-10,755, 1998b.

Warneck, P., Nitrogen compounds in the troposphere, in Chemistry of the Natural Atmosphere, Academic, San Diego, Calif., 1988.

Wesely, M. L., Parameterization of surface resistances to gaseous dry deposition in regional-scale numerical models, *Atmos. Environ., 23,* 1293-1304, 1989.

Wesely, M. L., and B. B. Hicks, Some factors that affect the deposition rates of sulfur dioxide and similar gases on vegetation, *J. Air Pollut. Contr. Assoc., 27,* 1110-1116, 1977.

West, J. J., C. Pilinis, A. Nenes, and S. N. Pandis, Marginal direct climate forcing by atmospheric aerosols, *Atmos. Environ., 32,* 2531-2542, 1998.

Wexler, A. S., and J. H. Seinfeld, The distribution of ammonium salts among a size and composition dispersed aerosol, *Atmos. Environ., Part A, 24*, 1231-1246, 1990.

Wexler, A. S., and J. H. Seinfeld, Second-generation inorganic aerosol model, *Atmos. Environ., Part A, 25*, 2731-2748, 1991.

Whelpdale, D. M., W. C. Keene, A. D. A. Hansen, and J. Boatman, Aircraft measurements of sulfur, nitrogen, and carbon species during WATOX-86, Global Biogeochem. *Cycles, 1,* 357-368, 1987.

Yoshizumi, K., and K. Asakuno, Characterization of atmospheric aerosols in Chichi of the Ogasawara (Bonin) Islands, *Atmos. Environ., 20,* 151-155, 1986.

Figure captions

Plate 2.1. GEIA ammonia emissions inventory [*Bouwman et al.*,1997]. Total ammonia emission fluxes (g N m^{-2} yr) of each GCM grid cell are shown.

Figure 2.1. Mass concentration of various aerosol components as a function of sulfate mass. These results were calculated by the aerosol thermodynamic equilibrium module, ISORROPIA, for 285 K, 80% relative humidity, 4.5 μg m^{-3} total NH_3, and 6.0 μg m^{-3} total HNO_3.

Plate 2.2. (a) Annual average of monthly nitric acid mixing ratio fields used as input by the GCM. (b) Annual average sulfate mixing ratios. Note that 1 μg m^{-3} SO_4^{2-} = 258 pptv SO_4^{2-} at 298 K and 1 bar. Above each plot, the pressure level of the corresponding model layer is indicated, as is the average mixing ratio in that layer. Contour lines are 1, 3, 10, 30, 100, 300, 1000, 3000, 10,000, and 30,000 pptv.

Figure 2.2. Scatter plot of simulated sulfate mixing ratios versus observations from (a) the EMEFS database, (b) the EMEP database, (c) polluted continental areas, (d) remote continental areas, and (e) marine areas. Dashed lines indicate 2:1 and 1:2 ratios.

Plate 2.3. (a) Annual average ammonia mixing ratios. Note that 1 μg m^{-3} NH_3 = 1457 pptv NH_3 at 298 K and 1 bar. (b) Annual average ammonium mixing ratios. Note that 1

$\mu g\ m^{-3}\ NH_4^+$ = 1377 pptv NH_4^+ at 298 K and 1 bar. (c) Annual average nitrate mixing ratios. Note that 1 $\mu g\ m^{-3}\ NO_3^-$ = 400 pptv NO_3^- at 298 K and 1 bar. Above each plot, the pressure level of the corresponding model layer is indicated, as is the average mixing ratio in that layer. Contour lines are 1, 3, 10, 30, 100, 300, 1000, 3000, 10,000, and 30,000 pptv.

Figure 2.3. Scatter plot of simulated ammonium mixing ratios versus observations taken from (a) the EMEFS database, (b) the EMEP database, (c) polluted continental areas, (d) remote continental areas, and (e) marine areas. Dashed lines indicate 2:1 and 1:2 ratios.

Figure 2.4. Scatter plot of simulated ammonia mixing ratios versus observations taken from (a) the EMEFS database, (b) polluted continental areas, and (c) remote continental areas. Dashed lines indicate 2:1 and 1:2 ratios.

Figure 2.5. Global and annual average ammonia budget. Arrows indicate net fluxes. Burdens and lifetimes of ammonia and ammonium are shown in their respective boxes. Values inside parentheses are taken from a sensitivity study in which nitric acid is neglected.

Figure 2.6. Scatter plot of simulated nitrate mixing ratios versus observations taken from (a) the EMEFS database, (b) the EMEP database, (c) polluted continental areas, (d) remote continental areas, and (e) marine areas. Dashed lines indicate 2:1 and 1:2 ratios.

Plate 2.4. (a) Percent of total HNO_3 occurring in the aerosol phase. (b) Percent of acidic anions (sulfate and nitrate) neutralized by aerosol ammonium (See definition of DON in text). (c) Nitrate to sulfate molar ratios. Above each plot, the pressure level of the corresponding model layer is indicated, as is the average value for that layer.

Plate 2.5. (a) The gas ratio (defined in text). (b) Annual average aerosol water mixing ratios. (c) Aerosol water to sulfate molar ratios. Above each plot, the pressure level of the corresponding model layer is indicated as well as average values for Plates 2.5b and 2.5c.

Plate 2.6. (a) Annual average aerosol mass mixing ratios. (b) Nitrate enhancement of total aerosol mass (ratio of annual average aerosol mass to that assuming no HNO_3). Above each plot, the pressure level of the corresponding model layer is indicated, as is the average value for that layer.

Figure 2.7. Comparison of simulated and observed seasonal cycles in the mixing ratios of model species at four EMEFS sites. Mixing ratios are monthly mean (ppbv). Solid lines indicate model values and squares indicate observed values.

Table 2.1. Summary of Assumptions Made About Aerosol Composition, Water Uptake, and Size Distribution in Calculations of Direct Radiative Forcing

Reference	Composition	RH	Hysteresis	Size Distribution
Chuang et al. [1997]	assumed $(NH_4)_2SO_4$	water uptake based on Kohler theory	optical properties averaged rising and falling RH cases	assumed lognormal r_m(dry)=0.05 μm σ=2.0
Feichter et al. [1997]	multiplied $[SO_4]$ by 1.46 to account for bound NH_4	assumed 80% constant		assumed lognormal r_m(dry)=0.07 μm σ=2.03
Haywood and Shine [1995]	assumed $(NH_4)_2SO_4$	uniform growth factor of 1.32		assumed lognormal r_m(dry)=0.05 μm σ=2.0
Haywood et al. [1997]	assumed $(NH_4)_2SO_4$	growth factor based on GCM RH	Three cases: ascending RH, descending RH, linear interpolation	assumed lognormal r_m(dry)=0.05 μm σ=2.0
Haywood and Ramaswamy [1998]	assumed $(NH_4)_2SO_4$	growth factor based on GCM RH	linear interpolation	assumed lognormal r_m(dry)=0.05 μm σ=2.0
Kiehl and Briegleb [1993]	assumed 75% H_2SO_4, 25% H_2O	f(RH) from observations, monthly mean RH from ECMWF		assumed lognormal r_m(dry)=0.05 μm σ=2.0
van Dorland et al. [1997]	assumed $(NH_4)_2SO_4$	Two cases: 80% constant; prescribed Oort [1983] in lower troposphere, fixed at 50% in upper troposphere		assumed lognormal r_m(dry)=0.021 μm σ=2.239

ECMWF, European Centre for Medium-Range Weather Forecasts; GCM, general circulation model; RH, relative humidity.

Table 2.2. Global Ammonia Emissions by Source

Source	Emission, Tg N yr^{-1}
Domesticated animals	21.6
Fertilizers	9.0
Oceans	8.2
Biomass burning	5.9
Crops	3.6
Humans	2.6
Soils under natural vegetation	2.4
Other	0.4
Total	53.6

From [*Bouwman et al.*, 1997]

Table 2.3. Equilibrium Relations and Constants Used in the Aerosol Thermodynamic Equilibrium Module ISORROPIA

Reaction	Equilibrium Constant Expression	K_o (298.15K)	$\frac{\Delta H^0(T_0)}{RT_0}$	$\frac{\Delta c_p^0}{R}$	Units
$HSO_{4(aq)}^- \overset{K_1}{\longleftrightarrow} H_{(aq)}^+ + SO_{4(aq)}^{2-}$	$\frac{[H^+][SO_4^{2-}]}{[HSO_4^-]}\frac{\gamma_{H^+}\gamma_{SO_4^{2-}}}{\gamma_{HSO_4^-}}$	1.015×10^{-2}	8.85	25.14	mol kg^{-1}
$NH_{3(g)} \overset{K_{21}}{\longleftrightarrow} NH_{3(aq)}$	$\frac{[NH_{3(aq)}]}{P_{NH_3}}\gamma_{NH_3}$	5.764×10^{1}	13.79	-5.39	mol kg^{-1} atm^{-1}
$NH_{3(aq)} + H_2O_{(aq)} \overset{K_{22}}{\longleftrightarrow} NH_{4(aq)}^+ + OH_{(aq)}^-$	$\frac{[NH_4^+][OH^-]}{[NH_{3(aq)}]a_w}\frac{\gamma_{NH_4^+}\gamma_{OH^-}}{\gamma_{NH_3}}$	1.805×10^{-5}	-1.50	26.92	mol kg^{-1}
$HNO_{3(g)} \overset{K_4}{\longleftrightarrow} H_{(aq)}^+ + NO_{3(aq)}^-$	$\frac{[H^+][NO_3^-]}{P_{HNO_3}}\gamma_{H^+}\gamma_{NO_3^-}$	2.511×10^{6}	29.17	16.83	mol^2 kg^{-2} atm^{-1}
$H_2O_{(aq)} \overset{K_w}{\longleftrightarrow} H_{(aq)}^+ + OH_{(aq)}^-$	$\frac{[H^+][OH^-]}{a_w}\gamma_{H^+}\gamma_{OH^-}$	1.010×10^{-14}	-22.52	26.92	mol^2 kg^{-2}
$(NH_4)_2SO_{4(s)} \overset{K_7}{\longleftrightarrow} 2NH_{4(aq)}^+ + SO_{4(aq)}^{2-}$	$[NH_4^+]^2[SO_4^{2-}]\gamma_{NH_4^+}^2\gamma_{SO_4^{2-}}$	1.817×10^{0}	-2.65	38.57	mol^3 kg^{-3}
$NH_4NO_{3(s)} \overset{K_{10}}{\longleftrightarrow} NH_{3(g)} + HNO_{3(g)}$	$P_{NH_3}P_{HNO_3}$	5.746×10^{-17}	-74.38	6.12	atm^2
$NH_4HSO_{4(s)} \overset{K_{12}}{\longleftrightarrow} NH_{4(aq)}^+ + HSO_{4(aq)}^-$	$[NH_4^+][HSO_4^-]\gamma_{NH_4^+}\gamma_{HSO_4^-}$	1.383×10^{0}	-2.87	15.83	mol^2 kg^{-2}
$(NH_4)_3H(SO_4)_{2(s)} \overset{K_{13}}{\longleftrightarrow}$ $3NH_{4(aq)}^+ + HSO_{4(aq)}^- + SO_{4(aq)}^{2-}$	$[NH_4^+]^3[SO_4^{2-}][HSO_4^-]x$ $\gamma_{NH_4^+}^3\gamma_{SO_4^{2-}}\gamma_{HSO_4^-}$	2.972×10^{1}	-5.19	54.40	mol^5 kg^{-5}

From [*Nenes et al.*, 1998].

Table 2.4. Thermodynamic Properties in the Aerosol Thermodynamic Equilibrium Module, ISORROPIA

Species	ΔG_f^0, kJ mol^{-1}	ΔH_f^0, kJ mol^{-1}	c_p^0, J mol^{-1} K^{-1}
$HNO_{3(g)}$	-74.720	-135.060	53.350
$NH_{3(g)}$	-16.450	-46.110	35.060
$H^+_{(aq)}$	0.000	0.000	0.000
$NH_4^+{}_{(aq)}$	-79.310	-132.510	79.900
$HSO_4^-{}_{(aq)}$	-755.910	-887.340	-84.000
$SO_4^{2-}{}_{(aq)}$	-744.530	-909.270	-293.000
$NO_3^-{}_{(aq)}$	-111.250	-207.360	-86.600
$OH^-_{(aq)}$	-157.244	-229.994	-148.500

From [*Nenes et al.*, 1998].

Table 2.5. Comparison of Simulated and Observed Mixing Ratios From the EMEFS Database.

			SO_4^{2-}		NO_3^-		NH_4^+		NH_3	
Location	Latitude, °N	Longitude, °W	Obs	Sim	Obs	Sim	Obs	Sim	Obs	Sim
Algoma, Ontario	47	84	664	1058	167	494	999	1656		334
Archbold, Florida	27	81	762	568	444	6	1107	664	1369	169
Arendtsville, Pennsylvania	40	77	1750	1739	848	614	3543	2514	581	426
Balsam Lake, Ontario	45	79	959	933	419	628	1594	1733		464
Bells, Tennessee	36	89	1337	1851	422	393	2250	2415	771	577
Benton, Kentucky	37	88	1753	2094	447	957	2787	3509	422	854
Big Moose, New York	44	75	969	1169	121	850	1463	2395	84	656
Brackney, Pennsylvania	42	76	1376	1613	316	1145	2230	3169	122	613
Brokensword, Ohio	41	83	1535	1892	1100	1219	3584	3568	823	730
Brookings, South Dakota	44	97	566	550	639	1086	1459	2016	3332	2048
Cadiz, Kentucky	37	88	1635	2094	445	957	3005	3509	1044	854
Caryville, Florida	31	86	1091	1153	228	72	1670	1285	371	228
Cedar Creek SP, West Virginia	39	81	1681	2271	130	746	2126	3069	70	443
Chalk River, Ontario	46	77	852	933	97	628	1163	1733		464
Chapais, Quebec	50	75	456	431	25	232	461	656		213
Charleston Lake, Ontario	45	76	711	933	274	628	1361	1733		464
Coweeta Forest, North Carolina	35	83	1311	1696	77	247	1696	2000	73	373
Cree Lake, Saskatchewan	57	107	242	317	23	110	250	399		111
Decatur, Pennsylvania	41	77	1561	1613	716	1145	3451	3169	1782	613
Deer Cr. Park, Ohio	40	83	1847	2271	892	746	3779	3069	574	443
Dorset, Ontario	45	79	819	933	197	628	1263	1733		464
Due West, South Carolina	34	82	1508	1696	229	247	2411	2000	355	373
E. Smithfield	42	77	1377	1613	553	1145	2829	3169	1142	613
E.L.A., Ontario	50	94	380	438	130	462	579	1038		551
Eddyville, Kentucky	37	88	1707	2094	452	957	2782	3509	242	854
Egbert, Ontario	44	80	1098	933	921	628	2472	1733	1010	464
Emporium, Pennsylvania	42	78	1421	1613	220	1145	1893	3169	57	613
Fernberg, Minnesota	48	91	358	639	184	1158	640	2167		1732
Ford City, Pennsylvania	41	80	1745	1613	405	1145	2909	3169	292	613
Fort Wayne, Indiana	41	85	1627	1449	1303	1548	3793	3524	1157	1149
Gaylord, Michigan	45	85	923	1058	298	494	1571	1656	250	334
Gowganda, Ontario	48	81	563	1058	89	494	808	1656		334
Hawthorne, Pennsylvania	41	79	1688	1613	328	1145	2622	3169	101	613
High Falls, Ontario	46	82	682	1058	148	494	1014	1656		334
Ithaca, New York	42	76	1290	1613	330	1145	2220	3169	133	613
Jerome, Missouri	38	92	1068	1546	326	1114	1873	3154	561	1532
Kane Forest, Pennsylvania	42	79	1481	1613	246	1145	2087	3169	47	613
Kejimkujik, Nova Scotia	44	65	734	608	90	262	680	965		297
Lancaster, Kansas	40	95	840	780	804	678	1686	2020	3080	2144
Leitchfield, Kentucky	37	86	1866	2094	479	957	3225	3509	399	854
LilleyCornett, Kentucky	37	83	1625	2271	177	746	2014	3069	263	443
Little Marsh, Pennsylvania	42	77	1390	1613	298	1145	2318	3169	165	613
Longwoods, Ontario	43	81	1266	1892	1056	1219	2769	3568		730
Marion, Alabama	33	87	1342	1851	235	393	2089	2415	510	577
Marshall, Texas	33	94	1320	1311	309	485	1884	2123	346	975
Montmorency, Quebec	47	71	630	760	54	696	833	1679		604
Moorhead, Kentucky	38	84	1929	2271	279	746	2689	3069	144	443
Morton, Mississippi	32	90	1210	1851	374	393	2364	2415	3143	577
Mountain Lake, Virginia	37	81	1733	2271	171	746	1892	3069	66	443
New Concord, Kentucky	37	88	1710	2094	271	957	2312	3509	164	854
North Orwell, Pennsylvania	42	76	1380	1613	430	1145	2490	3169	189	613
Parsons, West Virginia	39	80	1827	1739	245	614	2357	2514	165	426

Penn State, Pennsylvania	41	78	1626	1613	336	1145	2572	3169	125	613
Perryville, Kentucky	38	85	1936	2271	479	746	3222	3069	294	443
Piseco, New York	43	75	925	1169	118	850	1368	2395	52	656
Pittsboro, North Carolina	36	79	1561	1049	362	112	2825	1115	677	204
Renovo, Pennsylvania	41	78	1517	1613	238	1145	2075	3169	52	613
Roaring Creek, North Carolina	36	82	1439	2271	117	746	1613	3069	61	443
Round Lake, Wisconsin	46	92	571	639	361	1158	1230	2167	440	1732
Shawano, Wisconsin	45	89	880	874	1017	673	2524	1880	2715	701
Sutton, Quebec	45	73	984	760	228	696	1781	1679		604
Tunkhannock, Pennsylvania	42	76	1475	1613	349	1145	2514	3169	234	613
Underhill, Vermont	45	73	949	760	138	696	1454	1679	158	604
Uvalda, Georgia	32	82	1154	1696	263	247	1745	2000	357	373
Vincennes, Indiana	39	87	1731	2094	925	957	3371	3509	1038	854
Wartburg, Tennessee	36	85	1726	2271	238	746	2691	3069	196	443
Warwick, Massachusetts	43	72	1127	1169	159	850	1622	2395	127	656
Wayland, New York	43	78	1307	1613	433	1145	2479	3169	351	613
Wellesley, Ontario	43	81	1164	1892	1325	1219	3078	3568		730
Whiteface, New York	44	74	885	760	108	696	1201	1679	57	604
Williamsport, Pennsylvania	41	77	1599	1613	625	1145	3064	3169	338	613
Winterport, Maine	45	69	806	608	122	262	1146	965	118	297
Wirt, New York	42	78	1358	1613	249	1145	2016	3169	127	613
Yampa, Colorado	40	107	279	440	73	211	467	764	527	261
Zanesville, Ohio	40	82	1803	1892	644	1219	3130	3568	531	730

Mixing ratios are in parts per trillion by volume. EMEFS, Eulerian Model Evaluation Field Study.

Table 2.6. Comparison of Simulated and Observed Mixing Ratios [pptv] from the EMEP Database

			SO_4^{2-}		NO_3^-		NH_4^+		NH_3	
Location	Latitude	Longitude	Obs	Sim	Obs	Sim	Obs	Sim	Obs	Sim
Bilthoven, Netherlands	52° N	5° E	1138	984	1910	2008		3553		2214
Ispra, Italy	46° N	9° E	1447	1220	2440	1253	4687	2833		1057
Janiskoski, Russia	69° N	29° E	442	368	64	66	433	332		88
Jarczew, Poland	51° N	22° E	2360	1668		1727	3676	4354		2507
Kosetice, Czech Rep.	50° N	15° E	1798	2251	738	2029	2392	5601	10915	2197
K-puszta, Hungary	47° N	20° E	1489	2001	562	985	1910	4052	1541	1599
La Cartuja, Spain	37° N	4° W	1039	728		75	514	1224		915
Logrono, Spain	42° N	2° W	850	953		351	722	1715		800
Roquetas, Spain	41° N	1° W	969	953		351	867	1715		800
Suwalki, Poland	54° N	23° E	1608	1418		1722	1605	4014		2473
Svratouch, Czech Rep.	50° N	16° E	1475	2251	658	2029	4623	5601	12119	2197
Toledo, Spain	40° N	4° W	471	728		75	578	1224		915
Vysokoe, Belarus	52° N	23° E	1022	1418	742	1722	2263	4014		2473
Witteveen, Netherlands	53° N	7° E	976	984	1525	2008		3553		2214

Table 2.7. Comparison of Simulated and Observed Global Mixing Ratios

Location	Latitude	Longitude	Altitude	Time	SO_4^{2-}		NO_3^-		NH_4^+		NH_3		Reference
					Obs	Sim	Obs	Sim	Obs	Sim	Obs	Sim	
Polluted Continental Sites													
Agra, India	27 N	78 E	surf	Dec-Mar	3526	278		31	8344	601		9914	*Kulshrestha et al.* [1998]
Allegheny Mountain, Pennsylvania	41.5 N	78.5 W	surf	Jun-Aug	4494	2298	202	537	3865	3181		615	*Pierson et al.* [1989]
Beijing	40 N	116 E	surf	Oct	2050	768		929	2800	2295		3308	*Huebert et al.* [1988]
Boulder, Colorado	40 N	105 W	surf	Jan-Dec	281	423		497	600	1209		1289	*Langford, et al.* [1992]
Boulder, Colorado	40 N	105 W	surf	Jun-Aug	382	540	517	326	989	1318	5169	1932	*Langford, et al.* [1992]
Boulder, Colorado	40 N	105 W	surf	Dec-Feb	180	213	315	724	652	1044	1348	558	*Langford, et al.* [1992]
Changsha	28 N	113 E	surf	Oct	2050	1872		804	3880	4433		7696	*Huebert et al.* [1988]
England	52 N	3 E	surf	Jan-Dec	1100	954		975	2500	2373		567	*Hansen, et al.* [1990]
Farkasfa, Hungary	47 N	16.5 E	surf	Jan-Dec	2161	2001	1459	985	4650	4052		1599	*Meszaros and Horvath,* [1984]
Germany	53 N	10 E	surf	Jan-Dec		1245		2072	3400	4106		2026	*Lenhard and Gravenhorst,* [1980]
Hungary	47 N	20 E	surf	Jan-Dec	2500	1561		1102	1600	3665		2740	*Hanssen et al.* [1990]
Kinterbish, Alabama	32.3 N	88.2 W	surf	Jun-Aug	1258	2767	202	13	1955	2339	629	438	*Langford, et al.* [1992]
K-puszta, Hungary	47 N	19.3 E	surf	Jan-Dec	2060	2001	1568	985	4730	4052	1561	1599	*Meszaros and Horvath,* [1984]
Lake Isabella, California	35.6 N	118.5 W	surf	Dec-Feb	90	326	202	339	180	796	427	365	*Jacob et al.* [1986]
Lake Ozette	47 N	125 W	surf	Mar-May	100	540		80	110	684		293	*Covert,* [1988]
Lancaster, England	54 N	3 W	surf	Jan-Dec	1978	800	2291	926	5571	2092		822	*Harrison and Pio,* [1983]
Los Angeles, California	34 N	118 W	surf	Nov-Dec	1676	332		231	18113	764		575	*John et al.* [1990]
Los Angeles, California	34 N	118 W	surf	Jun-Aug	2247	311		5	12125	570		765	*John et al.* [1990]
Newtown, Connecticut	41.5 N	73.5 W	surf	Jun-Aug	1461	1849	112	331	2517	2503	764	570	*Keeler et al.* [1991]
Northern Michigan	45 N	85 W	surf	Dec-Feb	629	619	427	1409	966	2291	45	417	*Cadle et al.* [1985]
Oak Ridge, Tennessee	36 N	84 W	surf	Jun-Aug	3978	3858	539	177	5393	3107	202	351	*Langford, et al.* [1992]
Oak Ridge, Tennessee	36.1 N	84.2	surf	Jun-Aug	2337	3858	67	177	2989	3107	337	351	*Lindberg et al.* [1990]
Poona, India	19 N	74 E	surf	Jan-Dec	440	408		14	980	800		3940	*Khemani et al.* [1982]
Sapporo, Japan	43 N	141 E	surf	Aug	895	1146	55	21	1268	1595		436	*Ohta and Okita,* [1990]
Sapporo, Japan	43 N	14 E	surf	Sep	701	676	172	18	823	977		176	*Ohta and Okita,* [1990]
Sapporo, Japan	43 N	141 E	surf	Apr	1277	1186	607	159	1376	1789		500	*Ohta and Okita,* [1990]
Sapporo, Japan	43 N	141 E	surf	Jul	1118	1000	43	48	1363	1565		552	*Ohta and Okita,* [1990]
Sapporo, Japan	43 N	141 E	surf	Jun	1032	735	204	68	1255	1146		454	*Ohta and Okita,* [1990]
Sapporo, Japan	43 N	141 E	surf	Oct	837	584	415	37	998	820		265	*Ohta and Okita,* [1990]
Sapporo, Japan	43 N	141 E	surf	Jan-Dec	1074	734	374	87	1546	1124		589	*Ohta and Okita,* [1990]
Sapporo, Japan	43 N	141 E	surf	Mar	1351	899	603	134	2320	1495		1031	*Ohta and Okita,* [1990]
Sapporo, Japan	43 N	141 E	surf	May	1166	742	466	89	1282	1138		417	*Ohta and Okita,* [1990]
Sapporo, Japan	43 N	141 E	surf	Nov	992	582	431	81	1538	815		456	*Ohta and Okita,* [1990]
Sapporo, Japan	43 N	141 E	surf	Feb	1247	630	580	117	2401	952		1478	*Ohta and Okita,* [1990]
Sapporo, Japan	43 N	141 E	surf	Dec	1078	302	462	120	1767	552		790	*Ohta and Okita,* [1990]
Sapparo, Japan	43 N	141 E	surf	Jan	1191	322	447	156	2159	638		571	*Ohta and Okita,* [1990]

State College, Pennsylvania	41 N	78 W	surf	Jun-Aug	2810	2298		537	3837	3181		615	*Suh et al.* [1994]
Sweden	59 N	17 E	surf	Jan-Dec	840	691		845	1340	1840		647	*Hanssen et al.* [1990]
Tehachapi, California	35.2 N	118.4 W	surf	Dec-Feb	180	326	247	339	247	796	764	365	*Jacob et al.* [1986]
Veszprem, Hungary	47 N	18 E	surf	Jun-Aug	1533	3426	467	401	3350	5431		2122	*Meszaros et al.* [1997]
Veszprem, Hungary	47 N	18 E	surf	Dec-Feb	1809	1035	1712	1872	5628	3497		1213	*Meszaros et al.* [1997]
Xinlong	38 N	120 E	surf	Oct	1540	2001		683	2650	4398		1564	*Huebert et al.* [1988]
					Remote Continental Sites								
Amazon	3 N	60 W	bl	Apr-May	81	18	58	1	92	36		340	*Talbon et al.* [1990]
Amazon	3 N	60 W	bl	Jul-Aug	125	17		1	300	34		299	*Talbon et al.* [1990]
Amazon	3 N	60 W	ft	Apr-May	11	9	11	<1	37	9		5	*Talbon et al.* [1990]
Amazon	3 N	60 W	ft	Jul-Aug	20	12		<1	60	15		3	*Talbon et al.* [1990]
Arctic	55 N	160 W	bl	Jun-Aug	128	210	30	2	137	85		2	*Talbon et al.* [1990]
Arctic	55 N	160 W	ft	Jun-Aug	40	397	15	5	52	190		4	*Talbon et al.* [1990]
Arctic	65 N	160 W	bl	Jun-Aug	29	317	11	2	53	161		5	*Talbon et al.* [1990]
Arctic	65 N	160 W	ft	Jun-Aug	65	403	22	7	75	189		4	*Talbon et al.* [1990]
Congo	4 N	14 E	surf	Jun	216	89	447	69	902	236		1594	*Clairac et al.* [1988]
Congo	4 N	14 E	surf	Oct	268	29	70	133	533	175		1593	*Clairac et al.* [1988]
Guyana	4 N	58 W	surf	Jun	65	25	5	<1	154	44		256	*Gregory et al.* [1986]
Guyana	4 N	58 W	ft	Jun	26	9	2	<1	12	12		4	*Gregory et al.* [1986]
Niwot Ridge, Colorado	40.05 N	105.6 W	surf	Jan-Dec	113	440	224	211	259	764	236	261	*Langford et al.* [1992]
Niwot Ridge, Colorado	40.05 N	105.6 W	surf	Jun-Aug	135	388	427	95	315	719	337	453	*Langford et al.* [1992]
Niwot Ridge, Colorado	40.05 N	105.6 W	surf	Dec-Feb	90	241	22	369	202	606	135	106	*Langford et al.* [1992]
South Pole	-90 N	10 E	surf	Dec	32	28	3	2	70	25	19	<1	*Gras,* [1983]
Wright Valley	77 S	162 E	surf	Nov-Dec	50	28	23	1	58	13	13	1	*Gras,* [1983]
Yakutsk	62 N	130 E	surf	Jan-Dec	100	330		84	165	395		89	*Ohta et al.* [1992]
					Marine Sites								
Atlantic	10 N	60 W	surf	Jun	10	25		<1	14	45		67	*Talbot et al.* [1986]
Atlantic	28 N	60 W	surf	Jun	34	143		<1	60	150		36	*Talbot et al.* [1986]
Atlantic	32 N	31 W	surf	Apr-May	425	248		1	385	284		114	*Church et al.* [1991]
Atlantic	35 N	70 W	ft	Jan	100	119	89	1	135	81		5	*Whelpdale et al.* [1987]
Atlantic	37 N	25 W	bl	Jun	1260	152	716	1	1302	119		13	*Huebert et al.* [1996]
Atlantic	37 N	25 W	ft	Jun	393	292	382	<1	470	133		5	*Huebert et al.* [1996]
Atlantic	40 N	70 W	bl	Jan	124	428	166	457	1000	1064		263	*Whelpdale et al.* [1987]
Atlantic	45 N	55 W	surf	Apr-May	410	439		12	380	319		33	*Church et al.* [1991]
Bonin Island	27 N	142 E	surf	Nov-Dec	484	268	257	<1	750	219		39	*Yoshizumi and Asakuno,* [1986]
Pacific	2 N	170 E	surf	Apr-May	100	17		<1	140	33		192	*Quinn et al.* [1990]
Pacific	5 S	155 W	surf	Feb-Mar	160	48		<1	100	89		179	*Clarke and Porter,* [1993]
Pacific	5 N	155 W	surf	Feb-Mar	175	26		<1	130	50		187	*Clarke and Porter,* [1993]
Pacific	15 N	155 W	surf	Feb-Mar	125	51		<1	25	85		128	*Clarke and Porter,* [1993]
Pacific	23 N	170 E	surf	Apr-May	450	86		<1	130	152		59	*Quinn et al.* [1990]
Pacific	43 N	170 E	surf	Apr-May	325	575		19	400	570		173	*Quinn et al.* [1990]
Pacific	46 N	126 W	bl	May	60	553		1	75	314		15	*Andreae et al.* [1988]
Pacific	50 S	160 W	surf	Mar-May	250	57	96	<1	115	25		4	*Parungo et al.* [1986]
Pacific - Hawaii	20 N	160 W	surf	Mar-May	250	127		<1	115	156		43	*Parungo et al.* [1986]

Santa Maria island	37 N	25 W	surf	Jun	475	166	311	<1	461	160	200	30	*Huebert et al.* [1996]
Tasmania	43 S	144 E	surf	Dec	40	68	9	1	70	134		219	*Berresheim et al.* [1990]
West Atlantic	31 N	75 W	surf	Jan-Dec	828	293	289	1	1206	289		79	*Berresheim et al.* [1990]

Mixing ratios are in parts per trillion by volume.
* Abbreviations are bl, boundary layer; ft, free troposphere; surf, surface.

Table 2.8. Geometric mean ratios of simulated to observed values for each species and observational database.

Species	EMEFS	EMEP	Pol. Cont.	Rem. Cont.	Marine
SO_4^{2-}	1.15	1.04	0.73	1.09	0.68
NO_3^-	2.29	1.50	0.51	0.14	
NH_4^+	1.23	1.63	0.84	0.74	0.75
NH_3	1.95		0.94	0.28	

Table 2.9. Global and Annual Average Aerosol Burdens for Base Run and Sensitivity Cases

	No	Base	S Emissions		$[HNO_3]$		NH_3 Emissions	
Species	Nitrate	Run	-25%	+25%	-25%	+25%	-25%	+25%
			Aerosol Burden in Teragrams					
SO_4^{2-}	2.11	2.09	1.52	2.62	2.03	2.08	2.08	2.07
NO_3^-		0.13	0.15	0.11	0.1	0.15	0.09	0.17
NH_4^+	0.37	0.39	0.35	0.41	0.38	0.39	0.32	0.45
H_2O	4.23	4.88	3.85	5.89	4.68	4.97	4.85	4.9
Total	6.71	7.49	5.87	9.03	7.19	7.59	7.34	7.59
			Aerosol Burden as Percent of Base					
	No	Base	S Emissions		$[HNO_3]$		NH_3 Emissions	
Species	Nitrate	run	-25%	+25%	-25%	+25%	-25%	+25%
SO_4^{2-}	101	100	73	125	97	100	100	99
NO_3^-	0	100	115	85	77	115	69	131
NH_4^+	95	100	90	105	97	100	82	115
H_2O	87	100	79	121	96	102	99	100
Total	90	100	78	121	96	101	98	101

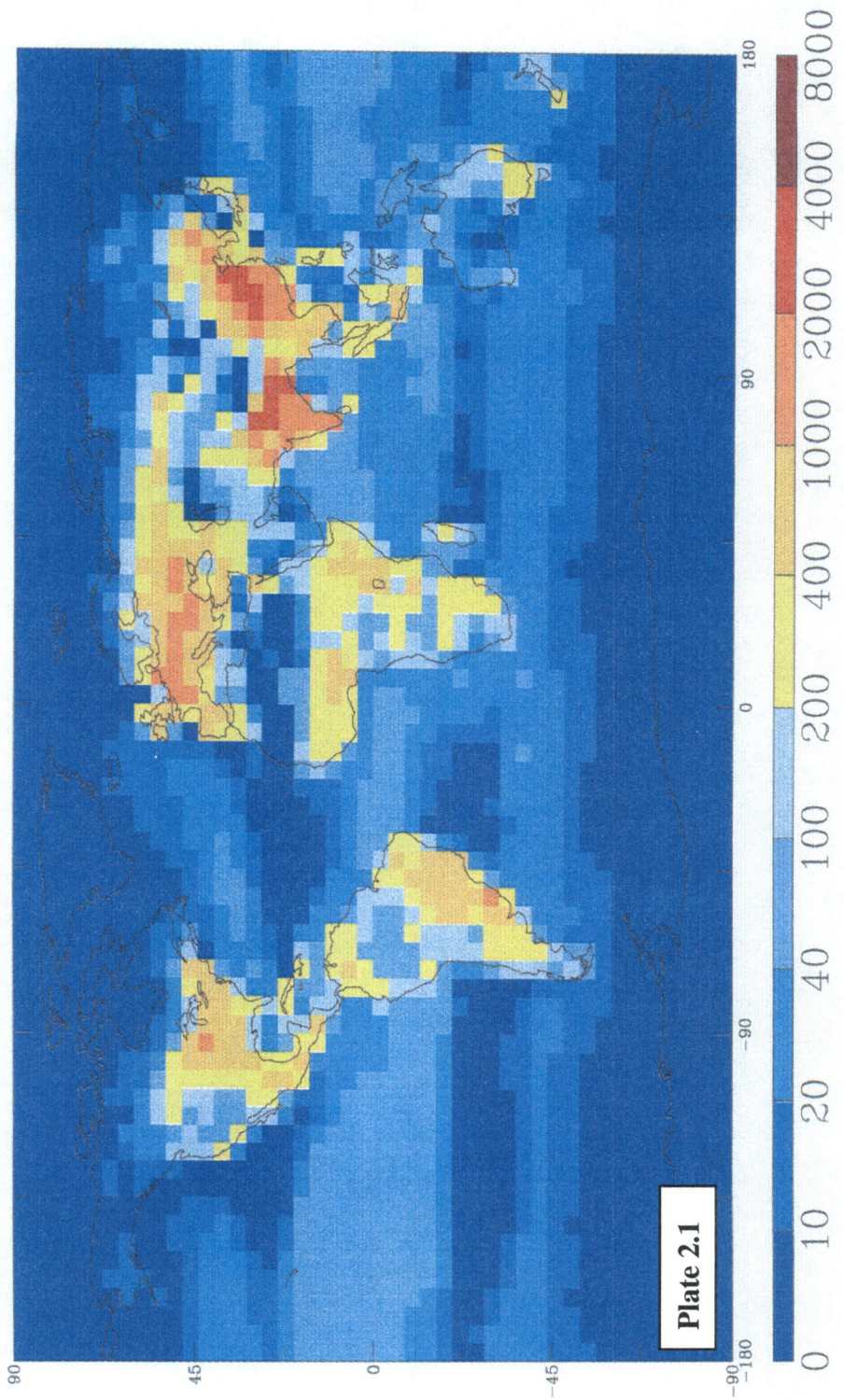
90
45
0
-45
-90
-180
-90
0
90
180
0
10
20
40
100
200
400
1000
2000
4000
8000
Plate 2.1

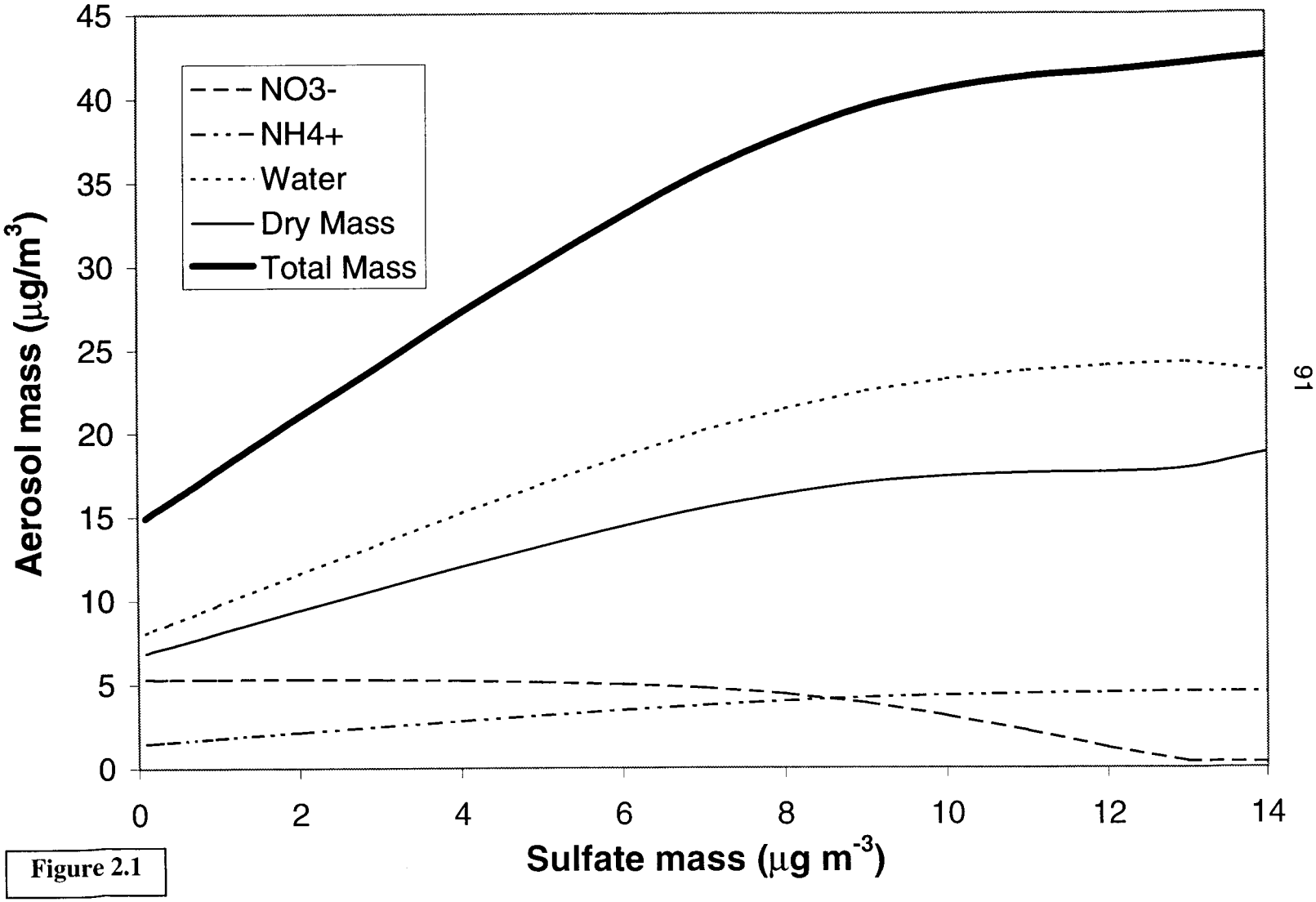
NO3-
NH4+
Water
Dry Mass
Total Mass
Aerosol mass (μg/m3)
Sulfate mass (μg m-3)
0
5
10
15
20
25
30
35
40
45
0
2
4
6
8
10
12
14

Figure 2.1

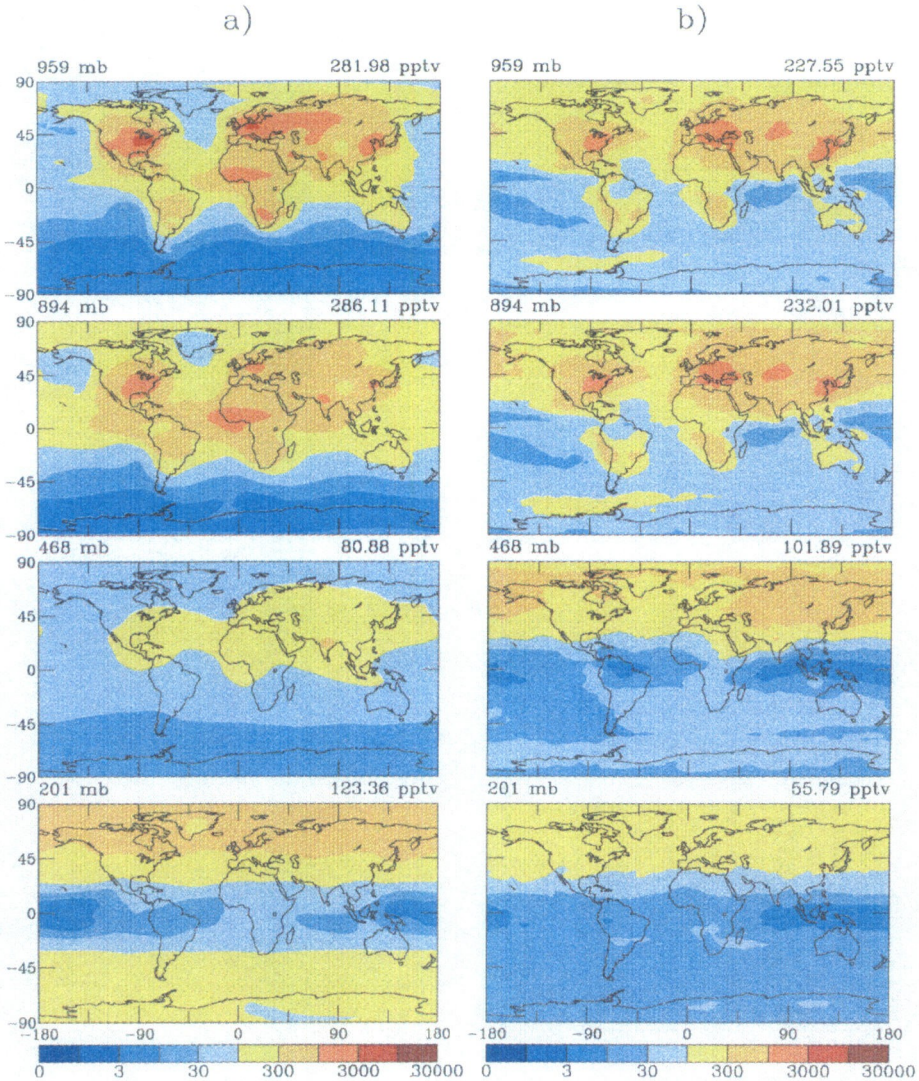
a)
b)
959 mb
281.98 pptv
959 mb
227.55 pptv
894 mb
286.11 pptv
894 mb
232.01 pptv
468 mb
80.88 pptv
468 mb
101.89 pptv
201 mb
123.36 pptv
201 mb
55.79 pptv
90
45
0
-45
-90
-180
-90
0
90
180
0
3
30
300
3000
30000

Plate 2.2

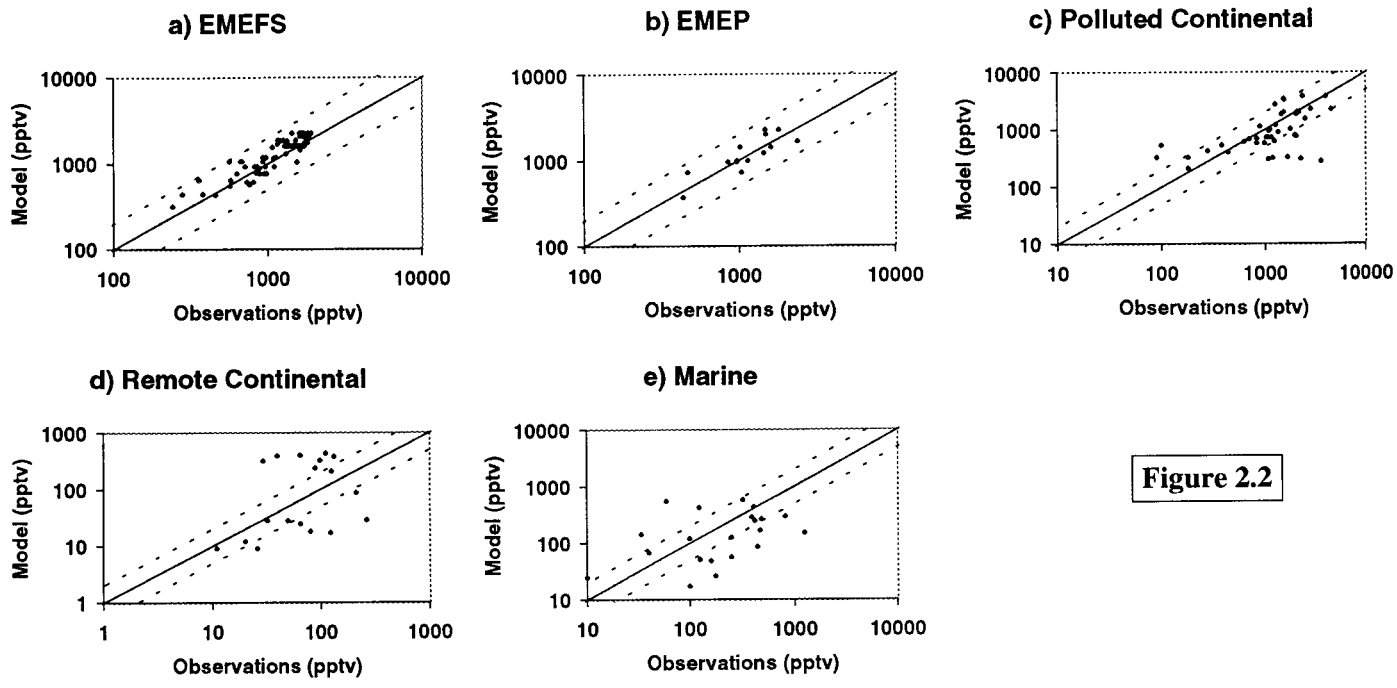
a) EMEFS
b) EMEP
c) Polluted Continental
d) Remote Continental
e) Marine
Model (pptv)
Observations (pptv)
10000
1000
100
10
1

Figure 2.2

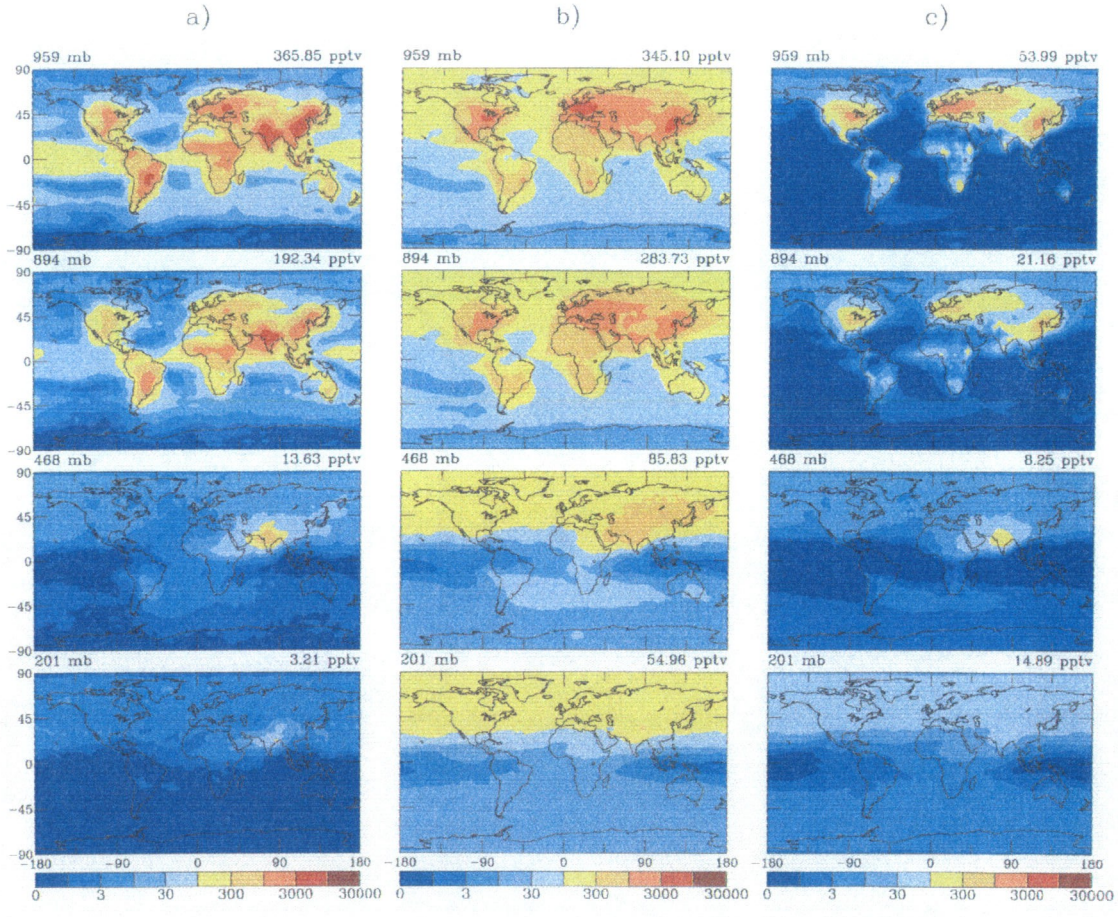
a)
b)
c)
959 mb
365.85 pptv
345.10 pptv
53.99 pptv
894 mb
192.34 pptv
283.73 pptv
21.16 pptv
468 mb
13.63 pptv
85.83 pptv
8.25 pptv
201 mb
3.21 pptv
54.96 pptv
14.89 pptv
90
45
0
-45
-90
-180
-90
0
90
180
0
3
30
300
3000
30000

Plate 2.3

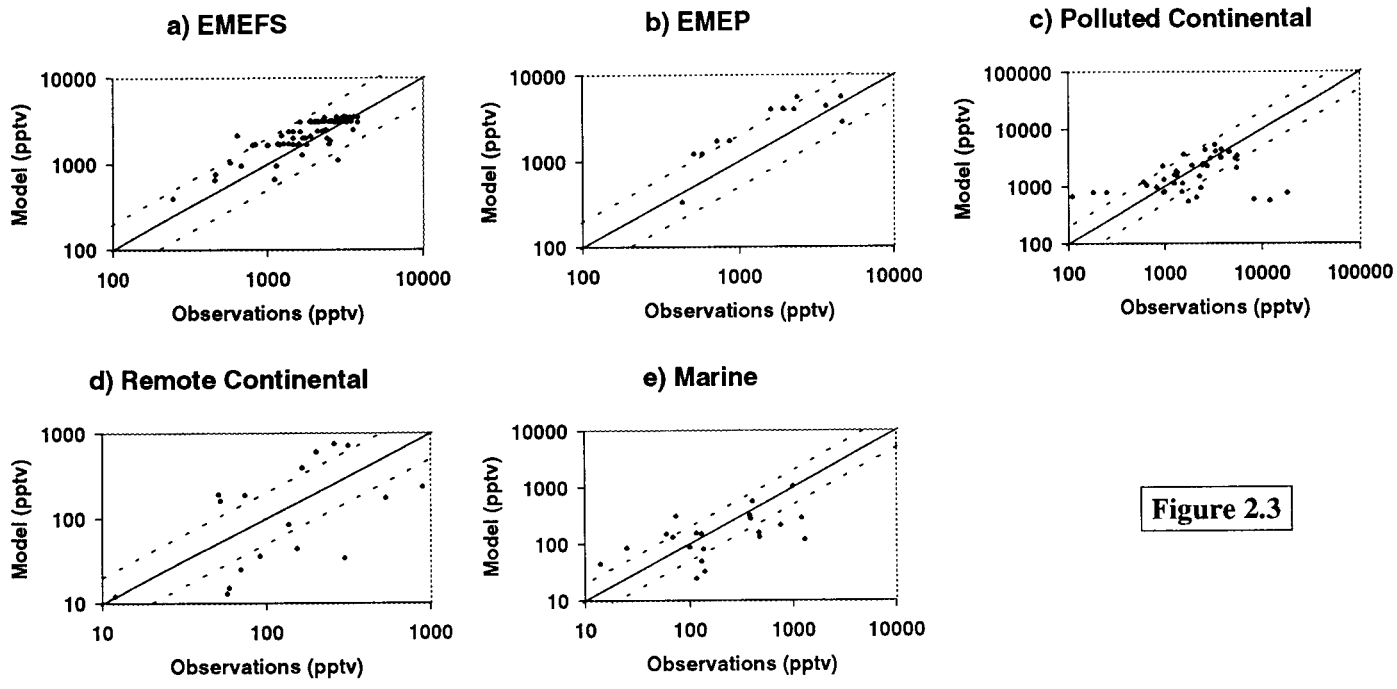
a) EMEFS
Model (pptv)
Observations (pptv)
10000
1000
100
b) EMEP
Model (pptv)
Observations (pptv)
10000
1000
100
c) Polluted Continental
Model (pptv)
Observations (pptv)
100000
10000
1000
100
d) Remote Continental
Model (pptv)
Observations (pptv)
1000
100
10
e) Marine
Model (pptv)
Observations (pptv)
10000
1000
100
10

Figure 2.3

a) EMEFS

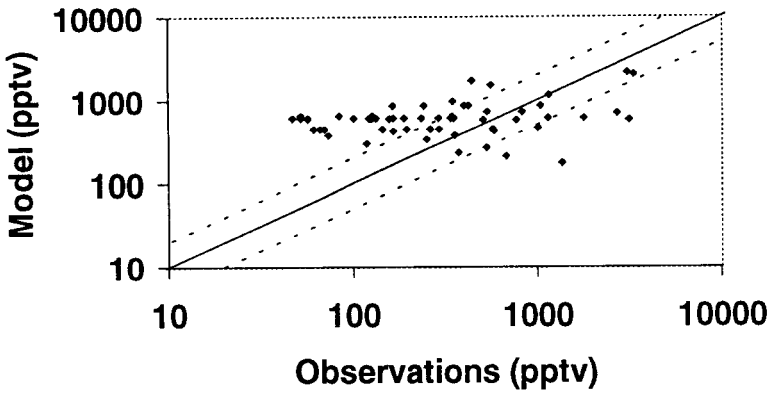

b) Polluted Continental

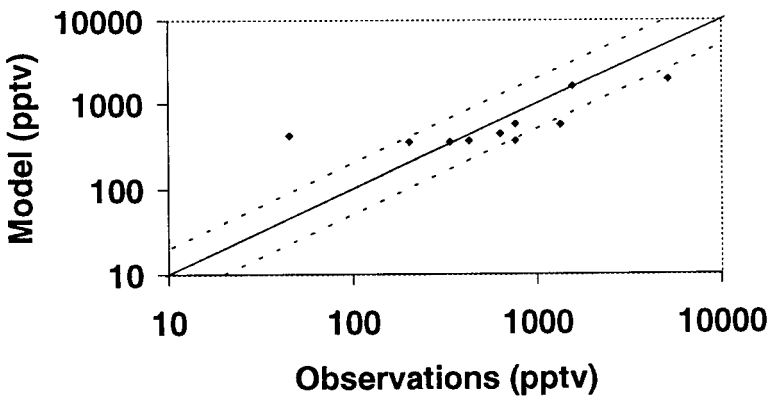

c) Remote Continental

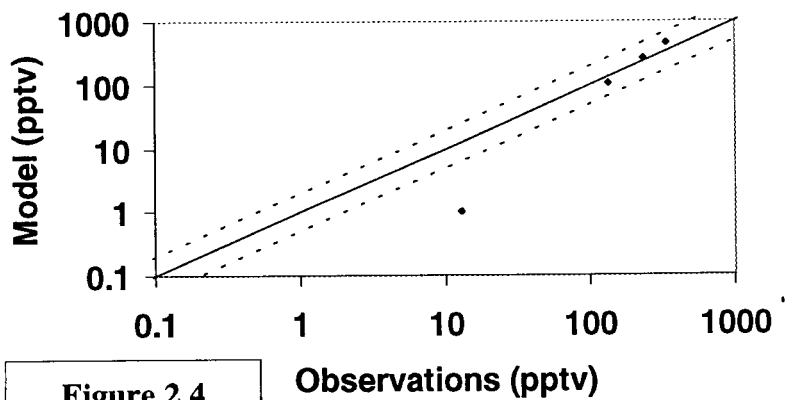

Figure 2.4

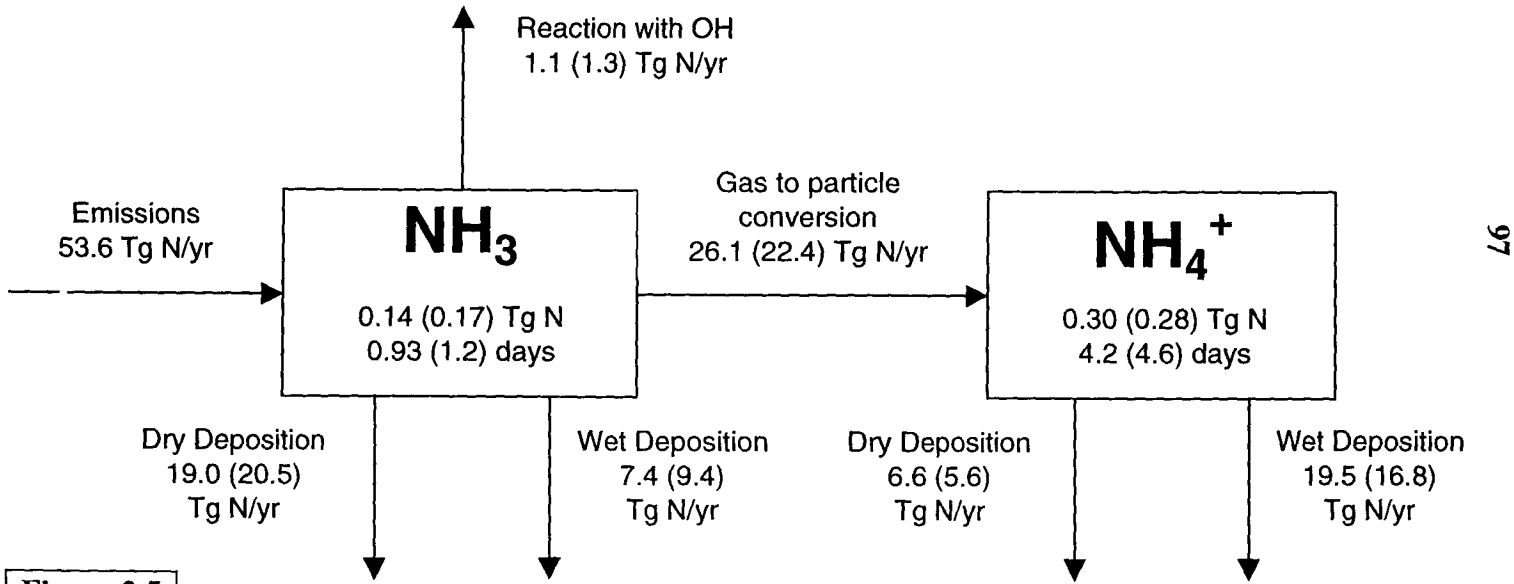
Reaction with OH
1.1 (1.3) Tg N/yr
Emissions
53.6 Tg N/yr
NH3
0.14 (0.17) Tg N
0.93 (1.2) days
Gas to particle
conversion
26.1 (22.4) Tg N/yr
NH4+
0.30 (0.28) Tg N
4.2 (4.6) days
Dry Deposition
19.0 (20.5)
Tg N/yr
Wet Deposition
7.4 (9.4)
Tg N/yr
Dry Deposition
6.6 (5.6)
Tg N/yr
Wet Deposition
19.5 (16.8)
Tg N/yr

Figure 2.5

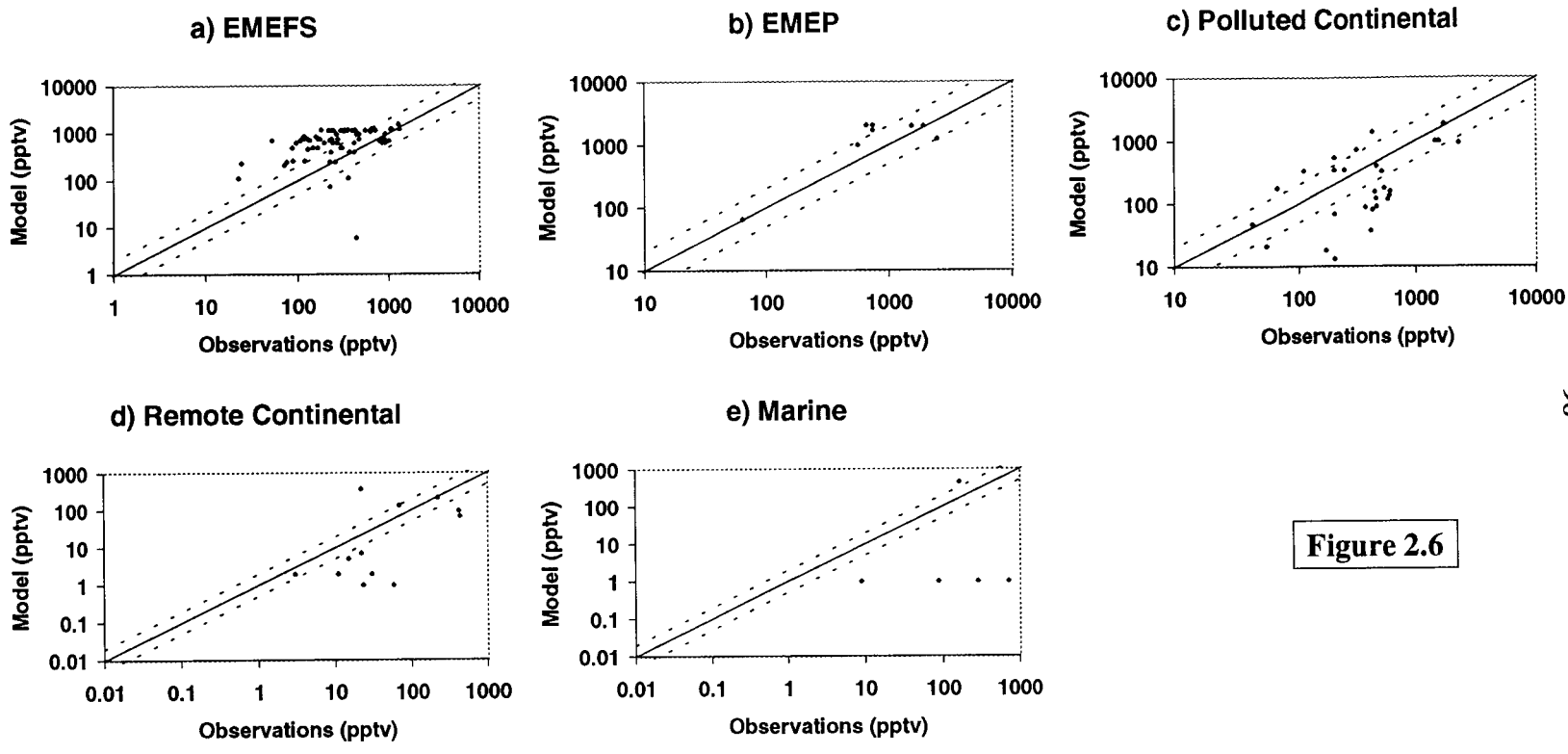
a) EMEFS
b) EMEP
c) Polluted Continental
d) Remote Continental
e) Marine
Model (pptv)
Observations (pptv)
10000
1000
100
10
1
0.1
0.01

Figure 2.6

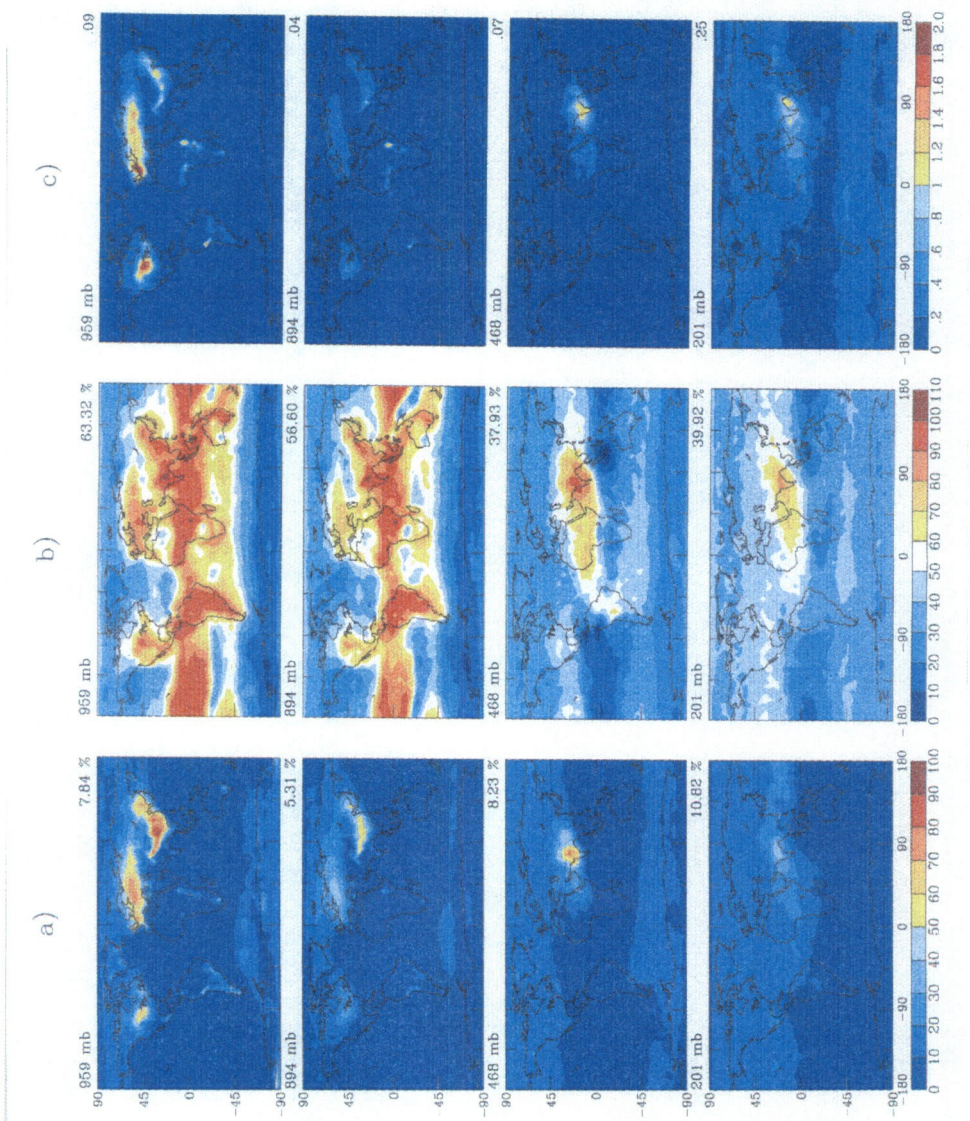
a)
b)
c)
959 mb
894 mb
468 mb
201 mb
7.84 %
5.31 %
8.23 %
10.82 %
63.32 %
56.60 %
37.93 %
39.92 %
.09
.04
.07
.25
90
45
0
-45
-90
-180
-90
0
90
180
0 10 20 30 40 50 60 70 80 90 100
0 10 20 30 40 50 60 70 80 90 100 110
0 .2 .4 .6 .8 1 1.2 1.4 1.6 1.8 2.0

Plate 2.4

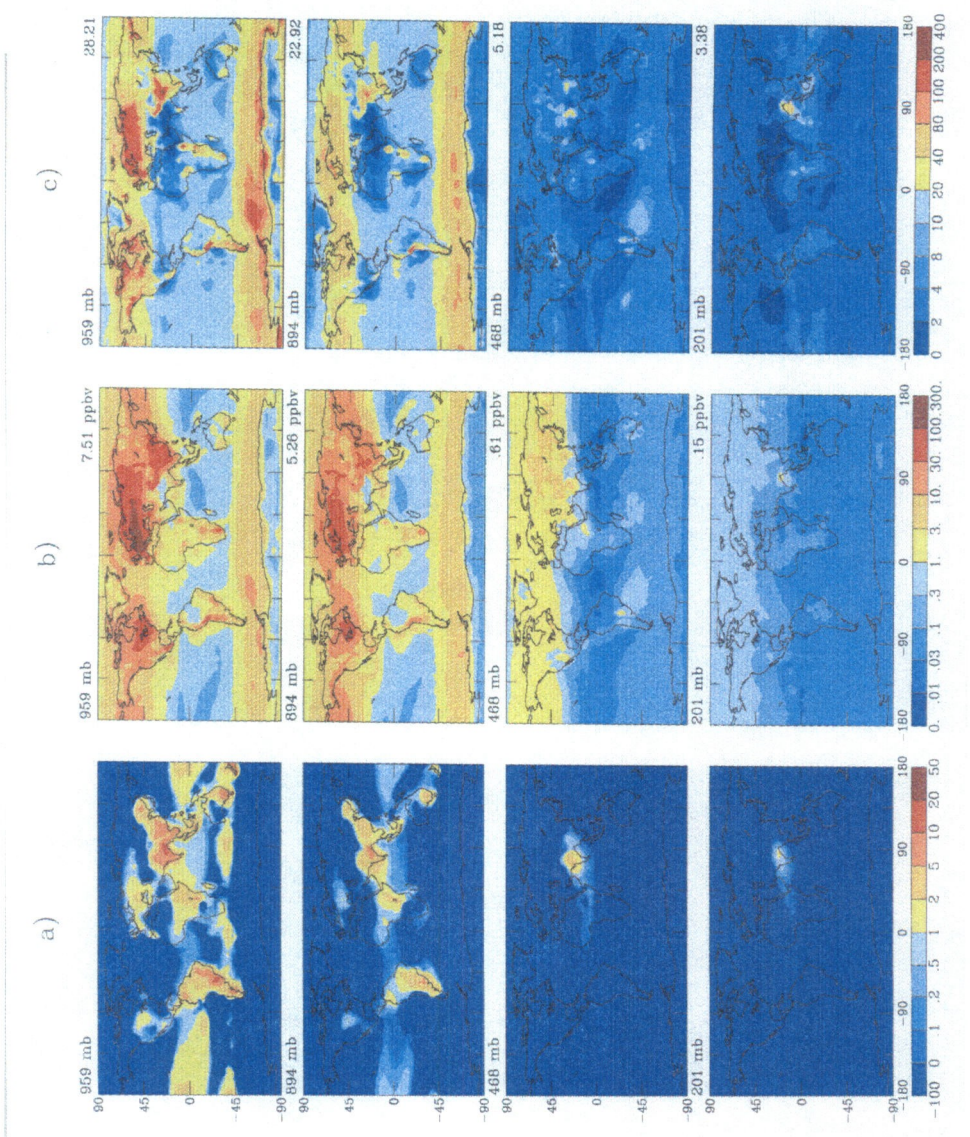
a)
b)
c)
959 mb
894 mb
468 mb
201 mb
7.51 ppbv
5.26 ppbv
.61 ppbv
.15 ppbv
28.21
22.92
5.18
3.38
90
45
0
-45
-90
-180
-90
0
90
180
-100 0 1 .2 .5 1 2 5 10 20 50
0. .01 .03 .1 .3 1. 3. 10. 30. 100.300.
0 2 4 8 10 20 40 80 100 200 400

Plate 2.5

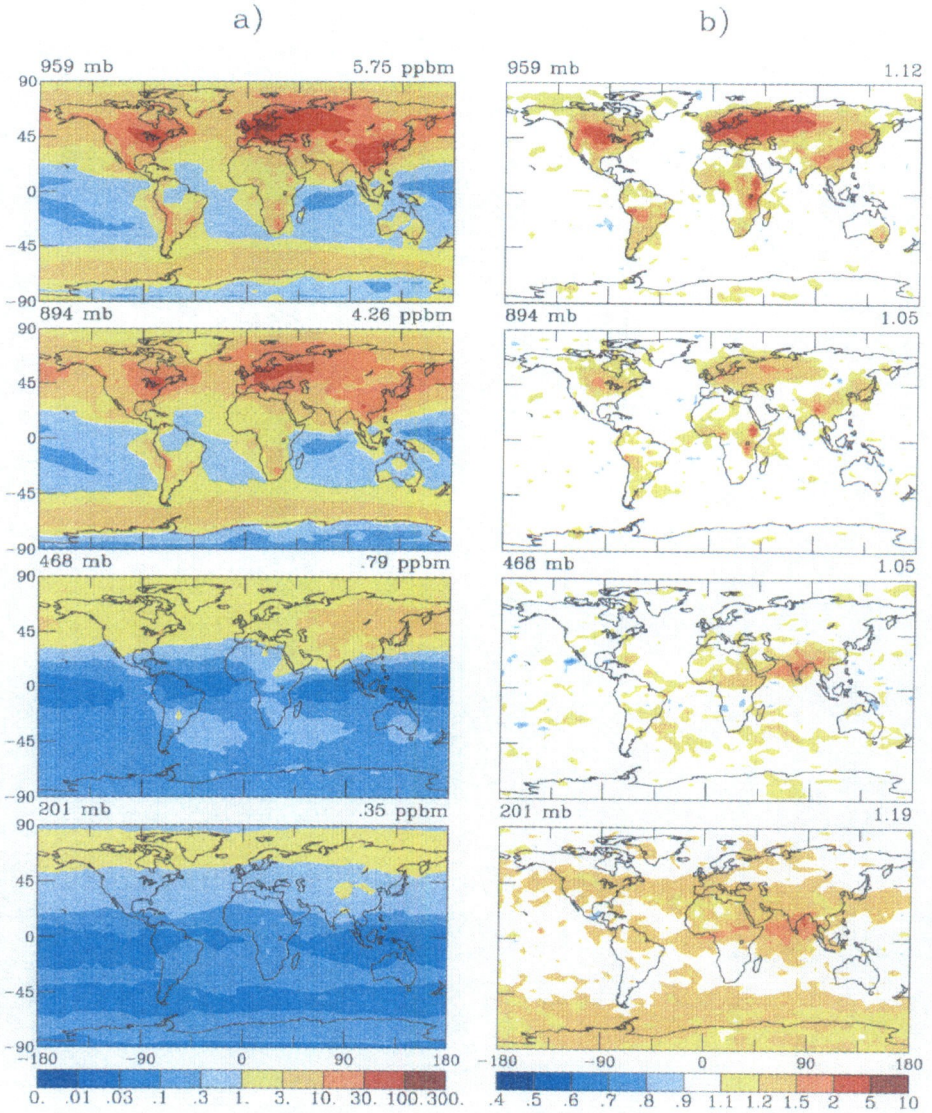
a)
b)
959 mb
5.75 ppbm
894 mb
4.26 ppbm
468 mb
.79 ppbm
201 mb
.35 ppbm
959 mb
1.12
894 mb
1.05
468 mb
1.05
201 mb
1.19
90
45
0
-45
-90
-180
-90
0
90
180
0. .01 .03 .1 .3 1. 3. 10. 30. 100. 300.
.4 .5 .6 .7 .8 .9 1.1 1.2 1.5 2 5 10

Plate 2.6

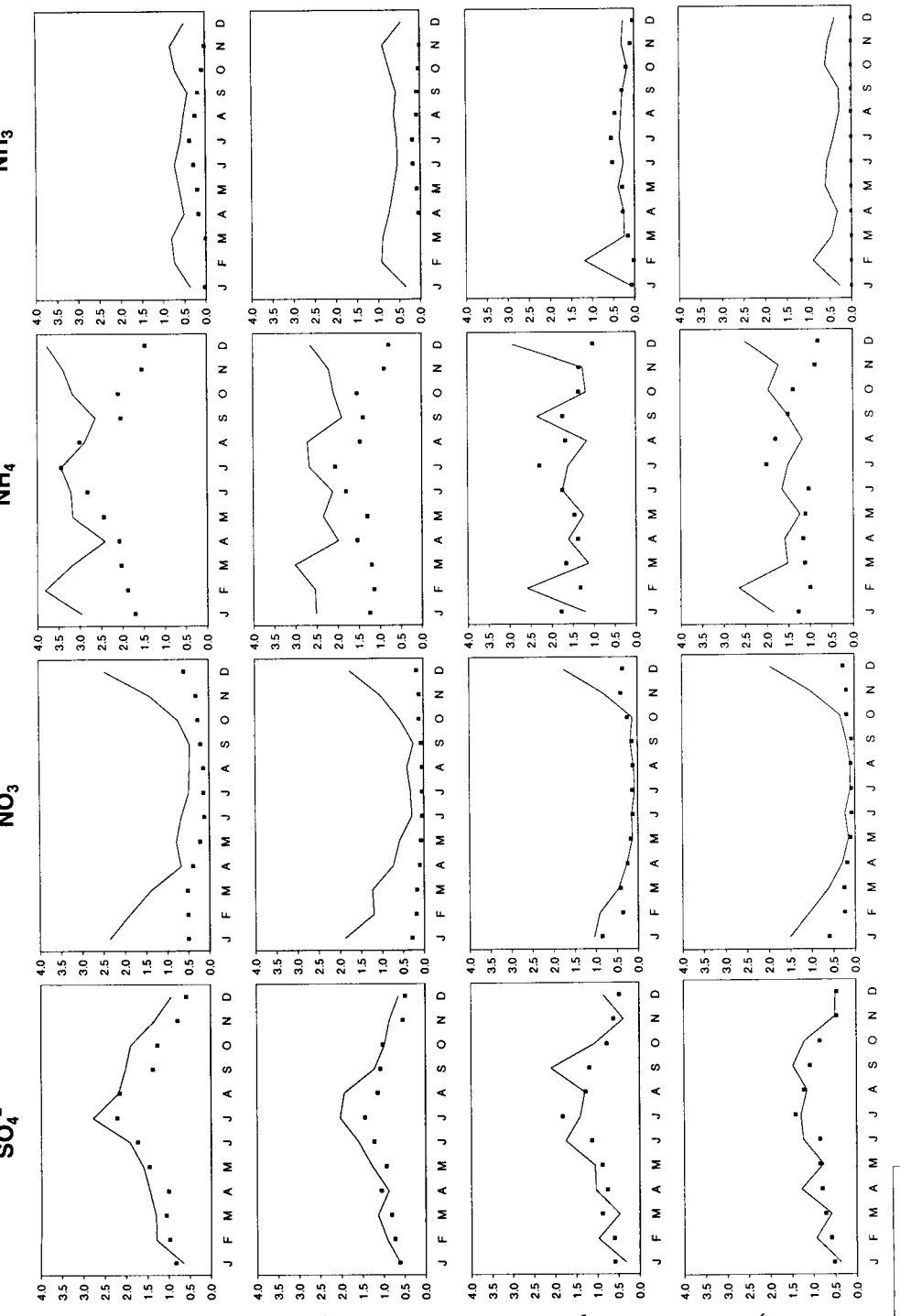
SO_4^{2-}
NO_3^-
NH_4^+
NH_3
Ithaca, NY
Pisece, NY
Gaylord, MI
Dorset, Ont.
J F M A M J J A S O N D
0.0 0.5 1.0 1.5 2.0 2.5 3.0 3.5 4.0

Figure 2.7

Chapter Three: General Circulation Model Assessment of Direct Radiative Forcing by the Sulfate-Nitrate-Ammonium-Water Inorganic Aerosol System

Reference: Adams, P. J., J. H. Seinfeld, D. Koch, L. Mickley, and D. J. Jacob, General circulation model assessment of direct radiative forcing by the sulfate-nitrate-ammonium-water inorganic aerosol system, *J. Geophys. Res., 106*, 1097-1111, 2001.

Abstract. An online simulation of aerosol sulfate, nitrate, ammonium, and water in the Goddard Institute for Space Studies General Circulation Model (GISS GCM II-prime) has been used to estimate direct aerosol radiative forcing for the years 1800, 2000, and 2100. This is the first direct forcing estimate based on the equilibrium water content of a changing SO_4^{2-}-NO_3^--NH_4^+ mixture and the first estimate of nitrate forcing based on a global model of nitrate aerosol. Present day global and annual average anthropogenic direct forcing is estimated to be –0.95 W m^{-2} and –0.19 W m^{-2} for sulfate and nitrate, respectively. Simulations with a future emissions scenario indicate that nitrate forcing could increase to –1.28 W m^{-2} by 2100, while sulfate forcing declines to –0.85 W m^{-2}. This result shows that future estimates of aerosol forcing based solely on predicted sulfate concentrations may be misleading, and that the potential for significant concentrations of ammonium nitrate needs to be considered in estimates of future climate change. Calculated direct aerosol forcing is highly sensitive to the model treatment of water uptake. By calculating the equilibrium water content of a SO_4^{2-}-NH_4^+ aerosol mixture and the optical properties of the wet aerosol, we estimate a forcing that is almost 35% greater than that derived from correcting a low relative humidity scattering coefficient with an empirical f(RH) factor. The discrepancy stems from the failure of the empirical parameterization to adequately account for water uptake above about 90% relative humidity. These results suggest that water uptake above 90% RH may make a substantial contribution to average direct forcing although subgrid scale variability makes it difficult to represent humid areas in a GCM.

3.1. Introduction

The scattering and absorption of radiation by tropospheric aerosols, or direct forcing, has been identified as a key process in anthropogenic climate change [*Intergovernmental Panel on Climate Change (IPCC)*, 1996]. Of all the chemical species present as atmospheric aerosol, sulfate is considered to be the largest contributor to anthropogenic direct forcing. Direct radiative forcing by sulfate aerosols has received considerable attention over the past decade; estimates of global mean forcing range between –0.29 W m^{-2} and –0.95 W m^{-2} [*Boucher and Anderson,* 1995; *Charlson et al.*, 1991; *Chuang et al.*, 1997; *Feichter et al.*, 1997; *Haywood et al.*, 1997b; *Kiehl and Briegleb*, 1993; *Kiehl et al.,* 2000; *Koch et al.,* 1999; *Penner et al.*, 1998; *Taylor and Penner*, 1994; *van Dorland et al.*, 1997].

Despite the numerous studies devoted to the subject, the IPCC [*IPCC*, 1996] estimates that the magnitude of direct sulfate forcing remains uncertain by a factor of two. Disagreement over the atmospheric sulfate burden and the fraction of that burden that is caused by human activities accounts for some, but not all, of this uncertainty. Figure 3.1 shows various anthropogenic sulfate direct forcing estimates as a function of the corresponding anthropogenic sulfate burden. This plot makes it clear that even researchers assuming the same amount of anthropogenic sulfate may reach very different conclusions about the magnitude of the resulting forcing. The sulfate forcing efficiency, defined as the amount of forcing per mass of sulfate, implicit in these numbers, varies from –130 W g^{-1} SO_4^{2-} to –370 W g^{-1} SO_4^{2-}. Some of this variation reflects differences in the radiation models used to generate these estimates, but larger discrepancies result from

other sources of uncertainty, including different assumptions regarding the optical properties of sulfate [*Boucher et al.,* 1998]. The sensitivity of forcing estimates to aerosol optical properties has motivated several recent publications [*Boucher and Anderson*, 1995; *Nemesure et al.*, 1995; *Pilinis et al.*, 1995]. The range of forcing efficiencies implicit in the literature is partly the result of a generation of aerosol models that predicted sulfate mass, but not sulfate optical properties per se. Narrowing the uncertainty in direct sulfate forcing requires, amongst other things, a more precise calculation of sulfate optical properties, especially the effect of water uptake. This, in turn, requires models that tell us more about the atmospheric aerosol than the mixing ratio of sulfate.

The size, shape, and refractive index of a particle uniquely determine its optical properties. Sulfate particles are generally hydrated, spherical droplets. Therefore, given the size distribution, total mass (or number) of particles and refractive index, their optical properties may be calculated from a routine application of Mie scattering theory.

In addition to sulfate, accumulation mode aerosols contain significant amounts of nitrate in polluted areas. Both nitrate and sulfate are generally neutralized to a substantial degree by ammonia, which exists in the aerosol phase as the ammonium cation. Most importantly, inorganic aerosols are hygroscopic and contain water under nearly all atmospheric conditions. The amount of aerosol nitrate, ammonium, and water influence, with sulfate, the optical properties of the aerosol.

Of all these components, water plays perhaps the greatest role in determining aerosol optical behavior, simply because it constitutes most of the aerosol mass. Therefore, the direct aerosol effect is similar to the indirect effect in the sense that shortwave radiation

interacts with more water than sulfate. Investigating the sensitivity of direct forcing to a variety of parameters, *Pilinis et al.* [1995] found that it is most sensitive to changes in relative humidity and the corresponding water content of the aerosol. Moreover, water uptake is highly nonlinear. Ammonium sulfate particles, for example, triple in volume as relative humidity increases from 85% to 95%, but grow by less than 20% (using the metastable hysteresis curve) from 50% to 60% RH. Water uptake also depends on the degree to which sulfate is neutralized by ammonia, with sulfuric acid being more hygroscopic than ammonium bisulfate or ammonium sulfate except near 100% RH. As a result, water uptake by inorganic aerosol is highly variable in time and space as relative humidity and aerosol composition change. Because it makes the dominant contribution to aerosol mass, water uptake influences the aerosol size distribution as particles grow and shrink with changing relative humidity. Particle size, in turn, influences its optical behavior. Water uptake also influences the refractive index of the aerosol mixture since its refractive index is lower than those of other aerosol species. For all these reasons, an accurate representation of aerosol forcing demands a realistic model of water uptake, including spatial and temporal variation resulting from changes in relative humidity and aerosol chemical composition.

Nitrate and ammonium each have a role in determining the optical properties of the aerosol mixture as well. As such, nitrate and ammonium contribute a small amount of mass to the inorganic aerosol, together only 7% of the total [*Adams et al.*, 1999]. More importantly, each influences water uptake. Ammonium nitrate is hygroscopic such that it and accompanying water make a significant contribution to total aerosol mass and aerosol light scattering in industrialized areas. A previous global modeling study [*Adams et al.*,

1999] concluded that ammonium nitrate is responsible for more aerosol mass than sulfate in much of Europe. The contribution of ammonium nitrate in North America and eastern Asia was predicted to be less, but still significant. Aerosol and light scattering measurements made by *ten Brink et al.* [1996, 1997] on the coast of The Netherlands show that ammonium nitrate scatters more sunlight than sulfate in this area. An analysis of observed aerosol concentrations in the eastern United States also shows that nitrate plays a key role in determining total aerosol mass, especially during winter [*West et al.*, 1999]. Ammonia can be absorbed by sulfate particles and thereby modify their optical properties. Ammonium bisulfate and ammonium sulfate are both less hygroscopic than sulfuric acid at low to moderate relative humidities but have higher refractive indices. The net result of these two competing factors is that one mole of sulfuric acid scatters about 25% more sunlight than one mole of ammonium bisulfate at 80% relative humidity. Ammonium sulfate is intermediate between the two [*Boucher and Anderson*, 1995].

Previous estimates of direct radiative forcing undertaken with models that compute only the sulfate concentration have addressed the presence of nitrate, ammonium, and water in various ways. *Van Dorland et al.* [1997] roughly estimated the radiative forcing due to nitrate by assuming an arbitrary fraction of nitric acid exists in the aerosol phase with the same optical properties as sulfate. Otherwise, no global estimate of nitrate forcing exists. *Dentener and Crutzen* [1994] and *Adams et al.* [1999] have simulated the ammonia cycle and concentrations of aerosol ammonium without considering radiative effects. Radiative forcing assessments for sulfate have accounted for ammonium by assuming sulfate exists uniformly as $(NH_4)_2SO_4$ or, in some studies, H_2SO_4. Changes in water uptake and refractive index as a result of varying amounts of aerosol ammonium

have therefore been neglected in previous work.

Previous work has accounted for the effect of water uptake on aerosol optical properties in various ways. In some studies [*Charlson et al.*, 1991; *Feichter et al.*, 1997], variations in relative humidity are ignored, and a single value of the aerosol scattering cross section, corresponding to 80% relative humidity, is used. A common approach [*Kiehl and Briegleb*, 1993; *Koch et al.*, 1999; *Taylor and Penner*, 1994] has been to take a low relative humidity value of the scattering coefficient, α, of 5 m^2 g^{-1} SO_4^{2-} and correct it at more humid conditions by multiplying it by an empirical correction factor, f, which is a function of relative humidity [*Charlson et al.*, 1984]. Figure 3.2 shows the aerosol scattering coefficient as a function of relative humidity calculated using this approach along with the results of Mie scattering calculations for comparison. This empirical approach is problematic for several reasons. First, this particular data set extends only up to somewhat less than 90% relative humidity, which requires that one extrapolate in order to obtain scattering coefficients for more humid conditions. Second, the data are based on ambient samples of aerosols with mixed chemical compositions, and it is not clear to what extent their properties reflect those of sulfate. Finally, the samples are processed in such a way that the measured water uptake corresponds to the rising-RH portion of the deliquescence-crystallization hysteresis. It is more likely, however, that most aerosol particles exist in the falling-RH, metastable, regime. Other investigators [*Chuang et al.*, 1997; *Kiehl et al.*, 2000; *Penner et al.*, 1998; *van Dorland et al.*, 1997] have computed water uptake based on Köhler theory and used the results as input for their own Mie scattering calculations. This approach avoids the drawbacks just mentioned with regard to the f(RH) approach, but still requires assumptions about the dry chemical composition

of the aerosol. Although using Köhler theory has the advantage of including the Kelvin effect, this is not important for accumulation mode particles that make the dominant contribution to direct forcing.

Although the aerosol size distribution affects optical properties, it has received little attention in global models because simulating it involves a computationally intensive model of aerosol microphysics and because aerosol optical behavior is less sensitive to uncertainties in particle size than water content [*Boucher and Anderson*, 1995; *Nemesure et al.*, 1995; *Pilinis et al.*, 1995]. Also, assuming a value for α alleviates the need to describe the size distribution since the effects of aerosol size are already implicit in the choice of α. Explicit description of the aerosol size distribution is necessary only if optical properties are derived from Mie theory. For purposes of Mie calculations, a lognormal distribution of dry particles is invariably assumed in this and previous work, usually with a geometric mean radius of 0.05 μm and a geometric standard deviation of 2.0, parameters that ensure consistency with observational data.

In this study, we simulate the concentrations of sulfate, nitrate, ammonium and aerosol water in a general circulation model [*Adams et al.*, 1999] to estimate global direct radiative forcing due to tropospheric sulfate and nitrate. Simulating the composition of the aerosol provides an explicit calculation of water uptake based on thermodynamic equilibrium, and therefore the most rigorous estimate of total aerosol mass to date. Aerosol optical properties, such as refractive index and optical depth, are calculated based on predicted composition. This approach alleviates the need for simplifying assumptions such as all sulfate existing as $(NH_4)_2SO_4$ or empirical f(RH) correction factors. Resolving the composition of the sulfate aerosol system therefore improves the description of both

its optical properties and its total mass, key uncertainties in previous direct forcing estimates.

The reader should bear in mind that potentially important interactions of sulfate and nitrate with other aerosol types are not yet adequately accounted for in this, or other, global modeling studies. Soot, for example, absorbs solar radiation, but its absorption efficiency is much stronger when internally mixed with sulfate than externally mixed [*Haywood et al.*, 1997b]. Similarly, the presence of mineral dust and sea salt can influence the size distribution of sulfate and, more especially, nitrate by allowing these components to condense into the coarse aerosol mode where they scatter sunlight less efficiently. Therefore, the results presented here are just part of the larger problem of aerosol radiative forcing that will ultimately require a more comprehensive and detailed treatment.

We present estimates of direct forcing for the years 1800 (preindustrial), 2000, and 2100 (IPCC SRES A2 emissions scenario, preliminary version). All four preliminary IPCC SRES emissions scenarios forecast lower SO_2 emissions in 2100 than 2000. We chose to simulate the A2 scenario because it showed the smallest decline in sulfur emissions between 2000 and 2100. Scenario A2 also has the largest increases in NO_x emissions. For each time period, a SO_4^{2-}-NO_3^--NH_4^+-H_2O simulation has been compared to a SO_4^{2-}-NH_4^+-H_2O simulation to ascertain how the relative contributions of sulfate and nitrate to direct forcing change over time. The ambient, wet size distributions of these aerosol components are not simulated here, but are parameterized in terms of calculated water uptake.

3.2. Methodology

3.2.1 Model Description

The radiative forcing estimates presented here were calculated using a version of the GISS GCM II-prime [*Hansen et al.*, 1983; *Rind and Lerner*, 1996] with an online aerosol simulation [*Koch et al.*, 1999; *Adams et al.*, 1999]. The GISS GCM II-prime has a horizontal resolution of 4 degrees latitude by 5 degrees longitude with nine vertical layers between the surface and 10 mb. The version of the GCM used for this study uses monthly mean ocean temperature maps. The GISS radiation scheme [*Lacis and Hansen*, 1974; *Hansen et al.*, 1983] uses the correlated *k* distribution method [*Lacis and Oinas*, 1991] to compute absorption by gases and particles. Six *k* intervals, one in the visible region and five near-IR, are used for the spectral dependence of Mie parameters of clouds and aerosols for the solar part of the spectrum. Light scattering by aerosols is calculated using the single gauss point doubling and adding approach. Annual average cloud cover over the course of the simulations was 47%.

This online aerosol simulation predicts the concentrations of H_2O_2, DMS, MSA, SO_2, NH_3, SO_4^{2-}, NO_3^-, NH_4^+, and aerosol water. Gas-phase reactions of DMS with OH and NO_3 radicals are included as well as oxidation of SO_2 by OH. In-cloud oxidation of SO_2 by H_2O_2 is also included, but aqueous oxidation by O_3 is neglected as it has been estimated to be a much less important pathway in the global sulfur budget [*Rasch et al.*, 2000]. As described in *Koch et al.* [1999], we use monthly average three-dimensional concentrations fields for the NO_3 radical taken from *Wang et al.* [1998a,b,c] and five day

average three-dimensional fields for OH concentrations. Therefore, changes in oxidant availability have been neglected except for changes in H_2O_2 resulting from changes in the sulfur cycle.

Aerosol dynamics and composition are treated with a simple bulk model of internally mixed accumulation mode SO_4^{2-}, NO_3^-, NH_4^+, and H_2O. This mixture is assumed to reach thermodynamic equilibrium with the gas phase, a reasonable assumption given the one-hour model time step [*Adams et al.*, 1999; *Meng and Seinfeld*, 1996]. The aerosol thermodynamic equilibrium module, ISORROPIA [*Nenes et al.*, 1998], is called by the aerosol simulation every time step to determine the partitioning of the volatile species, ammonia, nitrate, and water, between the gas and aerosol phases based on the prevailing conditions in each model grid cell. For reasons discussed in *Adams et al.* [1999], we believe that most atmospheric aerosol particles exist in a hydrated, metastable state between their crystallization and deliquescence humidities. Therefore, we assume that the upper, metastable branch of the aerosol deliquescence-crystallization hysteresis loop most accurately describes water uptake by atmospheric aerosols.

The model simulates both wet and dry deposition. Gas-phase tracers dissolve in cloud water according to their effective Henry's law constants. Aerosol species are assumed to be infinitely soluble. The fate of dissolved tracers generally follows the GCM treatment of liquid water [*Del Genio and Yao*, 1993; *Del Genio et al.*, 1996]. The fraction of cloud water that precipitates and reaches the surface determines the fraction of dissolved tracer that undergoes wet deposition. Alternatively, dissolved tracer may be returned to the gas phase when cloud water evaporates, either in the same model grid cell or another. Below clouds, both aerosols and soluble gases are scavenged according to a first-order

parameterization that depends on the amount of precipitation. Dry deposition occurs in the lowest model layer with a deposition velocity computed based on a resistance-in-series scheme [*Wesely and Hicks*, 1977]. The treatment is similar to that described by *Chin et al.* [1996] except that the aerodynamic resistances depend on the GCM surface momentum and heat fluxes.

The model computes emissions, transport, chemical reactions, and deposition of H_2O_2, DMS, MSA, SO_2, NH_3, SO_4^{2-}, and NH_4^+. Aerosol nitrate and water are handled somewhat differently. The computational expense of including full tropospheric photochemistry in the model is avoided by importing monthly average nitric acid fields from the Harvard-GISS General Circulation Model [*Mickley et al.*, 1999], which includes photochemistry as an online component in the GISS GCM II-prime. Since the Harvard photochemical model does not distinguish between gas-phase and aerosol nitrate, these values are taken to represent the total amount of nitric acid (HNO_3(g) plus aerosol NO_3^-) in a given model grid cell. The aerosol thermodynamic equilibrium module, therefore, determines what fraction of this total nitric acid occurs as aerosol nitrate depending on local temperature, relative humidity, as well as concentrations of sulfate and ammonia. Thus, the model does not compute a budget for aerosol nitrate. Similarly, the aerosol water content is computed thermodynamically based on the relative humidity and aerosol concentrations in the given GCM grid cell.

The concentrations predicted by the model have been compared extensively [*Adams et al.*, 1999] to a wide variety of observations consisting of the Eulerian Model Evaluation Field Study (EMEFS) database [*McNaughton and Vet,* 1996] for North America, the Co-operative Programme for Monitoring and Evaluation of the Long-Range Transmission of

Air Pollutants in Europe (European Monitoring and Evaluation Programme, EMEP) database [*Hjellbrekke and Hanssen,* 1998] for Europe as well as numerous other observations of continental and marine areas. Annual average sulfate and ammonium concentrations predicted by the model nearly always agreed with EMEFS and EMEP observations within a factor of two. Simulated nitrate concentrations matched observations not quite as well, mostly because the model predicted too much nitrate in polluted continental areas in the winter and too little in marine areas. The overprediction of nitrate in polluted areas during the winter was attributed to high concentrations of ammonia that resulted in excessive ammonium nitrate formation. The low simulated nitrate concentrations in marine areas result from the fact that the model does not capture the condensation of nitric acid onto coarse-mode sea salt particles.

All runs presented here represent 39-month integrations of the GCM. The first three months allow the concentrations of simulated species, which start at zero concentration, to equilibrate to realistic values. The results presented here are average values over the remaining three years of simulation. Meteorological quantities are initialized based on output from a previous climate model run. Radiative heating rates used for GCM meteorology were based on no aerosol forcing so aerosol feedbacks on climate were not allowed.

3.2.2 Updated Treatment of Ammonia and Nitric Acid

For purposes of this study, two significant changes have been made to the aerosol model described in *Adams et al.* [1999]. First, the annual cycle of ammonia emissions has been changed. Emissions of ammonia from livestock, fertilizer application, and crops

together constitute nearly two-thirds of total emissions [*Bouwman et al.*, 1997] and exhibit a seasonal character. This annual cycle is a result of seasonal changes in livestock housing, the timing of fertilizer application and the growing season as well as the dependence of ammonia volatilization on meteorological variables such as temperature and wind speed. In previous studies of the ammonia cycle [*Dentener and Crutzen,* 1994; *Adams et al.*, 1999], an annual cycle was, somewhat arbitrarily, applied to these agricultural emissions such that their emission rate was proportional to the number of daylight hours. As mentioned above, this approach results in wintertime ammonia concentrations that are higher than those observed in polluted areas and lead to excessive ammonium nitrate formation. Through trial and error, we have found that setting the emission rate of ammonia from agricultural sources proportional to the number of daylight hours to the fourth power results in ammonium and nitrate concentrations that are in substantially better agreement with the observations. Although this treatment may seem unusual and arbitrary, it is not inconsistent with the little that is known about the seasonal cycle of ammonia emissions [*Bouwman et al.*, 1997] and results in predictions that are more consistent with observations than the previous, equally arbitrary, treatment.

Second, the monthly average nitric acid concentration fields have been updated relative to those that were used in *Adams et al.* [1999]. Instead of importing them from the Harvard Chemical Transport Model (CTM) [*Horowitz et al.*, 1998], also based on GISS GCM meteorology, but with offline photochemistry, we use the online version known as the Harvard-GISS GCM [*Mickley et al.*, 1999]. Updating the nitric acid fields has two advantages. First, it improves the overall consistency of the model because the Harvard-GISS GCM photochemical model is based on the same version of the GISS

GCM II-prime as this work. Second, the Harvard-GISS GCM has been used to simulate the photochemistry of the preindustrial atmosphere and its results have been compared to the few observations that are available from that time period. The Harvard-GISS GCM can, therefore, provide a set of monthly average nitric acid concentration fields for the preindustrial period that allows us to examine how direct forcing by nitrate aerosol has changed since the Industrial Revolution. There are, however, significant differences between the newer Harvard-GISS GCM fields and the older Harvard CTM fields. The newer nitric acid (gas plus aerosol) concentrations are higher than the older ones by only 20% in the model surface layer, but are more than 3 times higher above about 500 mb.

Both the new annual cycle of agricultural ammonia emissions and the new nitric acid (gas plus aerosol) fields have noticeably altered the predicted aerosol ammonium and nitrate concentrations. Most important for this work is the fact that the nitrate burden resulting from the newer nitric acid fields, 0.09 Tg N, is three times that reported in *Adams et al.* [1999]. Most of the increased burden is above the boundary layer, a reflection of where the new nitric acid fields show the greatest increase. Nitrate concentrations in the model surface layer increase by only 20% on average over those found in *Adams et al.* [1999]. This results in slightly poorer agreement with observations, but does not radically undermine our confidence in model performance especially considering the difficulties and uncertainties inherent in measuring a volatile aerosol component such as nitrate. These changes have a relatively smaller impact on simulated ammonium concentrations. The new ammonium burden, 0.42 Tg N, is 40% greater than the one previously reported. The increased ammonium burden results partly from the increased nitrate burden and partly from increased ammonia emissions during summer.

Sulfate concentrations tend to be highest during the summertime such that ammonia is more likely to be converted to longer-lived aerosol ammonium during that time of year. As was the case with nitrate, the most dramatic increases occur higher up in the troposphere with ammonium concentrations doubling at 200 mb. At the surface, ammonium concentrations increase by only 15% on average, which causes no concern given the good agreement with observations.

3.2.3 Aerosol Optical Properties

The optical properties of the aerosol mixture have been computed using Mie scattering theory in such a way that they realistically reflect changes in aerosol composition and water uptake. Mie scattering calculations require knowledge of the aerosol refractive index to compute single-particle scattering and absorption cross sections for any given particle size. Given a collection of particles of various sizes, one can integrate over the aerosol size distribution to calculate average scattering and absorption cross sections for the entire aerosol population. These quantities, typically expressed in $m^2\ g^{-1}$, combined with the column burden of aerosol, give the corresponding optical depths. We ignore absorption of radiation by aerosols, an excellent approximation for the mixture of sulfate, nitrate, ammonium, and water treated here.

We use the method of partial molar refraction [*Stelson*, 1990] to compute the refractive index of the aerosol mixture present in a given GCM grid cell at a given time step based on laboratory measurements of single-component aerosol optical properties [*Tang and Munkelwitz*, 1994; *Tang*, 1996; *Tang*, 1997].

Given that this model, like other global aerosol models, does not resolve the aerosol

size distribution, one must be assumed for purposes of calculating aerosol optical properties. In common with nearly every other study that uses Mie theory to generate the optical properties, we assume a lognormal size distribution of dry particles having a geometric mean radius of 0.05 μm and geometric standard deviation of 2.0. Water uptake is taken into account by means of a "mass growth factor", defined as the ratio of wet aerosol mass to dry aerosol mass as calculated by the aerosol thermodynamic equilibrium module. This mass growth factor is converted into a similarly defined diameter growth factor given data on the dry and wet aerosol densities [*Tang and Munkelwitz*, 1994; *Tang*, 1996; *Tang*, 1997]. The diameter growth factor is used to calculate the geometric mean radius of the wet size distribution. The geometric standard deviation remains unchanged. Therefore, the model does not explicitly simulate the aerosol size distribution but parameterizes it in terms of an assumed dry lognormal distribution and the amount of water uptake in a given GCM cell.

Assuming that the nitrate aerosol we simulate is present in the accumulation mode size range requires some justification. The range of particle sizes in which nitrate aerosol might occur is expected to depend strongly on the cation with which it is associated. When nitrate reacts with sodium in sea salt aerosol or cations in mineral dust, it will be found in the larger particle size range characteristic of these aerosol types. We do not treat sea salt or mineral dust in this model, however, so these kinds of nitrate are neglected in this work. On the other hand, the formation of ammonium nitrate occurs when gas-phase ammonia and nitric acid condense onto whatever aerosol happens to be at hand. In the polluted continental regions in which most of the nitrate in this model occurs, one expects that ammonium and nitrate will condense primarily onto particles in

the submicron size range. Since nitrate in supermicron sized particles scatters light less efficiently, we will tend to overestimate the nitrate forcing to the extent that our assumption breaks down. On the other hand, the fact that this model does not capture nitrate associated with sea salt or mineral dust will cause us to underestimate the nitrate forcing somewhat. Overcoming these drawbacks will ultimately require a size-resolved aerosol simulation that treats sea salt and mineral dust as well.

Mie scattering calculations were performed offline to generate scattering cross sections and asymmetry parameters for a variety of aerosol refractive indices and mass growth factors (i.e., size distributions). These were compiled into a lookup table such that the appropriate scattering cross section and asymmetry parameter for any given aerosol mixture could be rapidly retrieved during GCM runs. The aerosol optical depth for a given GCM grid cell is computed as the product of the local scattering cross section and aerosol burden and is passed to the GCM radiation scheme.

Figure 3.2 shows sample scattering cross sections for ammonium sulfate and sulfuric acid as a function of relative humidity. These are shown for purposes of illustration only. In general, a GCM grid cell will contain a more complicated mixture that includes nitrate. For comparison, the cross sections one would compute by taking a low relative humidity scattering coefficient of 5 $m^2 g^{-1}$ SO_4^{2-} and correcting with the empirical f(RH) factor described above are also shown. This approach agrees fairly well with our results for ammonium sulfate at intermediate relative humidities, but important discrepancies should be noted. Most importantly, the empirical data upon which the f(RH) factor is based extend only a little past 85% RH. At higher relative humidities, scattering cross sections have been taken as constant in previous work that uses the f(RH) correction. Our results

show very substantial water uptake and higher scattering cross sections per unit sulfate at higher relative humidities. We will discuss later the sensitivity of overall direct aerosol forcing to the contribution made by water uptake at high relative humidity and the difficulty in representing this in GCMs. Similarly, it should be noted that the low relative humidity value of 5 m^2 g^{-1} SO_4^{2-} is appropriate for a relative humidity of about 50% and overestimates scattering at drier conditions. Finally, this parameterization of optical properties cannot distinguish between ammonium sulfate and sulfuric acid, nor account for the presence of nitrate in the mixture.

3.2.4 Emissions Scenarios

Several simulations have been performed to ascertain the anthropogenic aerosol forcing resulting from industrialization, project how forcing might change as the century progresses, determine the relative contributions of sulfate and nitrate, and the sensitivity to water uptake at high relative humidity. Three different time periods have been simulated: preindustrial (roughly corresponding to the year 1800), modern day (year 2000), and the year 2100. Table 3.1 summarizes sulfur and ammonia emissions as well as nitric acid fields for all three time periods. Note that all IPCC SRES emissions data is based on the preliminary versions of the scenarios.

For each run, the appropriate set of nitric acid concentration fields was taken from the Harvard-GISS GCM. The simulations that produced the preindustrial and modern day fields are documented in *Mickley et al.* [1999]. The year 2100 nitric acid fields were taken from a Harvard-GISS GCM run based on the IPCC SRES A2 emissions scenario. Given the uncertainty in projecting nitric acid concentrations 100 years into the future, the

year 2100 run was repeated with nitric acid fields from the Oslo CTM1 [*Berntsen and Isaksen,* 1997; *Jaffe et al.,* 1997]. Although these nitric acid fields were distinctly different than those from the Harvard-GISS GCM, the resulting aerosol nitrate burden and forcing was not substantially different and will not be presented here.

Sulfur emissions for the modern day and year 2100 run were also prescribed based on the IPCC SRES A2 emissions scenario. Preindustrial sulfur emissions included only DMS emissions from the oceans and volcanic SO_2 emissions. DMS emissions are assumed to be the same in all three time periods. This neglects the possibility that changes in wind patterns and speeds induced by climate change over the next century may influence emissions of trace gases from the ocean. More generally, the same climate was used to simulate all three time periods. The effects of climate changes on aerosol chemistry, transport, and deposition are therefore neglected, but are expected to be small compared to the effect of changes in anthropogenic emissions. Volcanic emissions of SO_2 are estimated to be 4.8 Tg S yr^{-1} in all scenarios [*Andres and Kasgnoc*, 1998]. Current sulfur emissions are estimated to be more than three times greater than their preindustrial levels, but decline slightly from their present day value by the year 2100.

Little work has been done on past and future ammonia emissions, so several assumptions were required. Ammonia emissions for all three time periods were based on the GEIA inventory [*Bouwman et al.*, 1997], which provides emissions for the year 1990, with appropriate modifications for 1800, 2000, and 2100. Natural emissions of ammonia from the oceans, undisturbed soils, and wild animals were assumed to be unchanged between 1800 and 2100. Although changes in land use are expected to affect the last two substantially, the oceans are the only natural source that contributes significantly to total

ammonia emissions. Emissions from synthetic fertilizers, industrial processes, and fossil fuels were excluded in the preindustrial run. Emissions from biomass burning were set to 10% of their present value [*Crutzen and Zimmermann,* 1991]. Emissions from livestock, crops, humans and pets were assumed to be proportional to human population, which was taken to be 20% of the present day value in 1800. Considering that agriculture is the main anthropogenic source of both N_2O and ammonia emissions, anthropogenic ammonia emissions for the years 2000 and 2100 were scaled with the N_2O emissions prescribed in the IPCC SRES A2 scenario (Frank Dentener, personal communication). Given these assumptions, we estimate that ammonia emissions increase from 18.7 Tg N yr^{-1} in 1800 to 57.6 Tg N yr^{-1} in 2000 to 122.2 Tg N yr^{-1} by the year 2100.

3.2.5 Sensitivity Runs

In addition to the base-case runs described above for each time period, several sensitivity runs were performed. First, for each time period a sensitivity run was performed in which nitrate aerosol concentrations were assumed to be zero. These allow us to determine how much of the overall aerosol forcing can be attributed to nitrate and also facilitate comparison with other published results based on models that only consider sulfate. The "nitrate forcing" is taken as the difference in forcing between runs with and without nitrate. It should be stressed, however, that sulfate and nitrate engage in a competition for available ammonia such that the total aerosol mass or forcing is a nonlinear function of either concentration [*Ansari and Pandis*, 1998; *West et al.*, 1998]. For example, a decline in sulfate concentrations frees ammonia that can react with nitric acid and result in enhanced ammonium nitrate concentrations.

Also, a sensitivity run was performed for each of the three time periods in which the forcing was calculated based only on the sulfate concentration with a low RH scattering coefficient of 5 m^2 g^{-1} SO_4^{2-} corrected with an empirical f(RH) factor. This lets us compare the forcing that results from the fundamental thermodynamic model of aerosol composition used here to the approximate approach sometimes seen in the literature.

Finally, the sensitivity of aerosol forcing to water uptake at high relative humidities was explored in a series of three sensitivity runs in which the maximum aerosol water uptake was varied. In the base-case scenario, aerosol water uptake was limited to that which occurred at a value of 99% RH. In the sensitivity runs, this value was set at 85%, 90%, and 95%.

3.3. Direct Forcing Estimates

3.3.1 Overview

Table 3.1 summarizes the emissions, input HNO_3 concentrations, burdens, and forcings calculated for each of the three time periods. The total direct aerosol forcing for each simulation is computed as the difference in net downward shortwave radiative flux at the top of the atmosphere with and without aerosols. Although sulfate aerosols can also absorb thermal radiation, the results of *Lacis and Mishchenko* [1995] show that the thermal forcing is just a few percent of the solar forcing for sulfate aerosols up to 3 km. Some of the direct aerosol forcing is the result of naturally occurring aerosols. We calculate the anthropogenic component of the forcing as the additional forcing found in the 2000 and 2100 scenarios when compared with the preindustrial scenario. Besides

apportioning the direct forcing into natural and anthropogenic components, we also break it down according to chemical species. Our base-case scenarios include the effects of both sulfate and nitrate. Sensitivity scenarios with only sulfate allow us to calculate the sulfate forcing; the remainder is considered to be nitrate forcing. Although aerosol ammonium and water play important roles in determining direct radiative forcing, no portion of the forcing is ascribed to them because they exist in the aerosol phase only by virtue of sulfate or nitrate. Unless stated otherwise, all forcing values are global and annual averages.

Present-day anthropogenic direct aerosol forcing is estimated to be –1.14 W m^{-2}, counting contributions from both sulfate and nitrate, which are found to be –0.95 W m^{-2} and –0.19 W m^{-2}, respectively. This estimate is significantly higher than most recent published estimates for two reasons. First, calculating the aerosol optical properties based upon the thermodynamic equilibrium water uptake shows that water uptake at high relative humidity contributes strongly to the radiative forcing, a contribution that has often been neglected in previous work. Second, nitrate, along with the accompanying ammonium and water, makes a small, but noticeable contribution. The effect of nitrate is even more important in the IPCC scenario for the year 2100. In this scenario, decreases in sulfur emissions lead to a slightly lower sulfate forcing of –0.85 W m^{-2}, but increases in NO_x and NH_3 emissions result in a dramatic increase in nitrate forcing to –1.28 W m^{-2}. These results demonstrate that, over the next century, ammonium nitrate aerosol could alter the earth's radiative balance to an even larger extent than sulfate. Therefore, GCM simulations of future climate changes need to take into account radiative forcing due to nitrate as well as other aerosol species and greenhouse gases that have already been

recognized as significant.

Figure 3.3 shows the geographical pattern of anthropogenic aerosol forcing for the modern day and year 2100 scenarios considered here. This figure shows the expected pattern with the most aerosol forcing in industrialized areas such as eastern North America, Europe and eastern Asia. Annual average anthropogenic aerosol forcings exceed -4 W m^{-2} across these areas for the present day scenario and are projected to exceed -10 W m^{-2} in smaller areas by the year 2100. The increased forcing in the year 2100 is especially dramatic over India and China. This is mostly a result of higher emissions of NO_x and ammonia leading to high concentrations of ammonium nitrate aerosol, but also results partly from increased sulfate concentrations over India.

3.3.2 Water Uptake

It has already been mentioned that parameterizing sulfate scattering behavior in terms of a low relative humidity value for α and a high relative humidity correction factor, f(RH), yields different results than the method adopted here. Specifically, the α and f(RH) method underestimates scattering cross sections at relative humidities greater than about 85% and overestimates them at low humidity. It also neglects differences between sulfate that is neutralized by ammonia and that which is not. We have performed side by side forcing calculations using each method to assess how much impact these discrepancies have on the global and annual average forcing. To facilitate comparison, this has been accomplished in the sensitivity runs in which nitrate was ignored.

We find a present day anthropogenic sulfate forcing of –0.71 W m^{-2} using the α and f(RH) method, considerably lower than the –0.95 W m^{-2} value found using our standard

method. The main reason for the difference is the additional water uptake at high relative humidity that is neglected by the f(RH) parameterization. This water makes a significant contribution to the total forcing despite the fact that the clouds that are typically present at high relative humidity partially mask its effect. Previous aerosol forcing studies in the GISS GCM [*Lacis and Mischenko*, 1995] indicate that the presence of clouds reduces the magnitude of aerosol forcing by a factor of 3.5 relative to its clear-sky value. However, the aerosol extinction coefficient increases in magnitude by a similar factor between 90% and 99% RH. Therefore, an aerosol particle at 99% RH in a cloudy region and another at 90% RH in clear skies will have about the same forcing efficiency. Our finding that water uptake at high relative humidities makes a significant contribution to global and annual average forcing agrees with the findings of *Kiehl et al.* [2000], where aerosol water uptake is calculated using Köhler theory. Although that model does not include nitrate nor take into account variations in ammonium content, the resulting scattering coefficients depend on relative humidity in a manner that is similar to those used here. Compared to the α and f(RH) parameterization used in their previous work, they found that the additional aerosol water uptake above 90% relative humidity resulted in a estimated direct forcing that was approximately 50% greater.

Figure 3.4 shows the spatial distribution of the difference in anthropogenic forcing between the two methods for the modern day scenario. The difference is negative in most areas, indicating that the current more rigorous approach results in more aerosol forcing than the f(RH) parameterization. The magnitude of the discrepancy is generally less than 1 W m^{-2}, but exceeds 2 W m^{-2} over parts of the Northern Hemisphere. The figure also shows, however, subtropical regions in which the opposite is true. This occurs because

the free troposphere above these regions is relatively dry. At these low relative humidities we calculate that the average aerosol scattering cross section is even lower than the minimum value of 5 m^2 g^{-1} SO_4^{2-} assumed in the f(RH) parameterization. Therefore, how one chooses to represent aerosol water uptake in a global model not only influences the global and annual average aerosol forcing, but also significantly modifies the geographical distribution of the forcing. Moreover, the effect of higher relative humidities is more pronounced in winter months so the temporal distribution is affected as well.

As previously noted, in the base-case scenario we limited aerosol water uptake to that which occurs at 99% RH. At such high relative humidities, subgrid-scale effects may be especially important and problematic. For example, in humid, cloudy areas, cloud cover, relative humidity, and aerosol optical depth will be correlated on length scales that GCMs do not resolve. These unresolved correlations may result in systematic biases in GCM estimates of aerosol forcing. For example, the GISS GCM II-prime assumes a uniform aerosol optical depth across a grid cell, but allows for cloudy and clear fractions in the same grid cell. Intuitively, one would expect the clear portion of the grid cell to have a lower average humidity and resulting aerosol optical depth than the cloudy portion. Because a small relative humidity difference can have a large effect on aerosol optical depth and because clouds mask some of the aerosol forcing, these effects could be important. Although a grid cell with a high relative humidity will certainly have a substantial cloudy portion that partly masks the aerosol forcing, the aerosol optical depth specified for the clear portion may be based on a grid cell average relative humidity that is too high for the clear portion. This could exaggerate the aerosol forcing. One,

somewhat unsatisfying, way to compensate for this bias would be to specify a RH cutoff that prevents unrealistically high RH and aerosol optical depths in clear areas. It is not obvious, however, what RH cutoff is most appropriate. Published estimates of aerosol forcing typically say little, if anything, about the choice of relative humidity cutoff. This is unfortunate because the global and annual average forcing is very sensitive to water uptake at high RH and whether the choice of RH cutoff allows this water uptake.

We performed sensitivity studies to evaluate the effect of different RH cutoff values. Figure 3.5 shows global and annual average direct forcing estimates for the modern day, sulfate-only scenario as a function of RH cutoff. For comparison, the forcing obtained from the f(RH) method is similar to that obtained with a 95% RH cutoff. What is striking about the figure is that the rise in aerosol forcing between 85% and 95% RH is a little bit less than 20%. The jump between 95% and 99% RH, however, is much more substantial, nearly 60%. *Penner et al.* [1998] describe a similar result in which increasing their RH from 90% to 99% increases the calculated forcing by 50%. This sensitivity in both models results from the exponential-like water uptake behavior of the aerosol at high relative humidity, but also indicates that many GCM grid cells spend a significant amount of time at these high relative humidities. It is not clear whether these GCM humidity distributions are realistic. Whereas water uptake by aerosols at high relative humidity is well understood and quantified, the ability of GCMs to represent very humid conditions is questionable. Evaluation of hydrological schemes for GCMs has tended to focus on obtaining realistic precipitation and cloud cover. Relative humidity values may not be as well simulated in GCMs, a potential problem for aerosol forcing calculations considering the sensitivity shown here.

The sensitivity of the forcing to aerosol behavior at high relative humidity naturally raises questions about how well the GISS GCM II-prime or any GCM can represent this behavior. For example, one expects substantial subgrid variability in the relative humidity. Given the nonlinear dependence of aerosol scattering on relative humidity, calculations based on the grid cell average humidity may contain systematic biases. Moreover, clouds will frequently occur in grid cells with high average relative humidity. Subgrid variation in cloudiness, relative humidity, and aerosol optical depth as well as potential correlations in these variables will not be captured in the GCM, but may be important. The GISS GCM II-prime radiation scheme used in this study, for example, allows cloudy and clear areas to exist within the same grid cell, but assumes uniform relative humidity and aerosol optical depth across a given grid cell.

Haywood et al. [1997a] provide partial answers to these questions. They used a limited-area model with 2 km by 2 km horizontal resolution to compute aerosol forcing and then compared their results with those based on GCM-scale average quantities. The meteorological conditions chosen for this comparison were humid areas (93% average RH) with scattered convective clouds covering approximately one-third of the domain. They found that the GCM calculations underestimate direct radiative forcing by 73% under their clear sky conditions and by 60% in cloudy regions. The discrepancy results from the nonlinearity in water uptake at high relative humidities that causes the forcing calculated from the average humidity across a GCM grid cell to be less than that calculated from a distribution of humidities within a grid cell. In this study, the presence of clouds reduced this effect slightly but did not eliminate it entirely. These results show that GCM calculations of direct forcing may underestimate the forcing because of subgrid

scale variations in relative humidity, although one does not expect these effects to be as dramatic in less humid or more cloudy conditions. Therefore, even the forcing estimates presented here, though high in comparison with other global models, may underestimate the aerosol forcing. Many questions remain, however, and more work clearly needs to be done to improve the representation of direct forcing in GCMs.

As noted above, we assume that atmospheric aerosol particles exist in a hydrated, metastable state between their crystallization and deliquescence humidities. Although we believe that this is the mostly likely situation under most atmospheric conditions, it is conceivable that some air parcels experience low enough relative humidity to provoke crystallization. Assuming metastability will overestimate water uptake and direct forcing to the extent that this assumption breaks down. This is not expected to occur frequently, however. Pure ammonium sulfate crystallizes only below 40% RH, ammonium bisulfate and ammonium nitrate below 10% RH, and sulfuric acid is hydrated at all values of RH. Therefore, only nearly pure ammonium sulfate is expected to crystallize under very dry conditions. Our results show that, globally averaged, the molar ratio of ammonium to sulfate is close to one. Only in limited areas such as the tropics, Europe, China, and India is sulfate substantially neutralized such that it might have a high crystallization RH similar to that of pure ammonium sulfate. In such areas, conditions would usually be too humid for crystallization. Therefore, crystallization of sulfate aerosol is not expected to occur frequently in the atmosphere. Moreover, *Boucher and Anderson* [1995] have shown that, for a pure ammonium sulfate aerosol, the difference in global and annual average forcing between the rising and falling branches of the hysteresis loop is only 18%. This is an upper bound on the error introduced by our assumption of metastable

aerosol. Considering that nearly pure ammonium sulfate is not often found in dry areas, we expect the actual error to be much lower.

3.3.3 Comparison With Other Work

To put these results in the context of previously reported work, we refer back to Figure 3.1, which shows published estimates of anthropogenic direct forcing as a function of anthropogenic sulfate burdens. When we consider only sulfate and parameterize its optical properties in terms of a low RH α and a f(RH) factor, we obtain a forcing estimate of –0.71 W m^{-2}. As expected, this matches very closely the –0.68 W m^{-2} found in *Koch et al.* [1999], which is based on the same sulfur model and uses the same α and f(RH) parameterization of sulfate optical properties. However, when we compute the radiative forcing based on the concentrations and optical properties of the SO_4^{2-}-NH_4^+-H_2O mixture simulated by the aerosol composition model, our estimate increases to –0.95 W m^{-2} for the same sulfate burden. Including nitrate raises the forcing to –1.14 W m^{-2}.

As mentioned in the introduction, the sulfate forcing efficiencies implicit in published forcing estimates vary by more than a factor of three, largely because of uncertainties associated with sulfate optical properties. This study has sought to reduce these uncertainties by explicitly simulating the composition of the sulfate aerosol, thereby alleviating the need for some of the assumptions previously necessary regarding neutralization by ammonia and degree of water uptake. Figure 3.1 shows that our forcing estimate of -0.95 W m^{-2} for sulfate, together with that of *Taylor and Penner* [1994] (not shown in Figure 3.1), is higher than all others cited here, partly because our anthropogenic sulfate burden is larger than others. Our sulfate forcing efficiency, -290 W

g^{-1} SO_4^{2-}, is higher than all others except those of *Charlson et al.* [1991] and *Penner et al.* [1998], but only 15% higher than that of *Kiehl et al.* [2000]. Of the studies shown in Figure 3.1, our method for computing aerosol optical properties is most similar to those of *Boucher and Anderson* [1995], *Penner et al.* [1998], and *Kiehl et al.* [2000]. Except for *Boucher and Anderson* [1995], who use laboratory data, these authors predict water uptake using Köhler theory. Both the laboratory data and Köhler theory should yield results for water uptake similar to ours. All three studies compute optical properties using Mie scattering calculations on hydrated lognormal size distributions just as we do. Despite the similarities in methodology, there are surprising discrepancies in the resulting sulfate forcing efficiencies. Our value agrees with that of *Kiehl et al.* [2000] to within 15%, but the forcing efficiency of *Penner et al.* [1998] is about 30% higher. The fact that their model allows relative humidity to reach 100% over an entire grid cell before forming clouds is a likely explanation for their high forcing efficiency. The forcing efficiency from *Boucher and Anderson* [1995], -125 W g^{-1} SO_4^{2-}, is surprisingly low compared to the others. They cap their relative humidity at 95% while the others allow water uptake up to 99%. Although this must explain some of the discrepancy, the sensitivity runs shown here and in other works make it clear that the difference in RH cutoff cannot explain the entire difference. A more systematic intercomparison of forcing efficiencies will be necessary to fully sort out the effects of various factors on forcing efficiency. These factors include treatment of water uptake, method of calculating optical properties, the radiation scheme used, and the distributions of relative humidity and cloud cover in the particular global model. Cloud amount is a potentially important difference between estimates from different models. For example, the simulated global mean cloud

cover for our 3-year period was 47%. A comparison with satellite data from the International Satellite Cloud Climatology Project (ISCCP) for the period beginning July 1983 and ending December 1990, during which the global mean cloud cover was estimated to be 63%, suggests that this value is probably too low [*Jakob*, 1999]. If this is indeed the case, this factor alone could cause the forcing estimates and forcing efficiencies we report here to be high by as much as 15%.

In summary, it is clear from this comparision that estimates of direct sulfate forcing, including those presented here, are subject to important uncertainties. First, there is the uncertainty regarding the anthropogenic sulfate burden, which varies by almost a factor of two amongst the estimates cited here. Second, given an anthropogenic sulfate burden, there is the uncertainty regarding its forcing efficiency, which varies by a factor of three. This uncertainty includes the effects of aerosol size distribution and chemical composition, biases in GCM cloud cover and relative humidity, and the difficulties associated with subgrid variations and correlations already discussed. Nevertheless, our results and others cited here suggest that, if sulfate at high relative humidities really does contribute significantly to direct forcing, this may have been underestimated in some previous work.

3.4. Summary and Conclusions

A model of aerosol composition that explicitly predicts the concentrations of nitrate, ammonium, and aerosol water as well as sulfate has been used to estimate direct radiative forcing by sulfate and nitrate. This is the first direct forcing estimate based on the equilibrium water content of a changing SO_4^{2-}-NO_3^--NH_4^+ mixture and the first estimate

of nitrate forcing based on a global model of nitrate aerosol. It is intended that the explicit simulation of aerosol composition, especially water uptake, help to constrain aerosol optical properties, a key uncertainty in assessing direct forcing.

We estimate the present day anthropogenic direct aerosol forcing to be –0.95 W m^{-2} for sulfate and –0.19 W m^{-2} for nitrate. Moreover, based on a plausible IPCC emissions scenario with especially strong increases in NO_x emissions, we predict that the nitrate forcing will increase to –1.28 W m^{-2} by the end of this century, even while sulfate forcing declines to -0.85 W m^{-2}. This result shows that future estimates of aerosol forcing based solely on predicted sulfate concentrations may be highly misleading and that the potential for significant amounts of ammonium nitrate aerosol needs to be considered in estimates of future climate change.

A key finding of this study is that the calculated direct forcing is extremely sensitive to how the effect of water uptake on aerosol scattering behavior is taken into account. In particular, we find that the large amount of water taken up by the aerosol above 95% relative humidity increases the total forcing by about 60%. This is important because a method commonly used in previous work for parameterizing the effect of water uptake on optical properties has been to assume a low RH scattering coefficient of 5 m^2 g^{-1} SO_4^{2-} and to correct for that at higher humidities with an empirical f(RH) factor. In principle, there is nothing wrong with this approach, but in practice lack of data about f(RH) at high relative humidity has caused investigators to conservatively limit it to values that are unrealistically low. Even in studies where water uptake has been computed based on Köhler theory or laboratory data, investigators, ourselves included, have had to arbitrarily specify a cutoff RH beyond which they do not allow further water uptake. We have

shown that the resulting estimate of aerosol forcing is very sensitive to the, often unspecified, choice of RH cutoff. Water uptake at high relative humidity, therefore, makes an important contribution to global forcing that has often been neglected without adequate discussion or even recognition of the consequences.

The results discussed here indicate several issues that require further attention. First, the large contribution to the forcing made by aerosol at high relative humidity emphasizes the need to understand potential correlations between aerosols, humidity, and clouds. Subgrid variability in these factors and correlations between them could be important for improving our estimate of direct aerosol forcing. These are effects that, by their nature, are not well represented in GCMs, the primary tool for global, long-term assessments of aerosol effects on climate. Little work has been done on this topic, but what has been done indicates that estimates of forcing based on GCM grid cell average humidity, such as the ones presented here, may be underestimates.

Second, further efforts should be made to evaluate GCM predictions of relative humidity. This will be difficult to achieve because there is a lack of data on the large spatial scales required to validate a global model with coarse resolution. Moreover, as long as one is interested primarily in cloud cover and precipitation rates, the details of the GCM-predicted relative humidity can be overlooked as long as they do not result in substantial errors in simulated clouds and rain. It is understandable, then, that GCM relative humidities have not been thoroughly and systematically evaluated. On the other hand, if one uses a GCM to estimate direct forcing of a hygroscopic aerosol, the details of the spatial and temporal distribution of grid-cell average relative humidity become important and require further attention.

Third, the potential for ammonium nitrate aerosol to contribute significantly to radiative forcing in the future highlights the need for a better understanding of tropospheric nitric acid and ammonia. Tropospheric photochemical models have generally had difficulty simulating nitric acid concentrations that match observations well, suggesting that important processes may be missing. This has not been a major problem as they have usually been used primarily to simulate ozone, but improving the treatment of nitric acid in tropospheric chemical models becomes more important in light of the potential future significance of nitrate aerosol forcing for climate change. Similarly, this study would have benefited from a more complete knowledge of ammonia emissions on a global scale. In particular, more data on past and future emissions and seasonal variability of emissions would help to improve and constrain model performance with regard to ammonia and ammonium nitrate aerosol.

Acknowledgements. This work has been supported by a graduate fellowship from the Fannie and John Hertz Foundation as well as by the National Aeronautics and Space Administration Earth Observing System Interdisciplinary Science program (NASA EOS-IDS). We also acknowledge Sigrun Karlsdottir and fellow researchers at the University of Oslo for providing nitric acid concentration fields from the Oslo CTM1.

References

Adams, P. J., J. H. Seinfeld, and D. M. Koch, Global concentrations of tropospheric sulfate, nitrate, and ammonium aerosol simulated in a general circulation model, *J. Geophys. Res.*, *104*, 13,791-13,823, 1999.

Andres, R. J., and A. D. Kasgnoc, A time-averaged inventory of subaerial volcanic sulfur emissions, *J. Geophys. Res.*, *103*, 25,251-25,261, 1998.

Ansari, A. S., and S. N. Pandis, Response of inorganic PM to precursor concentrations, *Environ. Sci. Technol.*, *32*, 2706-2714, 1998.

Berntsen, T. K. and I. S. A. Isaksen, A global three-dimensional chemical transport model for the troposphere: Model description and CO and O3 results, *J. Geophys. Res., 102,* 21,239-21,280, 1997.

Boucher, O., and T. L. Anderson, General circulation model assessment of the sensitivity of direct climate forcing by anthropogenic sulfate aerosols to aerosol size and chemistry, *J. Geophys. Res., 100*, 26,117-26,134, 1995.

Boucher, O., et al., Intercomparison of models representing direct shortwave radiative forcing by sulfate aerosols, *J. Geophys. Res.*, *103*, 16,979-16,998, 1998.

Bouwman, A. F., D. S. Lee, W. A. H. Asman, F. J. Dentener, K. W. Van Der Hoek, and J. G. J. Olivier, A global high-resolution emission inventory for ammonia, *Global Biogeochem. Cycles, 11,* 561-587, 1997.

Charlson, R. J., D. S. Covert, and T. V. Larson, Observation of the effect of humidity on light scattering by aerosols, in *Hygroscopic Aerosols*, edited by L. Ruhnke and A. Deepak, pp. 35-44, A. Deepak Publ., Hampton, VA, 1984.

Charlson, R. J., J. Langner, H. Rodhe, C. B. Leovy, and S. G. Warren, Perturbation of the northern hemisphere radiative balance by backscattering from anthropogenic sulfate aerosols, *Tellus, Ser. AB, 43,* 152-163, 1991.

Chin, M., D. J. Jacob, G. M. Gardner, M. S. Foreman-Fowler, and P. A. Spiro, A global three-dimensional model of tropospheric sulfate, *J. Geophys. Res., 101,* 3761-3778, 1997.

Chuang, C. C., J. E. Penner, K. E. Taylor, A. S. Grossman, and J. J. Walton, An assessment of the radiative effects of anthropogenic sulfate, *J. Geophys. Res., 102,* 3761-3778, 1997.

Crutzen, P. J., and P. H. Zimmermann, The changing photochemistry of the troposphere, *Tellus, 43AB,* 136-151, 1991.

Del Genio, A. D., and M.-S. Yao, Efficient cumulus parameterization for long-term climate studies: The GISS scheme, in *The Representation of Cumulus Convection in Numerical Models* Monogr. 46, edited by K. A. Emanuel and D. J. Raymond, pp. 181-184, Am. Meteorol. Soc., Boston, Mass., 1993.

Del Genio, A. D., M.-S. Yao, W. Kovari, and K. K.-W. Lo, A prognostic cloud water parameterization for global climate models, *J. Clim., 9,* 270-304, 1996.

Dentener, F. J., and P. Crutzen, A three-dimensional model of the global ammonia cycle, *J. Atmos. Chem., 19,* 331-369, 1994.

Feichter, J., U. Lohmann, and I. Schult, The atmospheric sulfur cycle in ECHAM-4 and its impact on the shortwave radiation, *Clim. Dyn., 13,* 235-246, 1997.

Hansen, J., G. Russell, D. Rind, P. Stone, A. Lacis, S. Lebedeff, R. Ruedy, and L. Travis, Efficient three-dimensional global models for climate studies: Models I and II., *Mon. Weather Rev., 111,* 609-662, 1983.

Haywood, J. M., V. Ramaswamy, and L. J. Donner, A limited-area-model case study of the effects of sub-grid scale variations in relative humidity and cloud upon the direct

radiative forcing of sulfate aerosol, *Geophys. Res. Lett., 24,* 143-146, 1997a.

Haywood, J. M., D. L. Roberts, A. Slingo, J. M. Edwards, and K. P. Shine, General circulation model calculations of the direct radiative forcing by anthropogenic sulfate and fossil-fuel soot aerosol, *J. Clim., 10,* 1562-1577, 1997b.

Hjellbrekke, A.-G., and J. E. Hanssen, Data report 1996, 1, Annual summaries, *EMEP/CCC Rep. 1/98,* 85 pp., Norw. Inst. For Air Res., Lillestrom, 1998.

Horowitz, L. W., J. Liang, G. M. Gardner, and D. J. Jacob, Export of reactive nitrogen from North America during summertime: Sensitivity to hydrocarbon chemistry, *J. Geophys. Res., 103,* 13,451-13,476, 1998.

Intergovernmental Panel on Climate Change (IPCC), *Climate Change 1995*, edited by J. T. Houghton et al., Cambridge Univ. Press, New York, 1996.

Jaffe, D., T. K. Berntsen, and I. S. A. Isaksen, A global three-dimensional chemical transport model 2. Nitrogen oxides and nonmethane hydrocarbon results, *J. Geophys. Res., 102,* 21,281-21,296, 1997.

Jakob, C, Cloud cover in the ECMWF reanalysis, *J. Clim., 12,* 947-959, 1999.

Kiehl, J. T., and B. P. Briegleb, The relative roles of sulfate aerosols and greenhouse gases in climate forcing, *Science, 260,* 311-314, 1993.

Kiehl, J. T., T. L. Schneider, P. J. Rasch, M. C. Barth, and J. Wong, Radiative forcing due to sulfate aerosols from simulations with the National Center for Atmospheric Research Community Climate Model, Version 3, *J. Geophys. Res., 105,* 1441-1457, 2000.

Koch, D. M., D. Jacob, I. Tegen, D. Rind, and M. Chin, Tropospheric sulfur simulation and sulfate direct radiative forcing in the GISS GCM, *J. Geophys. Res., 104,* 23,799-

23,822, 1999.

Lacis, A. A., and J. E. Hansen, Parameterization for the absorption of solar radiation in the Earth's atmosphere, *J. Atmos. Sci.*, *31*, 118-133, 1974.

Lacis, A. A., and M. I. Mishchenko, Climate forcing, climate sensitivity, and climate response: A radiative modeling perspective on atmospheric aerosols, in *Aerosol Forcing of Climate*, edited by R. J. Charlson and J. Heintzenberg, pp. 11-42, John Wiley, New York, 1995.

Lacis, A. A., and V. Oinas, A description of the correlated *k*-distribution method for modeling non-gray gaseous absorption, thermal emission, and multiple scattering in vertically inhomogeneous atmospheres, *J. Geophys. Res.*, *96*, 9027-9064, 1991.

McNaughton, D. J., and R. J. Vet, Eulerian model evaluation field study (EMEFS): A summary of surface network measurements and data quality, *Atmos. Environ., 30,* 227-238, 1996.

Meng, Z., and J. H. Seinfeld, Time scales to achieve atmospheric gas-aerosol equilibrium for volatile species, *Atmos. Environ., 30,* 2889-2900, 1996.

Mickley, L. J., P. Murti, D. Jacob, J. Logan, and D. Rind, Radiative forcing from tropospheric ozone calculated with a unified chemistry-climate model, *J. Geophys. Res., 104,* 30,153-30,172, 1999.

Nemesure, S., R. Wagener, and S. E. Schwartz, Direct shortwave forcing of climate by the anthropogenic sulfate aerosol: Sensitivity to particle size, composition, and relative humidity, *J. Geophys. Res., 100*, 26,105-26,116, 1995.

Nenes, A., C. Pilinis, and S. N. Pandis, ISORROPIA: A new thermodynamic equilibrium model for multiphase multicomponent inorganic aerosols, *Aquat. Geochem., 4,* 123-152, 1998.

Penner, J. E., C. C. Chuang, and K. Grant, Climate forcing by carbonaceous and sulfate aerosols, *Climate Dynamics, 14,* 839-851, 1998.

Pilinis, C., S. N. Pandis, and J. H. Seinfeld, Sensitivity of direct climate forcing by atmospheric aerosols to aerosol size and composition, *J. Geophys. Res., 100,* 18,739-18,754, 1995.

Rasch, P. J., M. C. Barth, J. T. Kiehl, S. E. Schwartz, and C. M. Benkovitz, A description of the global sulfur cycle and its controlling processes in the National Center for Atmospheric Research Community Climate Model, Version 3, *J. Geophys. Res., 105,* 1367-1385, 2000.

Rind, D., and J. Lerner, The use of on-line tracers as a diagnostic tool in general circulation model development, 1, Horizontal and vertical transport in the troposphere, *J. Geophys. Res., 101,* 12,667-12,683, 1996.

Stelson, A. W., Urban aerosol refractive index prediction by partial molar refraction approach, *Environ. Sci. Technol., 24,* 1676-1679, 1990.

Tang, I. N., Chemical and size effects of hygroscopic aerosols on light scattering coefficients, *J. Geophys. Res., 101,* 19,245-19,250, 1996.

Tang, I. N., Thermodynamic and optical properties of mixed-salt aerosols of atmospheric importance, *J. Geophys. Res., 102,* 1883-1893, 1997.

Tang, I. N., and H. R. Munkelwitz, Water activities, densities, and refractive indices of aqueous sulfates and sodium nitrate droplets of atmospheric importance, *J. Geophys. Res.*, *99*, 18,801-18,808, 1994.

Taylor, K. E., and J. E. Penner, Response of the climate system to atmospheric aerosols and greenhouse gases, *Nature, 369,* 734-737, 1994.

ten Brink, H. M., J. P. Veefkind, A. Waijers-Ijpelaan, and J. C. van der Hage, Aerosol light-scattering in The Netherlands, *Atmos. Env.*, *30*, 4521-4261, 1996.

ten Brink, H. M., C. Kruisz, G. P. A. Kos, and A. Berner, Composition/size of the light-scattering aerosol in The Netherlands, *Atmos. Env.*, *31*, 3955-3962, 1997.

Van Dorland, R., F. J. Dentener, and J. Lelieveld, Radiative forcing due to tropospheric ozone and sulfate aerosols, *J. Geophys. Res.*, *102*, 28,079-28,100, 1997.

Wang, Y., D. J. Jacob, and J. A. Logan, Global simulation of tropospheric O_3-NO_x-hydrocarbon chemistry, 1, Model formulation, *J. Geophys. Res.*, *103*, 10,713-10,726, 1998a.

Wang, Y., J. A. Logan and D. J. Jacob, Global simulation of tropospheric O_3-NO_x-hydrocarbon chemistry, 2, Model evaluation and global ozone budget, *J. Geophys. Res.*, *103*, 10,727-10,756, 1998b.

Wang, Y., D. J. Jacob, and J. A. Logan, Global simulation of tropospheric O_3-NO_x-hydrocarbon chemistry, 3, Origin of tropospheric ozone and effects of nonmethane hydrocarbons, *J. Geophys. Res.*, *103*, 10,757-10,768, 1998c.

Wesely, M. L., and B. B. Hicks, Some factors that affect the deposition rates of sulfur dioxide and similar gases on vegetation, *J. Air Pollut. Contr. Assoc., 27,* 1110-1116, 1977.

West, J. J., C. Pilinis, A. Nenes, and S. N. Pandis, Marginal direct climate forcing by atmospheric aerosols, *Atmos. Env.*, *32*, 2531-2542, 1998.

West, J. J., A. S. Ansari, and S. N. Pandis, Marginal PM 2.5: Nonlinear aerosol mass response to sulfate reductions in the Eastern United States, *Journal of the Air & Waste Management Association, 49,* 1415-1424, 1999.

Figure Captions

Figure 3.1. Estimates of anthropogenic sulfate direct forcing (W m^{-2}) versus anthropogenic sulfate burden (Tg S). Circles represent estimates from this work: SO_4^{2-}, sulfate forcing computed using composition-dependent optical properties; SO_4^{2-}/NO_3^-, sulfate and nitrate forcing using same method; SO_4^{2-} - *f*(RH), sulfate forcing computed using α x *f*(RH) parameterization of aerosol optical properties. Diamonds represent other published estimates: BA95, *Boucher and Anderson* [1995]; C91, *Charlson et al.* [1991]; F97, *Feichter et al.* [1997]; KB93, *Kiehl and Briegleb* [1993]; K99, *Koch et al.* [1999]; K00, *Kiehl et al.* [2000]; P98, *Penner et al.* [1998]. Dashed lines represent the range of sulfate forcing efficiencies implicit in these estimates.

Figure 3.2. Sulfate aerosol scattering cross sections (m^2 g^{-1} SO_4^{2-}) as a function of relative humidity (%). Solid lines illustrate optical properties for sulfuric acid and ammonium sulfate computed with the composition-dependent Mie scattering calculations described in this work. For comparison, the dashed line represents those computed with the α x *f*(RH) parameterization.

Figure 3.3. Geographic distribution of annual average anthropogenic total (sulfate and nitrate) direct aerosol forcing (W m^{-2}) for a) modern day (2000) and b) future (2100) emissions scenarios. Values in the upper right corner of each map show the corresponding global average forcing.

Figure 3.4. A comparison of anthropogenic forcing estimated based on composition-dependent optical properties with that based on the α x f(RH) parameterization. This map shows the geographic distribution of the difference in the calculated annual average forcings for the modern day scenario. Negative values, shown in blue, indicate areas where the composition-dependent approach results in more aerosol forcing.

Figure 3.5. Sensitivity of global and annual average aerosol forcing to relative humidity cutoff. The RH cutoff limits aerosol water uptake to the amount that occurs at that RH value.

Table 3.1. A summary of emissions, input nitric acid concentrations, aerosol burdens and forcings for the three time periods simulated in this study.

		Scenario		
		Preindustrial 1800	Modern Day 2000	IPCC SRES A2 2100
Emissions				
SO_2 (Tg S/yr)	Total	4.8	73.8	65.1
	Anthropogenic	0.0	69.0	60.3
	Volcanic	4.8	4.8	4.8
DMS (Tg S/yr)		26.0	26.0	26.0
NO_x (Tg N/yr)*		8.6	32.5	109.7
NH_3 (Tg N/yr)	Total	18.7	57.6	122.2
	Agricultural**	6.8	37.4	88.8
	Natural***	10.7	10.7	10.7
	Biomass burning	0.6	6.4	15.3
	Other****	0.6	3.1	7.4
Annual Average HNO_3 Concentrations (pptv)				
	Surface layer	59	356	1022
	634 mb	119	292	648
	201 mb	317	465	884
Aerosol Burdens (Tg)				
	Total	4.05	12.78	20.55
	SO_4^{2-}	0.74	2.41	2.23
	NO_3^-	0.10	0.38	1.79
	NH_4^+	0.12	0.54	1.04
	H_2O	3.11	9.45	15.48
Direct Forcings (W m^{-2})				
	Total	-0.63	-1.78	-2.77
	SO_4^{2-}	-0.52	-1.48	-1.38
	NO_3^-	-0.11	-0.30	-1.39
Anthropogenic Forcings (W m^{-2})				
	Total	N/A	-1.14	-2.13
	SO_4^{2-}	N/A	-0.95	-0.85
	NO_3^-	N/A	-0.19	-1.28

*NOx emissions are those used in the Harvard-GISS GCM [*Mickley et al.*, 1999]. Although not used directly in this work, they are presented to explain the trend in and assumptions behind the input nitric acid concentrations taken from this model.

**Agricultural emissions include the following categories from *Bouwman et al.* [1997]: domestic animals, synthetic fertilizers, and crops.

***Natural emissions include the following categories from *Bouwman et al.* [1997]: oceans, undisturbed soils, and wild animals.

****Other emissions include the following categories from *Bouwman et al.* [1997]: humans and pets, industrial processes and fossil fuels.

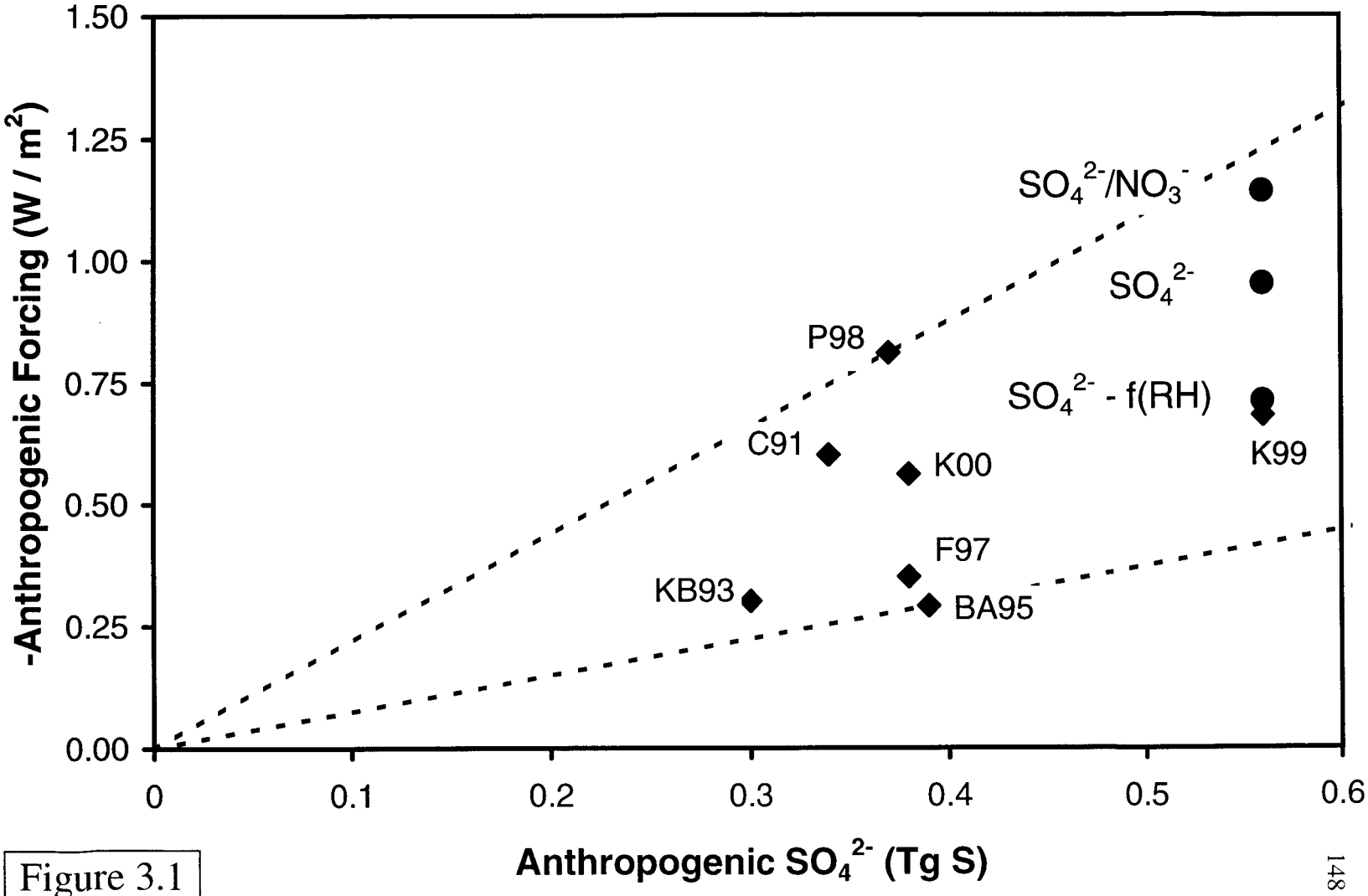
1.50
1.25
1.00
0.75
0.50
0.25
0.00
-Anthropogenic Forcing (W / m2)
0
0.1
0.2
0.3
0.4
0.5
0.6
Anthropogenic SO4 2- (Tg S)
SO4 2-/NO3 -
SO4 2-
SO4 2- - f(RH)
P98
C91
K00
K99
F97
KB93
BA95

Figure 3.1

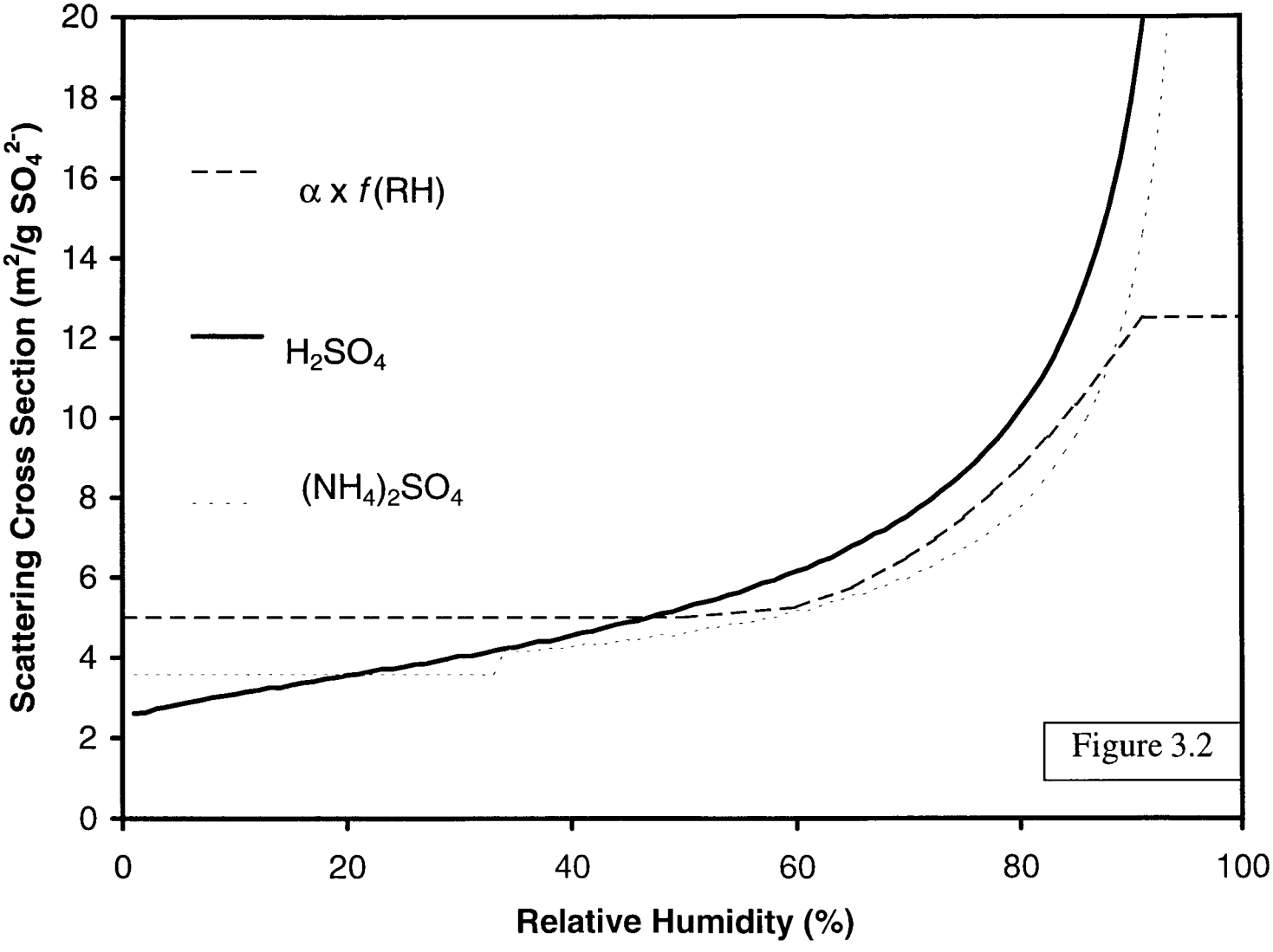
Scattering Cross Section ($m^2/g\ SO_4^{2-}$)
20
18
16
14
12
10
8
6
4
2
0
α x f(RH)
H_2SO_4
$(NH_4)_2SO_4$
0
20
40
60
80
100
Relative Humidity (%)

Figure 3.2

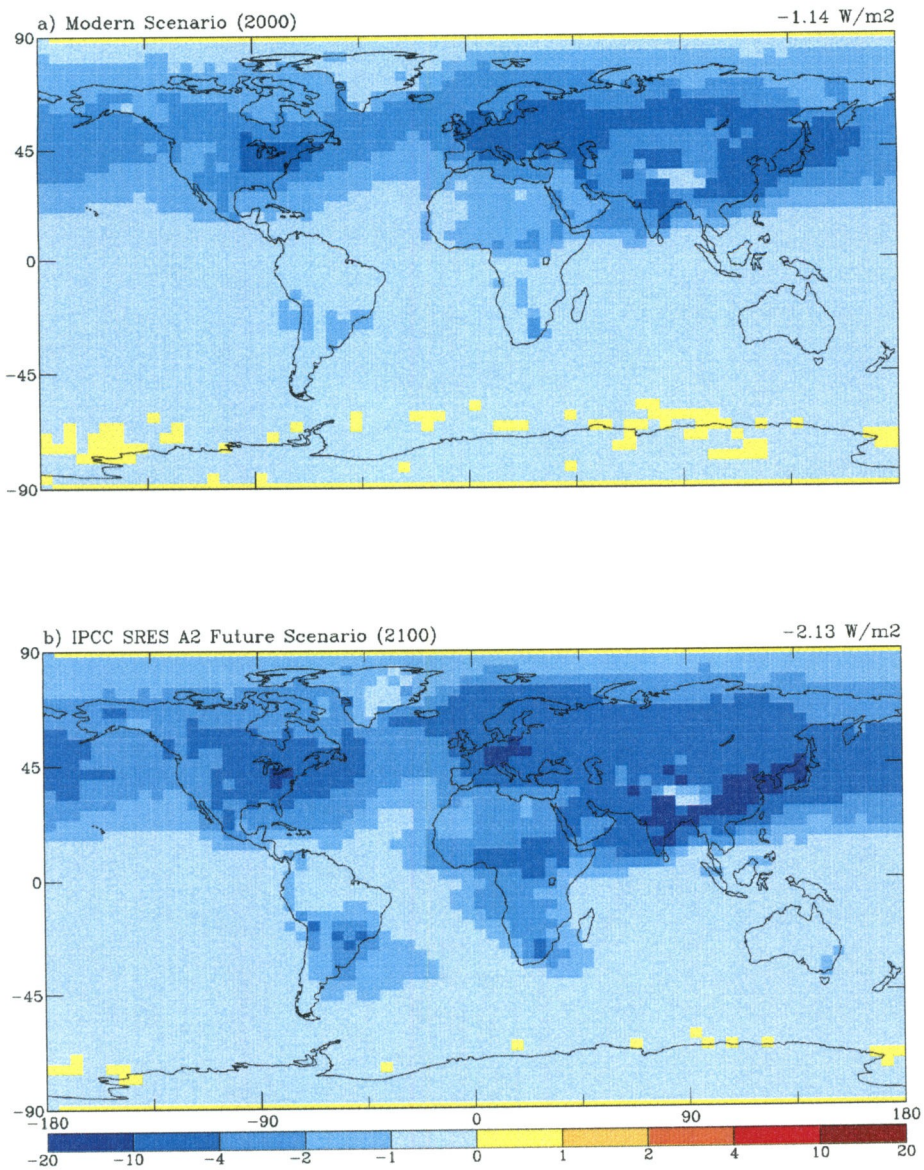
a) Modern Scenario (2000)
-1.14 W/m2
90
45
0
-45
-90
b) IPCC SRES A2 Future Scenario (2100)
-2.13 W/m2
90
45
0
-45
-90
-180
-90
0
90
180
-20
-10
-4
-2
-1
0
1
2
4
10
20

Figure 3.3

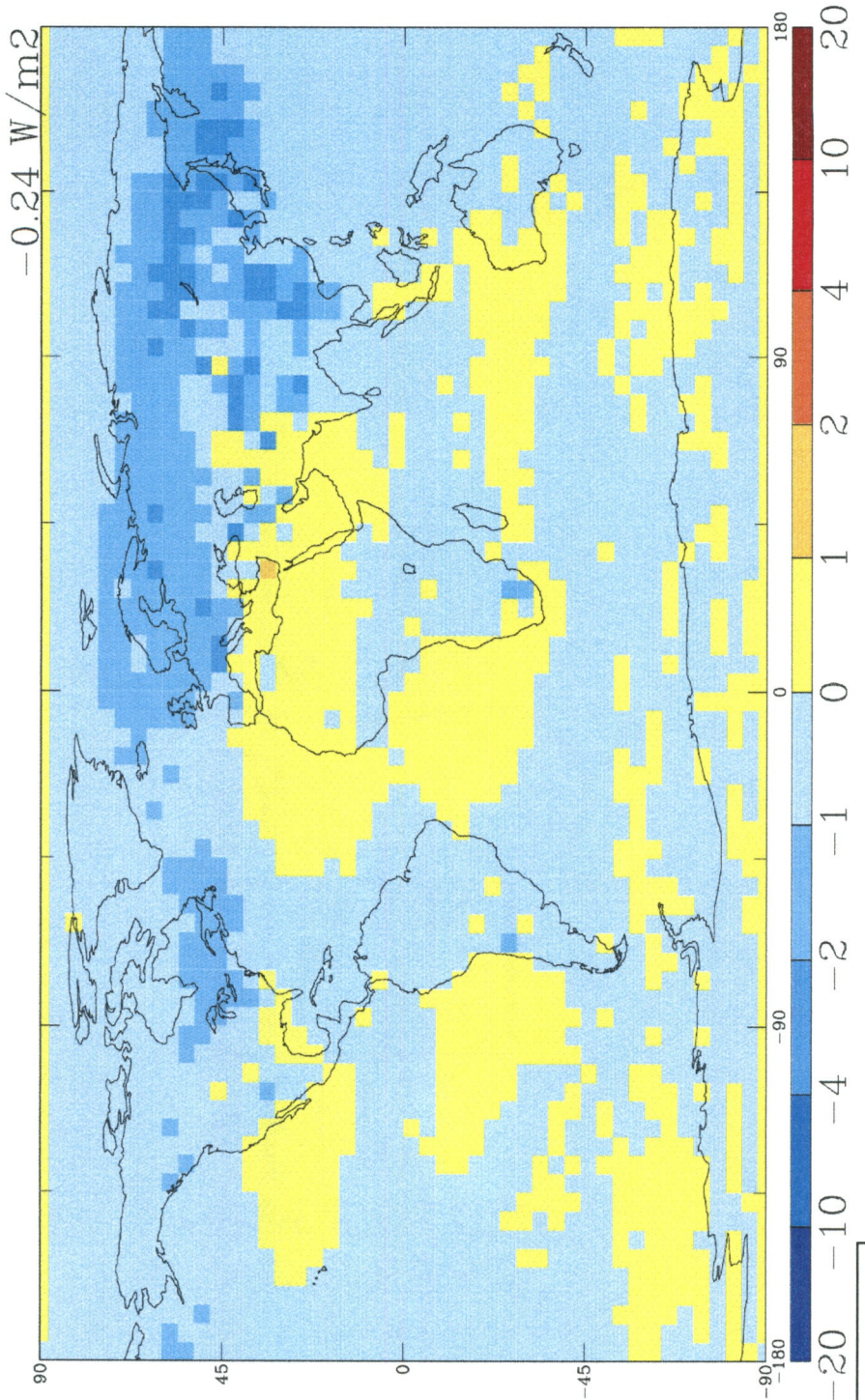

Figure 3.4

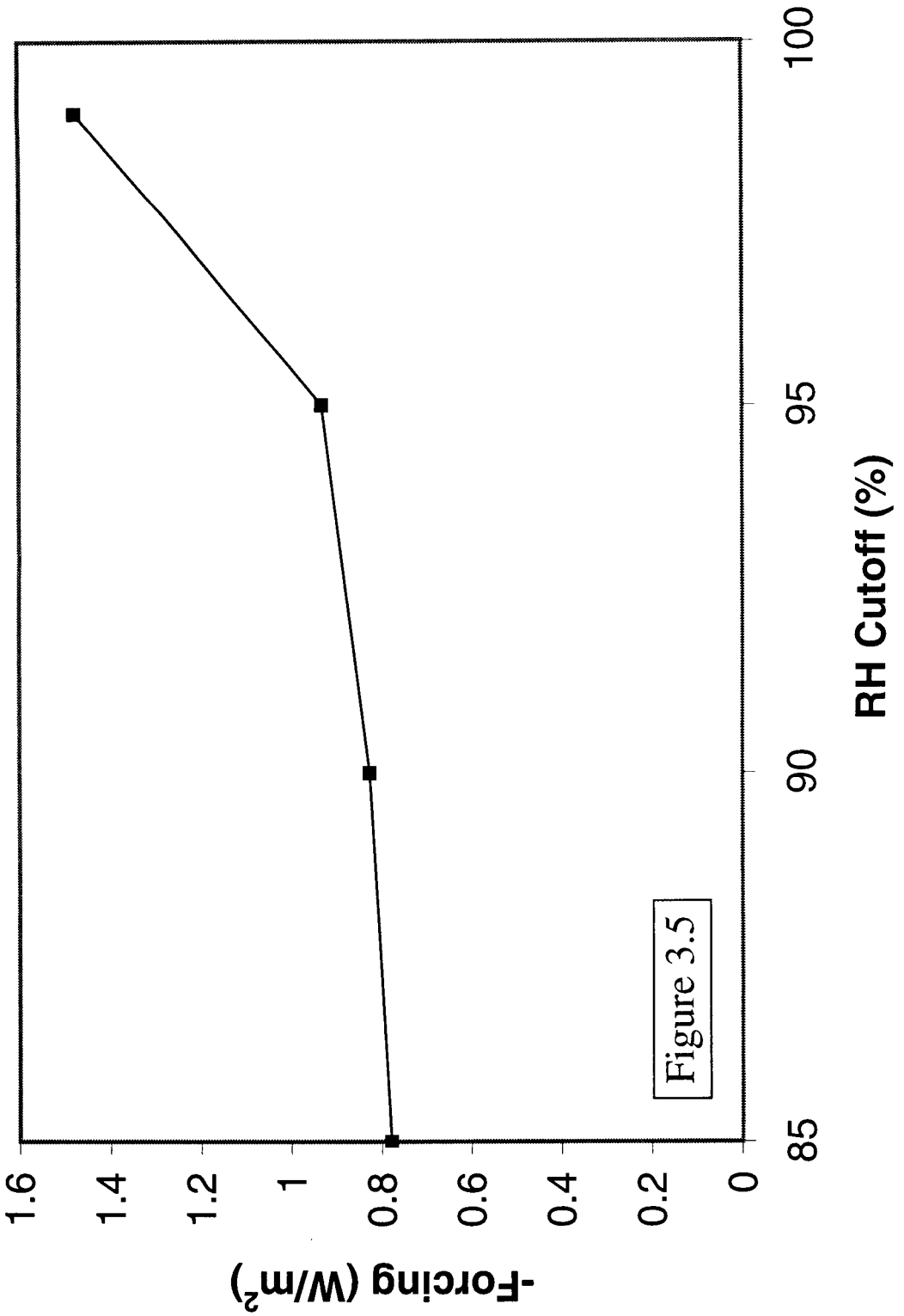

Figure 3.5

Chapter Four: Predicting Global Aerosol Size Distributions in General Circulation Models

Reference: Adams, P. J., and J. H. Seinfeld, Predicting global aerosol size distributions in general circulation models, Submitted to *Journal of Geophysical Research*, 2001.

Abstract. To better represent the indirect effect of aerosols on climate, a size-resolved simulation of aerosol microphysics, size distributions, number and mass concentrations has been incorporated into the GISS general circulation model (GCM). The two-moment sectional aerosol microphysics algorithm used conserves aerosol number as well as mass. It has high size resolution, 30 bins between 0.01 and 10 μm diameter. As a first application, a size-resolved simulation of sulfate has been performed. The model reproduces important features of the atmospheric aerosol such as number concentrations that increase with altitude and land-sea contrasts in aerosol number concentrations and size distributions. Comparisons with observations show that simulated size distributions are realistic and condensation nuclei (CN) concentrations agree with observations within about 25%. Predicted cloud condensation nuclei (CCN) concentrations are also in reasonable agreement with observations, although there are locations for which agreement would be improved by including other aerosol components such as sea salt and carbonaceous aerosols. Sensitivity scenarios show that uncertainties in nucleation and primary emissions from fossil fuels can have significant effects on predictions of CN and CCN concentrations.

4.1. Introduction

It is now accepted that anthropogenic aerosols have the potential to perturb the earth's climate by increasing cloud reflectance [*Twomey,* 1974; *Albrecht,* 1989; *Pincus and Baker,* 1994]. This is hypothesized to occur when anthropogenic activities increase

the number of aerosol particles that serve as nuclei upon which cloud droplets form (cloud condensation nuclei or CCN). The consequent increase in cloud droplet number concentrations (CDNC) leads to brighter clouds with longer lifetimes. The resulting increase in cloud reflectance is termed indirect aerosol radiative forcing. Uncertainty in the magnitude of the indirect effect has plagued efforts to quantify the sensitivity of climate to anthropogenic perturbations such as increased concentrations of greenhouse gases. The Intergovernmental Panel on Climate Change (IPCC) has estimated that the global and annual average indirect aerosol radiative forcing is somewhere between 0 and -2.0 W m^{-2}, as compared with $+2.5$ W m^{-2} imposed by changes in greenhouse gases [*IPCC*, 2001]. Moreover, this estimate includes only the effect of aerosols on cloud brightness that results from changing the size and number of cloud droplets. Aerosols may also increase cloud lifetime, leading to an additional negative radiative forcing of uncertain magnitude [*Albrecht,* 1989].

The key process in the indirect effect is the activation of aerosol particles, typically with diameters in the range of 0.1 to 1 μm, to form cloud droplets. The cutoff diameter between CCN particles and those too small to activate depends on local meteorological conditions, specifically the degree to which the atmosphere is supersaturated with water vapor. Cloud properties are determined by the size distribution of cloud droplets, which depends, in part, on aerosols through the activation process, but is also influenced by cloud microphysical processes such as condensation, collision, coalescence and droplet breakup. Physically speaking, the indirect climatic effect of aerosols is a function of the number concentration of CCN in a cloudy area.

Until recently, global aerosol models did not have the capability to explicitly predict aerosol number concentrations based on first principles, but found other ways to estimate the magnitude of the indirect effect. It is useful to think in terms of a "first generation" of global aerosol models that predict only the total mass of a given aerosol constituent without providing any description of the size distribution or number concentrations. Sulfate is the aerosol component that has received the most attention in global model studies [*Erickson et al.,* 1991; *Langner and Rodhe,* 1991; *Penner et al.,* 1994; *Pham et al.,* 1995; *Chin et al.,* 1996; *Feichter et al.,* 1996; *Chuang et al.,* 1997; *Feichter et al.,* 1997; *Kasibhatla et al.,* 1997; *Lelieveld et al.,* 1997; *Kjellstrom,* 1998; *Restad et al.,* 1998; *Roelofs et al.,* 1998; *Koch et al.,* 1999; *Barth et al.,* 2000; *Rasch et al.,* 2000]. Sulfate is especially important in estimating the indirect effect because of the demonstrated anthropogenic impact on sulfate concentrations and the readiness with which particles containing sulfate activate in clouds. Global modeling studies have also been reported for carbonaceous aerosols [*Cooke and Wilson,* 1996; *Liousse et al.,* 1996; *Kanakidou et al.,* 2000; *Tegen et al., 2000*] and mineral dust [*Tegen and Fung,* 1994; *Tegen and Lacis,* 1996; *Dentener et al.,* 1996]. With the exception of mineral dust, aerosol size and number have not been predicted in these studies.

As a result of the limited information provided by first-generation aerosol models, estimates of the magnitude of the indirect effect have relied on other information to predict CCN and cloud droplet number concentrations. A common approach is exemplified by that of *Boucher and Lohmann* [1995], in which observed correlations between sulfate mass and CDNC were used to predict CDNC based on predictions of sulfate mass. Another approach is to parameterize the size distribution of

sulfate in terms of the amount of anthropogenic sulfate being added to preexisting particles by condensation of gas-phase sulfuric acid and aqueous oxidation of sulfur dioxide [*Chuang and Penner,* 1995; *Chuang et al.,* 1997]. Finally, the indirect effect can be assessed based on satellite observations of cloud droplet effective radii [*Boucher,* 1995]. This approach has the advantage of constraining climate model radiative transfer calculations with realistic cloud optical properties; the disadvantage is that it does not allow one to probe the physical mechanisms that give rise to those optical properties and cannot make forecast estimates of the indirect effect based on future emissions scenarios.

Similarly, the empirical approach exemplified in the work of *Boucher and Lohmann* [1995] has strengths and weaknesses. Probably the chief strength of the approach is that, by imposing an observed sulfate-CDNC relationship, it forces the simulation to produce more or less realistic cloud optical properties. Another important advantage is that it requires prediction of only sulfate mass concentrations. Moreover, global sulfate mass models have been developed and evaluated by the community over the past decade, so they are well characterized and can be used with a certain degree of confidence. The empirical approach has resulted in much-needed estimates of the magnitude of the indirect effect and associated uncertainties [*Lohmann and Feichter,* 1997; *Kiehl et al.,* 2000].

However, as pointed out by *Kiehl et al.* [2000], there is not a single, unambiguous relationship between cloud droplet number and sulfate mass that can be assumed based on observational evidence. That study used several different published empirical relationships with resulting estimates of the indirect effect ranging from as low

as –0.40 W m^{-2} to –1.78 W m^{-2}. In fact, it is not surprising that the relationship between sulfate and cloud droplet number varies with space and time in the atmosphere according to changes in the aerosol size distribution. Besides the uncertainties inherent in the empirical approach, it has the disadvantage of concealing the physical processes that control CCN concentrations, limiting the amount of insight one can gain into the essential physics of the problem. Imposing a fixed sulfate-CDNC relationship means that one cannot easily test the sensitivity of model behavior to uncertainties in specific processes such as nucleation. Finally, extrapolating an observed sulfate-CDNC relationship to other locations, times of the year, or into the future, may introduce errors that are difficult to quantify.

All this points to the importance of a "second generation" of global aerosol models that take a mechanistic approach to predicting CCN concentrations. In such a second-generation model, physical processes such as nucleation, condensation, coagulation, cloud-processing, and deposition that determine aerosol size distributions, number concentrations, and CCN concentrations are explicitly simulated. The mechanistic approach gives additional physical insight into the nature of the indirect aerosol effect, permits testing a wide variety of sensitivity scenarios, and may result in more refined estimates of indirect radiative forcing. However, one must also be careful in adding greater physical detail to a global model. In particular, it becomes more important to characterize the strengths and weaknesses of the simulation and test that key quantities, such as CCN concentrations, are realistically reproduced.

Incorporating size-resolved aerosol microphysics into a global model is a challenging task and only recently have efforts been reported. A modal aerosol

microphysical algorithm has been used to predict CCN concentrations and estimate the magnitude of the indirect effect in the MIRAGE model, which is a global chemistry and aerosol model driven by a general circulation model [*Ghan et al.,* 2001ab]. A size-resolved aerosol microphysical algorithm has also been incorporated into the NARCM model [*von Salzen et al.,* 2000]. This model uses 12 size sections covering particle diameters from 0.01 to 41 μm and includes sulfate and sea salt. It has been used to predict CCN concentrations over a portion of the Northern Hemisphere. A drawback is that the model uses a single-moment sectional method that makes it difficult to accurately and efficiently conserve aerosol number concentrations.

This paper describes the incorporation of a two-moment sectional aerosol microphysics algorithm into a global climate model, the Goddard Institute for Space Studies General Circulation Model (GISS GCM II-prime). This provides a mechanistic simulation of global aerosol number concentrations, size distributions, and CCN concentrations. It represents the first implementation of a sectional aerosol microphysics algorithm in a global model. In comparison to previous global studies using MIRAGE, the sectional approach used here allows much greater size resolution, although this model does not yet take into account other significant aerosol types included in that work, such as organic carbon, elemental carbon, and sea salt. In comparison to the NARCM work, the model used here covers the entire globe, albeit with a coarser grid resolution. The NARCM model also includes sea salt, which is absent from this work. The two-moment sectional algorithm used here is also more numerically efficient and accurate and has the additional benefit of exactly and automatically conserving aerosol number concentrations.

The work presented here is limited in scope in that it considers only sulfate. The real atmospheric aerosol is a complicated mixture of many chemical constituents such as sulfate, nitrate, sea-salt, mineral dust, soot, and organic carbon. A difficulty in simulating the microphysical behavior of even one aerosol component is that it is coupled to other aerosol types. For example, the size distribution of sulfate depends on the distributions of other aerosol components that act as CCN via in-cloud chemical production of sulfate. It also depends on the distributions of other aerosol components that present significant amounts of aerosol surface area via condensation of gas-phase sulfuric acid. Therefore, this paper presents only a first, but nontrivial, step in model development towards simulating aerosol microphysics and predicting CCN concentrations in global models. It will be important in the future to extend this work by including other aerosol types. For this reason, we present only a limited comparison of aerosol properties predicted by this model with observations. Our comparisons will necessarily be focused on areas of the atmosphere where sulfate is the primary aerosol component with the goal of examining whether the model can adequately represent qualitative features such as vertical gradients and land-sea contrasts. We will also compare the results of this sulfate-only, size-resolved aerosol simulation with those from a bulk sulfate simulation in the same GCM [*Koch et al.*, 1999] to evaluate how incorporating size-resolved microphysics and deposition influences the model's sulfur cycle.

The following section describes the essential features of the size-resolved microphysical algorithm used for this work. Section 3 discusses how this algorithm has been coupled to the general circulation model. The main results of the model, CN and

CCN concentrations and aerosol size distributions, are presented in Section 4. A number of sensitivity scenarios have also been performed to assess model sensitivity to important uncertainties and to test how various processes control the aerosol size distribution. These are presented in Section 5. Finally, Section 6 discusses comparisons of model predictions with observations before conclusions are presented in Section 7.

4.2. Formulation of Aerosol Microphysics

4.2.1 Two-Moment Sectional Algorithm

To account for the aerosol microphysical processes of coagulation and condensation/evaporation, we use a set of two-moment sectional algorithms [*Tzivion et al.*, 1987, 1989] originally developed for cloud microphysics with appropriate modifications for treating aerosols. Although many sectional, or bin, algorithms exist for treating size-resolved aerosol microphysics, the unique advantage of those we use here is that they track two independent moments of the aerosol size distribution for each size bin or category. The two moments usually selected, which we also adopt in this work, are aerosol number and mass defined as follows,

$$N_k = \int_{x_k}^{x_{k+1}} n_k(x)dx \tag{1}$$

and

$$M_k = \int_{x_k}^{x_{k+1}} x n_k(x) dx \tag{2}$$

where N_k and M_k are the total number and mass of aerosol particles in the k-th size category, $n_k(x)$ is the number of particles with masses between x and $x + dx$, and x_k is the lower boundary of the k-th size category. N_k and M_k are independent prognostic variables in the sense that the ratio of mass to number of a given size bin, or average particle mass in that bin, is allowed to vary in space and time.

It is important here to stress some of the differences between this approach and more common single-moment algorithms. Typically, single-moment algorithms choose aerosol mass as the prognostic variable. For many applications, such as urban and regional air quality, this is the primary aerosol property of concern. In general, these algorithms do not conserve aerosol number concentrations. For estimating and understanding the effects of anthropogenic aerosol on clouds and climate, however, number concentrations are important and one requires an algorithm that conserves aerosol number. This has led to the development of single-moment algorithms that conserve number by shifting aerosol mass between size categories as appropriate [*Russell and Seinfeld,* 1998]. This approach is hampered by the discretization of the aerosol size spectrum implicit in single-moment schemes; the ratio of mass to number in a given size category is fixed to a constant value at all times such that the average particle mass cannot change. As a result, conserving aerosol number in a single-moment scheme is achieved only by sacrificing realism in the aerosol size distribution.

For example, imagine a small amount of gaseous sulfuric acid condensing onto a large number of monodisperse particles such that the growth of any given particle is small compared to the difference between size categories. Realistically, one would expect all the particles to stay within the original size bin, which would gain mass. The unchanged number concentration, however, implies an increase in average particle size for that bin. A single-moment, number-conserving algorithm in which average particle size for each category is fixed cannot accommodate this solution, however. Instead, aerosol number is conserved, in effect, by placing all the condensing mass onto a few particles that hop to the average size of the next size category. While total number concentrations are conserved, the aerosol size distribution is unrealistically distorted. This kind of numerical diffusion is a problem if one wants to predict CCN concentrations as these are a function not just of total aerosol number, but also of their size distribution.

In comparison, a two-moment sectional algorithm has a number of advantages. Physically, such an algorithm has the desirable property of predicting and conserving aerosol number, the important quantity for estimating the indirect aerosol effect. Another advantage is that it is more accurate than single-moment algorithms with the same size resolution [*Tzivion et al.*, 1987] or faster than single-moment algorithms with the higher resolution required to attain similar accuracy. In other words, the additional degree of freedom in a two-moment algorithm make it possible to simultaneously conserve aerosol number and minimize numerical diffusion, whereas single-moment algorithms require a tradeoff between these two goals.

Our application of the two-moment algorithm to the GISS GCM II-prime uses a moving sectional approach in which the boundaries between size bins are defined in terms of dry aerosol mass. The moving sectional approach is advantageous because condensation and evaporation of aerosol water in response to changes in atmospheric relative humidity do not move aerosol between size categories, a process that otherwise results in unwanted numerical diffusion. We use 30 size bins with the lower boundary of the smallest category at 10^{-21} kg dry aerosol mass per particle, close to 0.01 μm dry diameter for a typical aerosol density of 1.8 g cm^{-3}. Each successive boundary has double the mass of the previous such that the upper boundary of the largest category is about 10 μm diameter, or 10 size bins per decade of aerosol diameter.

This is rather high size resolution compared with other global or continental-scale models of aerosol microphysics that either use modal algorithms [*Ghan et al.*, 2001ab] or fewer size bins [*von Salzen et al.*, 2000]. The additional size resolution should be advantageous in the future when coupling the aerosol microphysical simulation to the GCM cloud scheme and predicting the number of activating particles for different supersaturations. Even with the high size resolution, the model runs reasonably fast because of the computational efficiency of the two-moment algorithm, an aerosol microphysics solver that uses adaptive time steps, and the somewhat coarse spatial resolution of the GISS GCM II-prime. The model requires one-hour on a single processor of an SGI Origin 2100 to simulate one day of model time, or two weeks to simulate one year, and further optimization may be possible.

4.2.2 Aerosol Physical Properties

At various times in the model, it is necessary to compute physical properties of the aerosol such as particle size and density. As currently implemented, the model predicts only sulfate concentrations so it is necessary to make an assumption regarding its chemical composition in order to compute physical properties. Although the actual chemical composition of sulfate aerosol varies from unneutralized sulfuric acid to fully neutralized ammonium sulfate in different parts of the atmosphere, for simplicity we assume that all sulfate exists uniformly as ammonium bisulfate, a global average chemical composition [*Adams et al.*, 1999]. Future work will include the ammonia cycle and its effect on aerosol properties. In order to calculate aerosol size, it is necessary to know the amount of water uptake by the sulfate. This has been done offline from the GCM for a range of relative humidity from 1 to 99% using the aerosol thermodynamic equilibrium module, ISORROPIA [*Nenes et al.*, 1998]. We generate a water uptake curve using results from ISORROPIA for ammonium bisulfate at 273 K and use this curve to specify the amount of aerosol water, whenever necessary, for current conditions of relative humidity in a GCM grid cell. The density of the resulting ammonium bisulfate-water mixture is calculated using the measurements of *Tang and Munkelwitz* [1994].

4.2.3 Coagulation

Coagulation of particles in the atmosphere is an important sink of aerosol number and a mechanism by which freshly nucleated particles grow to larger sizes. It is accounted for using the method developed by *Tzivion et al.* [1987]. Details of the derivation are given in that work which we summarize briefly here. The stochastic collection equation (the portion of the aerosol general dynamic equation relating to coagulation) is recast using the definitions of the two moments given in equations (1) and (2), resulting in a set of equations that describe how aerosol number and mass in each size category evolve with time. In doing so, one needs to evaluate several integrals of the aerosol size distribution, $n_k(x)$, of the following form,

$$\int_a^b x^j n_k(x)dx \tag{3}$$

In many cases, a and b correspond to bin boundaries and j is either 0 or 1 such that the integral is simply equal to one of the moments, N_k or M_k. In other cases, j is greater than one and the higher-order moment must be approximated in terms of N_k or M_k to attain closure. For example,

$$\int_{x_k}^{x_{k+1}} x^2 n_k(x)dx = \xi \frac{(M_k)^2}{N_k} \tag{4}$$

where ξ depends on the bin spacing and equals 1.0625 for the mass-doubling used here. Finally, in some cases a does not correspond to the boundary of a size category. In those cases, a linear distribution function is used to approximate $n_k(x)$ over the partial size bin in order to evaluate the integral. The resulting equations for the moments are,

$$\frac{dN_k}{dt} = \frac{1}{2}K_{k-1,k-1}N_{k-1}^2 - K_{k,k}N_k^2 - N_k\sum_{i=k+1}^{I}K_{k,i}N_i + \psi_{k-1}\sum_{i=1}^{k-2}K_{k-1,i}M_i$$
$$-\psi_k\sum_{i=1}^{k-1}K_{k,i}M_i + \frac{\psi_k - f_k}{2x_k}\xi\sum_{i=1}^{k-1}K_{k,i}M_i m_i - \frac{\psi_{k-1} - f_{k-1}}{2x_{k-1}}\xi\sum_{i=1}^{k-2}K_{k-1,i}M_i m_i \quad (5)$$

and

$$\frac{dM_k}{dt} = K_{k-1,k-1}N_{k-1}M_{k-1} - K_{k,k}N_k M_k + N_k\sum_{i=1}^{k-1}K_{k,i}M_i - M_k\sum_{i=k+1}^{I}K_{k,i}N_i$$
$$+\psi_{k-1}x_k\sum_{i=1}^{k-2}K_{k-1,i}M_i - \psi_k x_{k+1}\sum_{i=1}^{k-1}K_{k,i}M_i + \frac{f_{k-1}}{2}\xi\sum_{i=1}^{k-2}K_{k-1,i}M_i m_i - \frac{f_k}{2}\xi\sum_{i=1}^{k-1}K_{k,i}M_i m_i \quad (6)$$
$$+\frac{\psi_k - f_k}{2x_k}\xi^3\sum_{i=1}^{k-1}K_{k,i}M_i m_i^2 - \frac{\psi_{k-1} - f_{k-1}}{2x_{k-1}}\xi^3\sum_{i=1}^{k-2}K_{k-1,i}M_i m_i^2$$

where $K_{j,k}$ is the coagulation coefficient for particles in the j-th bin with particles in the k-th, f_k and ψ_k are parameters that describe the linear approximation to the number distribution that are defined in *Tzivion et al.* [1987], x_k is the lower boundary of the k-th size bin in terms of dry mass, m_k is the average mass of particles in the k-th bin, and I is the total number of size bins.

To calculate the coagulation kernel, $K_{j,k}$, we assume that aerosol particles coagulate via Brownian diffusion and neglect the effects of gravitational settling and

turbulence on coagulation rates. The kernel is recalculated at every grid cell and time step to take into account changes in particle size. We calculate the kernel, $K_{j,k}$, based on the average hydrated particle sizes in bins j and k, neglecting the variation of the kernel with particle size within a given bin.

Diffusivities of aerosol particles much larger than the mean free path of air molecules are calculated from the Stokes-Einstein formula,

$$D_i = \frac{kT}{3\pi\mu D_{pi}} \tag{7}$$

where D_i is the diffusivity of particles in the i-th size bin, k is the Boltzmann constant, T is the temperature, μ is the viscosity of air (corrected for its temperature dependence), and D_{pi} is the average diameter of particles in the i-th size bin. For particles smaller than about 0.1 μm, it is necessary to correct for the non-continuum effects that occur when a particle's diameter is comparable in magnitude to the mean free path of air molecules. We do so using the expression given by *Dahneke* [1983].

Equations (5) and (6) are solved using an adaptive time step where the time step is limited such that the aerosol number or mass concentration in any size category with numerically significant aerosol loading does not decrease by more than 25% or increase by more than an order of magnitude.

4.2.4 Condensation/Evaporation

Condensation of gas-phase sulfuric acid to existing aerosol particles is an important source of sulfate aerosol mass and a means by which small particles grow to CCN size. We use the algorithm, described briefly here, presented by *Tzivion et al.* [1989] to simulate this process. This algorithm uses an analytical solution for the rate of growth of individual particles to compute y_k, the initial mass of a particle before condensation that grows to a mass of x_k, corresponding to the lower boundary of size bin k. The mass and number moments at the end of the condensational time step are then computed from the following conservation equations,

$$N_k(t+\Delta t) = \int_{y_k}^{y_{k+1}} n_k(m,t)dm \tag{8}$$

and

$$M_k(t+\Delta t) = \int_{y_k}^{y_{k+1}} \left[m^{2/3} + \frac{2}{3}\tau \right]^{3/2} n_k(m,t)dm \tag{9}$$

where τ is a parameter that describes the driving force for condensation,

$$\tau = \frac{2\pi DM}{RT} \sqrt[3]{\frac{6}{\pi \rho_k}} F(Kn,\alpha) \int_t^{t+\Delta t} \Delta p(t)dt \tag{10}$$

In the above equation, D is the diffusivity of sulfuric acid in air, M is its molecular weight, R is the ideal gas constant, ρ_k is the density of aerosol in size category k, and F is a correction factor described below. The quantity Δp is the difference between the partial pressure of sulfuric acid and its equilibrium vapor pressure. For sulfuric acid, the equilibrium vapor pressure is assumed to be negligible such that Δp is always positive.

In this case, it is necessary to assume a functional form for n_k, the aerosol number distribution within size category k. For simplicity, a "top hat" function is prescribed in which n_k has a constant value within a given size range. The center of the "top hat" corresponds to the average particle mass in the size bin, the height is chosen to conserve aerosol number, and the width is chosen in such a way as to balance between having an artificially narrow distribution and one that lies too far outside the boundaries of the size category.

The correction factor, F, in equation (10) takes into account non-continuum effects for condensation to small particles as well as the possibility that not all gas-phase sulfuric acid molecules that encounter the surface of a particle stick to that particle. We use the expression proposed by *Dahneke* [1983] in which F is a function of Kn, the Knudsen number and α, the accommodation coefficient. We have chosen a value of 0.65 for the accommodation coefficient of sulfuric acid [*Pöschl et al.,* 1998].

To improve the efficiency of the condensation algorithm, equation (10) is written to take into account the decrease in the partial pressure of sulfuric acid as it condenses onto aerosol. This approach allows longer condensational time steps and faster solution. An analytical solution that describes how Δp changes with time is derived in *Tzivion et*

al. [1989] and used in equation (10). This solution is exact when changes in aerosol mass are negligible and approximate when they are not.

As with the coagulation algorithm, we use an adaptive time step to efficiently solve the equations for condensation. The length of the time step is chosen such that individual particles in any size bin do not grow by more than 10%, the partial pressure of sulfuric acid does not fall below 25% of its original value, and is never longer than 15 min.

4.3. Coupling Aerosol Microphysics to the GCM

The previous section presented a general description of the aerosol microphysical algorithm itself; here we present details regarding its coupling to the GISS GCM II-prime. This description relates to a single model experiment designated, somewhat arbitrarily, as the "base case". A number of sensitivity scenarios have also been realized with the model, and their unique features will be described later.

4.3.1 The GISS General Circulation Model

The aerosol model described here is run online in the GISS GCM II-prime [*Hansen et al.*, 1983; *Rind and Lerner*, 1996]. The version used here has a horizontal resolution of 4 degrees latitude and 5 degrees longitude and nine vertical layers between the surface and the model top at 10 mb. Typically, most of these layers are in the troposphere with only one or two in the stratosphere. The time step for tracer processes

is one hour. Advection of heat, moisture, and chemical tracers are all calculated using a quadratic upstream scheme. Sea surface temperatures are specified based on climatological averages.

The GCM uses two distinct parameterizations to simulate stratiform and convective clouds. Details regarding stratiform clouds are given in *Del Genio et al.* [1996]. This treatment carries liquid water content as a prognostic variable and assumes that stratiform clouds appear in a GCM grid cell once the average relative humidity exceeds 60%. The parameterization of subgrid scale convective clouds predicts the convective mass flux necessary to neutralize the buoyancy instability at cloud base [*Del Genio and Yao*, 1993]. It explicitly includes two updrafts, one entraining and one non-entraining. One third of this upward flux is balanced by a downdraft and the rest by large-scale subsidence. After the one-hour model time step, liquid water in convective clouds either precipitates, evaporates, or detrains from the convective plume to form a persistent stratiform cirrus anvil. That is, convective clouds do not persist from one time step to another.

4.3.2 Sulfur Cycle Model

This study builds upon an earlier sulfate model, without size resolution, described in *Koch et al.* [1999], hereafter referred to as K99. Gas-phase tracers included in the sulfate aerosol model are H_2O_2, DMS, SO_2, and H_2SO_4. In addition, 30 aerosol tracers each for both aerosol sulfate mass and aerosol number concentration are required to represent the moments of each size section in the two-moment microphysics

algorithm described in Section 2. Finally, a single bulk aerosol tracer representing MSA is included as it was in K99. Therefore, the model tracks a total of 65 tracers.

The model was integrated for a total of 25 months of simulation time for the base case and all sensitivity scenarios. All tracer concentrations were initially zero, and the first 13 months were discarded to allow the model to relax from these initial conditions. Unless otherwise noted, all results shown here are annual averages over the remaining 12 months.

Emissions of sulfur to the atmosphere are treated as in K99. Briefly, DMS emissions are specified using the sea-surface DMS concentrations given by *Kettle et al.* [1999] and the sea-to-air transfer function of *Liss and Merlivat* [1986]. Emissions of sulfur dioxide from industrial activity are taken from the 1985 inventory of the Global Emissions Inventory Activity (GEIA) [*Benkovitz et al.*, 1996], from *Spiro et al.* [1992] for biomass burning and noneruptive volcanoes, and from *Baughcum et al.* [1993] for aircraft. The one difference between the emissions used in K99 and those used in the base-case scenario here is that we assume that all anthropogenic sulfur emissions from the GEIA inventory are in the form of sulfur dioxide while K99 assumed that 3% were in the form of sulfate. The effects of particulate emissions will be evaluated in a sensitivity scenario.

The model of sulfur chemistry described in K99 is maintained here. This model includes oxidation of DMS by the hydroxyl radical to form sulfur dioxide and MSA and by the nitrate radical to form sulfur dioxide. Also, reactions of sulfur dioxide with the hydroxyl radical in the gas phase and with hydrogen peroxide in cloud drops are included. An important difference between the model used here and the K99 model is

that a gas-phase sulfuric acid tracer is introduced. Whereas in K99, the gas-phase sulfuric acid produced by the reaction of sulfur dioxide with the hydroxyl radical was assumed to condense immediately to form aerosol sulfate, here we distinguish between particulate and gaseous S(VI). This is necessary to simulate the competition between condensation of sulfuric acid onto existing aerosol particles and nucleation of new particles. Although we do not immediately combine the reaction product with particulate sulfate, the rate of the gas-phase reaction between sulfur dioxide and the hydroxyl radical is the same as in K99. The size distribution of sulfate produced in cloud is described below. At this point, we need only mention that hydrogen peroxide is a prognostic tracer here as it was in K99 such that the model accounts for oxidant limitation. Gas-phase reaction rates are calculated using 3-D fields of hydroxyl and nitrate radical concentrations. Hydroxyl concentrations are five-day averages from C. Spivakovsky (personal communication, 1998) and nitrate radical concentrations are monthly averages from *Wang et al.* [1998a,b,c].

4.3.3 Nucleation

Nucleation of new aerosol particles in the atmosphere from gas-phase precursors was unimportant and entirely neglected in the first-generation of global aerosol models that predicted only bulk aerosol mass. This was possible because new particle formation is a negligibly small pathway for gas-to-particle conversion in terms of aerosol mass. In a second-generation, microphysical aerosol model that predicts size distributions and number concentrations, one expects that nucleation will be an important process.

However, a number of problems complicate any treatment of nucleation in a global aerosol model. First, there are significant uncertainties surrounding both the mechanisms and rates of new particle formation in the atmosphere. While substantial efforts have aimed at understanding binary nucleation in the H_2SO_4-H_2O system [*Doyle,* 1961; *Mirabel and Katz,* 1974; *Heist and Reiss,* 1974; *Jaecker-Voirol and Mirabel,* 1989; *Kulmala and Laaksonen,* 1990; *Laaksonen et al.,* 1995], theoretical estimates [*Coffman and Hegg,* 1995; *Korhonen et al.,* 1999] suggest that, when ammonia also participates in a ternary system, nucleation rates can be orders of magnitude higher. Furthermore, atmospheric measurements [*Clarke et al.,* 1998b; *Kulmala et al.,* 2000] in which nucleation is observed even at sulfuric acid concentrations below those required by a binary nucleation mechanism suggest that ternary nucleation is indeed important in the atmosphere. Other work has suggested that biogenic and anthropogenic organic species [*Marti et al.,* 1997] or ion-ion recombination [*Turco et al.,* 1998] may play a role in new particle formation. Second, even given a particular mechanism of new particle formation and an accurate rate expression for that mechanism, the rate is highly sensitive to variations in temperature, relative humidity, gas-phase precursor concentration, and aerosol surface area.

Treatment of nucleation presents serious problems for global models with their coarse spatial resolution that cannot resolve potentially important subgrid variability in these quantities. For example, nucleation has been observed to occur in regions of cloud outflow where scavenging has reduced aerosol surface area such that sufficiently high concentrations of gas-phase sulfuric acid are allowed to accumulate [*Clarke et al.,* 1998a]. A recent modeling study [*Liu et al.,* 2001] similarly predicted new particle

formation in regions of cloud outflow and also found that the simulated nucleation rate depended strongly on the horizontal and temporal resolution of the model. As another example, a recent study has shown that fluctuations in temperature and vapor pressures resulting from atmospheric waves have the potential to enhance nucleation rates up to five orders of magnitude over those that would be predicted based on large-scale average conditions [*Nilsson et al.*, 2000]. Both of these examples suggest that directly applying expressions for nucleation rates, accurate for a given point in space, to entire GCM grid cells using large-scale average quantities may well be inaccurate. This is because such averaging neglects the effect that important processes have when they produce variability in new particle formation rates on spatial scales that the GCM cannot resolve.

Given the uncertainties and difficulties just discussed, we choose to incorporate a simple treatment of new particle formation in the GISS GCM II-prime and to determine the sensitivity of model behavior in a separate scenario. In this treatment, we allow gas-phase sulfuric acid one model time step (one hour) to condense onto existing aerosol particles. At the end of the time step, the remaining gas-phase sulfuric acid concentration is compared against a critical concentration necessary for significant new particle formation,

$$C_{crit} = 0.16\exp(0.1T - 3.5RH - 27.7) \tag{11}$$

where C_{crit} is the critical sulfuric acid concentration in $\mu g\ m^{-3}$, T is temperature in K, and RH is relative humidity on a scale of 0 to 1. Equation (11) is an empirical fit [*Wexler et al.*, 1994] to nucleation rate calculations [*Jaecker-Voirol and Mirabel,* 1988] using a

new particle formation rate of 1 cm^{-3} s^{-1} as the criterion for rapid nucleation. If the sulfuric acid concentration at the end of the time step exceeds the critical value, the excess mass is assumed to nucleate and the mass and number of the smallest size bin is increased accordingly. Otherwise, no nucleation occurs.

The reader should note that omitting ternary nucleation and subgrid scale pockets of intense nucleation such as can occur in cloud outflow regions will tend to underestimate nucleation rates in the atmosphere rather than overestimate them. Although such a description of new particle formation in the atmosphere is obviously far from perfect, current knowledge does not warrant a more sophisticated treatment. We will examine the sensitivity of model behavior to such uncertainties in a sensitivity scenario with enhanced nucleation.

4.3.4 In-Cloud Sulfur Oxidation

Production of sulfate by the reaction in cloud droplets of sulfur dioxide with hydrogen peroxide is important both because it is the largest source of atmospheric sulfate and because it strongly influences the aerosol size distribution. This occurs as particles activate into cloud droplets, gain solute via in-cloud chemistry, and often evaporate, resulting in particles that are larger than before cloud processing. In this version of the model, we retain the treatment of in-cloud chemistry described in K99. This assumes that the rate of formation of sulfate can be described by a bulk chemistry formulation that depends on the volume of liquid water in the GCM grid cell and the concentrations of dissolved hydrogen peroxide and S(IV). Therefore, any effects on the

rate of sulfate formation stemming from the differing chemical compositions of distinct cloud droplets are neglected in this work.

In the model, sulfate produced by aqueous oxidation of sulfur dioxide is distributed across only those size sections representing particles large enough to activate. We assume that the GCM's stratiform clouds experience a maximum supersaturation of 0.19% such that particles with dry diameters larger than 0.082 μm activate. Similarly, particles larger than 0.033 μm activate in the more vigorous convective clouds, corresponding to a supersaturation of 0.75%. In order to partition the newly produced sulfate across the various activated size sections, we make two assumptions. First, we assume that particles from any given activated size section grow to the same size on average as those from any other size section. Second, we assume that the rate of sulfate production in a given size section is proportional to the volume of cloud water associated with that section. Therefore, we distribute the newly formed sulfate across the activated size sections in proportion to the number of particles in that size section.

To account for the growth of some particles from their initial size bin to a larger size category by cloud processing, we use the same algorithm as described above for condensation/evaporation. In this case, we choose the τ parameter defined above in equation (10) for each size bin such that the sulfate added to that size bin, before accounting for transfer of particles to larger bins, is proportional to the number of particles initially in that category. That is, we calculate τ_j for the j-th size section such that,

$$m_{fj} = \left[m_{ij}^{2/3} + \frac{2}{3}\tau_j \right]^{3/2} \tag{12}$$

where

$$m_{fj} = m_{ij} + \frac{\Delta m}{N_{act}} \tag{13}$$

where m_{ij} is the average mass of a single particle in size section j before cloud processing, m_{fj} is the average mass of a particle in size section j after cloud processing, Δm is the total amount of new sulfate produced in that particular GCM grid cell during the current model time step, and N_{act} is the total number of activated particles in that grid cell.

Although certain aspects of the in-cloud chemistry treatment presented here are crude, in particular the assumptions of a single supersaturation for a given cloud type and bulk cloud chemistry, we feel that this is all that is warranted at the current time. Future work will refine these assumptions as more sophisticated treatments of aerosol activation and cloud microphysics and chemistry are developed for the GISS GCM II-prime.

4.3.5 Size-Resolved Dry Deposition

Dry deposition of gaseous species and the bulk aerosol MSA tracer is calculated as in K99. For size-resolved sulfate mass and number, however, a size-dependent parameterization of dry deposition has been implemented. The scheme uses a version of the resistance in series approach [*Wesely and Hicks,* 1977] developed by *Chin et al.* [1996] and modified as in K99. For aerosols, the resistance in series approach has to be modified slightly to account for gravitational settling of particles [*Seinfeld and Pandis*, 1998],

$$v_d = \frac{1}{r_a + r_b + r_a r_b v_s} + v_s \tag{14}$$

In this expression, v_d is the deposition velocity of a given size bin, v_s is the settling velocity of the size bin, r_a is the aerodynamic resistance that describes the efficiency with which particles are transported from the bulk of the lowest model layer to the quasi-laminar layer near the surface, and r_b is the quasi-laminar layer resistance that describes transport through this layer to the earth's surface. Note that the surface resistance is assumed to be zero for aerosols. The aerodynamic resistance is calculated from GCM surface momentum and heat fluxes as in K99 and has no size dependence. The resistance in the quasi-laminar layer is calculated from,

$$r_b = \frac{1}{u_* \left(Sc^{-2/3} + 10^{-3/St} \right)} \tag{15}$$

where u_* is the friction velocity, a quantity calculated by the GCM surface flux parameterizations, *Sc* is the particle Schmidt number, and *St* is the particle Stokes number. For particles larger than about 1 μm diameter, the Stokes term describing inertial impaction dominates, while Brownian diffusion described by the Schmidt number dominates for particles smaller than 0.1 μm. Between 0.1 μm and 1 μm, neither mechanism is very efficient and deposition velocities are minimal.

Figure 4.1 shows annual-average dry deposition velocities that result from this method as a function of size bin. These are shown with the dry diameter of the size bin on the horizontal axis although the computed deposition velocities in fact depend on the amount of water uptake by the particles at any instant. Moreover, the velocities shown are an average across the earth's surface such that ocean areas, which tend to have low deposition velocities, dominate. Deposition velocities are higher on average over land where most sulfate exists. The deposition velocities exhibit a well-known minimum in the 0.1 to 1 μm diameter size range. As most of the aerosol mass resides in this size range, these low velocities determine the removal of sulfate mass by dry deposition. Note that these tend to be lower than those used in previous model studies that did not take into account the size dependence of deposition velocities. Consequently, dry deposition is much less important as a sink of sulfate mass in this model than in previous studies.

4.3.6 Size-Resolved Wet Deposition

Precipitation removes aerosol from the atmosphere when particles activate to form cloud drops that later precipitate and when falling rain drops impact and scavenge particles below cloud. Removal of aerosol from the atmosphere via wet deposition is treated here in much the same way as in K99. A complete description is given in that work; here it suffices to say that they assume that all aerosol mass in convective plumes is fully dissolved in cloud water via nucleation (in-cloud) scavenging and use a first-order rate loss parameterization to describe this process in stratiform clouds. Subsequently, dissolved aerosol generally mimics the GCM's cloud liquid water in its behavior with a fraction that is removed via wet deposition as precipitation reaches the ground, another fraction evaporating (potentially in a different GCM vertical layer), and some detraining from convective clouds. A first-order removal is also applied to aerosol below precipitating clouds to simulate below-cloud scavenging. Here we have made simple changes to this treatment to account for the size dependence in these processes.

For nucleation scavenging, we assume that only those particles large enough to activate are dissolved in cloud liquid water, using the same activation criteria described earlier in the section on aqueous oxidation. Smaller particles are not affected by wet deposition in the base-case scenario except that they can be carried with convective plumes, downdrafts or subsidence to different vertical layers in the same way that undissolved gases are. The fraction of aerosol that activates and is subject to wet removal accounts for essentially all the aerosol mass, such that sulfate mass concentrations and lifetimes with respect to wet deposition are not significantly different

than in K99. The main effect of this assumption is to exempt a significant fraction of aerosol number in the smallest size bins from wet removal. This treatment of in-cloud scavenging neglects the possibility that inactivated aerosol particles in clouds, so-called interstitial aerosol, may be incorporated in cloud water and removed by wet deposition if they collide with cloud drops. Therefore, we may underestimate removal of smaller, Aitken mode particles in the base-case scenario. This possibility is examined in a sensitivity scenario in which interstitial aerosol is scavenged.

Below precipitating clouds, we use the same first-order removal rate formulation discussed in K99. In that work, aerosol mass was scavenged below cloud with a 0.1 mm^{-1} washout rate constant. Here we use a size-dependent washout rate constant taken from Figure 2 of *Dana and Hales* [1976]. Their Figure 2 shows theoretical washout rate coefficients as a function of aerosol size for both monodisperse and polydisperse aerosol size distributions. As our size bins are fairly narrow, we apply the appropriate rate constant taken from the monodisperse curve to each size bin. These washout rate coefficients were calculated taking into account Brownian diffusion, interception, and inertial impaction and assuming a typical lognormal frontal rain drop size distribution with geometric mean radius of 0.02 cm and geometric standard deviation of 1.86. We use these calculated coefficients for all precipitation, both convective and stratiform.

4.4. Simulated Microphysics of Tropospheric Sulfate

4.4.1 Sulfate Mass

Table 4.1 shows the sulfur budgets calculated with various scenarios of the microphysical model and compares them to the one calculated with K99's model that lacked size-resolution. Except for the bulk dry deposition scenario, each will be discussed in detail in Section 5, so we only briefly summarize them here. The primary emissions scenario assumes that 3% of the GEIA sulfur emissions occur as particulate sulfate with a large number of particles emitted in the 10 to 30 nm diameter size range. In the enhanced nucleation scenario, the critical concentration of sulfuric acid required for new particle formation is lowered by an order of magnitude compared to the base case. Bulk dry deposition applies a uniform dry deposition velocity to particles of any size. In this scenario, the deposition velocity is calculated as in K99 to facilitate comparison with that version of the model. Finally, the pre-industrial scenario excludes anthropogenic sulfur emissions. The base-case, primary emissions, and enhanced nucleation scenarios are collectively referred to as "modern-day scenarios" and serve to illustrate the microphysical impact of primary particles and nucleation.

All of the modern-day budgets, with or without size-resolved aerosol microphysics, are similar. Because the K99 results were compared extensively with observations, this gives us confidence that our simulation of sulfate mass is realistic. The agreement between the various size-resolved simulations in terms of sulfate mass disguise, however, important differences in predicted CN and CCN concentrations that

will be discussed in greater detail below. One minor difference between these results and those from K99 is the somewhat higher wet deposition of sulfur dioxide reported here. This is because K99 counts sulfur dioxide oxidized to sulfate and immediately removed via wet deposition in the same cloud cycle as sulfate deposition whereas it is counted as sulfur dioxide deposition in this work.

A more significant difference is dry deposition of sulfate, with the rates reported here being an order of magnitude lower than those in K99. This can be explained by recalling Figure 4.1, which shows that dry deposition velocities are smallest in the accumulation mode size range where most sulfate mass resides. For reference, the dashed horizontal line shows the average dry deposition velocity used in K99. Running the aerosol microphysical model with the K99 dry deposition parameterization applied to all size sections results in a sulfate budget that agrees with K99 as shown in the "bulk dry deposition" scenario. The slower dry deposition in this work accounts for the higher lifetime and burden of sulfate as well as the increased wet deposition of sulfate, which partly compensates for the slower dry deposition.

A small caveat is that a more realistic size-resolved simulation, one that includes coarse particles such as dust and sea salt and allows sulfate to partition onto those particles, would result in higher average deposition velocities. To the extent that sulfate in the atmosphere partitions onto coarse particles, the current treatment will underestimate dry deposition.

4.4.2 Aerosol Number Concentrations

4.4.2.1 Vertical Profiles. Figure 4.2 shows the vertical profiles of sulfate mass, CN number, and CCN (0.2%) number concentrations at STP conditions (273 K and 1 atm). Results are shown for the base-case, enhanced nucleation, primary emissions, and pre-industrial scenarios. Of the several scenarios realized, these four were chosen for demonstrating important factors influencing aerosol behavior in the global troposphere. Each point in the vertical profile represents the global and annual average for that model layer. The decreasing sulfate concentration with altitude is familiar and is easily explained by the dominance of sulfur dioxide emissions at the surface and aqueous oxidation to produce sulfate in boundary layer clouds. Of the various modern-day scenarios performed as part of this study, we show only the primary emissions scenario as the others differ by less than 10% in terms of sulfate mass.

In contrast to sulfate mass, CN concentrations generally increase with altitude. This vertical profile results from the higher rates of nucleation in the upper troposphere and tropopause region and is consistent with observations. An important caveat is that the magnitude of this trend depends on the details of the nucleation mechanism. It might have been less strong, for example, had we implemented a ternary nucleation mechanism, as the presence of ammonia would have tended to enhance new particle formation primarily in the boundary layer. An important exception to this overall trend is the local maximum in particle concentrations at the surface in the primary emissions scenario. This maximum is also consistent with observations so the primary emissions scenario must be considered the most realistic in this respect.

Number concentrations of CCN, on the other hand, exhibit a decrease with altitude, similar to sulfate mass. The correlation with sulfate mass is not surprising because particles have to be relatively large in order to function as CCN and also because in-cloud production of sulfate, the largest source of sulfate, contributes further to the mass of CCN particles. However, CCN number concentrations differ from sulfate mass concentrations in that they exhibit significant differences from one modern-day scenario to another. These sensitivities to model formulation will be discussed in greater detail below. For now, it is enough to mention that, although CCN number and sulfate mass are correlated, the correlation is not absolute and a given sulfate mass may be consistent with significantly different CCN concentrations. The exact nature of the sulfate-CCN relationship depends, of course, on the details of the aerosol size distribution and varies not just between different model scenarios, but also with space and time in the earth's atmosphere. An aerosol simulation with explicit microphysics, such as the one presented here, allows one to capture and explore this kind of variability in ways that would be difficult or impossible in a model with a fixed, empirical sulfate-CCN relationship.

4.4.2.2 Zonal Averages. Plate 4.1, in which zonal average CN and CCN number concentrations (cm^{-3} at STP conditions of 273 K and 1 atm) are presented, demonstrates some other features of the atmospheric aerosol. For example, strong convection in equatorial regions has significant impacts on aerosol microphysical behavior. In all scenarios, CCN concentrations are significantly depleted in the tropical upper troposphere as convective precipitation removes most of the available CCN. A direct

consequence is the large numbers of CN in roughly the same region, but shifted slightly to higher altitudes. The cold temperatures of the upper troposphere and low aerosol surface areas and high humidity associated with regions of cloud outflow create ideal conditions for new particle formation. This behavior is consistent with the results of models with more detailed cloud dynamics and microphysics [*Zhang et al.,* 1998] and also with observational evidence from recent field campaigns in the eastern Pacific [*Clarke et al.,* 1999].

Contrasts between hemispheres are also evident in Plate 4.1. These are not very pronounced for CN number concentrations with the important exception of the primary emissions scenario. This suggests that new particle formation is somewhat insensitive to gas-phase anthropogenic emissions, but primary particles are significant. On the other hand, strong contrasts between hemispheres in CCN concentrations are evident in all modern-day scenarios. One can conclude that the impact of anthropogenic sulfur dioxide emissions on CCN concentrations is less about forming new particles than contributing extra sulfate mass to a pool of existing particles such that they grow to sizes where they can activate in clouds. In the boundary layer, average Northern Hemisphere CCN concentrations are 275 cm^{-3} compared with 65 cm^{-3} in the Southern Hemisphere.

4.4.2.3 Latitude-Longitude Maps. Plates 2 to 4 present predicted annual average CN and CCN concentrations (cm^{-3} at STP conditions of 273 K and 1 atm) near the surface, in the free troposphere, and in the tropopause region, respectively. One feature of the atmospheric aerosol that is captured is the higher number concentrations over land than over oceans. This can be seen in all the boundary layer results, but is most pronounced

when primary emissions are included. Predicted CN concentrations exceed 10,000 cm^{-3} in the most polluted industrialized regions of the Northern Hemisphere as a consequence of primary emissions. In other scenarios, continental CN concentrations typically fall in the 200-1000 cm^{-3} range. In remote marine areas, predicted CN concentrations are lower, generally 100-200 cm^{-3}. Marine concentrations are higher in some situations, however, such as areas closer to land or in the enhanced nucleation scenario when they exceed 200 cm^{-3}.

Comparing the four scenarios presented in Plate 4.2 suggests some conclusions. First, the contrast between the primary emissions scenario and the others indicates that primary particles make a significant, even dominant, contribution to aerosol number concentrations in the polluted continental boundary layer. A comparison of the base-case and pre-industrial scenarios, on the other hand, shows very little difference. In other words, gas-phase emissions of sulfur dioxide increase particle concentrations in the upper troposphere, where the nucleation process is active, but have little impact on CN concentrations in the boundary layer.

CCN concentrations also tend to be higher over land than over the oceans, a contrast that the model also captures well. Plate 4.2 shows that, over land, CCN (0.2%) concentrations in the primary emission scenario are greater than 100 cm^{-3} nearly everywhere and exceed 1000 cm^{-3} in industrialized areas. Leaving aside the extremes of highly polluted and very remote, annual average CCN (0.2%) concentrations in most continental areas fall in the range of 200-1000 cm^{-3}. The primary emissions scenario, therefore, gives CCN concentrations in good agreement with expected values. The two other modern-day scenarios, on the other hand, predict lower CCN concentrations, from

100-500 cm^{-3}. These are somewhat lower than expected, so the primary emissions scenario seems to be the most realistic in this regard. Similarly, this scenario gives marine CCN (0.2%) concentrations mostly in the 10-200 cm^{-3} range, also in good agreement with expected values. The other modern-day scenarios also have a similarly realistic range of marine CCN concentrations, although they exceed 100 cm^{-3} much less frequently.

Primary emissions, therefore, dramatically impact both CCN and CN concentrations in polluted regions of the boundary layer. Comparing scenarios with and without them clearly indicates that including a source magnitude on the order of 3% of anthropogenic sulfur emissions is necessary to adequately represent continental CN and CCN concentrations. Their impact on marine areas is also noticeable throughout much of the Northern Hemisphere.

In comparison to the modern-day scenarios, the pre-industrial scenario has very low CCN concentrations, typically around 30 cm^{-3} and rarely exceeding 50 cm^{-3}. Important natural aerosols that contribute to CCN concentrations such as sea salt and biogenic organics are not accounted for, however, so this cannot be considered to be a realistic simulation of the pre-industrial atmosphere. Still, the magnitude of the difference in CCN concentrations between pre-industrial and modern-day scenarios suggests that anthropogenic emissions of sulfur have significantly changed CCN concentrations.

4.4.3 Factors Controlling CN and CCN Concentrations

Figure 4.3 shows sources and sinks of aerosol number for three modern-day and one pre-industrial scenario. This plot demonstrates which processes control aerosol number concentrations and lifetimes and serves as a rough estimate of the uncertainties associated with estimated sources and sinks. The values presented in this figure were derived by taking global and annual average source and sink rates and converting to volumetric rates assuming an average tropopause height of 12 km.

The upper part of the figure gives a rough idea of the range of estimated rates for the production or emission of new particles to the atmosphere. The base-case scenario using binary nucleation theory results in an average production rate of about 6×10^{-4} cm^{-3} s^{-1}. The corresponding rate for the sensitivity scenario with enhanced nucleation is higher by a factor of three. Other, equally plausible, parameterizations of nucleation might yield a still larger range of rates. Note that the specified rate implicitly depends on the lower limit of the aerosol size spectrum, 10 nm diameter in this case. If ultrafine particles as small as 3 nm were included in the simulated size range, our reported production rate would be higher.

The primary emissions scenario indicates that primary particles are a source of new aerosol number comparable to, or perhaps substantially larger than, the nucleation source. However, similar uncertainties exist for emissions of primary particles. Our scenario assumed that 3% of anthropogenic sulfur emissions are particulate sulfate. Others have estimated this fraction at 5% [*Eliassen,* 1978; *Langner and Rodhe,* 1991]. It appears that this fraction has only been estimated with enough precision to verify that

it makes a small contribution to sulfate mass concentrations. One or two percent by mass of anthropogenic sulfur emissions, however, represents a significant uncertainty in the number of emitted particles.

These estimates would, of course, be different in a more comprehensive model that included other aerosol types. Including primary emissions of black carbon, sea salt, and mineral dust would tend to suppress nucleation in the atmosphere, but the emissions of these species are also less well quantified than sulfate. The budget of aerosol number is, therefore, largely unconstrained, and future experimental, field, and modeling studies should seek to better understand and quantify these processes.

Sinks of aerosol number show a similar range of magnitudes across the various scenarios, as they must if they are to balance the source terms. Wet and dry deposition of particles are relatively unimportant sinks in terms of aerosol number. By far the dominant sink globally for particle number is coagulation. Because its rate depends on the square of aerosol number, coagulation acts as a powerful control against large fluctuations in number concentrations. Consequently, even the threefold increase in nucleation between the base-case and the enhanced nucleation scenario results only in a twofold increase in average CN concentrations. Another example of how coagulation influences aerosol number concentrations can be seen by comparing the enhanced nucleation scenario with the primary emissions scenario. Although they have the same source magnitude to within 25%, the resulting average CN concentrations differ by a bit more than 65%. In the primary emissions scenario, the particle source is concentrated in the polluted boundary layer, and coagulation efficiently scavenges particles resulting in the low particle lifetime. The enhanced nucleation source, in contrast, is spread more

diffusely throughout the upper troposphere such that coagulation is less efficient and the particle lifetime longer.

In the base-case scenario, the average CN concentration is approximately 500 cm^{-3}, with a lifetime of around 10 days. For the modern-day scenarios with higher source terms, higher concentrations result. The nonlinearity inherent in the process of coagulation explains the shorter lifetimes in these scenarios. In comparison, it is interesting to note that the lifetime of sulfate mass is 6.5 days for each of the three modern-day scenarios shown in Figure 4.3. The lifetime of individual aerosol particles, however, varies from 5 to 10 days in the various scenarios. That is, the lifetime of aerosol number can be higher or lower than that of aerosol mass, depending on whether condensation or coagulation dominates.

The base-case scenario may be taken as an example of a situation in which condensation dominates and the lifetime of aerosol number is higher than for aerosol mass. An idealized particle trajectory in this scenario might go something like this. A particle is formed in the upper troposphere during a nucleation event and grows by condensation of sulfuric acid. Particle concentrations are relatively low and coagulation is unimportant, such that the particle floats around the free troposphere, maintaining a small size of 10-40 nm diameter. Eventually, after several days, the particle grows to sufficiently large size to activate and is entrained into the boundary layer. It now grows principally by in-cloud oxidation of sulfur dioxide to a much larger size, 0.2-0.4 μm, before being removed from the atmosphere by wet deposition after 6 days or so. In this condensation-dominated case, the particle had a lifetime of around 10 days while most of the sulfate mass had a shorter lifetime of around 6 days. Conversely, the primary

emissions scenario exemplifies a situation in which coagulation determines the particle lifetime. In this case, a primary particle is emitted in a polluted region with high number concentrations such that it coagulates with another after a couple of days. The mass associated with that particle, however, persists in the atmosphere for several more days.

The preceding discussion of the aerosol number budget applies to CN number concentrations and is, in fact, dominated by the behavior of particles 10 to 30 nm in size. One is also interested, of course, in the factors that control CCN number concentrations. The dominant source of particles large enough to serve as CCN is condensation of gas-phase sulfuric acid onto smaller particles until they grow to sizes that can activate in clouds. This mechanism is effective in the 30 to 100 nm diameter size range. In-cloud oxidation, on the other hand, is the dominant mechanism by which particles grow larger than 100 nm in size.

In strong contrast to the results presented above for CN number, the main sink for particles larger than 30 nm is wet deposition. Between 30 and 100 nm, both wet deposition and coagulation are of roughly equal importance as sinks of particle number. Above 100 nm, coagulation is not a significant source or sink of particles. Although particles do grow to a certain extent by coagulation, it is not an important source of CCN number. This is because the large numbers of ultrafine particles lost by coagulation tend to coagulate with much larger particles with diameters between 0.2 and 0.6 μm. These particles are already large enough to activate even with very low supersaturations. Moreover, the additional mass these larger, accumulation mode particles gain by scavenging Aitken-mode particles from the atmosphere is small compared to what they gain through aqueous oxidation of sulfur dioxide.

In summary, the picture of aerosol microphysics that emerges from this simulation is already familiar. Ultrafine particles are produced in the atmosphere by nucleation. Most are scavenged by coagulating with accumulation mode particles, but a few survive and grow by gas-phase condensation to CCN size. Subsequently, cloud processing is the dominant growth mechanism such that they hardly notice the mass they gain by coagulation with the smaller particles. Finally, CCN are removed mostly by wet deposition.

4.4.4 Size distributions

In this section we present and describe simulated number size distributions for different regions of the atmosphere. As a first step in model evaluation, we compare our results with typical lognormal distributions suggested by *Jaenicke* [1993]. Here we focus on results from the primary emissions scenario as these are considered to be the most realistic. More detailed comparisons with individual observations are described in Section 6.

4.4.4.1 Marine Size Distribution. Figure 4.4a shows the annual average aerosol number distribution in the remote South Pacific (180° W to 120° W and 60° S to 0° S). The model reproduces the bimodal nature of the marine aerosol size distribution. As explained by *Hoppel et al.* [1985, 1986], the two modes correspond to a smaller, inactivated "nuclei" mode and a larger accumulation mode of CCN particles. The gap between the modes results from cloud processing. An important feature of the marine

aerosol that is missing here is a coarse mode of sea salt particles. Future work will focus on adding sea salt and other types of aerosol to the model. The total number of particles predicted by the model, 190 cm^{-3}, is in good agreement with Jaenicke's typical value of 200 cm^{-3}. Including sea salt would increase the value by 5 to 30 cm^{-3}.

The predicted location of the smaller mode from the model, 46 nm, does not match Jaenicke's value of 8 nm well at all. The 8 nm diameter Jaenicke reports is, in fact, surprisingly small. *Fitzgerald* [1991] has also reviewed and summarized observed marine aerosol size distributions. The half dozen size distributions shown in that work all show a bimodal distribution with peaks at 0.03 and 0.15 μm, very similar to the predictions shown in Figure 4.4a. The predicted size of the larger mode, 0.13 μm, is also in better agreement with Jaenicke's value of 0.266 μm. Although our accumulation mode particles are a little small in comparison, it is worth noting that our DMS emissions, 10.8 Tg S yr^{-1}, are towards the low end of the range used in global models. Higher DMS emissions would tend to result in larger particles. Moreover, the data in *Fitzgerald* [1991] show that, in the Southern Hemisphere, there are fewer particles in the larger mode while the two modes are of roughly equal size in the Northern Hemisphere. Although not shown here, examining the model's predicted size distributions in corresponding marine areas shows that it reproduces this trend.

4.4.4.2 Remote Continental Size Distribution. The model does not simulate the size distribution of aerosol in remote continental areas as well as it does in marine areas. The predicted remote continental size distribution presented in Figure 4.4a is an average over the Amazon region (75° W to 50° W and 16° S to 8° N). In this region, secondary

organic aerosol is an important aerosol type not included in this model. Although the predicted locations of the modes, 0.037 and 0.1 μm, are not very different than Jaenicke's values of 0.02 and 0.116 μm, the predicted particle concentration of 630 cm^{-3} is much lower than the 6000 cm^{-3} reported there. Part of the discrepancy may result from not including organic aerosols in this first version of the model. Also, the Amazon is the continental area in which the model predicts the lowest number concentrations. Other remote continental areas have particle concentrations as high as 2000 cm^{-3}, for example in Siberia, although these are still not high enough to fully reconcile the discrepancy. A more detailed investigation of model behavior in remote continental areas must await a more comprehensive model.

4.4.4.3 Polluted Continental Size Distribution. Figure 4.4b shows size distributions from three polluted continental regions: North America (100° W to 70° W and 28° N to 48° N), Europe (0° E to 25° E and 40° N to 56° N), and East Asia (105° E to 145° E and 24° N to 48° N). In this case, we compare against Jaenicke's "rural" size distributions rather than the "urban" ones because the coarse horizontal resolution of a global model makes it impossible to resolve truly urban areas. Once again, the model produces a bimodal aerosol size distribution. The smaller mode, at 0.015 μm, coincides with Jaenicke's. However, the size of the larger mode, 0.12 to 0.15 μm, depending on which of the three industrialized regions one chooses, is slightly large in comparison with the 0.084 μm from Jaenicke. In the model, particle concentrations in polluted areas range from an average of 6600 cm^{-3} in East Asia up to 15,000 cm^{-3} in Europe, with North

America intermediate at 9000 cm^{-3}. Jaenicke's lognormal parameters result in a total number concentration of about 9000 cm^{-3}, so the model seems to be performing well in this regard. Qualitatively, the model correctly places the majority of the particles in the smaller mode, but in fact underestimates the number in the larger mode. Primary emissions play a dominant role here, and the crude assumptions made here regarding the number and size distributions of primary particles are a likely source of this discrepancy. Another likely possibility is that these results are for sulfate only. Including the contribution of other aerosol types to aerosol mass would tend to shift some of the smaller particles up to larger sizes.

4.4.4.4 Free Tropospheric Size Distribution. We compare the free tropospheric size distributions from the model presented in Figure 4.4c with the corresponding "background" size distributions from *Jaenicke* [1993]. The size distributions shown in the figure are global averages over individual model layers. The model predicts, in agreement with observational evidence shown later, a strong vertical concentration gradient in the free troposphere, so we show results at 634, 468, and 321 mb. Whereas Jaenicke's parameters give two distinct modes in the free troposphere, we predict only one broad mode. The difference is that Jaenicke's bimodal aerosol shows evidence of cloud processing that seems to be lacking in our data. It may be that the observed air masses, mostly from mountain tops and in subsiding air, upon which Jaenicke based these parameters, are, in fact, subject to more cloud processing than the free troposphere as a whole. Predicted number concentrations (250 cm^{-3}, ambient conditions) agree well with Jaenicke's assessment.

4.4.4.5 Upper Tropospheric Size Distribution. Finally, we present an average upper tropospheric size distribution taken as a global average of the 201 mb model layer. Jaenicke does not give parameters for this part of the atmosphere so no comparison is possible. Looking at Figure 4.4c, it can be seen that the size distribution is heavily skewed towards small particles in the 10 to 20 nm size range. This is the area of the atmosphere in which nucleation is most active, at least as parameterized in this model, and this process has a dominant effect on the size distribution. Sulfur dioxide concentrations are low in the upper troposphere, so these freshly nucleated particles have little opportunity to grow to larger sizes. Moreover, larger particles are not likely to be carried aloft by deep convection as they serve as the nuclei for cloud droplets and tend to be removed by precipitation.

4.4.5 Seasonal Cycles

Figure 4.5 shows the predicted seasonal cycles in Northern Hemisphere average sulfate burden, CN and CCN (0.2%) number concentrations. The hemispheric sulfate burden peaks during summer months, a well-known phenomenon driven not by higher emissions, but by higher oxidant concentrations. Looking at CN and CCN (0.2%) concentrations, summer maxima are also observed, although the magnitude of the cycle in CN concentrations is markedly less pronounced than for CCN or sulfate. The CN cycle also results from higher summertime oxidant concentrations and the CCN cycle may be considered a result of the other two. The fact that sulfate mass varies by more

than CN concentrations implies a larger average particle size in the summer than winter. Looking at the size distributions, one notes that this occurs not by a shift in the size of the location of the Aitken or accumulation mode, but by a transfer of particles from one mode to the other.

4.5. Sensitivity Scenarios

4.5.1 Enhanced Nucleation

Earlier, we discussed the difficulties inherent in trying to represent new particle formation in a global aerosol microphysical model. The simplified approach we took in our base-case simulation is a logical starting point, namely binary nucleation of sulfuric acid and water, but may underestimate new particle formation rates. Here we determine the sensitivity of the microphysical simulation to an increase in nucleation. This is accomplished by reducing the critical concentration of sulfuric acid required for nucleation from equation (11) by a factor of ten. Physically, this can be interpreted as a simple way to simulate enhanced rates of nucleation that may result from a ternary nucleation mechanism in which ammonia participates [*Coffman and Hegg,* 1995; *Korhonen et al.,* 1999] or from the nonlinear dependence of nucleation rates on subgrid scale variability in sulfuric acid production, aerosol surface area, temperature, and relative humidity. Indeed, nucleation bursts have been observed to occur in the atmosphere when sulfuric acid concentrations were approximately an order of magnitude below the critical concentration predicted from binary theory [*Clarke et al.,*

1998b], so the order of magnitude reduction we employ here is plausible based on observations.

First, it is worth noting that the change in the nucleation parameterization has a negligible effect on the tropospheric sulfate budget, not surprising because nucleation is not a significant gas-to-particle conversion pathway in terms of mass. Only at the tropopause, where sulfate concentrations are low and nucleation rates high, does the change in nucleation parameterization noticeably affect sulfate concentrations. Even here, it does so only by 5-10%.

The changes in the budget of aerosol number are significant, however, and illustrate the robustness of atmospheric aerosol number concentrations with respect to nucleation. For example, an order of magnitude change in the critical concentration required for nucleation results in a three-fold increase in average nucleation rates. This, in turn, results in CN concentrations that are a factor of two higher, and CCN (0.2%) concentrations generally increase by only 10-35% depending on which part of the atmosphere one examines. There are at least two reasons for this chain of diminishing impacts from nucleation to CCN concentrations. One is the, already noted, nature of the coagulation process that, being second order in number concentrations, tends to dampen any attempt to disturb them. Another is that it takes a substantial amount of sulfate mass for a particle to grow to CCN size, such that the fixed emissions of sulfur serve to limit the number of nucleated particles that can grow this large.

Given the uncertainties associated with atmospheric nucleation, it is comforting that predicted CCN concentrations are relatively insensitive to the exact details of this process. One should resist, however, the temptation to ignore such uncertainties

entirely. In this sensitivity scenario, CCN (0.2%) concentrations increase approximately 35% on average in the boundary layer, an increase that is certainly large enough to have a significant impact on accompanying simulations of cloud microphysics and albedo. In the free troposphere, CCN (0.2%) concentrations increase by 10-20%.

Given the noticeable impacts the enhancement in nucleation rates has on model behavior, especially with respect to CN concentrations in the upper troposphere, a natural question is whether such changes are realistic or not. In a later section, we will show that observations of CN in the upper troposphere agree better with the results from the base-case scenario than with those from this sensitivity scenario. Given the difficulties associated with simulating nucleation in a global model, it is somewhat surprising that the simple approach adopted in the base case gives realistic results. A caveat is that predicted aerosol number distributions in the marine boundary layer, although less sensitive to nucleation than upper tropospheric CN concentrations, tend to be more realistic with the enhanced nucleation rate. This suggests that a ternary nucleation mechanism might give the best results because taking into account ammonia would tend to enhance nucleation more in the boundary layer and less in the upper troposphere.

4.5.2 Primary Emissions from Fossil Fuel Combustion

The first generation of global sulfate mass simulations did not emphasize including a realistic treatment of primary sulfate aerosol emissions. Previous global model studies of sulfate have estimated the fraction of anthropogenic sulfur emitted in

the form of sulfate at 3-5% or neglected it entirely [*Langner and Rodhe,* 1991; *Pham et al.,* 1995; *Chin et al.,* 1996; *Koch et al.,* 1999]. Greater sophistication or precision was unnecessary for calculating sulfate mass loadings as the anthropogenic contribution to sulfate mass is overwhelmingly through emissions of gas-phase sulfur dioxide and subsequent oxidation in the atmosphere to form aerosol sulfate. Although primary emissions of sulfate do not contribute significantly to sulfate mass loadings, this is not necessarily true of aerosol number. If primary emissions are a significant source of new atmospheric particles, it follows that second generation aerosol microphysical models that predict number concentrations need to take better account of such emissions. Here we describe results of a sensitivity scenario in which primary sulfate emissions from fossil fuel combustion are included to determine their contribution to aerosol number concentrations.

The subgrid scale plume immediately downwind of a power plant stack has unique chemistry on shorter length scales than can be resolved with the coarse horizontal resolution of climate models. Therefore, we use emissions estimates that represent the air some tens of kilometers downwind of a stack that begins to mix with the larger environment rather than estimates of emissions at the exit of the stack itself. Note that the only primary sulfate emissions included in this scenario are those from anthropogenic combustion of fossil fuels. Primary emissions from biomass burning and aircraft are not considered in this scenario, although primary emissions from aircraft will be examined in another. As in K99, we assume here that 3% of anthropogenic sulfur emissions from the GEIA inventory [*Benkovitz et al.,* 1996] occur as aerosol sulfate. Similar to the approach used in regional models [*Binkowski and Shankar,* 1995] and

based on the work of *Whitby* [1978], we divide the primary emissions into a nuclei and an accumulation mode. Fifteen percent of the emissions by mass are assumed to occur in the nuclei mode and the balance in the accumulation mode. Emissions rates into individual size sections are based on the lognormal parameters reported by *Whitby* [1978]. These are geometric mean diameters of 10 and 70 nm and standard deviations of 1.6 and 2.0, respectively.

As expected, primary sulfate emissions have a negligible impact on the sulfur mass budget. Compared with the base-case scenario, the annual average sulfur dioxide burden decreases and the sulfate burden increases by about 3%. More interesting is the effect that primary emissions have on the budget of aerosol number. Given the mass of sulfur emitted as primary sulfate and the assumed size distribution of those emissions, the global source of primary sulfate particles from anthropogenic fossil fuel emissions is approximately twice as large as the nucleation source in the base-case scenario. This confirms that primary emissions are a significant source of new particles to the atmosphere.

It is interesting to note that, even with this additional source of particles, the global and annual average nucleation rate in this scenario is only 20% lower than that estimated for the base case. Nucleation continues to occur in the free and upper troposphere more or less at the same rate despite the large source of primary particles, which are mostly confined to the boundary layer. Because primary emissions are mostly confined to the boundary layer, both dry and wet deposition increase substantially, but loss of particle number via coagulation is still the dominant sink. In fact, the average coagulation rate increases by a factor of two and a half, more than one would expect

based on the more modest increase in average number concentrations. This can be explained by recalling that that the coagulation rate is proportional to the number concentration squared and that the increase in number concentrations is highly localized in the polluted continental boundary layer where primary emissions have raised CN concentrations by more than an order of magnitude.

Overall, the global average increase in CN concentrations resulting from primary emissions is only 20%, although this global average hides the enormous increase in the most polluted regions of the atmosphere. It is interesting to compare the average CN concentrations of the primary emissions and enhanced nucleation scenarios. Although both have roughly the same total source rate of new particles to the atmosphere, the average number concentrations are much higher in the enhanced nucleation scenario. This is because the nucleation source is much more dispersed than are primary emissions, implying that coagulation will be more effective in the primary emissions scenario. The shorter average lifetime of particles in the primary emissions scenario demonstrates this.

It is clear from Figure 4.2 and Plate 4.2 and not at all surprising that the increased CN concentrations from primary emissions are highly localized in the polluted boundary layer. Figure 4.2 also shows some impact in the lower portion of the free troposphere, but this region is not as sensitive to primary emissions as it is to the nucleation source. Primary emissions result in CN concentrations in excess of 5000 cm^{-3} in industrialized regions when they were only 200-500 cm^{-3} without them.

More surprising is the sensitivity of CCN concentrations to primary emissions. Compared with the base case, CCN (0.2%) concentrations are approximately double in

the boundary layer and 30-50% higher in the free troposphere (see Figure 4.2). This is not so much a result of the few particles that are emitted already large enough to act as CCN as the ability of the increased numbers of CN emitted in polluted conditions to grow to the CCN size range. Although the fixed mass of sulfur emissions, in principle, limits the number of CN that can grow to CCN sizes, there is sufficient excess gas-phase sulfur that this turns out to not be limiting. The average particle size of the CCN mode is, in fact, smaller in the primary emissions scenario than in the base case, but still large enough to function as CCN.

Although it is not useful to do a detailed comparison to observations in the polluted boundary layer with an aerosol model that includes only sulfate, a quick check of predicted CN concentrations against observations is enough to indicate that the results from the primary emissions scenario are more realistic. This sensitivity scenario has shown that primary particles, besides making the dominant contribution to CN number in the polluted boundary layer, can significantly enhance CCN concentrations. This result suggests that better emissions inventories of primary particles are needed. First-generation sulfate models can adequately predict sulfate mass concentrations with only crude estimates of sulfate emissions, but the sensitivities of CN and CCN concentrations demonstrated here indicate that these are no longer sufficient. Although this sensitivity scenario considers only primary particles from anthropogenic fossil fuel combustion, one can assume that the same lessons apply to primary emissions from biomass burning and other sources.

4.5.3 Primary Emissions from Aircraft

Another sensitivity scenario performed during this study examines the impact of particles emitted by, or produced in the near wake of, aircraft. Although the number of particles emitted by aircraft is much smaller than the number emitted by fossil fuel combustion, we test the hypothesis that their location in the upper troposphere gives them a disproportionate impact.

Primary particles emitted by aircraft are, in fact, predominantly composed of black carbon, not sulfate [*Brasseur et al.,* 1998; *Petzold and Schröder,* 1998; *Petzold et al.,* 1999]. It seems likely, however, that some of the sulfur dioxide emitted by the aircraft is oxidized within the subgrid scale plume such that these particles are coated with sulfate by the time they mix with the surrounding air [*Brasseur et al.,* 1998; *Brown et al.,* 1996; *Schumann et al.,* 1996], although the precise amount of the sulfur dioxide that gets oxidized is uncertain [*Fahey et al.,* 1995; *Petzold and Schröder,* 1998]. In this study, we are more concerned with the contribution of these particles to tropospheric number concentrations than their chemical composition so, for simplicity, we treat them as being composed entirely of sulfate.

For an estimate of total sulfur emitted as well as the spatial distribution of those emissions, we use the same inventory for aircraft as was used in K99 [*Baughcum et al.,* 1993] and that was also used in the base-case scenario. In the base case, all aircraft sulfur was emitted as sulfur dioxide. In this sensitivity scenario, we assume that 50% of aircraft sulfur is emitted as sulfate. This is on the high end of estimates for the conversion of fuel sulfur to sulfate within the plume of the aircraft, but was chosen

because it represents a more realistic estimate of the number of particles, principally soot, emitted by aircraft. Even so, this amounts to approximately 3 x 10^{15} particles per kilogram of fuel burned, on the low end of the estimated range. Particle emissions from jet aircraft could be an order of magnitude higher. We assume a lognormal size distribution of the primary particles with a geometric mean diameter of 45 nm and geometric standard deviation of 1.5, values that are representative of the size distribution of soot emitted by aircraft [*Petzold and Schröder;* 1998].

Changing a fraction of aircraft sulfur dioxide emissions to particulate sulfate has a negligible effect on simulated sulfate mass concentrations, a result also obtained by *Kjellstrom et al.* [1999]. In terms of the global budget of aerosol particles, primary emissions from aircraft are also small. For these emissions estimates, primary particles amount to less than 1% of the nucleation source, not to mention a source of primary particles from the surface of similar magnitude. Higher, but still realistic, emissions estimates would give a source that is less than 10% of the nucleation source. Changes in CN and CCN (0.2%) concentrations are also small, less than 1% in layer averages even for the free troposphere and upper troposphere. In fact, CN concentrations actually decrease slightly when primary emissions from aircraft are included. The reason for this is that, for the size distribution of emissions assumed here, there are enough larger particles to suppress nucleation slightly. Recent work on the impact of aircraft on upper tropospheric CN concentrations estimated that primary particles from aircraft increase concentrations by 6% [*Anderson et al.,* 1999]. *Anderson et al.* [1999] used a much higher emissions index (5 x 10^{16} particles emitted per kg aircraft fuel) and did not take into account potential microphysical feedbacks, such as the suppression of nucleation by

larger particles. The estimated impact would be lower had they taken this feedback into account. Our work suggests that primary emission from aircraft have only a very small impact on the global scale.

4.5.4 In-Cloud Scavenging of Interstitial Aerosol

In the base-case scenario, we made the simple assumption that interstitial aerosol particles, those not large enough to activate in clouds, were not subject to in-cloud scavenging. These smaller particles were subject to only a small amount of wet deposition via below-cloud scavenging by falling rain drops. In reality, some fraction of the interstitial aerosol will collide and coalesce with cloud drops and be removed by wet deposition.

Without resorting to detailed simulation of microphysical processes in clouds, a simple scenario tests the sensitivity of the model to assumptions about the scavenging of interstitial aerosol particles. In this scenario, we assume that all such particles are fully incorporated into cloud drops and subject to the same wet deposition processes as the activated particles. The true behavior of the atmosphere lies somewhere between the two extreme assumptions of no scavenging (base case) and complete scavenging (this scenario), but this comparison allows us to bound the range of feasible behaviors.

This sensitivity scenario predicts concentrations of sulfate mass that are nearly identical to those predicted in the base-case scenario, a result of the fact that interstitial aerosol particles, being small in size, do not account for much of the total sulfate mass. CN number concentrations decrease by 10-20% on average in the boundary layer, but

increase by a few percent in the free troposphere such that the global average is nearly unchanged. This is because scavenging the interstitial aerosol leads to an increase in new particle formation. The absolute increase in nucleation rates is largest in the upper troposphere. The relative increase is greatest in the surface layer, but this is not terribly important because the model predicts little new particle formation there to begin with. Wet deposition of CN particles increases by about 50% such that particle lifetime is decreased from 10.3 days to 9.3 days. Overall, the impact on CN concentrations is small because increased rates of new particle formation largely compensate for faster removal rates. Concentrations of CCN (0.2%) decrease by about 10% throughout most of the troposphere. In summary, the two extreme assumptions made regarding in-cloud scavenging of interstitial aerosol result in CN and CCN concentrations that differ by 10% or less in most areas. Therefore, it is not necessary to incorporate detailed simulations of this process in global models.

4.5.5 Pre-industrial Atmosphere

The final model scenario represents a first approximation of aerosol microphysics in the pre-industrial atmosphere. The motivation is, of course, to make a preliminary assessment of the impact of anthropogenic sulfur emissions on CN and, more especially, CCN concentrations, the key quantity needed to estimate the magnitude of the indirect aerosol effect. We use the same assumptions regarding sulfur emissions to the pre-industrial atmosphere as in K99 and *Adams et al.* [2001]: no anthropogenic sulfur emissions, DMS and volcanic sulfur dioxide emissions that are the same as the

modern-day scenarios, and biomass burning sulfur dioxide emissions that are 10% of their modern-day values. The lack of important natural aerosol types such as sea salt, biogenic organics, and dust, combined with the relatively low DMS emissions will tend to underestimate pre-industrial aerosol concentrations and, consequently, overestimate anthropogenic impacts. Even so, the scenario provides a useful, albeit preliminary, benchmark against which to compare modern-day aerosol levels.

Pre-industrial sulfate concentrations resulting from this set of emissions assumptions have been presented before in K99. We will not discuss them except to note that the estimated modern-day sulfate burden, 0.77 Tg S, is five times the pre-industrial, 0.15 Tg S. The vertical profile of average pre-industrial sulfate concentrations is shown in Figure 4.2a. The comparison between pre-industrial and modern-day scenarios depends on whether one compares against the modern-day scenario with or without primary sulfate emissions. We have already discussed the impact of primary emissions above, so here we focus on a comparison with the base-case scenario without primary emissions in order to discuss the impact of anthropogenic emissions of gas-phase sulfur dioxide. Figure 4.3 shows that CN concentrations are 20% higher in the modern-day scenario than in the pre-industrial, a result of a 65% increase in nucleation. These results suggest that anthropogenic sulfur dioxide emissions do, in fact, lead to new particle formation. Increased coagulation results in a shorter lifetime in the modern-day scenario, 10 days as opposed to 14 days, compensating somewhat for the increased nucleation. In fact, the increased CN concentrations are most evident in the upper troposphere where they are as high as 25%. How much impact this would have on boundary layer aerosols and clouds is

questionable, however, because CN number concentrations are only 5% higher by the time they work their way down to this altitude. Looking at CCN (0.2%) concentrations, on the other hand, shows more clear evidence for the potential of sulfur dioxide emissions to contribute to CCN. CCN (0.2%) concentrations are approximately two and a half times higher in the base-case scenario than in the pre-industrial. So, although sulfur dioxide emissions increase CN concentrations, they are more effective at increasing CCN concentrations simply by contributing extra mass to existing particles such that they grow to CCN size.

4.6. Comparison with Observations

Although we have made some preliminary assessments of model performance in Section 4, here we present and discuss more detailed comparisons with observational data. Assessing the performance of a detailed model of aerosol microphysics in a GCM is challenging for a number of reasons. First, because the GCM produces its own meteorology, it does not reproduce the weather conditions of any particular time period when observations have been made. The ideal comparison would be against a long-term, climatological data set that averages over the various meteorological regimes that influence aerosol behavior. Unfortunately, such data are rare. Although detailed observations of aerosol composition and size distributions do exist, they tend to be from field campaigns lasting several weeks, not a sufficiently long period to be considered climatological. On the other hand, long-term, multi-year observations are often filter pack measurements that give no information about size distributions and number

concentrations. A second difficulty is that we have included only aerosol sulfate in the current study. Therefore, we will focus on observations in regions where sulfate is a significant constituent of the aerosol.

4.6.1 Marine Boundary Layer

One such region is the marine boundary layer. It has already been mentioned that the model lacks the dominant contribution that sea salt makes to aerosol mass above 0.6 μm diameter. Total aerosol number concentrations and the aerosol size distribution below 0.6 μm, however, are dominated by non-sea salt sulfate so it is valid to test whether the model can reproduce these features.

Over the last decade, ships have extensively sampled aerosol number concentrations and other properties over large regions of the Pacific Ocean as part of the MAGE92, RITS93, RITS94, and ACE1 field campaigns [*Quinn et al.,* 1995; *Covert et al.,* 1996; *Bates et al.,* 1998]. Here we focus on CN12 (particles larger than 12 nm diameter) concentrations measured with a condensation particle counter during portions of the cruises over the central Pacific Ocean (155° W to 130° W and 32° S to 20° N). Taken together, these data represent approximately six months of total sampling time covering all months of the year except June through September over a period of four calendar years from 1992 to 1995. To remove some of the variability evident on short temporal and spatial scales, the data were binned into four-degree latitudinal bands corresponding to the GCM's latitudinal resolution.

Average CN12 concentrations for the latitudinal bins mostly fall into a range between 200 and 400 cm^{-3} with an average of 325 cm^{-3}. Somewhat surprisingly, the data do not show any clear latitudinal gradient. The annual and regional average CN12 concentration from the base-case scenario is 190 cm^{-3}. Looking within the region, some grid cells predict annual average CN12 concentrations below 150 cm^{-3}, while most were in a range between 150 and 250 cm^{-3}. The base-case scenario, therefore, produces CN12 concentrations that are mostly within the range of observations but are too low on average. Even assuming an additional 30 cm^{-3} of sea salt particles would be insufficient to close the gap. On average, CN12 concentrations from the primary emissions scenario were 215 cm^{-3}. Primary particles, therefore, have a small, but not entirely negligible, effect on CN12 concentrations even in this remote marine region. They too, however, are insufficient to explain the tendency of the model to under-predict marine number concentrations. The enhanced nucleation scenario, on the other hand, shows much higher marine CN12 concentrations with an average of 420 cm^{-3}, now an overprediction of the number of particles. This occurs despite the fact that most of the nucleation in this scenario, as in the base-case scenario, occurs in the upper troposphere, not the marine boundary layer.

In summary, the model reasonably represents CN concentrations in the marine boundary layer. Including primary emissions from industrialized areas and assuming 30 cm^{-3} of sea salt particles, predicted CN12 concentrations are in the range of observed values, but tend to be too low by about 25%. A sensitivity scenario with enhanced nucleation indicates that the discrepancy may result from a slight underprediction in the rate of nucleation, although the nucleation rate in that scenario is almost certainly too

high. Alternatively, the GCM may be underestimating subsidence of air with higher particle concentrations from the free troposphere, or perhaps it is necessary to invoke a ternary nucleation mechanism to account for CN concentrations in marine areas.

Measurements of aerosol size distributions in the North Atlantic are available from a cruise undertaken as part of the Joint Global Ocean Flux Study (JGOFS) [*Van Dingenen et al.,* 1995]. These data were taken with a differential mobility particle sizer consisting of an electrostatic classifier and a condensation nuclei counter. The cruise track followed a course from Halifax, Nova Scotia to the Canary Islands and back during September and October of 1992. *Van Dingenen et al.* [1995] report number size distributions for clean, modified, and polluted conditions classified using air mass back trajectories. Because this study does not account for substantial concentrations of carbonaceous aerosols that were observed under modified and polluted conditions, we compare our results against their clean size distribution. The predicted size distribution represents a September/October average over a portion of the North Atlantic (50° W to 25° W and 30° N to 45° N) where the cruise ship encountered the most clean conditions.

Figure 4.6a shows the lognormal fit to the cruise data and the size distributions predicted in the base-case, primary emissions, and enhanced nucleation scenarios. As discussed earlier, the simulated and observed marine aerosol size distributions show a bimodal character with a larger mode of cloud-processed CCN particles and a smaller "Aitken" mode. There is a close correspondence between the sizes of the simulated and observed modes and the "Hoppel" gap between them. The small dip at 0.046 μm diameter in the simulated Aitken mode results from processing by the GCM's

convective clouds, which were assumed to have a higher supersaturation than the stratiform clouds that accounts for the more prominent gap at 0.09 μm.

As was the case in the Pacific, the base-case scenario underpredicts number concentrations, having a total of 150 cm^{-3} compared against the 400 cm^{-3} that were measured. In contrast to the Pacific, primary particles are important and the model predicts total number concentrations of 330 cm^{-3} when they are included. The enhanced nucleation scenario also results in particle concentrations of 330 cm^{-3}. Once again, a combination of primary emissions and a modest enhancement in nucleation rates would result in the best agreement.

The underprediction is more severe if one looks at CCN particles above 0.09 μm diameter, obviously a concern if one is interested in estimating the indirect effect of aerosols. The observations show particle concentrations of 200 cm^{-3} between 0.09 and 1 μm diameter. Predictions are 65, 110, and 80 cm^{-3} in the base-case, primary emissions, and enhanced nucleation scenarios, respectively. A comparison shows that the simulated sulfate mass concentrations are similar to those observed on the cruise so it is unlikely that this is the source of the discrepancy. A more likely explanation is the absence of sea salt and other aerosol types. Although sea salt is often associated with aerosol in the supermicron size range, significant amounts are also found in the size range below 1 μm, so some sea salt particles were probably sampled and contributed to the observed CCN mode. Another important possibility is that organic aerosol is contributing a significant number of particles in this size range. Even the central region of the North Atlantic cannot be considered remote and is substantially impacted by anthropogenic activity. Evidence for this comes from observations from the cruise ship,

in which measured MSA to sulfate ratios indicated that most of the sulfate was in fact anthropogenic.

To summarize, the agreement between the observed and simulated shapes of the size distribution indicates that the model is successfully capturing the microphysics of marine aerosol. Sensitivity scenarios suggest that it is necessary to accurately account for nucleation in remote marine areas and primary emissions in those closer to land in order to predict accurately number concentrations. In addition, it appears that, even in the central North Atlantic, anthropogenic aerosol contributes significantly to the number of particles in the accumulation mode.

4.6.2 Free Troposphere

To characterize aerosol number concentrations, size distributions, and microphysics, *Schröder et al.* [2001] carried out a number of measurements as part of the Lindenberg Aerosol Characterization Experiment (LACE98) in July and August of 1998. These comprise data taken during 7 flights, or about 11 hours of sampling time, in the boundary layer, free troposphere, and upper troposphere. The aerosol size distributions they present are composite data from condensation nucleus counters and optical spectrometers. The region sampled by the aircraft (14° W to 2° W and 47° N to 53° N) includes southern Ireland, most of Wales, southwestern England, Brittany and portions of the Atlantic Ocean between them.

Figure 4.6b shows a comparison of predicted average number size distributions for three vertical layers in the troposphere with the median distribution measured during

the LACE98 campaign. First, the predicted total number concentrations are reasonable, but somewhat lower than the measured values. Predicted CN14 concentrations range over 250-270 cm^{-3} (ambient conditions), depending on which vertical layer one considers, compared with 360 cm^{-3} from the observations. Observed CN concentrations are therefore reproduced to within 25% in this situation.

Looking at the size distributions themselves, the observations show a unimodal structure that is typical of the free troposphere. There are high concentrations of Aitken mode particles with a peak around 40 nm diameter, which are products of new particle formation that is occurring in the free troposphere and upper troposphere. Freshly nucleated particles grow to these sizes by condensation of gas-phase sulfuric acid. The lack of an accumulation mode is evidence that these particles have not undergone cloud processing to a significant degree.

In contrast, the Aitken mode particles in the simulation tend to be larger, with a peak in the 50-70 nm diameter range. Also, a distinct accumulation mode is present, especially in the lower, 634 mb size distribution. K99 noted that this model may overpredict sulfate concentrations in the free troposphere, but it is difficult to say for certain because aircraft measurements of sulfate may be biased low because of losses in sampling lines. If the model does indeed overpredict sulfate mass concentrations in the free troposphere, this might explain the shift in the predicted size distributions to larger sizes. Overall, we conclude that the model accurately represents aerosol microphysical processes in the free troposphere, considering the early stage of model development as well as the relatively short sampling time of the data with which we are comparing.

4.6.3 Upper Troposphere

In the upper troposphere and tropopause region, we compare the model predictions against two data sets. This region is most sensitive to changes in the nucleation parameterization, so it is the best location to assess predicted rates of new particle formation.

The first data set is a result of a flight from Darwin, Australia to Tokyo, Japan [*Clarke,* 1992]. Amongst other measurements that were made, a condensation particle counter was used to sample CN15 concentrations of volatile particles. Looking at averages over 100-200 km flight segments, CN15 concentrations varied between 1000 and 2000 cm^{-3} (STP conditions). No clear latitudinal gradient is discernible and the observed variability is more likely the result of local weather conditions encountered by the aircraft as it made the transect. Average CN15 concentrations predicted by the model for the same location and time period are in good agreement, 1200 cm^{-3} for the primary emissions scenario. Predicted CN concentrations from the enhanced nucleation scenario, on the other hand, are 2000 cm^{-3} on average, towards the high end of the observations. It is also interesting to note that the observed ultrafine concentrations, defined as the difference between measured CN3 and CN15 concentrations, show clear evidence that the equatorial upper troposphere is a region with high rates of new particle formation. The current microphysical algorithm does not include particles smaller than 10 nm, so no quantitative comparison is possible, but this observation is in qualitative agreement with the predicted maximum in nucleation rates in this region.

The *Schröder et al.* [2001] data, described in the previous section on the free troposphere, offer another set of CN concentrations as well as size distributions for testing the performance of the model. Figure 4.6c shows a comparison between the median of observations made in the 10-12 km altitude range and average predictions for the same region, altitude, and time period. The observations show median particle concentrations of 410 cm^{-3} (ambient conditions). Our scenario with primary emissions is in reasonable agreement at 290 cm^{-3}, although about 25% lower than the observations. In this case, the scenario without primary emissions actually gives better agreement with average CN concentrations of 370 cm^{-3}, although the primary emissions scenario is still considered more realistic and gives better agreement with observations overall. Similar to the result for the *Clarke* [1992] data, the scenario with enhanced nucleation overpredicts CN concentrations. The overprediction is, however, much more severe in this comparison with average CN concentrations of 920 cm^{-3}.

Looking at the shape of the size distributions, there is remarkably good agreement between observations and model results. The most obvious difference between the size distributions is the peak in the predicted size distribution at 15 nm. The fact that the model has a lower size boundary of 10 nm diameter and that this is a region where nucleation is producing large numbers of ultrafine particles in the 3 to 10 nm size range may account for the discrepancy. The lower size boundary may force an artificial lumping of these ultrafine particles with particles in the first and second size bins resulting in an apparent overprediction by the model for these bins. Alternatively, this discrepancy may be a statistical artifact. We are comparing average model results with the median of the observations. If nucleation events produce large numbers of small

particles at sporadic intervals, the occasionally very high number concentrations will show up in the predicted average value but not in the observational median.

The model, therefore, performs quite well in predicting CN concentrations and size distributions in the upper troposphere. It also appears that the simple parameterization of binary nucleation theory accurately predicts new particle formation rates, at least in the upper troposphere, and that much enhancement of nucleation rates leads to an overprediction of CN concentrations.

4.6.4 Vertical Profiles

The CN concentrations and size distributions measured by *Schröder et al.* [2001] in the free and upper troposphere have already been compared to predictions. The same data set also provides CN concentrations, but not size distributions, in the polluted boundary layer. Although other aerosol types besides sulfate need to be included before a detailed comparison is meaningful for the polluted boundary layer, a brief discussion of boundary layer CN concentrations completes the vertical profile and leads to two relevant conclusions. Measured CN14 concentrations in the polluted boundary layer exhibit a strong vertical gradient with concentrations in excess of 10,000 cm^{-3} at the surface and declining to 1,000 cm^{-3} at 2 km altitude. Above the boundary layer, CN14 concentrations reach a minimum and then increase until a local maximum is reached at the tropopause.

When emissions of primary particles are included, the boundary layer gradient is reproduced more or less accurately. For this scenario, CN14 concentrations predicted

for the surface layer, which is approximately 0.7 km thick, are 3,000 cm^{-3} and decrease to 1,300 cm^{-3} for the second layer that extends to 1.4 km. Direct comparison is difficult given the coarse vertical resolution of the model. Another complication is that the research aircraft presumably took off and landed at a location that was more polluted than the sampling region as a whole. In contrast, without primary emissions CN14 concentrations are grossly underpredicted, being only 50-200 cm^{-3} in this same area. One can conclude that the crude assumptions made here about primary emissions are approximately correct and necessary for accurately representing aerosol microphysics in the boundary layer. Further refinements that include better inventories of primary particles, incorporation of other aerosol types into the model, and more detailed comparison with observations are necessary, however.

Another important feature of the observational evidence that is reproduced by the model is the increase in CN concentrations (at STP conditions, the relevant metric for comparisons between different altitudes) above the boundary layer. This implies high nucleation rates near the tropopause and that the upper troposphere is a net source of new particles for lower levels. Although nucleation events in the marine boundary layer have been observed [*Clarke et al.,* 1998b], such observational evidence suggests that nucleation rates are higher, on average, in the free and upper troposphere.

4.7. Conclusions

A size-resolved aerosol microphysical simulation has been incorporated into the GISS GCM II-prime general circulation model as an online component. The

microphysical algorithm includes condensation/evaporation, coagulation, and nucleation. A two-moment sectional algorithm has been selected to represent aerosol microphysics. This algorithm has the desirable property of explicitly predicting and conserving both aerosol mass and number. Using two moments for each size section is numerically more accurate and efficient than single moment methods that track only aerosol mass. Moreover, conservation of aerosol number is an especially useful feature for predicting CCN number concentrations. The high size resolution of the algorithm, 30 size sections between 0.01 and 10 μm diameter, make this the most detailed simulation of aerosol size distributions in a global model to date. It also represents a significant step towards including the indirect effect of aerosols in climate models in a mechanistic, rather than empirical, fashion.

As a first application of the algorithm, the size distribution, mass, and number concentrations of sulfate aerosol have been predicted. Although, clearly there are many situations in which one would like to include other aerosol types, this is left for future work. Mass concentrations of sulfate predicted by the size-resolved model are essentially unchanged from previous model versions that lacked size resolution. The model also qualitatively reproduces several important features of the atmospheric aerosol. These include a large nucleation source in the upper troposphere, especially in the tropics, CN concentrations that increase with altitude, higher number concentrations over land than sea, and bimodal size distributions in marine areas that result from cloud processing. Quantitatively, predicted CCN concentrations are also within the expected range for both continental and marine locations. More detailed comparisons with observations show good agreement for size distributions, CN and CCN concentrations.

Predicted CN concentrations are within 25% of observations although predictions may be biased low. Other discrepancies between observations and predictions, such as low CCN concentrations in the North Atlantic, may be explained by the absence of sea salt and carbonaceous aerosols.

Sensitivity scenarios performed as part of this study make it clear that there are significant uncertainties with respect to sources of particles to the atmosphere. Emissions of primary particles to the atmosphere during fossil fuel combustion make the dominant contribution to CN concentrations in the polluted boundary layer and a have a noticeable impact in all but the most remote marine locations. It is clear that these need to be accurately included in global models that predict CN and CCN concentrations. Doing so will require more precise estimates of particulate emissions, including characterizing their size distributions. As a rough indication of the uncertainty associated with nucleation, a sensitivity scenario with a changed parameterization resulted in rates of new particle formation that were three times higher than the base case. Impact on CCN concentrations, however, was smaller but still significant, on the order of 25%. Comparison with observations suggested that the lower nucleation rates from the base-case scenario, based on binary nucleation theory, generally resulted in the best predictions of CN concentrations. While this was true in the free and upper troposphere where nucleation has the largest impact, higher nucleation rates seemed to improve model performance in the marine boundary layer. A formulation based on ternary nucleation theory may offer the best agreement at all altitudes. In contrast to the important sensitivities to surface-based primary emissions and nucleation, sensitivity scenarios exploring the effects of primary emissions from aircraft and scavenging of

interstitial aerosol showed that the model is much less sensitive to these processes. A preliminary simulation of the pre-industrial sulfate aerosol confirms that anthropogenic emissions have likely increased CCN concentrations significantly, but more conclusive results will await inclusion of other aerosol types.

Acknowledgments

The authors would like to thank Graham Feingold for answering questions regarding the microphysics algorithm and providing sample code. Bernd Kärcher provided observational data in advance of publication. We thank Tim Bates and others at PMEL for making data sets from cruises available. This study has been supported by a graduate fellowship from the Fannie and John Hertz Foundation as well as by the National Aeronautics and Space Administration Earth Observing System Interdisciplinary Science program (NASA EOS-IDS).

References

Adams, P. J., J. H. Seinfeld, and D. M. Koch, Global concentrations of tropospheric sulfate, nitrate, and ammonium aerosol simulated in a general circulation model, *J. Geophys. Res., 104,* 13,791-13,823, 1999.

Adams, P. J., J. H. Seinfeld, D. Koch, L. Mickley, and D. Jacob, General circulation model assessment of direct radiative forcing by the sulfate-nitrate-ammonium-water inorganic aerosol system, *J. Geophys. Res., 106,* 1097-1111, 2001.

Albrecht, B. A., Aerosols, cloud microphysics, and fractional cloudiness, *Science, 245,* 1227-1230, 1989.

Anderson, B. E., W. R. Cofer, J. Crawford, G. L. Gregory, S. A. Vay, K. E. Brunke, Y. Kondo, M. Koike, H. Schlager, S. L. Baughcum, E. Jensen, Y. J. Zhao, K. Kita, An assessment of aircraft as a source of particles to the upper troposphere, *Geophys. Res. Lett., 26,* 3069-3072, 1999.

Barth, M. C., P. J. Rasch, J. T. Kiehl, C. M. Benkovitz, and S. E. Schwartz, Sulfur chemistry in the National Center for Atmospheric Research Community Climate Model: Description, evaluation, features, and sensitivity to aqueous chemistry, *J. Geophys. Res., 105,* 1387-1415, 2000.

Bates, T. S., V. N. Kasputin, P.K. Quinn, D. S. Covert, D. J. Coffman, C. Mari, P. A. Durkee, W. DeBruyn, and E. Saltzman, Processes controlling the distribution of aerosol particles in the lower marine boundary layer during the First Aerosol Characterization Experiment (ACE 1), *J. Geophys. Res., 103,* 16,369-16,384, 1998.

Baughcum, S. L., D. M. Chan, S. M. Happenny, S. C. Henderson, P. S. Hertel, T. Higman, D. R. Maggiora, and C. A. Oncina, Emissions scenarios development: Scheduled 1990 and projected 2015 subsonic, Mach 2.0 and Mach 2.4 aircraft, in *The Atmospheric Effects of Stratospheric Aircraft: A Third Program Report, NASA RF. Publ., 1313,* 89-131, Nov. 1993.

Benkovitz, C. M., M. T. Scholtz, J. Pacyna, L. Tarrason, J. Dignon, E. C. Voldner, P. A. Spiro, J. A. Logan, and T. E. Graedel, Global gridded inventories of anthropogenic emissions of sulfur and nitrogen, *J. Geophys. Res., 101,* 29,239-29,253, 1996.

Binkowski, F. S., and U. Shankar, The regional particulate matter model, 1. Model description and preliminary results, *J. Geophys. Res., 100,* 26,191-26,209, 1995.

Boucher, O., GCM estimate of the indirect aerosol forcing using satellite-retrieved cloud droplet effective radii, *J. Climate, 8,* 1403-1409, 1995.

Boucher, O., and U. Lohmann, The sulfate-CCN-cloud albedo effect, *Tellus, 47B,* 281-300, 1995.

Brasseur, G. P., R. A. Cox, D. Hauglustaine, I. Isaksen, J. Lelieveld, D. H. Lister, R. Sausen, U. Schumann, A. Wahner, and P. Wiesen, European scientific assessment of the atmospheric effects of aircraft emissions, *Atmos. Environ., 32,* 2329-2418, 1998.

Brown, R. C., R. C. MiakeLye, M. R. Anderson, C. E. Kolb, and T. J. Resch, Aerosol dynamics in near-field aircraft plumes, *J. Geophys. Res., 101,* 22,939-22,953, 1996.

Chin, M., D. J. Jacob, G. M. Gardner, M. S. Foreman-Fowler, and P. A. Spiro, A global three-dimensional model of tropospheric sulfate, *J. Geophys. Res., 101,* 18,667-18,690, 1996.

Chuang, C. C., and J. E. Penner, Effects of anthropogenic sulfate on cloud drop nucleation and optical properties, *Tellus, 47B,* 566-577, 1995.

Chuang, C. C., J. E. Penner, K. E. Taylor, A. S. Grossman, and J. J. Walton, An assessment of the radiative effects of anthropogenic sulfate, *J. Geophys. Res., 102,* 3761-3778, 1997.

Clarke, A. D., Atmospheric nuclei in the remote free-troposphere, *J. Atmos. Chem., 14,* 479-488, 1992.

Clarke, A. D., J. L. Varner, F. Eisele, R. L. Mauldin, D. Tanner, and M. Litchy, Particle production in the remote marine atmosphere: Cloud outflow and subsidence during ACE 1, *J. Geophys. Res., 103,* 16,397-16,409, 1998a.

Clarke, A. D., D. Davis, V. N. Kasputin, F. Eisele, G. Chen, I. Paluch, D. Lenschow, A. R. Bandy, D. Thornton, K. Moore, L. Mauldin, D. Tanner, M. Litchy, M. A. Carroll, J. Collins, G. Albercook, Particle nucleation in the tropical boundary layer and its coupling to marine sulfur sources, *Science, 282,* 89-92, 1998b.

Clarke, A. D., F. Eisele, V. N. Kasputin, K. Moore, D. Tanner, L. Mauldin, M. Litchy, B. Lienert, M. A. Carroll, and G. Albercook, Nucleation in the equatorial free troposphere: favorable environments during PEM-Tropics, *J. Geophys. Res., 104,* 5735-5744, 1999.

Coffman, D. J., and Hegg, D. A., A preliminary study of the effect of ammonia on particle nucleation in the marine boundary-layer, *J. Geophys. Res., 100,* 7147-7160, 1995.

Cooke, W. F., and J. J. N. Wilson, A global black carbon aerosol model, *J. Geophys. Res., 101,* 19,395-19,409, 1996.

Covert, D. S., V. N. Kasputin, T. S. Bates, and P. K. Quinn, Physical properties of marine boundary layer aerosol particles of the mid-Pacific in relation to sources and meteorological transport, *J. Geophys. Res., 101,* 6919-6930, 1996.

Dahneke, B., Simple kinetic theory of Brownian diffusion in vapors and aerosols, in *Theory of Dispersed Multiphase Flow*, edited by R. E. Meyer, pp. 97-138, Academic Press, New York, 1983.

Dana, M. T., and J. M. Hales, Statistical aspects of the washout of polydisperse aerosols, *Atmos. Environ., 10,* 45-50, 1976.

Del Genio, A. D., and M.-S. Yao, Efficient cumulus parameterization for long-term climate studies: The GISS scheme, in *The Representation of Cumulus Convection in Numerical Models* Monogr. 46, edited by K. A. Emanuel and D. J. Raymond, pp. 181-184, Am. Meteorol. Soc., Boston, Mass., 1993.

Del Genio, A. D., M.-S. Yao, W. Kovari, and K. K.-W. Lo, A prognostic cloud water parameterization for global climate models, *J. Clim., 9,* 270-304, 1996.

Dentener, F. J., G. R. Carmichael, Y. Zhang, J. Lelieveld, and P. J. Crutzen, Role of mineral aerosol as a reactive surface in the global troposphere, *J. Geophys. Res., 101,* 22,869-22,889, 1996.

Doyle, G. J., Self-nucleation in the sulfuric acid-water system, *J. Chem. Phys., 35,* 795-799, 1961.

Erickson, D. J., R. J. Oglesby, and S. Marshall, Climate response to indirect anthropogenic sulfate forcing, *Geophys. Res. Lett., 22,* 2017-2020, 1995.

Fahey, D. W., et al., Emission measurements of the Concorde supersonic aircraft in the lower stratosphere, *Science, 270,* 70-73, 1995.

Feichter, J., E. Kjellstrom, H. Rodhe, F. Dentener, J. Lelieveld, and G.-J. Roelofs, Simulation of the tropospheric sulfur cycle in a global climate model, *Atmos. Environ., 30,* 1693-1707, 1996.

Feichter, J., U. Lohmann, and I. Schult, The atmospheric sulfur cycle in ECHAM-4 and its impact on the shortwave radiation, *Climate Dynamics, 13,* 235-246, 1997.

Fitzgerald, J. W., Marine aerosols: a review, *Atmos. Environ., 25,* 533-545, 1991.

Ghan, S. J., R. C. Easter, E. G. Chapman, H. Abdul-Razzak, Y. Zhang, L. R. Leung, N. S. Laulainen, R. D. Saylor, and R. A. Zaveri, A physically based estimate of radiative forcing by anthropogenic sulfate aerosol, *J. Geophys. Res., 106,* 5279-5293, 2001a.

Ghan, S., R. Easter, J. Hudson, and F.-M. Bréon, Evaluation of aerosol indirect radiative forcing in MIRAGE, *J. Geophys. Res., 106,* 5317-5334, 2001.

Hansen, J., G. Russell, D. Rind, P. Stone, A. Lacis, S. Lebedeff, R. Ruedy, and L. Travis, Efficient three-dimensional global models for climate studies: Models I and II., *Mon. Weather Rev., 111,* 609-662, 1983.

Heist, R. H., and H. Reiss, Hydrates in supersaturated sulfuric acid-water vapor, *J. Chem. Phys., 61,* 573-581, 1974.

Hoppel, W. A., J. W. Fitzgerald, and R. E. Larson, Aerosol size distributions in air masses advecting off the East Coast of the United States, *J. Geophys. Res., 90,* 2365-2379, 1985.

Hoppel, W. A., G. M. Frick, and R. E. Larson, Effect of nonprecipitating clouds on the aerosol size distribution in the marine boundary layer, *Geophys. Res. Lett., 13,* 125-128, 1986.

Intergovernmental Panel on Climate Change (IPCC), *Third Assessment Report*, in press, 2001.

Jaecker-Voirol, A., and P. Mirabel, Nucleation rate in a binary mixture of sulfuric acid and water vapor, *J. Phys. Chem., 92,* 3518-3521, 1988.

Jaecker-Voirol, A., and P. Mirabel, Heteromolecular nucleation in the sulfuric acid-water system, *Atmos. Environ., 23,* 2053-2057, 1989.

Jaenicke, R., Tropospheric aerosols, in *Aerosol-Cloud-Climate Interactions*, edited by P. V. Hobbs, pp. 1-31, Academic Press, San Diego, 1993.

Kanakidou, M., K. Tsigaridis, F. J. Dentener, and P. J. Crutzen, Human-activity-enhanced formation of organic aerosols by biogenic hydrocarbon oxidation, *J. Geophys. Res., 105,* 9243-9254, 2000.

Kasibhatla, P., W. L. Chameides, and J. St. John, A three-dimensional global model investigation of seasonal variations in the atmospheric burden of anthropogenic aerosols, *J. Geophys. Res., 102,* 3737-3759, 1997.

Kettle, A. J., et al., A global database of sea surface dimethyl-sulfide (DMS) measurements and a procedure to predict sea surface DMS as a function of latitude, longitude and month, *Global Biogeochem. Cycles, 13,* 394-444, 1999.

Kiehl, J. T., T. L. Schneider, P. J. Rasch, M. C. Barth, and J. Wong, Radiative forcing due to sulfate aerosols from simulations with the National Center for Atmospheric Research Community Climate Model, Version 3, *J. Geophys. Res., 105,* 1441-1457, 2000.

Kjellstrom, E., A three-dimensional global model study of carbonyl sulfide in the troposphere and the lower stratosphere, *J. Atmos. Chem., 29,* 151-177, 1998.

Kjellstrom, E., J. Feichter, R. Sausen, and R. Hein, The contribution of aircraft emissions to the atmospheric sulfur budget, *Atmos. Environ., 33,* 3455-3465, 1999.

Koch, D., D. Jacob, I. Tegen, D. Rind, and M. Chin, Tropospheric sulfur simulation and sulfate direct radiative forcing in the Goddard Institute for Space Studies general circulation model, *J. Geophys. Res., 104,* 23,799-23,822, 1999.

Korhonen, P., M. Kulmala, A. Laaksonen, Y. Viisanen, R. McGraw, and J. H. Seinfeld, Ternary nucleation of H2SO4, NH3, and H2O in the atmosphere, *J. Geophys. Res., 104,* 26,349-26,353, 1999.

Kulmala, M., and A. Laaksonen, Binary nucleation of water-sulfuric acid system: comparison of classical theories with different H_2SO_4 saturation vapor pressures, *J. Chem. Phys., 93,* 696-701, 1990.

Kulmala, M., U. Pirjola, and J. M. Makela, Stable sulphate clusters as a source of new atmospheric particles, *Nature, 404,* 66-69, 2000.

Laaksonen, A., V. Talanquer, and D. W. Oxtoby, Nucleation: measurements, theory, and atmospheric applications, *Annu. Rev. Phys. Chem., 46,* 489-524, 1995.

Langner, J., and H. Rodhe, A global three-dimensional model of the tropospheric sulfur cycle, *J. Atmos. Chem., 13,* 225-263, 1991.

Lelieveld, J., G.-J. Roelofs, L. Ganzeveld, J. Feichter, and H. Rodhe, Terrestrial sources and distribution of atmospheric sulfur, *Philos. Trans. R. Soc. London, 352,* 149-158, 1997.

Liousse, C., J. E. Penner, C. Chuang, J. J. Walton, H. Eddleman, and H. Cachier, A global three-dimensional model study of carbonaceous aerosols, *J. Geophys. Res., 101,* 19,411-19,432, 1996.

Liss, P. S., and L. Merlivat, Air-sea gas exchange rates: Introduction and synthesis, in *The Role of Air-Sea Exchange in Geochemical Cycling*, pp. 113-127, D. Reidel, Norwell, Mass., 1986.

Liu, X. H., D. A. Hegg, and M. T. Stoelinga, Numerical simulation of new particle formation over the northwest Atlantic using the MM5 mesoscale model coupled with sulfur chemistry, *J. Geophys. Res., 106,* 9697-9715, 2001.

Lohmann, U., and J. Feichter, Impact of sulfate aerosols on albedo and lifetime of clouds: A sensitivity study with the ECHAM4 GCM, *J. Geophys. Res., 102,* 13,685-13,700, 1997.

Marti, J. J., R. J. Weber, P. H. McMurry, F. Eisele, D. Tanner, and A. Jefferson, New particle formation at a remote continental site: assessing the contributions of SO_2 and organic precursors, *J. Geophys. Res., 102,* 6331-6339, 1997.

Mirabel, P., and J. L. Katz, Binary homogeneous nucleation as a mechanism for the formation of aerosols, *J. Chem. Phys., 60,* 1138-1144, 1974.

Nenes, A., C. Pilinis, and S. N. Pandis, Isorropia: A new thermodynamic equilibrium model for multiphase multicomponent inorganic aerosols, *Aquat. Geochem., 4,* 123-152, 1998.

Nilsson, E. D., Pirjola L., and M. Kulmala, The effect of atmospheric waves on aerosol nucleation and size distribution, *J. Geophys. Res., 105,* 19,917-19,926, 2000.

Penner, J. E., C. S. Atherton, and T. E. Graedel, *Global emissions and models of photochemically active compounds, in Global Atmospheric-Biospheric Chemistry,* edited by R. G. Prinn, pp. 223-247, Plenum, New York, 1994.

Petzold, A., and F. P. Schröder, Jet engine exhaust aerosol characterization, *Aerosol Sci. Tech., 28,* 62-76, 1998.

Petzold, A., A. Dopelheuer, C. A. Brock, and F. Schröder, In situ observations and model calculations of black carbon emission by aircraft at cruise altitude, *J. Geophys. Res., 104,* 22,171-22,181, 1999.

Pham, M., J.-F. Müller, G. P. Brasseur, C. Granier, and G. Mégie, A three-dimensional study of the tropospheric sulfur cycle, *J. Geophys. Res., 100,* 26,061-26,092, 1995.

Pincus, R., and M. Baker, Effect of precipitation on the albedo susceptibility of clouds in the marine boundary layer, *Nature, 372,* 250-252, 1994.

Pöschl, U., M. Canagaratna, J. T. Jayne, L. T. Molina, D. R. Worsnop, C. E. Kolb, and M. J. Molina, Mass accommodation coefficient of H_2SO_4 vapor on aqueous sulfuric acid surfaces and gaseous diffusion coefficient of H_2SO_4 in N_2/H_2O, *J. Phys. Chem. A, 102,* 10,082-10,089, 1998.

Quinn, P. K., S. F. Marshall, T. S. Bates, D. S. Covert, and V. N. Kasputin, Comparison of measured and calculated aerosol properties relevant to the direct radiative forcing of tropospheric sulfate aerosol on climate, *J. Geophys. Res., 100,* 8977-8991, 1995.

Raes, F., R. Van Dingenen, E. Cuevas, P. F. J. Van Velthoven, and J. M. Prospero, Observations of aerosols in the free troposphere and marine boundary layer of the subtropical Northeast Atlantic: discussion of processes determining their size distribution, *J. Geophys. Res., 102,* 21,315-21,328, 1997.

Rasch, P. J., M. C. Barth, J. T. Kiehl, S. E. Schwartz, and C. M. Benkovitz, A description of the global sulfur cycle and its controlling processes in the National Center for Atmospheric Research Community Climate Model, Version 3, *J. Geophys. Res., 105,* 1367-1385, 2000.

Restad, K., I. S. A. Isaksen, and T. K. Berntsen, Global distribution of sulphate in the troposphere. A three-dimensional model study, *Atmos. Environ., 32,* 3593-3609, 1998.

Rind, D., and J. Lerner, The use of on-line tracers as a diagnostic tool in general circulation model development, 1, Horizontal and vertical transport in the troposphere, *J. Geophys. Res., 101,* 12,667-12,683, 1996.

Roelofs, G.-J., J. Lelieveld, and L. Ganzeveld, Simulation of global sulfate distribution and the influence on effective cloud drop radii with a coupled photochemistry-sulfur cycle model, *Tellus, 50B,* 224-242, 1998.

Russell, L. M., and J. H. Seinfeld, Size- and composition-resolved externally mixed aerosol model, *Aerosol Science and Technology, 28,* 403-416, 1998.

Schröder, F. P., B. Kärcher, A. Petzold, and M. Fiebig, Aerosol sources and transformation processes in the free troposphere and tropopause region at northern midlatitudes, submitted to *J. Geophys. Res.,* 2000.

Schumann, U., J. Strom, R. Busen, R. Baumann, K. Gierens, M. Krautstrunk, F. P. Schröder, and J. Stingl, In situ observations of particles in jet aircraft exhausts and contrails for different sulfur-containing fuels, *J. Geophys. Res., 101,* 6853-6869, 1996.

Spiro, P. A., D. J. Jacob, and J. A. Logan, Global inventory of sulfur emissions with 1°x1° resolution, *J. Geophys. Res., 97,* 6023-6036, 1992.

Tang, I. N., and H. R. Munkelwitz, Water activities, densities, and refractive indices of aqueous sulfates and sodium nitrate droplets of atmospheric importance, *J. Geophys. Res., 99,* 18,801-18,808, 1994.

Tegen, I., and I. Fung, Modeling of mineral dust in the atmosphere; sources, transport, and optical thickness, *J. Geophys. Res., 99,* 22,897-22,914, 1994.

Tegen, I., and A. A. Lacis, Modeling of particle size distribution and its influence on the radiative properties of mineral dust aerosol, *J. Geophys. Res., 101,* 19,237-19,244, 1996.

Tegen, I., D. Koch, A. A. Lacis, and M. Sato, Trends in tropospheric aerosol loads and corresponding impact on direct radiative forcing between 1950 and 1990: a model study, *J. Geophys. Res., 105,* 26,971-26,989, 2000.

Turco, R. P., J.-X. Zhao, and F. Yu, A new source of tropospheric aerosols: ion-ion recombination, *Geophys. Res. Lett., 25,* 635-638, 1998.

Twomey, S., Pollution and the planetary albedo, *Atmos. Environ., 8,* 1251-1256, 1974.

Tzivion, S., G. Feingold, and Z. Levin, An efficient numerical solution to the stochastic collection equation, *J. Atmos. Sci., 44,* 3139-3149, 1987.

Tzivion, S., G. Feingold, and Z. Levin, The evolution of raindrop spectra. Part II: Collisional collection/breakup and evaporation in a rainshaft, *J. Atmos. Sci., 46,* 3312-3327, 1989.

Van Dingenen, R., F. Raes, and N. R. Jensen, Evidence for anthropogenic impact on number concentration and sulfate content of cloud-processed aerosol particles over the North Atlantic, *J. Geophys. Res., 100,* 21,057-21,067, 1995.

von Salzen, K., H. G. Leighton, P. A. Ariya, L. A. Barrie, S. L. Gong, J. P. Blanchet, L. Spacek, U. Lohmann, L. I. Kleinman, Sensitivity of sulphate aerosol size distributions and CCN concentrations over North America to SO_x emissions and H_2O_2 concentrations, *J. Geophys. Res., 105,* 9741-9765, 2000.

Wang, Y., D. J. Jacob, and J. A. Logan, Global simulation of tropospheric O_3-NO_x-hydrocarbon chemistry, 1, Model formulation, *J. Geophys. Res.*, *103*, 10,713-10,726, 1998a.

Wang, Y., J. A. Logan and D. J. Jacob, Global simulation of tropospheric O_3-NO_x-hydrocarbon chemistry, 2, Model evaluation and global ozone budget, *J. Geophys. Res.*, *103*, 10,727-10,756, 1998b.

Wang, Y., D. J. Jacob, and J. A. Logan, Global simulation of tropospheric O_3-NO_x-hydrocarbon chemistry, 3, Origin of tropospheric ozone and effects of nonmethane hydrocarbons, *J. Geophys. Res.*, *103*, 10,757-10,768, 1998c.

Wesely, M. L., and B. B. Hicks, Some factors that affect the deposition rates of sulfur dioxide and similar gases on vegetation, *J. Air Pollut. Control Assoc., 27,* 1110-1116, 1977.

Wexler, A. S., F. W. Lurmann, and J. H. Seinfeld, Modeling urban and regional aerosols – I. Model development, *Atmos. Environ., 28,* 531-546, 1994.

Whitby, K. T., The physical characteristics of sulfur aerosols, *Atmos. Environ., 12,* 135-159, 1978.

Zhang, Y. P., S. Kreidenweis, and G. R. Taylor, The effects of clouds on aerosol and chemical species production and distribution. Part III: Aerosol model description and sensitivity analysis, *J. Atmos. Sci., 55,* 921-939, 1998.

Figure Captions

Figure 4.1. Global and annual average dry deposition velocities (cm s^{-1}) as a function of particle size (solid curve). For comparison, the global and annual average dry deposition velocity used for bulk sulfate in K99 is also shown (dashed line).

Figure 4.2. Vertical profiles of a) sulfate mass (μg m^{-3}), b) CN concentrations (cm^{-3} at STP), and c) CCN (0.2%) concentrations (cm^{-3} at STP) for four model scenarios: pre-industrial (lightweight dashed line), base case (lightweight solid line), enhanced nucleation (heavyweight dashed line), and primary emissions (heavyweight solid line).

Figure 4.3. Sources and sinks of aerosol particles for four model scenarios. Values in boxes are average CN concentration (cm^{-3}) and particle lifetime (days).

Figure 4.4. Model predictions of aerosol number size distributions taken from the primary emissions scenario for a) remote marine and continental locations, b) polluted boundary layer locations, and c) free and upper troposphere.

Figure 4.5. Seasonal variation in Northern Hemispheric sulfate burden (Tg S), average CN concentrations (cm^{-3}), and CCN concentrations (cm^{-3}).

Figure 4.6. Model predictions of aerosol size distributions compared with observed size distributions for a) the North Atlantic, b) the free troposphere, and c) tropopause. For part a), model predictions from three modern-day scenarios are shown. In parts b) and

c), only predictions from the primary emissions scenario, judged to be the most realistic overall, are shown.

Plate 4.1. Zonal average CN and CCN (0.2%) concentrations (cm^{-3}) for four model scenarios. Contours of CN concentrations are 0, 10, 20, 50, 100, 200, 500, 1000, 2000, 5000, and 10,000. Contours of CCN (0.2%) concentrations are 0, 1, 2, 5, 10, 20, 50, 100, 200, 500, and 1000.

Plate 4.2. Latitude-longitude map of annual-average a) CN and b) CCN (0.2%) concentrations (cm^{-3}) in the model surface layer for four model scenarios. Values in the upper right corners represent layer averages.

Plate 4.3. Latitude-longitude map of annual-average a) CN and b) CCN (0.2%) concentrations (cm^{-3}) in the free troposphere (634 mb) for four model scenarios. Values in the upper right corners represent layer averages.

Plate 4.4. Latitude-longitude map of annual-average a) CN and b) CCN (0.2%) concentrations (cm^{-3}) in the tropopause region (201 mb) for four model scenarios. Values in the upper right corners represent layer averages.

Table 4.1. Comparison of sulfur budgets computed with size-resolved aerosol microphysics and previous model version without microphysics [*Koch et al.*, 1999]

	Base Case	Primary Emissions	Enhanced Nucleation	Bulk Dry Deposition	Preindustrial	K99
DMS						
Sources (Tg S yr^{-1})						
Emissions	10.8	10.8	10.8	10.8	10.8	10.7
Sinks (Tg S yr^{-1})						
Oxidation	10.7	10.7	10.7	10.7	10.7	10.7
Burden (Tg S)	0.05	0.05	0.05	0.05	0.05	0.06
Lifetime (d)	1.7	1.7	1.7	1.7	1.7	1.9
SO_2						
Sources (Tg S yr^{-1})						
Emissions	72.8	70.8	72.8	72.8	3.8	70.8
DMS oxidation	9.7	9.7	9.7	9.7	9.7	9.6
Total	82.5	80.5	82.5	82.5	13.5	80.4
Sinks (Tg S yr^{-1})						
SO_2 + OH	15.3	14.8	15.3	15.3	2.7	13.1
$SO_2 + H_2O_2$	27.9	27.5	27.9	27.9	7.5	31.6
Dry deposition	37.9	36.7	37.9	37.9	3.2	35.5
Wet deposition	1.5	1.4	1.5	1.5	0.1	0.2
Total	82.6	80.5	82.6	82.6	13.5	80.4
Burden (Tg S)	0.68	0.66	0.68	0.68	0.08	0.56
Lifetime (d)	3.0	3.0	3.0	3.0	2.3	2.6
SO_4^{2-}						
Sources (Tg S yr^{-1})						
Emissions	0.0	2.0	0.0	0.0	0.0	1.9
Nucleation	0.05	0.04	0.16	0.05	0.03	0.00
Condensation of H_2SO_4	15.2	14.8	15.1	15.2	2.6	13.1
$SO_2 + H_2O_2$	27.9	27.5	27.9	27.9	7.5	31.6
Total	43.2	44.3	43.2	43.2	10.1	46.6
Sinks (Tg S yr^{-1})						
Dry deposition	0.8	1.0	0.9	7.8	0.2	9.2
Wet deposition	42.3	43.3	42.3	35.3	9.9	37.4
Total	43.2	44.3	43.2	43.2	10.1	46.6
Burden (Tg S)	0.77	0.80	0.78	0.63	0.15	0.73
Lifetime (d)	6.5	6.6	6.6	5.4	5.5	5.7
MSA						
Sources (Tg S yr^{-1})						
DMS oxidation	1.0	1.0	1.0	1.0	1.0	1.1
Sinks (Tg S yr^{-1})						
Dry deposition	0.2	0.2	0.2	0.2	0.2	0.2
Wet deposition	0.9	0.9	0.9	0.9	0.9	0.9
Total	1.0	1.0	1.0	1.0	1.0	1.1
Burden (Tg S)	0.02	0.02	0.02	0.02	0.02	0.02
Lifetime (d)	7.5	7.5	7.5	7.5	7.5	7.6

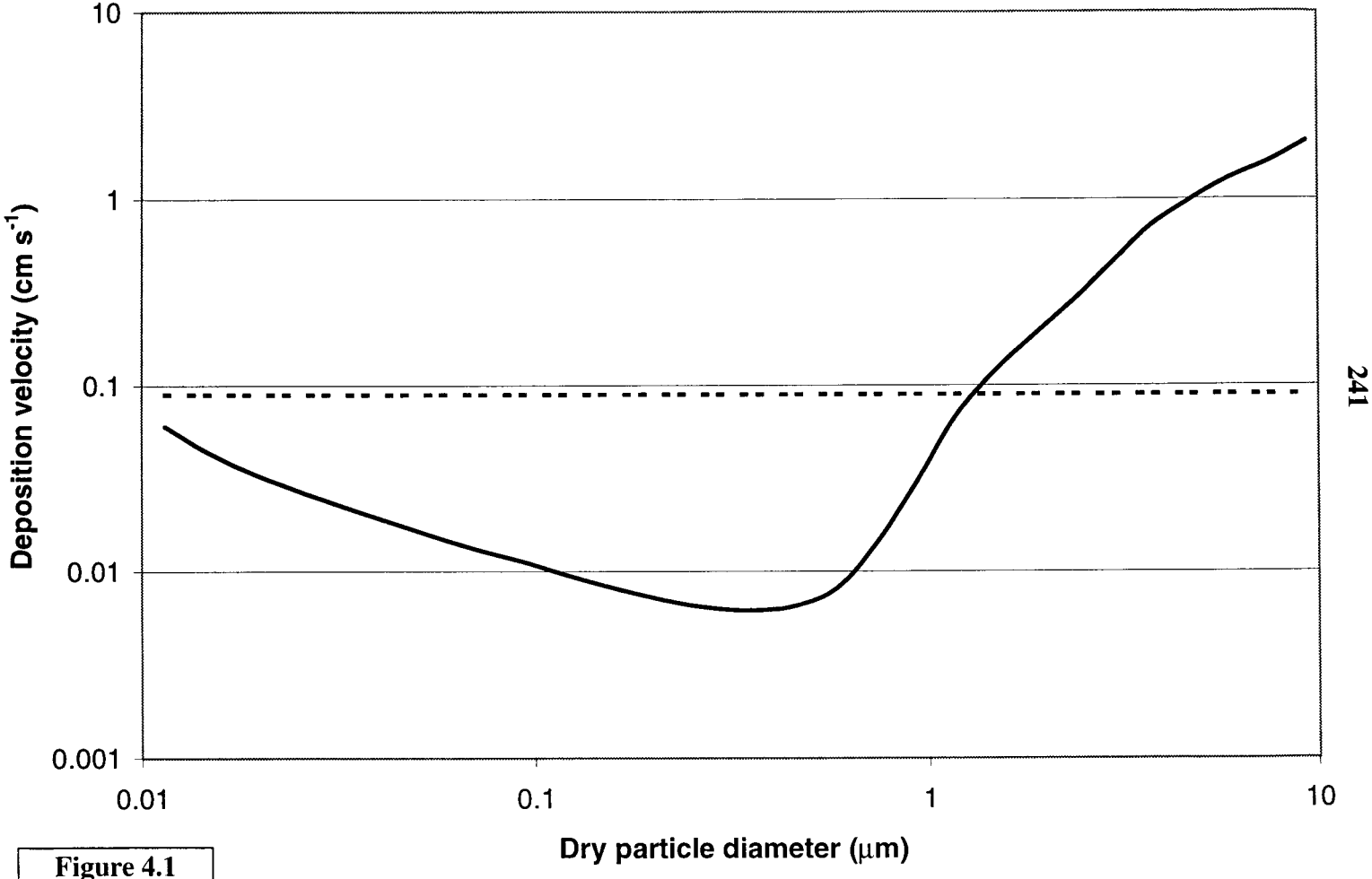
10
1
0.1
0.01
0.001
Deposition velocity (cm s-1)
0.01
0.1
1
10
Dry particle diameter (μm)

Figure 4.1

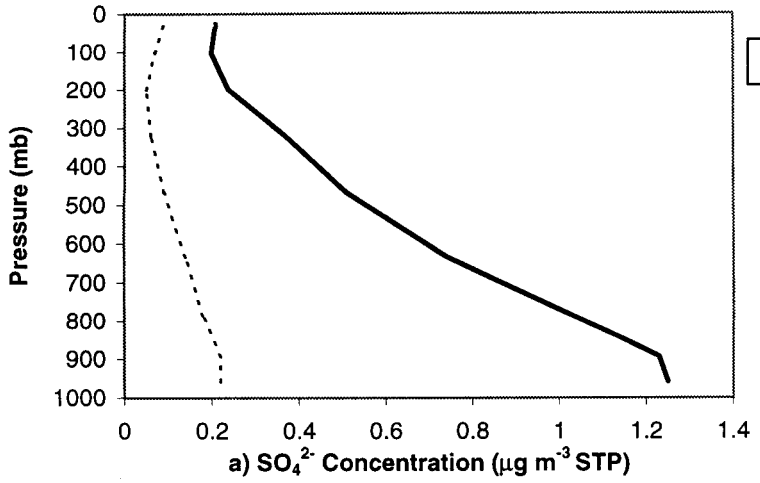
Pressure (mb)
0
100
200
300
400
500
600
700
800
900
1000
0
0.2
0.4
0.6
0.8
1
1.2
1.4
a) SO_4^{2-} Concentration (μg m^{-3} STP)

Figure 4.2

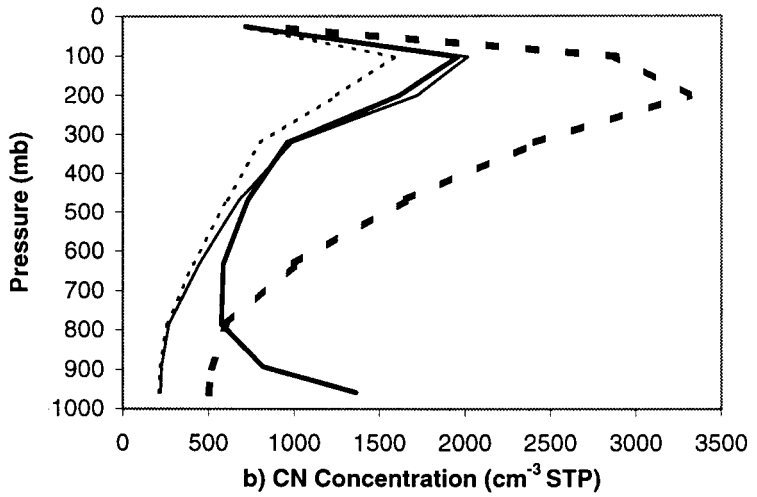
Pressure (mb)
0
100
200
300
400
500
600
700
800
900
1000
0
500
1000
1500
2000
2500
3000
3500
b) CN Concentration (cm^{-3} STP)

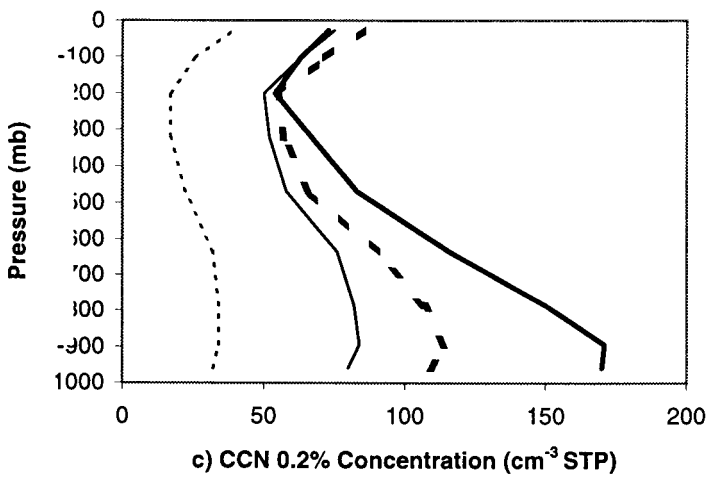
Pressure (mb)
0
1000
0
50
100
150
200
c) CCN 0.2% Concentration (cm^{-3} STP)

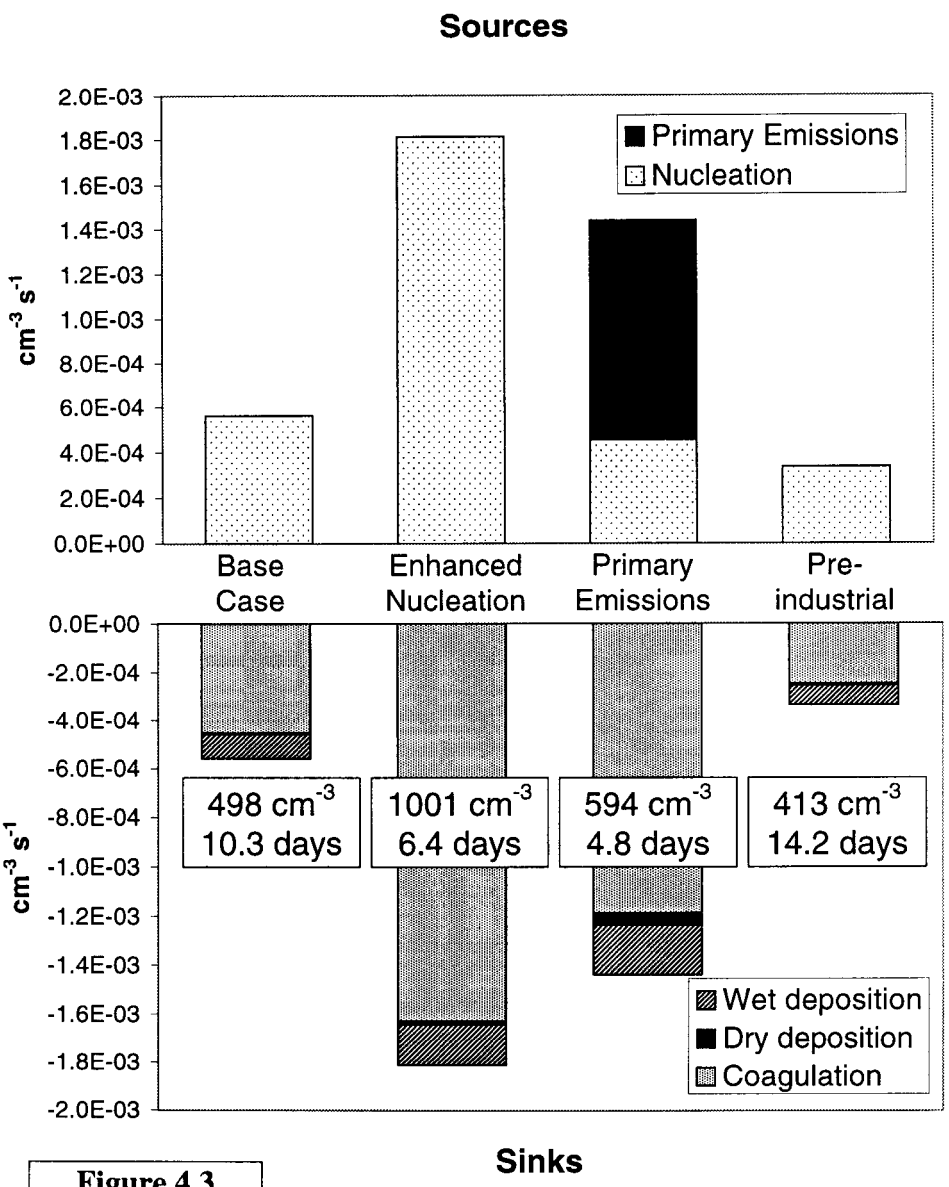
Sources
2.0E-03
1.8E-03
1.6E-03
1.4E-03
1.2E-03
1.0E-03
8.0E-04
6.0E-04
4.0E-04
2.0E-04
0.0E+00
cm-3 s-1
Primary Emissions
Nucleation
Base Case
Enhanced Nucleation
Primary Emissions
Pre-industrial
0.0E+00
-2.0E-04
-4.0E-04
-6.0E-04
-8.0E-04
-1.0E-03
-1.2E-03
-1.4E-03
-1.6E-03
-1.8E-03
-2.0E-03
498 cm-3
10.3 days
1001 cm-3
6.4 days
594 cm-3
4.8 days
413 cm-3
14.2 days
Wet deposition
Dry deposition
Coagulation
Sinks

Figure 4.3

a)

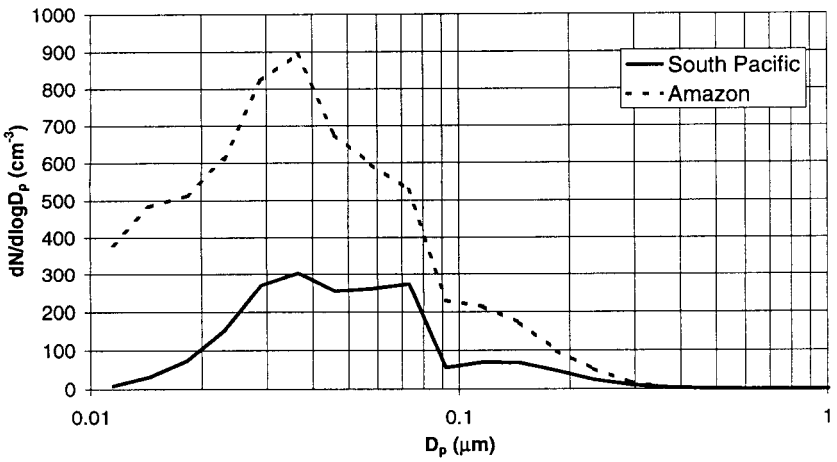

b)

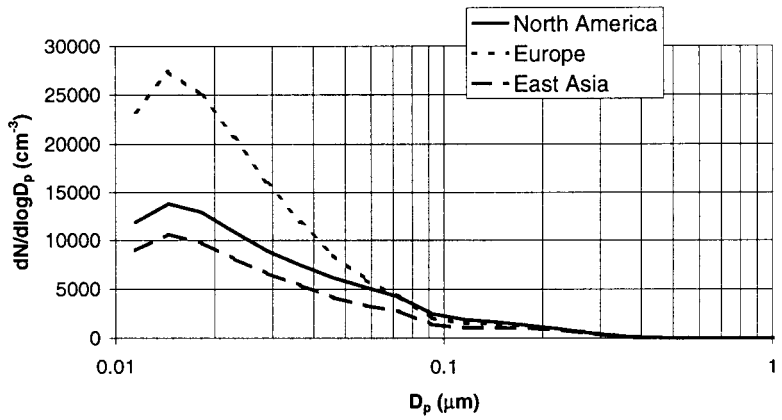

c)

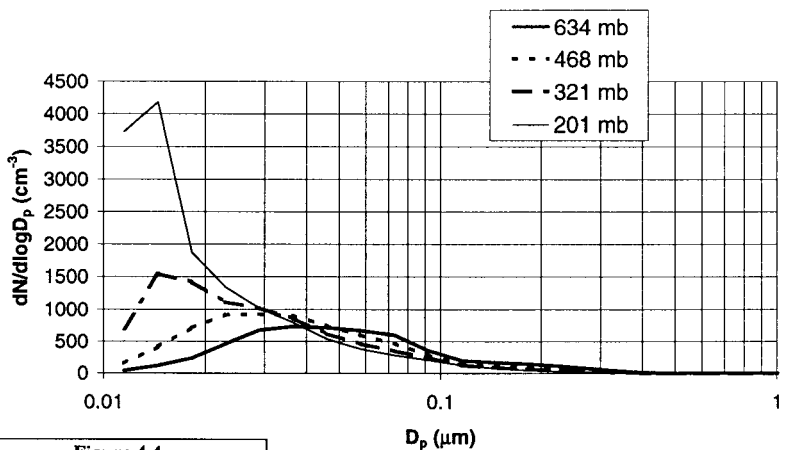

Figure 4.4

Figure 4.5

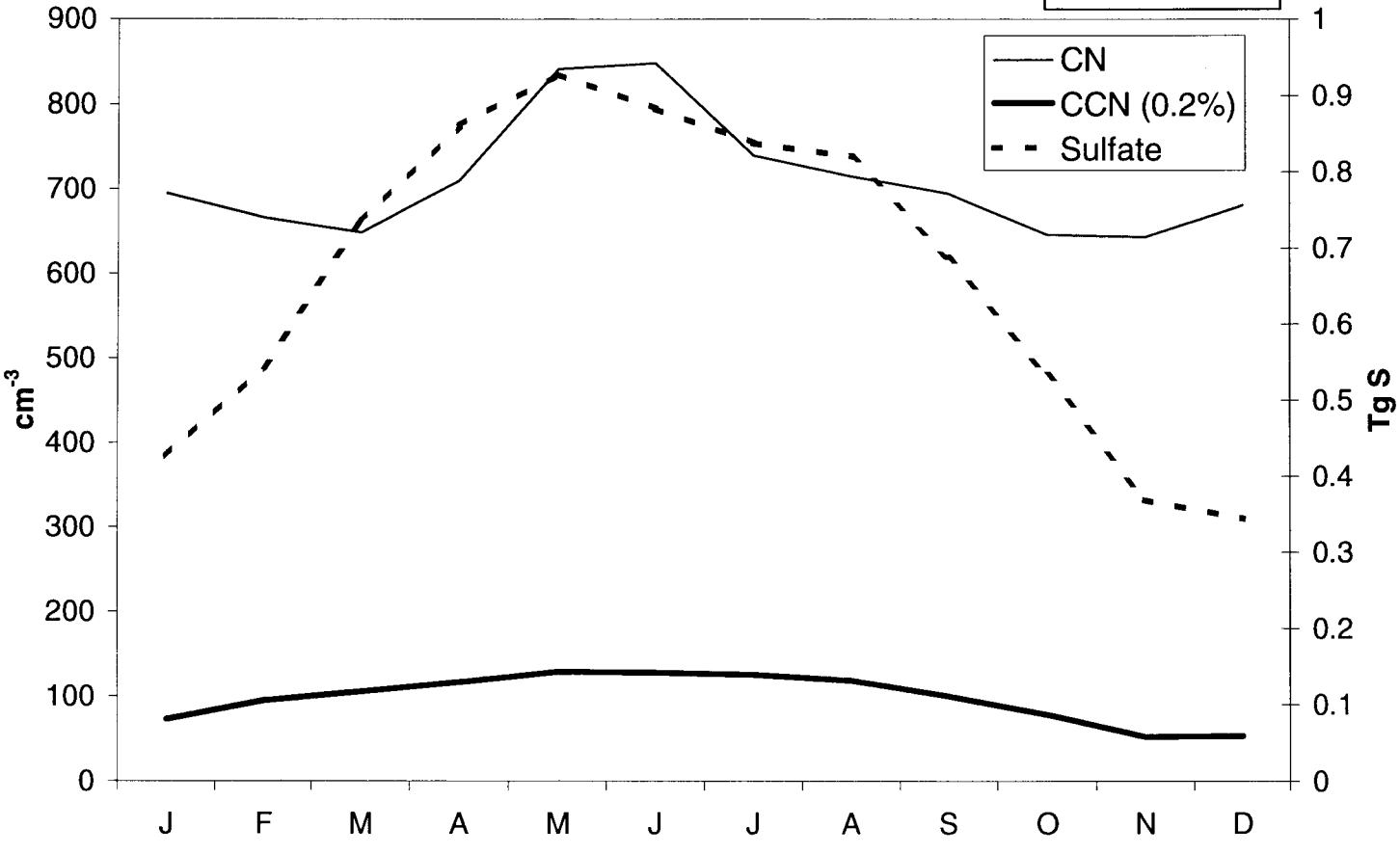
CN
CCN (0.2%)
Sulfate
cm-3
Tg S
900
800
700
600
500
400
300
200
100
0
1
0.9
0.8
0.7
0.6
0.5
0.4
0.3
0.2
0.1
0
J
F
M
A
M
J
J
A
S
O
N
D

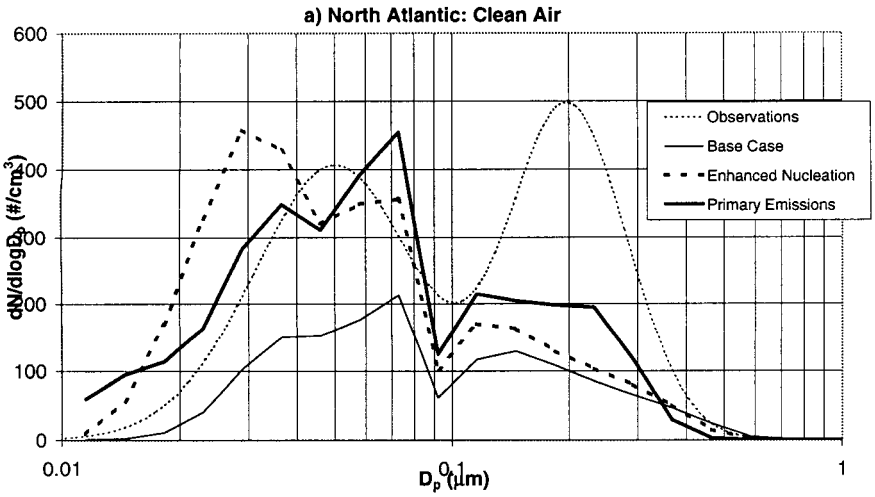
a) North Atlantic: Clean Air
600
500
400
300
200
100
0
0.01
0.1
1
dN/dlogDp (#/cm3)
Dp (μm)
Observations
Base Case
Enhanced Nucleation
Primary Emissions

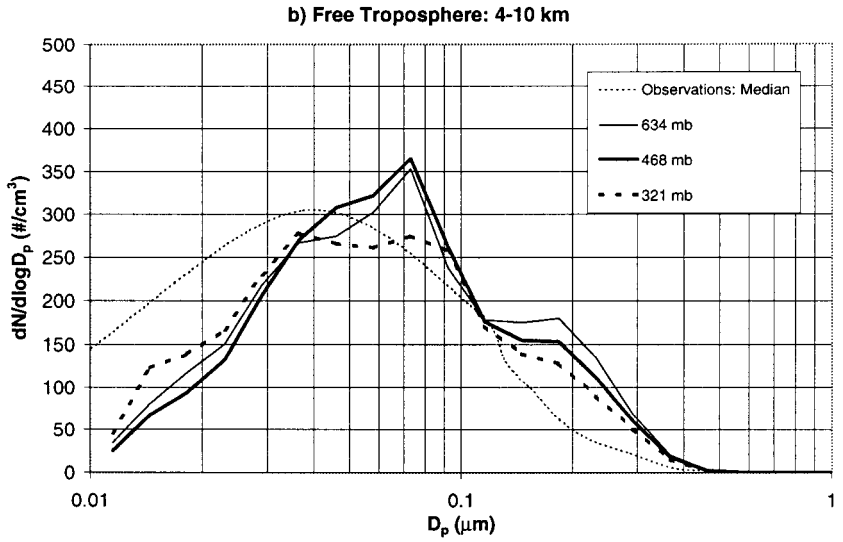
b) Free Troposphere: 4-10 km
500
450
400
350
300
250
200
150
100
50
0
0.01
0.1
1
dN/dlogDp (#/cm3)
Dp (μm)
Observations: Median
634 mb
468 mb
321 mb

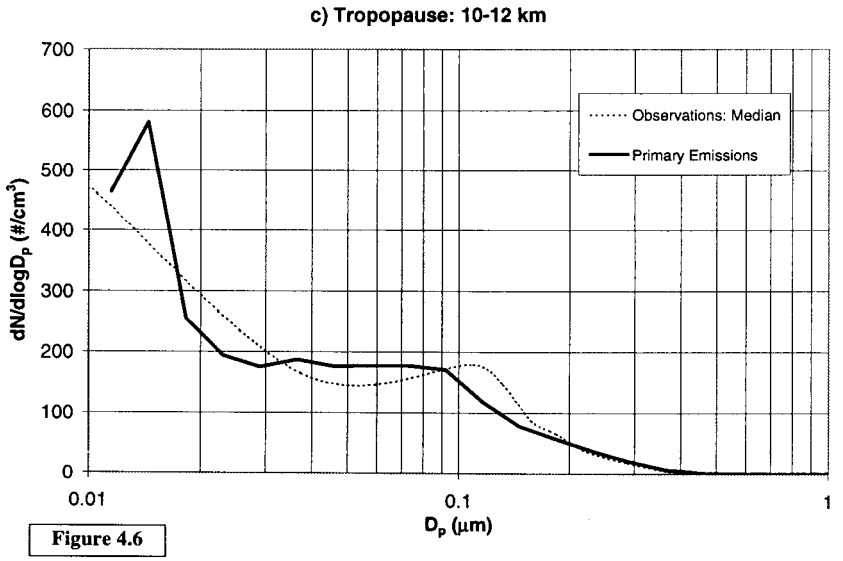
c) Tropopause: 10-12 km
700
600
500
400
300
200
100
0
0.01
0.1
1
dN/dlogDp (#/cm3)
Dp (μm)
Observations: Median
Primary Emissions

Figure 4.6

Plate 4.1

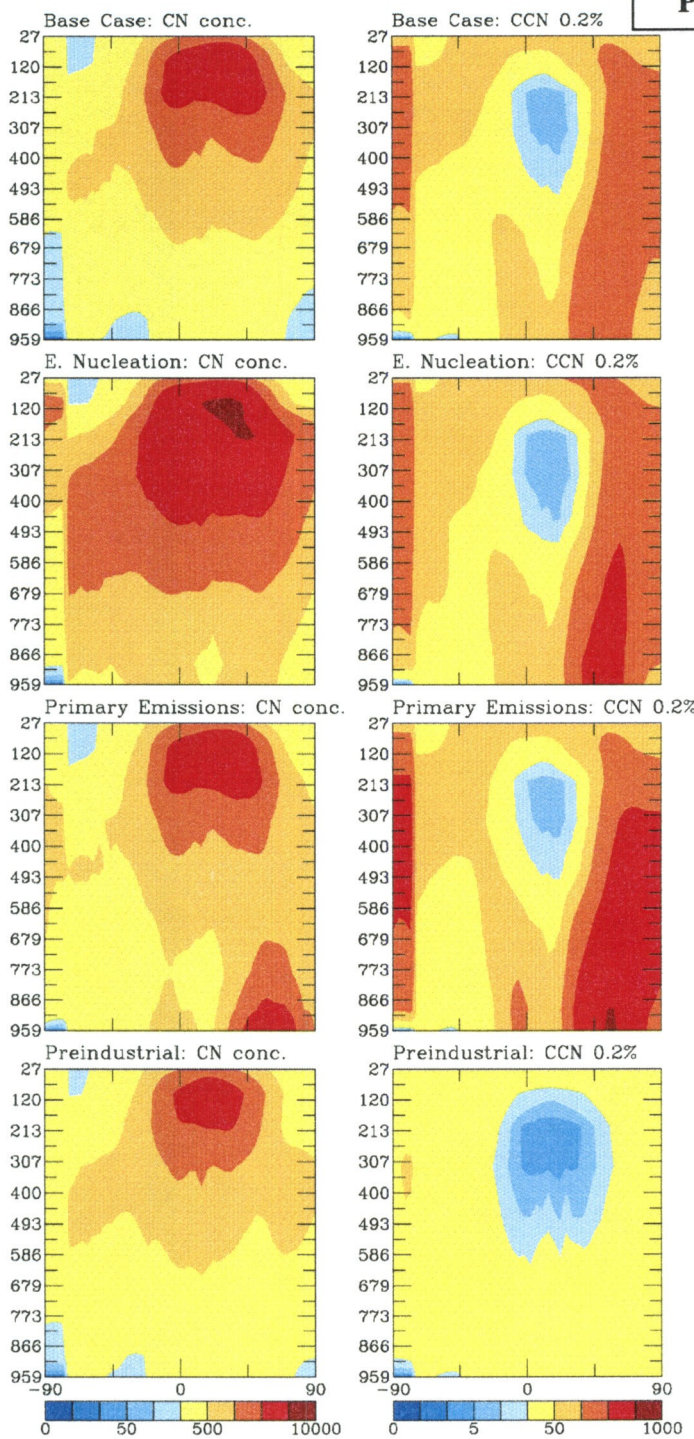
Base Case: CN conc.
Base Case: CCN 0.2%
E. Nucleation: CN conc.
E. Nucleation: CCN 0.2%
Primary Emissions: CN conc.
Primary Emissions: CCN 0.2%
Preindustrial: CN conc.
Preindustrial: CCN 0.2%
27
120
213
307
400
493
586
679
773
866
959
−90
0
90
0
50
500
10000
0
5
50
1000

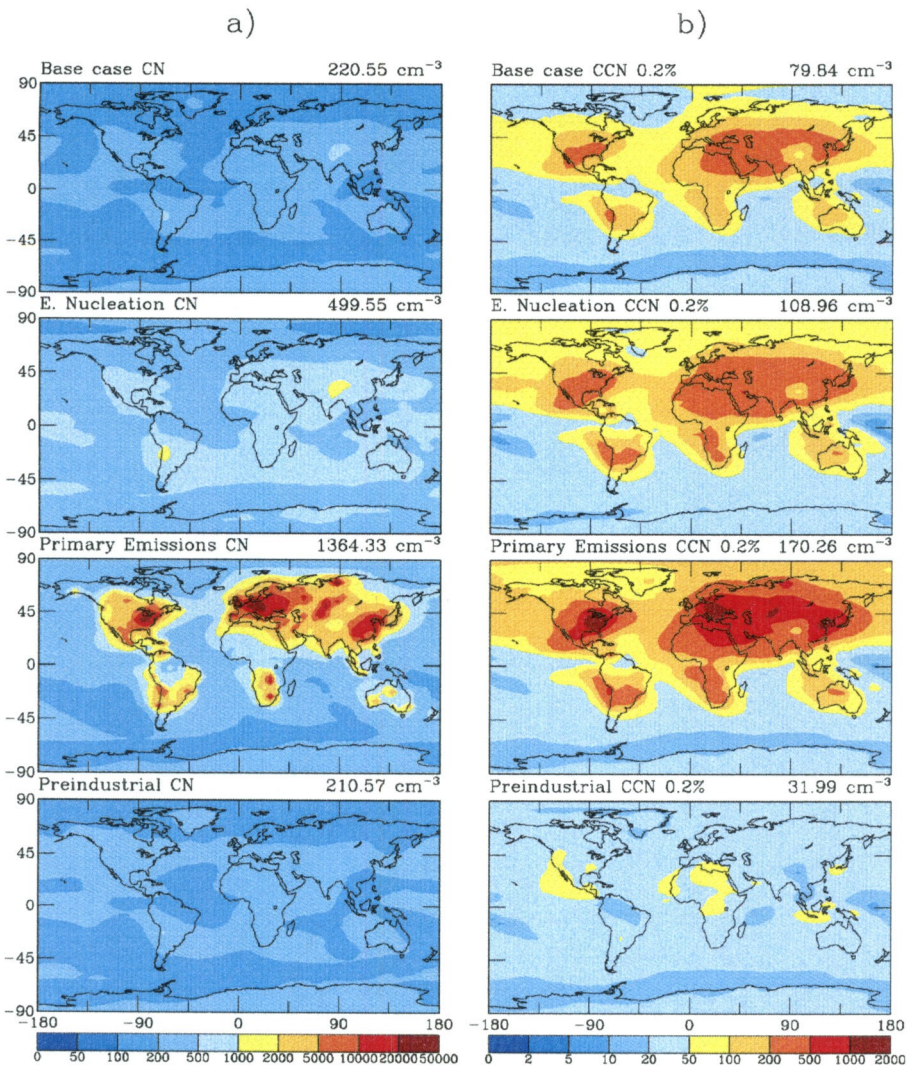
a)
b)
Base case CN 220.55 cm^{-3}
Base case CCN 0.2% 79.84 cm^{-3}
E. Nucleation CN 499.55 cm^{-3}
E. Nucleation CCN 0.2% 108.96 cm^{-3}
Primary Emissions CN 1364.33 cm^{-3}
Primary Emissions CCN 0.2% 170.26 cm^{-3}
Preindustrial CN 210.57 cm^{-3}
Preindustrial CCN 0.2% 31.99 cm^{-3}
90
45
0
−45
−90
−180
−90
0
90
180
0 50 100 200 500 1000 2000 5000 10000 20000 50000
0 2 5 10 20 50 100 200 500 1000 2000

Plate 4.2

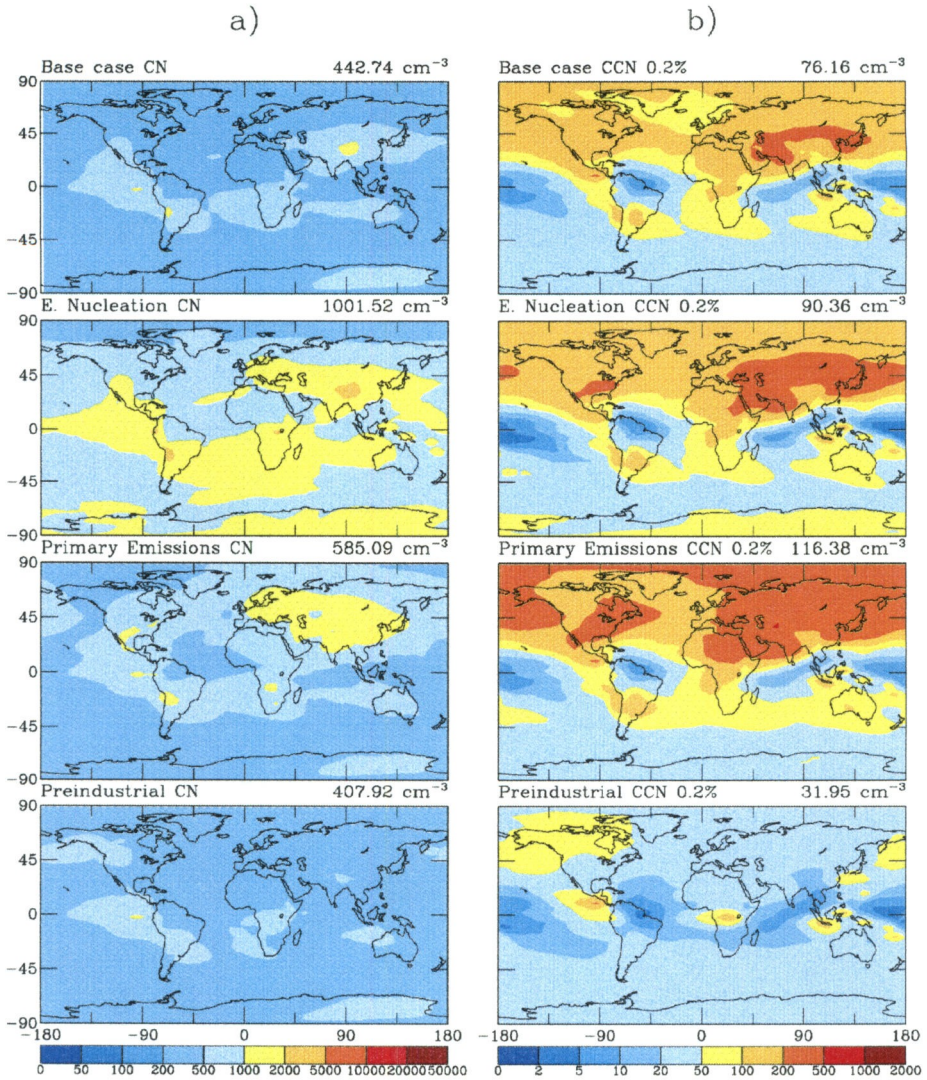
a)
b)
Base case CN 442.74 cm^{-3}
Base case CCN 0.2% 76.16 cm^{-3}
E. Nucleation CN 1001.52 cm^{-3}
E. Nucleation CCN 0.2% 90.36 cm^{-3}
Primary Emissions CN 585.09 cm^{-3}
Primary Emissions CCN 0.2% 116.38 cm^{-3}
Preindustrial CN 407.92 cm^{-3}
Preindustrial CCN 0.2% 31.95 cm^{-3}
90
45
0
-45
-90
-180
-90
0
90
180
0 50 100 200 500 1000 2000 5000 10000 20000 50000
0 2 5 10 20 50 100 200 500 1000 2000

Plate 4.3

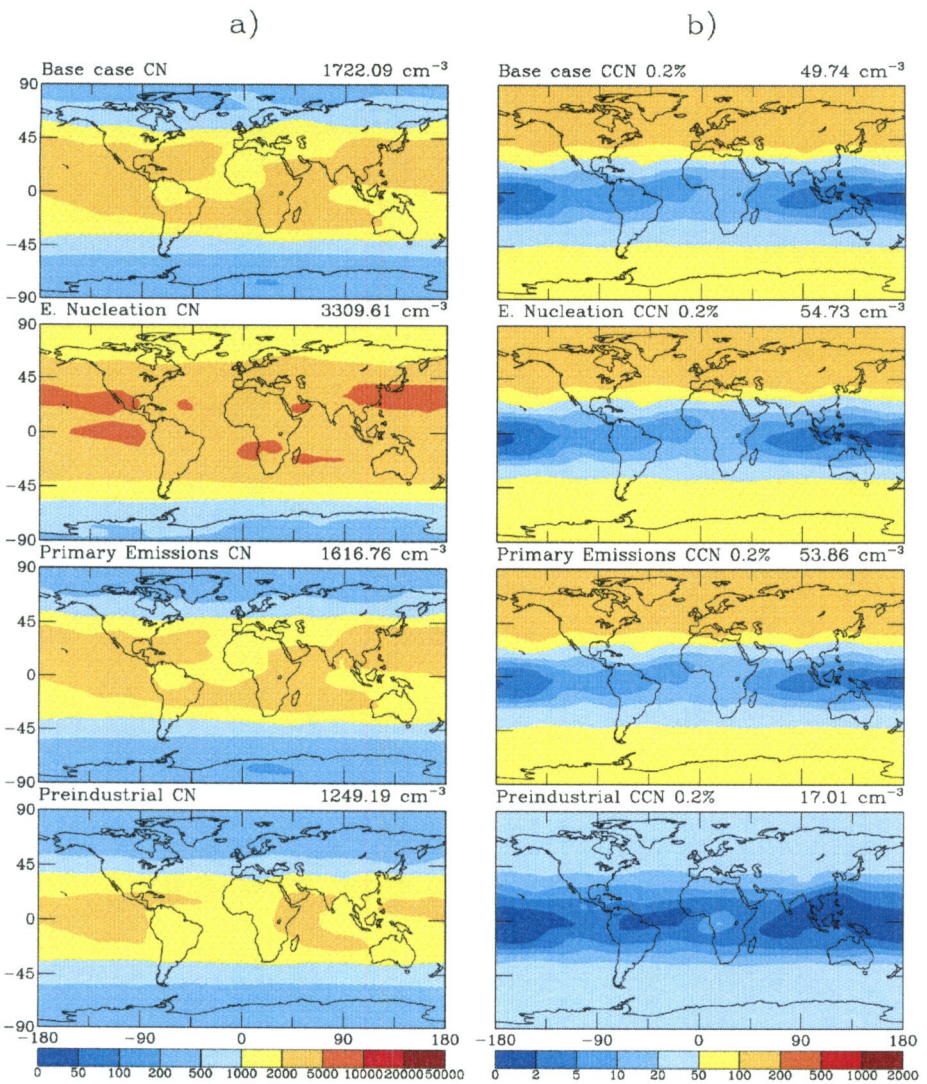
a)
b)
Base case CN 1722.09 cm^{-3}
Base case CCN 0.2% 49.74 cm^{-3}
E. Nucleation CN 3309.61 cm^{-3}
E. Nucleation CCN 0.2% 54.73 cm^{-3}
Primary Emissions CN 1616.76 cm^{-3}
Primary Emissions CCN 0.2% 53.86 cm^{-3}
Preindustrial CN 1249.19 cm^{-3}
Preindustrial CCN 0.2% 17.01 cm^{-3}
90
45
0
−45
−90
−180
−90
0
90
180
0 50 100 200 500 1000 2000 5000 10000 20000 50000
0 2 5 10 20 50 100 200 500 1000 2000

Plate 4.4

Chapter Five: Summary and Conclusions

In an effort to better understand and quantify aerosol effects on climate, the representation of aerosols in a general circulation model (GCM) has been greatly enhanced. Work has been done to move beyond representing simply the total mass concentration of sulfate and introduce chemical and size resolution to the aerosol model. In each case, interesting and unexpected results have emerged from the simulations.

Chapter 2 reported the incorporation of an aerosol thermodynamic model into a GCM, allowing the model to predict the concentrations of semi-volatile species such as nitrate and ammonia. Predicted ammonium concentrations generally agreed with observations within a factor of two while agreement on nitrate concentrations was much less satisfactory. Given the difficulty inherent in measuring ammonium and nitrate concentrations with filter packs, it is difficult to say in what ways the model needs to be improved. The simulations reported in Chapter 2 confirm that nitrate aerosol makes a significant contribution to total aerosol mass in polluted areas. Because the competition between sulfate and nitrate for ammonia results in a nonlinear dependence of total aerosol mass on precursor concentrations, it is important to include ammonia and nitrate in global models to accurately predict aerosol concentrations in industrialized regions.

In Chapter 3, the direct radiative forcing of the sulfate-nitrate-ammonium-water system was estimated for the present day and for a future emissions scenario. One interesting result of this work is the possibility that direct radiative forcing attributable to nitrate aerosol may exceed that from sulfate by the year 2100. The conclusion is that, although present-day nitrate forcing is estimated to be only –0.19 W m^{-2}, future assessments of climate change need to account for the possibility of much larger

contributions. Another important conclusion from this work was the sensitivity of the direct aerosol forcing estimate to the assumptions made about aerosol behavior at relative humidity above 90%. This suggests that global aerosol models need to improve their description of aerosols in partly cloudy regions.

Finally, Chapter 4 discussed the incorporation of aerosol microphysics into a global climate model. Such a size-resolved aerosol model offers the possibility of representing the indirect effect of aerosols in a mechanistic, rather than empirical, fashion. This work used a two-moment sectional algorithm that more accurately and efficiently predicts and conserves aerosol number concentrations than microphysics algorithms used in previous work. The algorithm has been tested by simulating the number concentrations and size distributions of tropospheric sulfate. Predicted CN concentrations generally agree with observations to within 25%. Simulated size distributions also closely resemble observations, although the absence of other aerosol components probably accounts for the underprediction of CCN concentrations in regions such as the North Atlantic. Sensitivity simulations also make it clear that there are significant uncertainties in the budget of aerosol number. In particular, uncertainties in the number of particles emitted and in the rate of new particle formation have significant impacts on predicted CN and CCN concentrations.

At this point, the improvements made in representing the chemical composition of the aerosol described in Chapters 2 and 3 have remained separate from those made in representing the microphysics of the aerosol described in Chapter 4. Furthermore, this work has not considered the impacts of other important classes of aerosol such as sea salt, organic carbon, black carbon, and mineral dust. Future work will address these

deficiencies by combining the thermodynamic and microphysical simulations and adding other aerosol types to the model. This will improve model performance in most areas and allow for a comparison against a broader range of observational data. As aerosol models become more realistic, it becomes increasingly important to test them in greater detail against observations. The preliminary comparisons made in this work make it clear that there is much work to be done in this regard. Another logical step is to couple the aerosol microphysical simulation presented here to the climate model cloud scheme to generate estimates of the magnitude of the indirect aerosol effect.